EXPERIMENTAL STUDY OF THE BEHAVIOUR OF THE SYNTHETIC JETS FOR EFFECTIVE FLOW SEPARATION CONTROL

A thesis submitted to the University of Manchester for the degree of Doctor of Philosophy in the Faculty of Engineering and Physical Sciences

2010

Fushui Guo

School of Mechanical, Aerospace and Civil Engineering

Contents

List of Figures

List of Tables

Nomenclature

a	Speed of sound
A	Orifice area
b	Laser bean diameter
B	Magnetic field
c	Aerofoil chord
c_f	Skin friction coefficient
C_e	Effectiveness of the control effect
C_f	Skin friction coefficient (= $\tau_w/(\frac{1}{2}\rho U_\infty^2)$)
C_{Lmax}	Maximum lift coefficient
C_μ	Jet momentum coefficient (= $2h/c(U_o/U_\infty)^2$)
d	The ratio of boundary layer thickness to orifice diameter (= δ/D_o)
d_{IA}	The size of interrogation area
d_p	Seeding particle diameter
D_c	Cavity diameter
D_o	Orifice diameter
E	Energy provided by the piston (Chapter 2); Total uncertainty in PIV measurements (Chapter 3)
E_R	Energy required for a steady ring
E_α	Non-dimensional energy
f	Diaphragm oscillation frequency (Chapters 1-7); Focal length of lens (Chapter 3)
f_H	Helmholtz resonant frequency
F^+	Non-dimensional excitation frequency (= fL_s/U_∞)
g	Acceleration due to gravity (= 9.81m/s^2)
h	Orifice depth (Chapters 1-7); Slot width (Chapter 2)
H	Cavity height
j	Current-density field
l	Vortex ring spacing
L	Dimensionless stroke length (=L_o/D_o)
L_b	Three-dimensional body force
L_o	Stroke length
L_s	Length of separated region
M	Mach number (Chapter 2); Magnification (Chapter 3)
$\dot{M}_o$	Instantaneous momentum flux rate
$\overline{\dot{M}_o}$	Time-averaged momentum flux rate
n	Distance between streamlines
p	Pressure

P	Velocity program factor
q	Freestream dynamic pressure
$\dot{Q}_o(t)$	Instantaneous mass flux rate
$\overline{\dot{Q}_o}$	Time-averaged mass flux rate
r	Radial distance from diaphragm/orifice centre
r_c	Radius of diaphragm
Re	Reynolds number (= $\overline{U_o} D_o / \nu$)
Re_L	Reynolds number (= $\overline{U_o} L_o / \nu$)
Re_{peak}	Reynolds number (= $U_{peak} D_o / \nu$)
Re_Γ	Reynolds number (=Γ/ν)
S	Stokes number (Chapters 2, 4-6); Point of separation (Chapter 2); Saddle point (Chapter 5)
St	Strouhal number (= $fD_o / \overline{U_o}$; = fD_o / U_∞)
Str_b	Jet spread rate
t	Time
T	Period of oscillation cycle
u	Velocity
$\widetilde{u}_o$	Instantaneous space-averaged jet velocity
U_g	Seeding particle settling velocity
U_o	Space-averaged jet velocity
$\overline{U_o}$	Time-averaged jet velocity
U_{peak}	Peak jet velocity
U_r	Velocity relative to vortex ring
U_x	Streamwise velocity component
U_y	Wall-normal velocity component
U_τ	Friction velocity
U_∞	Freestream velocity
v	Velocity
V	Peak-to-peak voltage
V_{max}	The maximum velocity
VR	Jet-to-freestream velocity ratio (=$\overline{U_o} / U_\infty$; = U_{peak} / U_∞)
x	x Streamwise distance from orifice exit
y	y Normal distance from orifice exit
z	z Spanwise distance from orifice exit
Greek Symbols	
α	Inclined angle of airfoil (Chapter 2); Angle formed between the dye line at the baseline condition and the horizontal direction
β	Angle formed between the dye line under the controlled conditions

	and the horizontal direction
γ	Azimuthal angel of jet actuators (Chapter 2); Inclined angle of the flap (Chapter 6)
Γ	Vortex circulation
Γ_o	Initial (or total) circulation
δ	Boundary layer thickness (Chapters 2-3, 5-6); Diaphragm deformation (Chapter 4)
δ^*	Boundary layer displacement thickness
Δ	Peak-to-peak displacement at the diaphragm centre
Δx	x Spacing of velocity vectors in x-direction
Δy	y Spacing of velocity vectors in y-direction
θ	Boundary layer momentum thickness
λ	Light wavelength
μ	Molecular dynamic viscosity
ν	Molecular kinematic viscosity
ρ	Density
ρ_p	Seeding particle density
τ	Shear stress
$\overline{\tau}$	Spanwise-averaged wall shear stress
τ_o	Undisturbed wall shear stress
τ_w	Wall shear stress
ω	Vorticity
Subscripts	
c	Cavity value
e	Uncertainty value
o	Orifice value
w	Wall value

Abstract

The increase in fuel price and the enforcement of more restrictive regulations have presented significant challenges to the aircraft industry and forced the development and implementation of revolutionary technologies so as to reduce operational costs and environmental impact of aircraft transportation. The development of active flow control is believed to be one of the key measures to meet these challenges.

Synthetic jet actuators, as a promising method for flow separation control, are capable of injecting momentum to the external flow with zero-net-mass-flux, which negate the need for air supplies and complex piping systems. So far, the capability of synthetic jets in controlling flow separation has been demonstrated in many laboratory-based investigations. However, our understanding of the fluid mechanics of synthetic jets is still limited. An improved understanding is essential to the optimisation of the synthetic jet actuator operating conditions for a given flow so as to maximise their flow control effectiveness for a practical setting. The present research is aimed at achieving this goal through a series of carefully designed experiments.

Firstly, PIV measurements and smoke-wire flow visualisation of circular synthetic jets in quiescent air are undertaken to study the effect of dimensionless parameters on the formation and the extent of vortex roll-up. The results show the dimensionless stroke length (L) affects the onset of suction cycle on the vortex ring and the Stokes number (S) determines the strength of vortex roll-up. A criterion for vortex roll-up is also established. Based on PIV (Particle Image Velocimetry) measurements of both micro-scale and macro-scale synthetic jets, it is confirmed that the characteristic of synthetic jets of different scales will be identical when the L, S and Re_L are the same.

Dye visualisation of round synthetic jets issued into a zero-pressure gradient laminar boundary layer is carried out in a water flume. Three different types of vortical structures are found to be produced as a result of the interaction of a synthetic jet with a laminar boundary layer as the operating condition of synthetic jets changes, i.e., hairpin vortices, stretched vortex rings and tilted vortex rings. Hairpin vortices and stretched vortex rings are formed as the result of the upstream branches of the vortex rings being weakened by the resident vorticity in the boundary layer. In the case of tilted vortex rings, the vortex rings remain intact as they emerge from the boundary layer due to an increased jet strength.

Finally, laser induced fluorescent flow visualisation and PIV measurement are undertaken to study the flow separation control effectiveness of a synthetic jet array issued upstream of a separated laminar flow over a flap in water. Based on the results from the experiment, parameter maps showing the effectiveness of separation control at different actuator operating conditions are produced. It is found that a good control effect is associated with the presence of hairpin type of structures and a velocity ratio (VR) in the range of 0.3 and 0.7. For the experimental conditions tested in this thesis, operating the synthetic jets at a dimensionless stroke length (L) around 2 and velocity ratio (VR) around 0.6 would deliver the best flow control effect with the least energy consumption.

Declaration

No portion of the work referred to in this thesis has been submitted in support of an application for another degree or qualification of this or any other university or other institution of learning.

Copyright

Acknowledgement

I would like to express my sincere gratitude and deep appreciation to my supervisor, Dr. Shan Zhong, for her excellent supervision on this work and her great assistance in the preparation of this thesis. Especially during the period of the writing up, she has spent a tremendous amount of time to improve the thesis. Her inspiration and warm personality have won my highest respect and love.

I would also like to sincerely thank the technical staff at the Goldstein Research Laboratory, Mike, Ken, David, Stuart, Andrew and Ian, for the help and support to the manufacturing needs and advice of this project.

Sincere thanks are due to colleagues (and friends), Xiaoan Mao, Meng Li, Mark Jabbal, Bilkay Gulacti, Hui Tang, Jue Zhou, Qingfeng Xia, Lei Shi and many others for all their help, encouragement and inspiration.

Thanks are also due to The University of Manchester and Universities UK for the financial support. The latter provided the Overseas Research Student Award (ORS) for my PhD research.

And last, but by no means least, I am eternally grateful to my family and Miss Jing Ji for all their support, understanding and encouragement.

1 Introduction

1.1 Background

The manufacturing industry of civil transport aircraft is well established, with operational costs and efficiencies far exceeding those of only a couple of decades ago. The increase in the fuel price, the enforcement of more restrictive noise regulations, and the need to operate bigger airplanes so as to reduce costs, however, have presented significant challenge to the aircraft industry and forced the development and implementation of new technologies. Revolutionary technologies will have a significant role to play towards reducing the economic and environmental impact of future aircraft in order to accommodate a more sustainable growth in air traffic. Amongst these new developed technologies, the development of active flow control is believed to be one of the key measures towards to the realisation of these goals (Kral, 1998; Collis *et al*, 2004 and Reneaux, 2004).

As defined by Flatt (1961), the term "boundary layer control" includes any mechanism or process through which the boundary layer is caused to behave differently than it normally would, were the flow developing naturally along a smooth straight surface. Flow control technologies that are ultimately deemed successful for aircraft implementation will be those that produce the desired effect outweighing the economic and energy costs associated with their implementation.

The possible varieties of flow control that could be implemented on an aircraft wing are shown in figure 1.1. Separation control utilised at the leading and trailing edges of the wing could primarily be used during the take-off and landing regimes of the flight envelope to reduce the pressure drag. Laminar, transition and turbulence flow control technologies could be utilised on the main wing during cruise flight to reduce the skin friction drag. Shock wave control could also be utilised during cruise flight to reduce wave drag encountered at high Mach numbers.

Flow separation occurs when a boundary layer encounters a sufficiently large adverse pressure gradient. This poses a significant problem for the high-lift system utilised on the wings of many civil transport aircrafts, as shown in figure 1.2. The high-lift system consists of a main wing as well as its leading edge devices (slat) and trailing edge devices (flap). These devices are deployed to enhance the low-speed performance of an aircraft by increasing lift coefficient during the take-off and landing phases of the

flight envelop, where the boundary layer would have separated at a much lower angle of incidence without these devices.

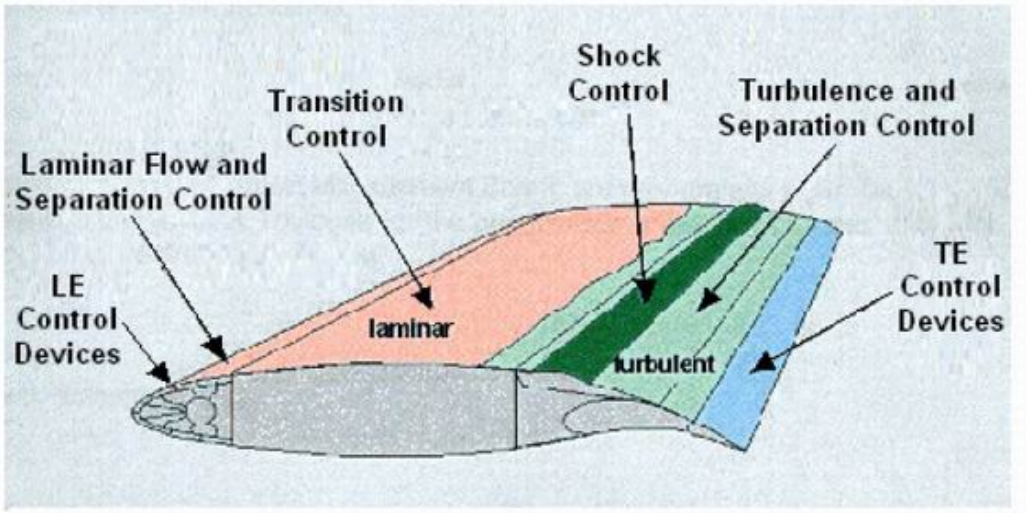

Figure 1.1 Schematic illustrating the potential of flow control technologies for aircraft wing application (modified from Sellars, 2003)

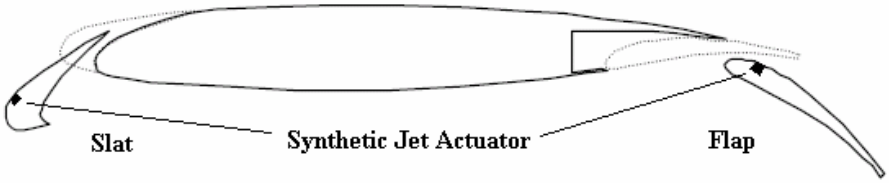

Figure 1.2 Position of synthetic jet actuators for potential flow control on high lift systems

Flow separation control, which has the potential to alleviate separation further, can lead to a reduction in the size and deflection angle of the leading and trailing edge devices. These will subsequently lead to savings on weight and a reduction of system complexity (Lin *et al*, 1994; Harrison 2006), which finally can be translated into a reduction in fuel consumption hence an increase in profitability, a reduction in the level of pollutant emissions will also be achieved accordingly. To underline the importance of drag reduction of an airline fleet, a study by Reneaux (2004) estimated a 1% reduction in drag could lead to a 0.2% reduction in the direct operating costs of a civil transport aircraft. This drag reduction could also lead to 1.6 tons saving in the aircraft operating empty weight.

Commonly used flow separation control methods include vortex generators, steady suction/blowing and periodic excitation, which works by energising the fluid flow in the boundary layer via an increased local mixing. The vane vortex generators have already been routinely applied to civil transport aircrafts to delay flow separation.

Although the vortex generators are easy to implement, they produce unwanted parasitic drag during the cruise flight and their effectiveness is also limited within small operational range.

The concept of a blowing technique via an array of steady jets to prevent or delay separation is well established. An injection of high momentum fluid into the boundary layer increases the near-wall momentum, thereby enhancing the ability of the boundary layer to withstand an adverse pressure gradient (Schlichting and Gersten, 2000). However, the method requires a complex internal compressed air supply system, which carries a large weight penalty hence limiting its operational gain. The other similar technique is the suction, which has been demonstrated to be an effective means of delaying separation from the pioneering experiments of Prandtl (1904). However, like the steady blowing, the high energy consumption, the requirement for a complex internal vacuum system and the problems associated with the orifice blockage currently render it impractical for aircraft implementation.

Periodic excitation was introduced as a method for flow separation control in the 1970's and has recently received more attention due to the advantage to delivery a similar level of control effectiveness compared to its steady counterpart, but with a reduced net mass flux. A good review on this topic can be found in Greenblatt and Wygnanski (2000). Periodic excitation generates large-scale coherent vortex structures in a separated flow, which transport momentum across the boundary layer hence delay flow separation. Furthermore, these coherent structures can be phase-locked to the natural instability of a separated flow to make the separated flow reattached (Nishri and Wygnanski, 1998). A good example of the period excitation is pulsed jets, which has been found to be an effective means of preventing flow separation (Seifert *et al*, 1993; McManus and Magill, 1996; Magill and McManus, 2001). Despite its proven effectiveness and reduced energy consumption, this method still requires a complex internal piping system.

Synthetic jets have received a lot of research attention since the mid of 1990s due to their ability to impart periodic excitation with no net mass flux. Figure 1.3 shows a typical synthetic jet actuator (SJA), which consists of a cylindrical cavity (with a diameter D_c and height H) bounded by rigid side walls with an oscillating diaphragm clamped at one end and an orifice plate (with a depth h and orifice diameter D_o) at the other. As the diaphragm moves away from the orifice, the volume of the cavity increases and the ambient fluid is entrained into the cavity (suction stroke). When the

diaphragm moves towards the orifice, the cavity volume (blowing stroke) is reduced. The shear layer forms along the walls of the orifice separates at the lip of the orifice exit which subsequently rolls up to form a vortex ring. Repeating this process at a certain frequency produces a succession of vortex rings that propagate away from the orifice under the influence of their own self-induced velocity. Hence, in the time-averaged sense, a jet is 'synthesised' from the ambient fluid without an external fluid supply.

So far, the capability of synthetic jets in controlling flow separation has been demonstrated in many laboratory-based investigations, such as on bluff bodies (e.g. Amitay *et al*, 1998; Crook *et al*, 1999; Rediniotis, 1999; Glezer and Amitay, 2002), and lift-producing bodies (Amitay *et al*, 1998, 1999, 2002; Smith *et al*, 1998; McCormick, 2000) with a characteristic Reynolds number up to 10^6. In these investigations, it has been observed that the separation line in the laminar or turbulent boundary layer was significantly pushed downstream and for some aerofoil models, the flow became fully attached with the application of synthetic jets. Synthetic jet actuators also can be micro fabricated using manufacturing techniques common to micro-electro-mechanical systems (MEMS) (Janhavi *et al*, 2008; Warsop, 2004; Warsop *et al*, 2007).

Despite the proven demonstrations of the global effect of synthetic jet injection for flow separation control in the laboratory, little is known about the fluid mechanics of their interaction with a boundary layer. Such an understanding is essential to optimising the synthetic jet actuator operating conditions for a given flow so as to maximise their flow control effectiveness for a practical setting.

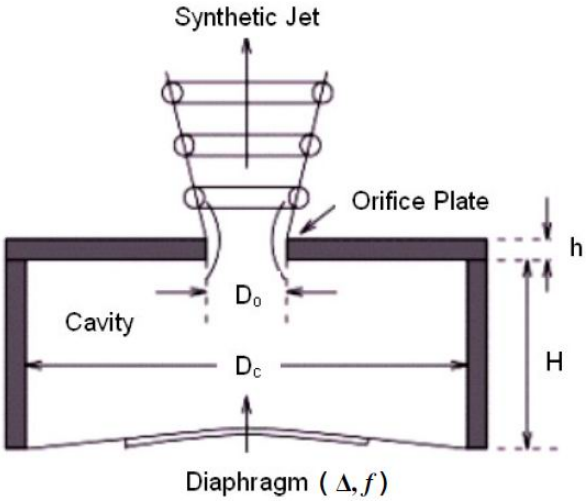

Figure 1.3 Schematic of synthetic jet actuator (Crook and Wood, 2000)

At the University of Manchester, the research on synthetic jets has been undertaken since 1998. This follows the legacy work of synthetic jets by Crook (2002),

who demonstrated the delay of a turbulent flow separation on a circular cylinder using an array of synthetic jet actuators. Subsequent work has included an investigation of synthetic jets in quiescent conditions towards improving understanding of the effects of operating conditions and actuator geometry on synthetic jet actuators performance (Crook and Wood, 2001) and the behaviour of synthetic jets in a cross flow (Crook *et al*, 2000) and a boundary layer (Zhong *et al*, 2005).

However, many issues still remain to be addressed before synthetic jets can be designed and used on aircraft with confidence. Firstly, for delaying flow separation on the leading and trailing edge devices at full-scale conditions, synthetic jet actuators with an orifice diameter of ten to hundred micros operating at frequency of a few kilohertz could be used. Performing detailed flow measurements as such devices is often beyond the capability of laboratory instrumentation. Hence the studies have to be undertaken on generic rigs operating at benign conditions unrepresentative of those at which synthetic jet actuators will have to operate. A need to identify the dimensionless scaling parameters for actuators of different scales therefore arises so as to enable the research finding in laboratory to be applicable to the actual devices. Secondly, it is known that synthetic jets produce streamwise vortices in a boundary layer which are capable of delaying flow separation. The strength of these vortices is directly linked to the strength of the vortex rings which are formed at the orifice exit. It would be hence desirable to know which actuator parameter determines the strength of the vortex roll-up for the synthetic jet actuator. Thirdly, in order to understand the interaction between the synthetic jets with a boundary layer, it is useful to understand how the nature of the vortical structures formed varies as the operating conditions of the synthetic jet changes. Finally, for practical applications it is essential to know at what these actuators should be operated in order to maximise their flow control effect for a given external flow. The research work in this project aims to address to these issues.

1.2 Aims and Objectives of the Research

The aims of the present research are to achieve an improved understanding of the fluid mechanics of synthetic jets issued into a quiescent flow, an attached boundary layer and upstream of a separated boundary layer for the purpose of maximizing their flow control effectiveness. To achieve these aims, a series of objectives are formulated as follows:

- To investigate the criteria for the vortex roll-up of synthetic jets in quiescent conditions as well as to investigate the performance of micro-scale synthetic jets so as to confirm the dimensionless parameters adequate for the scaling effect
- To study the nature of the vortical structures as a result of the interaction synthetic jets with a zero-pressure gradient laminar boundary layer
- To investigate the effectiveness of flow separation control using an array of synthetic jets and to identify the type of flow structures for the best flow control effect

Within the present context, in general macro-scale refers to actuators with orifices diameters of the order of a few millimetres whereas micro-scale refers to actuators with orifices diameters of the order of ten to hundred micrometers.

In the current study, the diaphragm of synthetic jet actuator is driven by a permanent magnetic shaker since it allows the actuation frequency f and the peak-to-peak displacement Δ, of the diaphragm to be varied independently. This set up has the advantage of allowing the effect of Δ and f to be studied in isolation.

The measurement techniques chosen depend on the objectives of each experiment. In quiescent conditions, Smoke-wire visualisation is used to study the vortex roll-up in quiescent condition due to its effectiveness. Particle image velocimetry (PIV) is used to quantify the effect of the actuator operating parameters and geometry. PIV is non-intrusive technique which allows the velocity field to be obtained simultaneously on a chosen 2D plane. PIV also has the advantage of being able to detect reverse flows. For the study of the interaction of synthetic jet and a boundary layer, and the separation control effectiveness of the synthetic jet array, water is chosen as the flow medium. The visualisation of vortical structures in water is clearer and more readily attainable than in air. Fluorescent dye visualisation and PIV are used to study the effectiveness of flow separation control.

In order to simplify the measurements and computations, the present study was undertaken in a laminar boundary layer. Most flows that occur in practical applications, including the flow over aircraft wings tend to be turbulent. However, it is believed that some commonalities exist in the interaction mechanisms between synthetic jets and a boundary layer no matter it is laminar or turbulent. Firstly, the basic effect of shear in a boundary layer and the effect of suction cycle on the formation of coherent structures produced by synthetic jets in the boundary layer are similar regardless of whether the boundary layer is laminar or turbulent. Secondly, the entrainment brought about by the

coherent vortices produced by the synthetic jets is an important flow separation mechanism in both flows. In the authors' opinion, understanding the behaviour of synthetic jets in a laminar flow is the first logical step towards understanding the complex behaviour of synthetic jets in a turbulent flow, and the finding from this work could shed some light on the design of synthetic jet actuators for flow control at practical settings.

Acarlar and Smith (1987) have studied the behavioural aspects of hairpin vortices in a laminar flow to improve their understanding of the interaction mechanism of hairpin vortices in turbulent flows. They demonstrated that hairpin vortices generated in an otherwise laminar environment give rise to qualitative patterns (dye and hydrogen bubble visualisation) that are essentially the same as those obtained in turbulent boundary layers. Furthermore, hot wire measurements revealed that the mean velocity profiles produced by the interaction between hairpin vortices and a laminar boundary layer develop a logarithmic region reminiscent of a turbulent profile. Therefore, the similarity in vortex interaction between laminar and turbulent flows justifies the present methodology.

1.3 Layout of the Thesis

This thesis aims to meet the project objectives by documenting this research work in seven chapters.

Chapter 2 provides a review of the literature relevant to this project. This includes the phenomenon of flow separation, various flow separation control technologies and the research undertaken so far on synthetic jets. Chapter 3 describes the experimental facilities and methods used to fulfil the aforementioned objectives. The results and discussion in the main body of this thesis are divided into three chapters, according to the order of the work that was carried out. Chapter 4 presents the results from the synthetic jet actuator in a quiescent environment. In the first part of this chapter, the effect of the non-dimensional jet flow parameters is described. In the second part, the criterion for vortex roll-up for synthetic jets and the performance of micro-scale synthetic jets are discussed. Chapter 5 examines the vortical structures produced as a result of the synthetic jet-boundary layer interaction in a zero-pressure-gradient boundary layer. Chapter 6 investigates the effectiveness of flow separation control using an array of synthetic jets. Finally, in Chapter 7 the key finding from this work is summarised and suggestions for future work are made.

2 Literature Review

The purpose of this chapter is to present a comprehensive review of the work that has been done about the synthetic jets and synthetic jet actuators in the context of flow separation control. This review also identifies the areas where further research is required.

2.1 Flow Separation

Prandtl (1904) pioneered the modern use of the flow control in his epoch-making presentation to the third International Congress of Mathematicians held at Heidelberg, Germany. In just 8 pages (as required for acceptance by the Congress) of paper entitled "On the Motion of a Fluid with Very Small Viscosity (translated)", Prandtl introduced the boundary layer theory, explained the mechanism of steady separation, opened the way for understanding the motion of real fluids, and described several experiments in which the boundary layer was controlled.

Prandtl was the first to recognise the physical cause of separation at high Reynolds numbers as being associated with the separation of boundary layers that must form on all solid surfaces. In accordance with the Prandtl's theory, a high Reynolds number flow past a rigid body has to be subdivided into two characteristic regions. The main part of the flow field may be treated as inviscid. However, for all Reynolds numbers, no matter how large, there always exists a thin region near the wall where the flow is predominantly viscous. Prandtl termed this region the boundary layer, and suggested that it is because of the specific behaviour of this layer that flow separation takes place.

Flow development in the boundary layer depends on the pressure distribution along the wall. If the pressure gradient is favourable, i.e. the pressure decreases downstream, then the boundary layer remains well attached to the wall. However with an adverse pressure gradient, when the pressure starts to rise in the direction of the flow, the boundary layer tends to separate from the body surface. The reason for separation was explained by Prandtl in the following way. Since the velocity in the boundary layer drops towards the wall, the kinetic energy of fluid particles inside the boundary layer appears to be less than that at the outer edge of the boundary layer, in fact the closer a fluid particle is to the wall the smaller appears to be its kinetic energy. This means that

while the pressure rise in the outer flow may be quite significant, the fluid particles inside the boundary layer may not be able to get over it. Even a small increase of pressure may cause the fluid particles near the wall to stop and then turn back to form a recirculating flow region characteristic of separated flows.

The flow behaviour close to separation in terms of the changes experienced by the boundary layer velocity profiles in an adverse pressure gradient flow developing over an object surface, are represented schematically in figure 2.1. Since the velocity at the wall is always zero, the gradient $[\partial u/\partial y]_{y=0}$ must be positive upstream of separation, zero at the point of separation, and negative in the reverse flow region. Downstream of the separation point the shear layer either passes over the region of recirculating fluid and reattaches to the body surface or forms a wake and never reattaches to the body. The characteristic dimension of the recirculating region is quite large in the later case and is of the order of the body height.

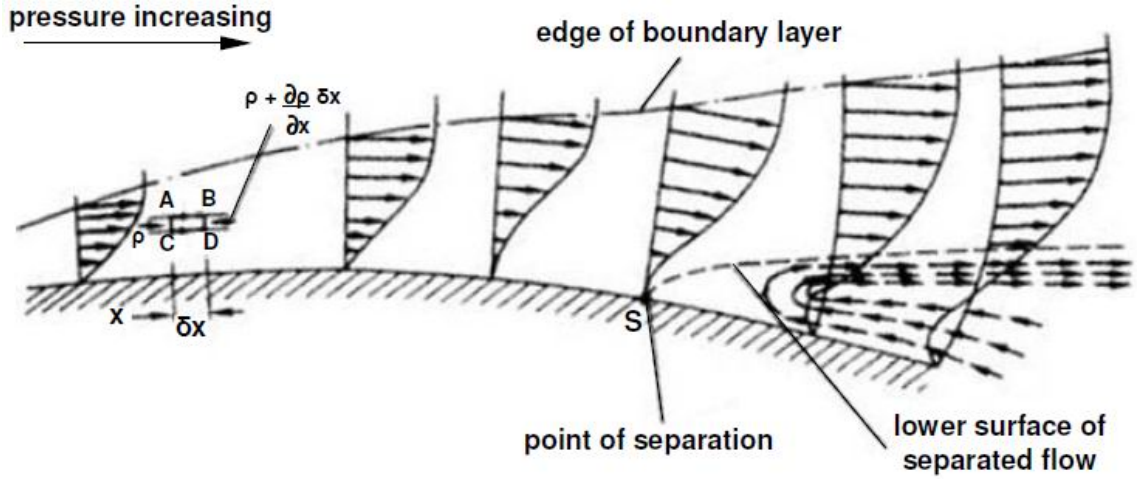

Figure 2.1 Schematic of separated flow induced by an adverse pressure gradient (Modified from Houghton and Carpenter, 2003).

2.2 Flow Separation Control

2.2.1 Control Goals and the Interrelation

An external wall-bounded flow, such as that developing on the exterior surface of an aircraft or a submarine, can be manipulated to achieve transition delay, separation postponement, lift increment, skin-friction and pressure drag reduction, turbulence augmentation, heat transfer enhancement, or noise suppression. These objectives are not necessarily mutually exclusive. Figure 2.2 is a schematic representation of the interrelation between one control goal and another. To focus on the discussion further,

think of the flow developing on a lifting surface such as an aircraft wing. If the boundary layer becomes turbulent, its resistance to separation is enhanced and more lift could be obtained at an increased incidence. On the other hand, the skin-friction drag of a laminar boundary layer can be an order of magnitude less than that for a turbulent one. If transition is delayed, lower skin friction as well as lower flow-induced noise can be achieved. However, the laminar boundary layer can only sustain a very small adverse pressure gradient without separation, and subsequent loss of lift and increase in form drag occur. Once the laminar boundary layer separates, a free-shear layer forms and for moderate Reynolds numbers transition to turbulence takes place. An increased entrainment of high-speed fluid due to the turbulent mixing may result in reattachment of the separated region and a formation of a laminar separation bubble. At a higher incidence, the bubble breaks down so that the flow separates completely or a longer bubble is formed. In either case, the form drag increases and the lift-curve's slop decreases. The ultimate goal of all this is to improve the aerofoil's performance by increasing the lift-to drag ratio. As more lift is generated at a higher incidence, the form drag is also increase. However, an induced drag is also caused by the lift generated on a lifting surface with a finite span.

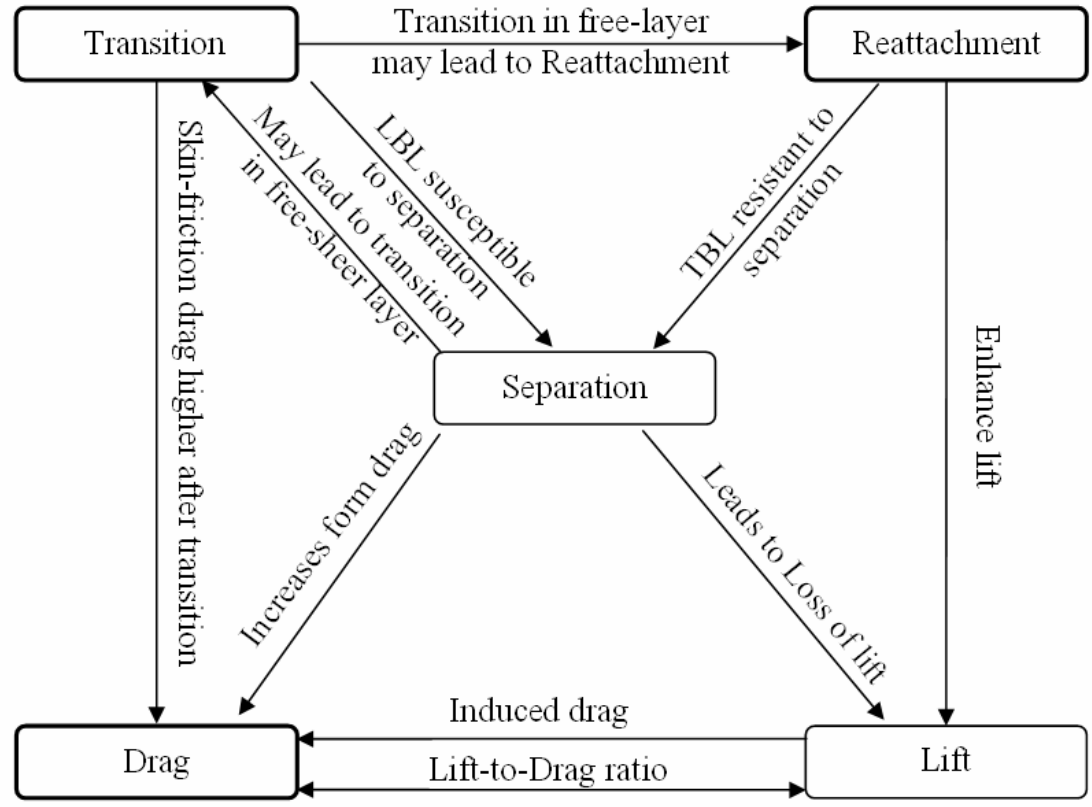

Figure 2.2 Interrelation between flow control goals (After Gad-el-Hak, 1998)

All of above reveals to potential conflicts as one tries to achieve a particular control goal only to adversely affect another goal. Therefore continuous compromises have to be made to achieve a particular design goal.

2.2.2 Classification of Flow Control Methods

There are different classification schemes for flow control methods. One is to consider whether the technique is applied at the wall or away from it. Surface parameters that can influence the flow include shape, roughness, curvature, rigid-wall motion, compliance, temperature porosity and etc. Heating and cooling of the surface can also influence the flow by changing the viscosity and the density gradient of the fluid. Mass transfer can take place through a porous wall or a wall with slots. Suction and injection of primary fluid can have significant effects on the flow field, influencing particularly the shape of the velocity profile near the wall and thus the boundary layer susceptibility to transition and separation. Different additives, such as polymers, surfactants, micro-bubbles, droplets, particles, dust or fibres can also be injected through the surface in water or air wall-bound flows. Control devices located away from the surface can also be beneficial. Large-eddy break-up devices (also called outer-layer devices or OLDs), acoustic waves bombarding a shear layer from outside, additives introduced in the middle of a shear layer, manipulation of freestream turbulence levels and spectra, gust and magneto- and electro-hydrodynamic body forces are examples of flow control strategies applied away from the wall.

The second classification scheme is to consider whether the control technique directly modifies the shape of the instantaneous/mean velocity profile or selectively influence the small dissipative eddies. An inspection of the Navier-Stokes equations written at the surface (see, for example, Gad-el-Hak, 1998), indicates that the spanwise and streamwise vorticity fluxes at the wall can be changed, either instantaneously or in the mean, via wall motion/compliance, curvature, suction/injection, streamwise or spanwise pressure-gradient (respectively), or normal viscosity gradient. These vorticity fluxes determine the fullness of the corresponding velocity profiles. For example, suction, a favourable pressure-gradient or a lower wall-viscosity results in vorticity flux away from the wall, making the surface a source of spanwise and streamwise vorticity. The corresponding fuller velocity profiles have negative curvature at the wall and are more resistant to transition and to separation but are associated with higher skin-friction drag. Conversely, an inflectional velocity profile can be produced by injection, an

adverse pressure-gradient or a higher wall viscosity. Such a profile is more susceptible to transition and to separation and is associated with lower, even negative, skin friction. Note that many techniques are available to affect a wall viscosity-gradient; for example surface heating/cooling, film boiling, cavitation, sublimation, chemical reaction, wall injection of lower/higher viscosity fluid, and the presence of shear thinning/thickening additive.

Flow control devices can alternatively target certain scales of motion rather than globally changing the velocity profile. Polymers, riblets and LEBUs (large eddy breakup devices), for example, appear to selectively damp only the small dissipative eddies in turbulent wall-bounded flows. These eddies are responsible for the (instantaneous) inflectional profile and the secondary instability in the buffer zone, and their suppression leads to increased scales, a delay in the reduction of the velocity-profile slope, and consequent thickening of the wall region. In the buffer zone, the scales of the dissipative and energy containing eddies are roughly the same and, hence, the energy containing eddies will also be suppressed resulting in the reduced Reynolds stress production, momentum transport and skin friction.

A yet another scheme for classifying flow control methods considers energy expenditure and the control loop involved. As shown in the schematic in figure 2.3, a control device can be passive which requires no auxiliary power or active in which energy or auxiliary power is induced into the flow. As for the action of passive devices, some prefer to use the term flow management rather flow control (Fiedler and Fernholz, 1990), reserving the latter terminology for dynamic processes. Active control is further divided into predetermined and interactive. A predetermined control includes the application of steady or unsteady energy input without regard to the particular state of the flow field. Examples of predetermined active flow control include jet vectoring using piezoelectric actuators (Smith and Glezer, 1997) and post-stall lift enhancement and form drag reduction using oscillatory blowing (Seifert and Pack, 1999a). The predetermined open-loop control schemes can be very effective in modifying the flow field. The control loop in this case is open as shown in figure 2.4a, and no sensors are required. Interactive control is a special class of active control where the control input is continuously adjusted based on some form of measurement elements. The control loop in this case can either be an open, feed- forward one (figure 2.4b) or a closed, feed-back loop (figure 2.4c). The classical control theory deals, for the most part, with the interactive control.

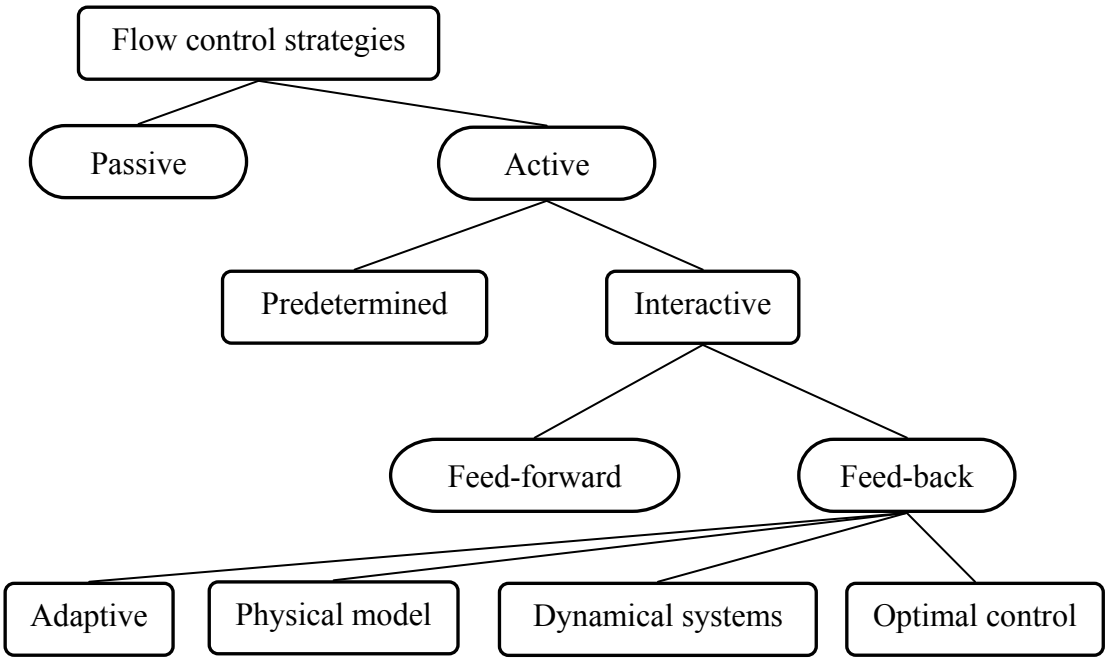

Figure 2.3 Classification of flow control strategies (After Gad-el-Hak, 1998)

The distinction between feed-forward and feed-back is particularly important when dealing with the control of flow structures which convect over stationary sensors and actuators. In feed-forward control, the measured variable and the controlled variable differ. For example, the pressure or velocity can be sensed at an upstream location, and the resulting signal is used together with an appropriate control law to trigger an actuator which in turn influences the velocity at a downstream position. The small-scale manipulation of the turbulent fluctuations is a challenging technological problem. In cases in which the control must interact with a specific set of turbulent fluctuations already present in the flow, such as random coherent structures, the effectiveness of an open-loop system is reduced. Feed-back control, on the other hand, necessitates that the controlled variable be measured, fed back and compared with a reference input. A feedback control law is utilized to control the energy introduced at the actuator. Interactive feedback control is further classified into four categories: adaptive, physical model-based, dynamical systems-based and optimal control based on the extent to which they are based on the governing flow equations (Moin and Bewley, 1994). A depiction of a closed-loop system is shown in figure 2.5 for a boundary layer (Kral, 1998).

As mentioned by Kral (1998), the active flow control involves the triad of flow phenomena, actuators/sensors, and controls as depicted in figure 2.6. Typical flow

phenomena targeted for application of active flow control are listed along with actuators, sensors and methods of control. Bewley (2001) discusses the future of feedback flow control and the need for a renaissance approach where research must be conducted at the intersection of the traditional fields of fluid mechanics, mathematics, and control theory for successful application of feedback control schemes. A consideration of both the fundamental flow physics and the requirements and the limitations of control algorithms must be understood.

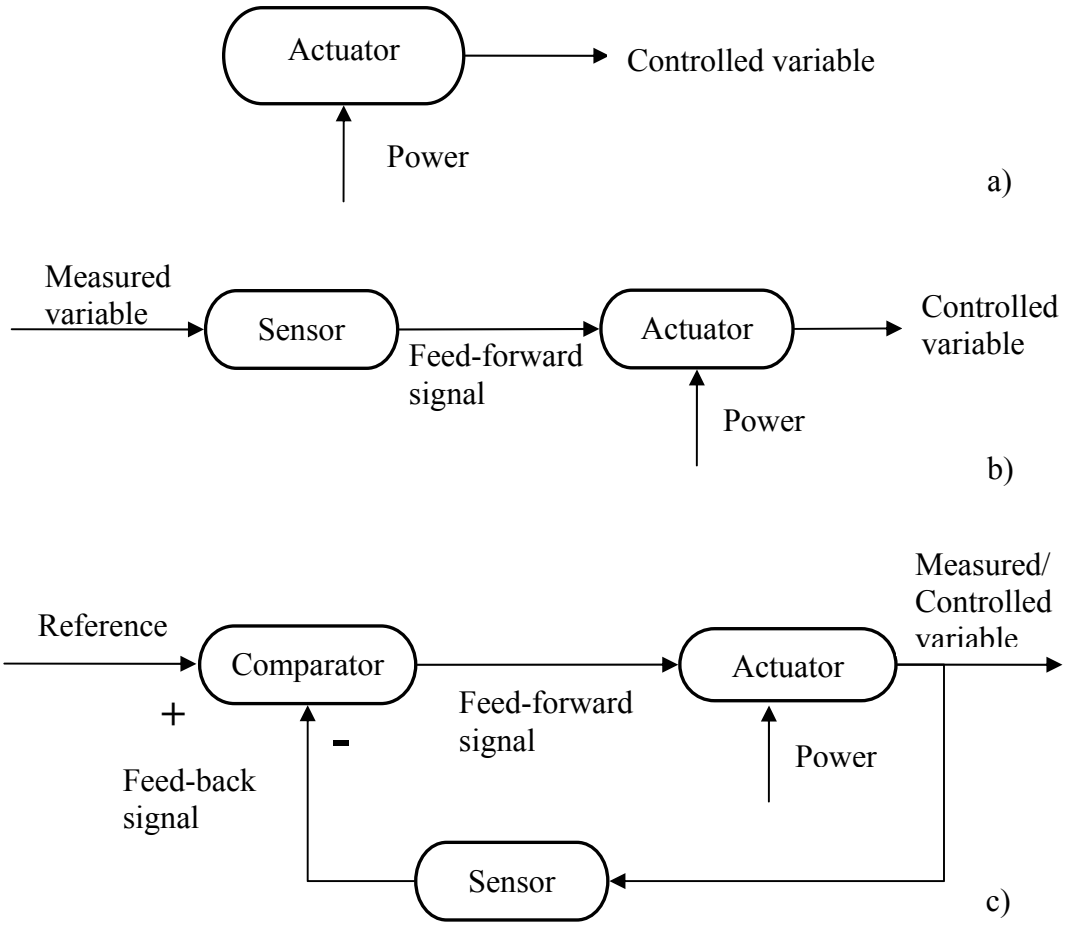

Figure 2.4 Different control loops for active flow control (Kral, 1998)

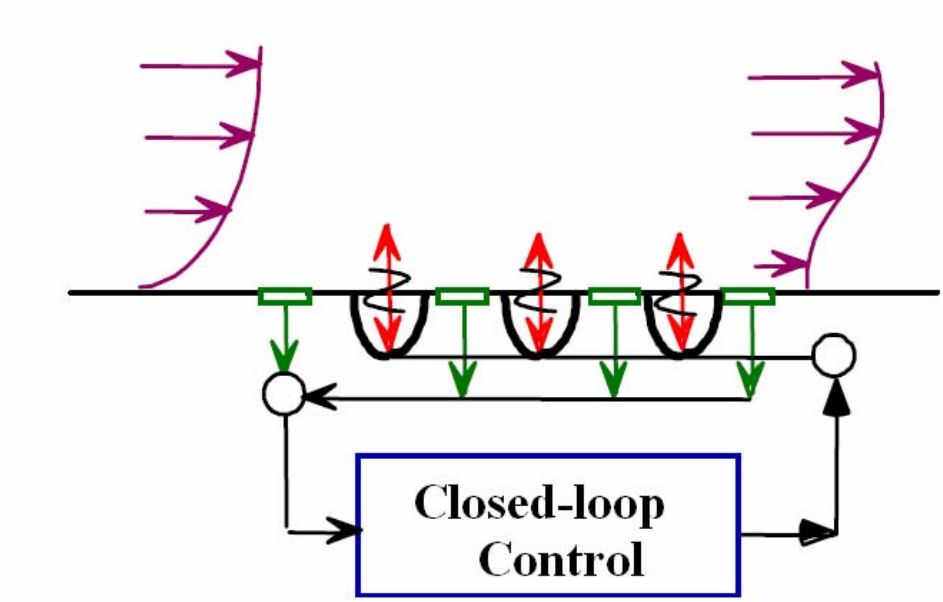

Figure 2.5 Feed –back control loop for active flow control (Kral, 1998)

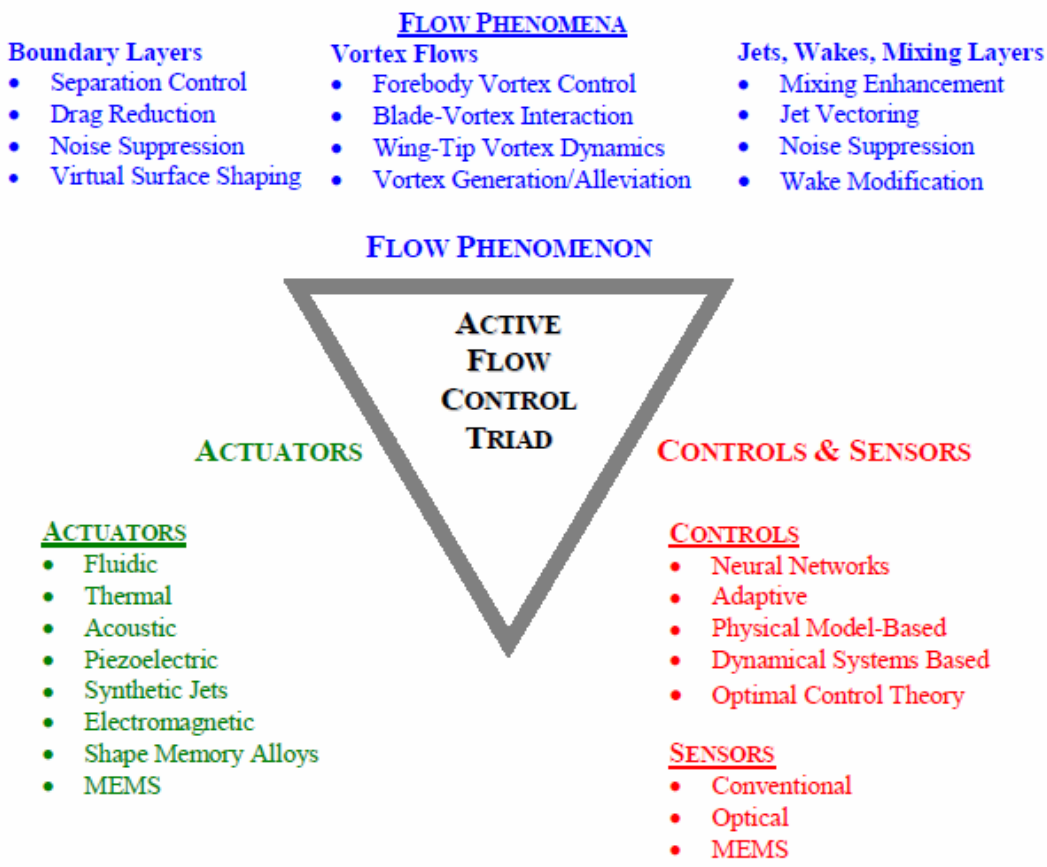

Figure 2.6 Active flow control triad (Kral, 1998)

There are two primary advantages to active flow control that are not achievable by passive techniques. First, active flow control technology leverages and controls a natural stability of the flow to attain a large effect using small, localized energy input.

Control is most effective when the control input is introduced locally at a high receptivity region. For example, the effects of a control scheme can be dramatic when applied near the transition point of a boundary layer flow, the separation point on an airfoil, or the nozzle of a jet. Secondly, active control can be used to control complex, dynamical processes like turbulence production in turbulent boundary layers to reduce skin friction, and hence viscous drag, where the reduction is proportional to the surface area covered by the actuators. The mechanism of turbulence production in boundary layers is understood as a complex series of dynamical events associated with organized, near-wall, low-speed streaks and their instabilities. This process culminates in a sudden eruption, or bursts, of low-momentum fluid away from the wall. As discussed by Bushnell (1985), the correct phasing of the control inputs with respect to the organized flow structures may be the key factor in the success of a control scheme. Lumley and Blossey (1998) present several applications of active control of turbulent flow using the latter approach of modifying the production of turbulence.

For the flow sensor, it needs to be robust and not significantly alter the flow field that is measured. For practical reasons, most flow sensors for active flow control are flush mounted on a solid surface. At the solid surface, typically wall pressure and/or skin friction can be measured. For situations in which the wall pressure is important, there are many devices for measuring pressure fluctuations, which are essentially small microphones. Some examples of sensors for measuring wall shear stress include floating element sensors, hot films, and shear stress crystals (Onsrud *et al*, 1987; Fujisawa *et al*, 2009 and Sumer *et al*, 1993) .

For the actuators which can be used in the active flow control, some of which have been list in figure 2.6, one of the greatest challenges in making active flow control technology practical is to develop robust actuators. Desired characteristics of actuators include low power consumption, fast response, reliability, and low cost. Among the actuators listed in figure 2.6, the synthetic jet actuator is a recent breakthrough in the actuator concept, initially developed at Georgia Institute of Technology (Glezer and Amitay, 2002). And the main investigation object of this thesis will conduct on the synthetic jet actuator which has a moving diaphragm attached to a cavity and its details will be introduced later.

Another actuator concept highlighted here is a Lorentz-force actuator. Experiments performed by Nosenchuck and Brown (1992), Nosenchuck *et al* (1995), and Nosenchuck (1996) using a specific electromagnetic forcing have indicated that

viscous drag can be reduced by as much as 90%. Flush-mounted Lorentz force actuators are used to induce a current-density field, j, and a magnetic field, B, in the vicinity of the wall to provide a three-dimensional body force $L_b = j \times B$. A schematic of a Lorentz force actuator is shown in figure 2.7. The actuator is comprised of a pair of subsurface permanent magnets and two surface-mounted. The magnets and electrodes are arranged such that the electric and magnetic fields intersect and create a three dimensional Lorentz force above the actuator. The curl of the Lorentz force represents a source of vorticity. Donovan *et al* (1997) and Cary *et al* (1999) have performed a detailed analysis of the vorticity generated over a single EMTC (electromagnetic Turbulence Control) actuator.

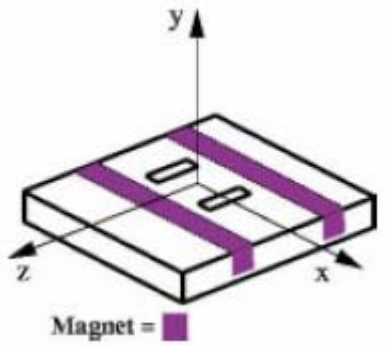

Figure 2.7 Schematic of a Lorentz force actuator

One of the major advances in flow control is the emergence of Micro Electro Mechanical Systems (MEMS) technology, which employs the methods developed for the fabrication of silicon chips to construct very small-scale mechanical devices. The significance of micro-machine technology is that it makes it possible to provide mechanical parts of micron size, batch fabricated in large quantities, and integrated with electronics. Miniaturization to this scale is necessary for both sensors and actuators for successful feedback control of turbulence due to the very small scales of the coherent structures in high-Reynolds-number flows of engineering interest. Miniaturized actuators also simplify the integration of the control system with the overall structure or subsystem. MEMS fabrication processes provide not only miniaturization, but also modular integration of sensors, actuators, and electronics and the affordability enabled by batch processing. However, micro devices for active flow control do not obviate the role of mesoscale devices in flow control technologies. Recent review articles on the use of MEMS for active flow control include those by McMichael (1996) and Ho and Tai (1996, 1998).

2.2.3 Flow Separation Control Methods

Flow control, as a means of preventing separation, has traditionally been associated with the injection of fluid to, or the removal of a fluid from, a boundary layer; or the motion of a surface in the general direction of the stream (Flatt, 1961 and Schlichting, 2000)

Historically, suction was the first method ever proposed for the control of separation (Prandtl, 1904). The basic principle is to remove decelerated fluid near a surface and deflect the high-momentum free-stream fluid towards the surface. The remarkable effects of suction were demonstrated on a variety of wind tunnel models and even on experimental aircraft (Betz, 1961 and Head, 1961) but, to date, the method has not been applied to the wings or control surfaces of a production aircraft. Due to the mechanical complexity and additional weight, any aerodynamic gains made by suction are offset by the power required to operate the suction device (Betz, 1961).

The purpose of steady blowing is to directly impart additional momentum to retarded fluid within the boundary layer near the surface and thus delay separation (Head, 1961; Carriere and Eichelbrenner, 1961). Blowing is usually achieved by an auxiliary blower or compressor bleed (Attinello, 1952), but can also be achieved passively by diverting fluid from the freestream to the surface. (Probably the most successful application of passive blowing is through the use of a slot that allows air from the lower surface of an upstream wing-element to pass over the upper surface of a downstream wing-element) Steady blowing has been investigated for a variety of different locations on wings but the most successful application was that at the shoulder of a deflected flap (Attinello, 1961).

Poisson-Quinton (1948) showed that separation control is governed by momentum (rather than mass) addition and that a quantity, similar to the thrust coefficient, was required in order to quantify the propulsive effect of blowing. Dimensional considerations give rise to the so-called momentum coefficient, C_μ, which remains a standard measure of the relative momentum addition. In certain circumstances, particularly when the momentum coefficient is “low”, i.e. $C_\mu < 2\%$, blowing can be detrimental (Attinello, 1961; Seifert *et al*, 1996). (Note that momentum coefficient is quoted throughout in percentage terms for convenience when compared with excitation.) Thus many investigations of steady blowing present data for $C_\mu > 3\%$. This is primarily due to a local decrease in the near-wall momentum if the jet velocity does not exceed

the local velocity outside the boundary layer. Furthermore, Poisson-Quinton and Lepage (1961) showed that for C_μ < 5%, blowing is most effective with the largest dC_L/dC_μ being measured in this range. For larger C_μ, boundary layer control is superseded by circulation control which is less effective, i.e. although lift continues to increase, dC_L/dC_μ is reduced.

Boundary layer control by means of surface motion generally involves moving the surface at or close to the free-stream velocity and thereby eliminating the boundary layer. Such methods are mostly used in wind tunnels, for studying ground effect and aerodynamics of cars. Research on rotating cylinders located at blunt trailing edges (e.g. for truck applications, Modi *et al*, 1995) continues to date. In the context of excitation, surface motion generally applies to a fliperon (small oscillating flap), fence, ribbon or any other mechanical device which oscillates in some manner, thereby introducing oscillatory momentum into the flow.

Until the 1960s, successful and practical approaches to separation control relied on the principle of direct momentum addition to the near-wall region, as discussed in the previous section. In 1975, however, Collins and Zelenevitz (1975) demonstrated that acoustic excitation can increase the momentum near the surface by transferring it from the free-stream, without resorting to the traditional, direct injection of momentum. Following this experiment, acoustic excitation was demonstrated on a variety of airfoils and experimental facilities, usually at low Reynolds Numbers (4×10^4–1.4×10^5). The technique involves introducing sound into a wind-tunnel from the walls of the test section by using speakers or acoustic drivers (Zaman *et al*, 1987 and Ahuja *et al*, 1983). An example of how these disturbances are introduced is provided by Zaman *et al* (1987) who showed that excitation was effective whenever acoustic standing waves in the tunnel induced a transverse velocity component close to the airfoil surface. These investigations provided some impetus for current advances because they demonstrated that separation control can be achieved by means of an externally supplied excitation source.

However, the drawbacks outweigh the positive aspects. The excitation is facility dependent, since the acoustic drivers effectively exited the respective wind tunnel's resonant modes, which in turn excited the separating shear layers, thus leaving serious doubts concerning aircraft applications. This was reflected, for example, by significant lift increases at some incidence angles, with lift decrement at others. Moreover, high

levels of excitation were required up to 156 db in order to obtain some significant effects, making the practical application of this method questionable. Furthermore, the method has only been demonstrated for low Reynolds numbers. Namely $Re < 600{,}000$, and therefore its effect on transition is intertwined with its effect on separation. An additional drawback is the large range of effective reduced frequencies $St = f_p c / U_\infty$ which varies widely by two orders of magnitude from O(1) to O(100). Certain investigations however indicate a pronounced shift to lower *St* when the excitation levels are high. For example, Zaman (1992) showed that when the excitation amplitude is increased, the optimum Strouhal number can be orders of magnitude lower than that corresponding to the linear invisicid stability of the separated shear flow.

Despite the above-mentioned drawbacks, acoustic excitation illustrated the effectiveness of excitation per se and the principle that separation delay is effective at lower frequencies when excitation amplitudes are large.

Active mechanical devices located inside the boundary layer (i.e., a vibrating fliperon attached to the surfaces (Neuburger and Wygnanski, 1987) or an oscillating fence (Shepshelovich *et al*, 1989) or wire (Katz *et al*, 1992)) also provide vorticity fluctuations that are amplified by the shear flow near the surface and effectively delay separation. For example, the maximum lift coefficient generated by an NACA 0015 airfoil was increased by 30% because the angle of incidence at which the airfoil stalled was increased from 12 to 16 deg (Neuburger and Wygnanski, 1987). On the IAI P-255 airfoil, where the location of natural separation crept slowly upstream with increasing incidence, an active mechanical device located near the leading edge prevented this type of drag creep at $2 < \alpha < 12$ deg and delayed the deep stall by $\Delta\alpha = 4$ deg. This can be deduced best from the drag polar measured at $R_c = 0.2 \times 10^6$ where a constant drag was maintained between $0.6 < C_L < 1.6$ as a consequence of the active flow control. In both examples mentioned, the control mechanism consisted of a small flap that was forced to oscillate up and down at a prescribed frequency and amplitude. The effectiveness of this device depends on its size, inertia, and location on the airfoil surface in addition to the particular characteristics of the airfoil and its angle of attack. In short, there is a close coupling between the airfoil geometry and the device.

It has been known that large coherent structures could enhance the entrainment by transporting momentum effectively across a shear layer. Therefore, as a combination of steady blowing and excitation, pulsed blowing becomes a very effective tool for

separation control and is observed to significantly enhance airfoil performance (Seifert *et al*, 1996). The efficiency of flapped airfoils is observed to be greatly increased by the pulsed blowing, where the efficiency is measured by the enhancement of lift and the concomitant reduction in drag at all angles of incidence and Reynolds numbers. The amount of blowing and power required to achieve these effects is at times an order of the magnitude smaller than the amount required to achieve comparable gains by using steady blowing. This is because the introduction of periodic motion accelerates and regulates the generation of large coherent structures, particularly when the mean flow is unstable to the imposed periodicity. Since the effectiveness of the method is largely determined by the receptivity of the flow to the imposed disturbances, these have to be of the right scale and be introduced at the right location.

Despite the obvious effect which periodic excitation (pulsed blowing) offers to delay separation, the aerodynamic gains are offset due to the requirement of bleed air from the engine, which results in a complex pipe system and an additional weight. As a novel type of active flow control device, synthetic jets were introduced by Smith and Glezer (1998). Unlike the pulsed jet, a unique feature of synthetic jets is that they are formed from the working fluid of the flow system in which they are deployed, and thus transfer a linear momentum to the flow system without a net mass injection across the system boundary. Some flow control examples will be shown in the following section.

2.3 Flow Separation Control Using Synthetic Jets

A synthetic jet actuator (SJA) is a device that uses an electrically powered oscillating diaphragm on one side of a cavity, which alternately draws in (suction stroke) and ejects (blowing stroke) fluid through an orifice (Figure 1.3). When the oscillation consists of equal periods and amplitude of blowing and suction, the net mass-flow rate is zero and so, the ejected jet is ‘synthesised’ from the working fluid in which the SJA is deployed.

The effectiveness of the resulting synthetic jet arises from the net injection of vorticity in the form of a train of vortex rings (Smith and Glezer, 1998 and Glezer and Amitay, 2002). The ability to generate coherent vortices that can provide a favourable control effect without the need for a net mass flux makes SJAs very attractive for flow separation control on high-lift systems.

SJAs also offer the potential for micro-fabrication for integration into microelectro- mechanical systems (MEMS). Such systems encompass sensors, actuators and distributed electronics on a common semi-conductor substrate and can be made

small (tens or hundreds of millimetres) and manufactured inexpensively using batch manufacturing techniques (Warsop, 2004). This is not only important from an economic viewpoint or in terms of reducing the potential density of the actuator system in the wing, but can be considered as a prerequisite for aircraft implementation. For a typical multi-element high lift system at the take-off condition, the local Mach number on the leading edge devices ranges between 0.5 and 1 and the local boundary layer thickness is in the region of 1 to 3mm. For the trailing edge devices, the local Mach number ranges between 0.2 and 0.4 and the local boundary layer thickness is in the region of 1 to 10mm. Thus, relative to the boundary layer, both conditions require micro-scale SJA orifices.

As well as the advantages of utilising SJAs for controlling flow separation on high-lift systems, there are also some potential drawbacks. A notable one is that of debris ingestion, which can cause orifice blockage, especially during the suction stroke. This however may be offset by the fact that blowing constitutes half the total cyclic motion, unlike pure suction.

Liddle and Crowther (2008) also proposed the use of electro-active, polymer-based orifice closure devices as a viable means to sealing orifices when SJA operation is not required hence reducing the risk of any environmental impact. The use of closures would also eliminate the potential interference of inactive actuators, which may act as sources of noise and disturbance owing to Helmholtz resonance via flow passing over the orifices (Lockerby et al, 2007).

The capability of synthetic jet actuators for the suppression of separation was demonstrated on an unconventional symmetric airfoil (Amitay *et al*, 2001). The symmetric airfoil comprises the aft portion of a NACA four-digit serious airfoil and a leading edge section that is one-half of a round cylinder as shown in figure 2.8. The thickness of the assembled airfoil is 6.22cm and the combined cylinder-fairing chord is 25.4cm, that is, t/c = 0.24. The Reynolds numbers (Re_c) based on the chord of the profile was from 3.1×10^5 to 7.25×10^5. The control jet is synthesized from two, side-by-side, 0.5mm wide, rectangular synthetic jet actuators that are parallel along their long spanwise dimension and are 2.5mm apart in the freestream direction. The jet actuators span the centre 140mm of the cylinder and can be positioned at an azimuthal angle γ between -90 to +90 (at $\alpha = 0$) relative to the incoming flow direction by rotating the cylinder independently of the fairing.

In the absence of control, the airfoil stalls for $\alpha > 5$ degree; however, with control, fully attached flow can be achieved for $\alpha < 17.5$ degree, and partial reattachment with some recovery of lift is achieved up to the maximum angle tested, $\alpha = 25$ degree. It has been shown that both the location and the strength of the control input affect the extent of the reattached flow. Dramatic increase in lift up to 100% and decreases in pressure drag up to 45% are observed as a result of flow reattachment, although for $\alpha > 17.5$ degree, the increase in lift is accompanied by an increase in drag. Control is effective up to a chord Reynolds number of 7.25×10^5, and the data suggest that for a given C_μ and jet angle γ the lift-to-pressure drag ratio is independent of the Reynolds number. The measurements also reveal that the location of the control γ or the momentum coefficient C_μ may be manipulated to obtain the best performance of the airfoil for the entire range of angles of attack if either the separation location is unknown or practical limitations preclude control near separation.

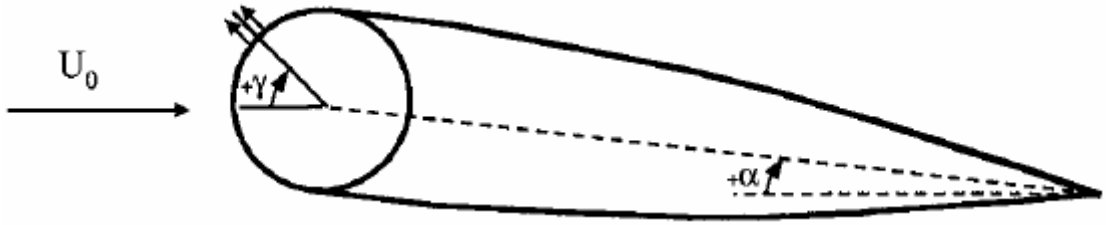

Figure 2.8 Cross-section view of airfoil model based on NACA four-digit airfoil and circular cylinder (Amitay *et al*, 2001)

In addition, the effect of the actuator operating frequency is also considered. The synthetic jets are operated over a range of frequencies up a non-dimension frequency $F^+ = 20$, which is defined as $F^+ = fL_s/U_\infty$ (f is the actuation frequency, L_s is the length of the separated area and U_∞ is the freestream velocity) and is about 30 times higher than the natural shedding frequency of the separated flow over the airfoil. Two distinct performance regimes are observed. When the operating frequency is of the same order as the shedding frequency of the stalled airfoil, $F^+ < 4$, an increase in the actuation frequency leads to a reduction in the recovered lift-to-pressured drag ratio. When the operating frequency is more than an order of magnitude larger than the shedding frequency, $F^+ > 10$, the lift-to pressure drag ratio is much larger and appears to be invariant with the actuation frequency. It has also been shown that the performance of actuators with large cavities is degraded when these actuators are driven at high frequencies. The performance degradation is due, in part, to three-dimensional acoustic effects inside of the cavity and velocity non-uniformities along the actuator orifices.

The sensitivity of the attached flow (and the restored lift) to the excitation frequency is also demonstrated in the numerical simulation of Donovan *et al* (1998) who investigated flow reattachment over a NACA 0012 air-foil using time-harmonic zero mass flux blowing at $St = 1$. These simulation showed a 20% post-stall increase in lift at $\alpha = 22$ degree. However, the reattachment was similar to a Coanda-like effect where the forced shear layer deflected towards the airfoil surface, and the time periodic vortex shedding form the top surface of the airfoil, led to 20% oscillations in the lift coefficient. Similarity, the more recent numerical simulations of Wu *et al* (1998) reaffirmed that a separated flow can be effectively manipulated by low-level periodic blowing/suction near the leading edge. The forcing modulates the evolution of vortical structures within the separated shear layer and promotes the formation of concentrated lifting vortices, which in turn interact with trailing-edge vortices and thereby alter the global stalled flow. In a certain range of post-stall angles of attack and actuation frequencies, the flow becomes periodic and is accompanied by a significant lift enhancement.

Additional work has been done about the transients associated with flow reattachment and separation using amplitude modulation of the actuation waveform (Amitay and Glezer, 2002). It has been presented that flow attachment over the stalled airfoil begins with the advection of a strong clockwise vortex (trapped vorticity) past the measurement station indicating a reduction in lift that is followed closely by a stronger counter-clockwise vortex indicating the reestablishment of lift. For the high-frequency actuation the reduced wake of the attached flow ultimately reaches a quasi-steady state of symmetric vorticity distribution. In contrast to the reattachment at $St \sim O(10)$, when the reduced actuation frequency is O(1), the reattachment is followed by the coherent shedding of a train of strong vortices at the actuation frequency. When the flow reattachment begins, the phase-averaged change in circulation with respect to the baseline flow, $-\left\langle \Delta\hat{\Gamma} \right\rangle$, exhibits a similar transient at both control frequencies. However, while for high frequency forcing the circulation (and thus the lift coefficient) ultimately reaches a steady level, low-frequency actuation results in oscillations of $\left\langle \Delta\hat{\Gamma} \right\rangle$ (and C_L) at the actuation frequency with peak-to-peak fluctuation of up to 55% of the mean level for attached flow.

The flow mechanisms associated with the reattachment process are demonstrated in a sequence of smoke visualization images as shown in figure 2.9.

Following the activation of the control a vortex with a negative vorticity is formed near the leading edge. This vortex is due to the negative vorticity associated with the separated flow. The vortex is advected downstream and increases in size and a second vortex is formed near the leading edge. As time progresses these two vortices continue to increase in size, and near the trailing edge the size of the first vortex is more than half of the airfoil's chord. Following the transient, the flow is completely attached to the surface of the airfoil and there is no evidence of vortical structures.

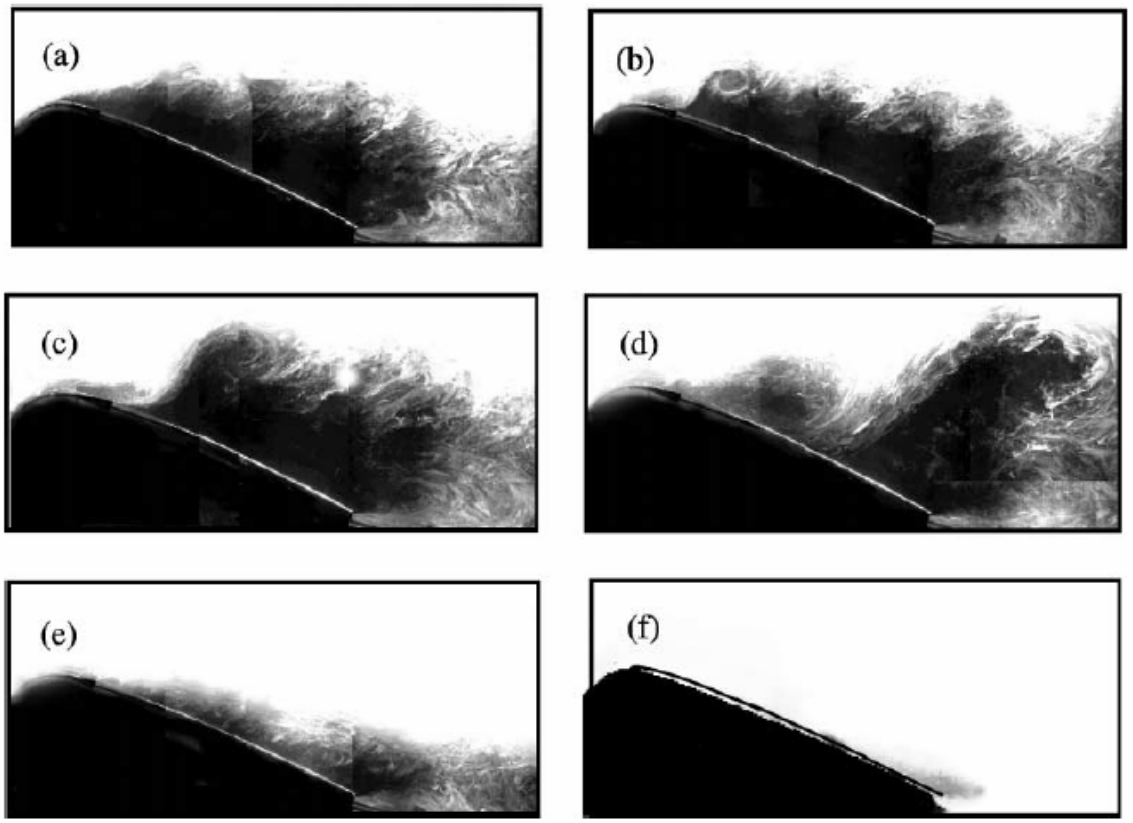

Figure 2.9 Phase-averaged images during the reattachment process for α = 17.5°, γ = 60°, and *St* = 10, *t/T* = 0 a) 8 b) 18 c) 24 d) 33 e) 50 and f) 125 (Amitay and Glezer, 2002)

McCormick (2000) investigated the leading-edge separation control effectiveness of synthetic jets on a 2-D airfoil section, which had a small span-to-chord ratio (0.44 m chord, 0.53 m span). The synthetic jet actuators were installed at a 4% chord wise location, upstream of the leading-edge separation (approximately 8% chord), by laser drilling a slot inclined approximately 20° from the surface over the span into the hollow leading edge. The airfoil was set up at a post-stall angle of attack $\alpha = 24^{o}$. The wind tunnel speed was $M = 0.025$ ($Re = 2.5 \times 10^5$) and the actuation frequency was 50Hz. Flow visualization was used to test the control result at three momentum

coefficient C_μ, which was defined as the ratio of the orifice momentum to freestream momentum, as shown in figure 2.10. Without actuation ($C_\mu = 0$), the flow was observed to separated from the leading edge, shedding vortical structures in the shear layer as indicated in the sketch below. At $C_\mu = 0.005$, the flow had clearly turned much more and there existed three vortical structures over the airfoil cord which were locked to the forcing effect. At a level of $C_\mu = 0.01 – 0.015$, the flow was completely attached with no coherent structures. This was the synthetic jet operating at its full potential, completely suppressing separating via boundary layer energisation. At even higher levels of forcing $C_\mu = 0.04 – 0.068$, vortical structures were again visible, but of the opposite sense. This flow behaviour was more analogous to the synthetic jets in quiescent air and was clearly above the optimal forcing level.

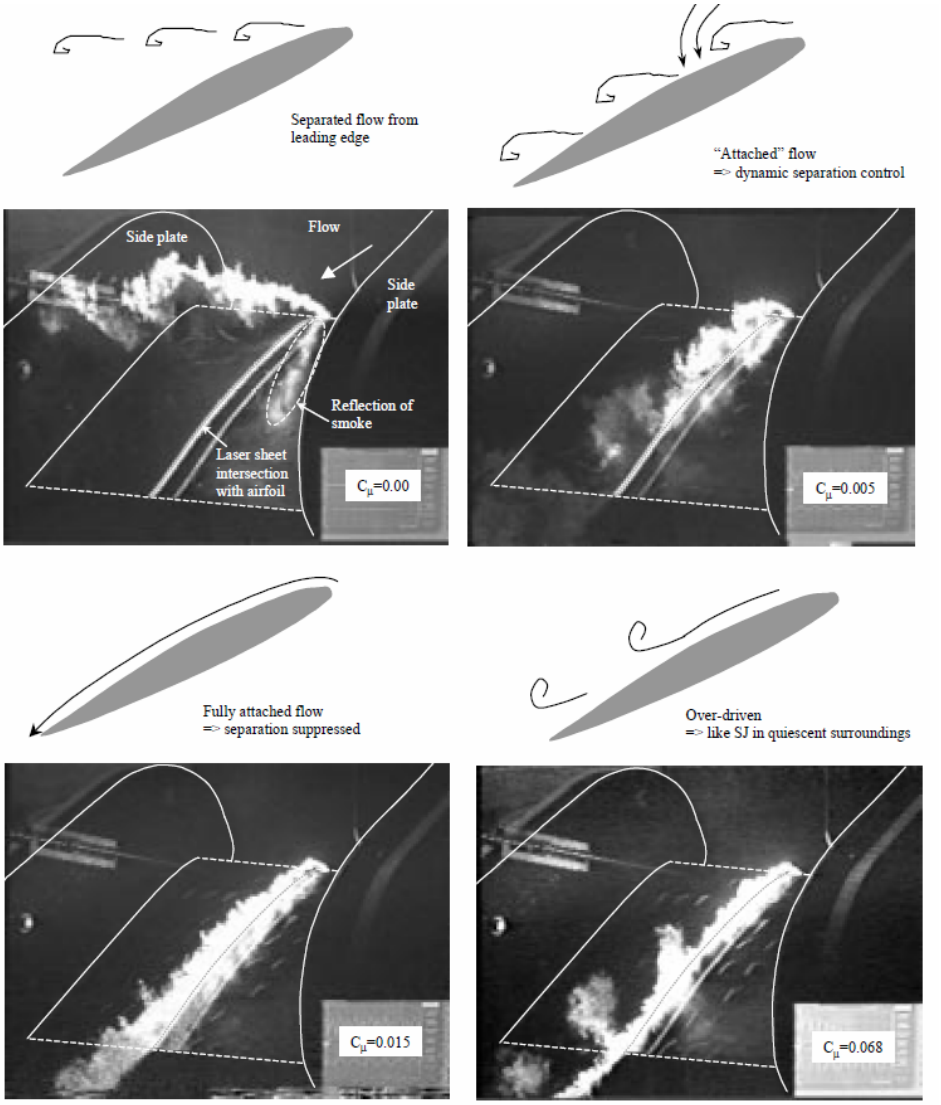

Figure 2.10 Flow visualization of flow separation control at various conditions (McCormick, 2000)

The majority of the aforementioned studies generating synthetic jet via two-dimensional slots in bluff bodies and aerofoils have operated the synthetic jets actuators clost to or at the onset of flow separation, with emphasis on achieving flow reattachment. This mechanism of flow reattachment relies on a lower synthetic jet actuators energy input relative to direct momentum injection, by exploiting the dynamic interaction of the spanwise vortices generated by synthetic jet actuators with those in the separated flow region.

Unlike synthetic jets generated by slots, it is believed that round synthetic jet actuators subject to certain operating conditions (i.e. actuation frequency and amplitude) can generate predominantly streamwise-aligned, vortical structures similar to passive and active vortex generators. At the University of Manchester, Crook (2002) investigated the flow control effectiveness of a spanwise array of synthetic jet actuators with round orifices normal to the surface of a circular cylinder upstream of its separation line in a turbulent boundary layer (Re_{Dcyl} = 550,000). Surface oil patterns showed that with the actuators active (operating at their resonant frequency), the separation line was noticeably pushed downstream, as shown in figure 2.11.

In particular the oil flow revealed footprints that were consistent with a coherent longitudinal vortex pair (in the time-averaged view) embedded in the boundary layer downstream of each synthetic jet actuators orifice that appeared to persist for a long distance downstream and interact with the separated flow. It is well known from the flow physics of vane vortex generators and vortex generating jets that embedded, streamwise longitudinal vortices are capable of transporting high momentum fluid from the edge of the boundary layer to the near wall region, thereby enhancing fluid mixing and creating a fuller velocity profile that is better resistant to separation.

For implementing SJAs at civil aircraft scale, the use of circular synthetic jet actuators may be preferable to slotted synthetic jet actuators. One of the reasons for this is that the dynamic loading of high-lift system components by the generation of large spanwise vortices from synthetic jet actuator slots could potentially limit fatigue life, requiring a heavier system to reduce stressing (Liddle, 2007). The use of slotted SJAs is more suited to conventional engineer solutions at smaller scale. A case in point is the slotted SJAs demonstrated on the Bell XV-15 Tiltrotor aircraft (Nagib et al, 2004). Actuators were retrofitted to the wing flaps to improve hover performance by reducing download on the wings due to flow separation induced by the rotor downwash.

Conversely, round synthetic jet actuators operated in a similar manner to pulsed vortex generating jets offer realisation through MEMS technology. Warsop *et al.* (2007) designed and tested a microfabricated, round-pulsed air-jet actuator suited for practical application to separation control at full-scale operating conditions on a large air vehicle. Thus the study of round SJAs is justified and forms the basis for the present study.

The global characteristics and manifestations of synthetic jet injection for flow separation control has been demonstrated, however little is still known about the detailed flow physical processes. Although the synthetic jet actuator effect of Crook (2002) shown in figure 2.11 can be likened to that of a passive vortex generator, the detailed mechanisms differ substantially, with those in the former being dominated by the periodic formation and interaction of ejected vortex rings. For flow control purposes, the vortical structures formed by the interaction of synthetic jets with a boundary layer and their impact near the wall must be considered if light is to be shed on which type of structure produces maximum resistance to separation. In the next two sections the understanding of the behaviour of synthetic jets in quiescent conditions and their interaction with uniform cross flows and boundary layers is reviewed.

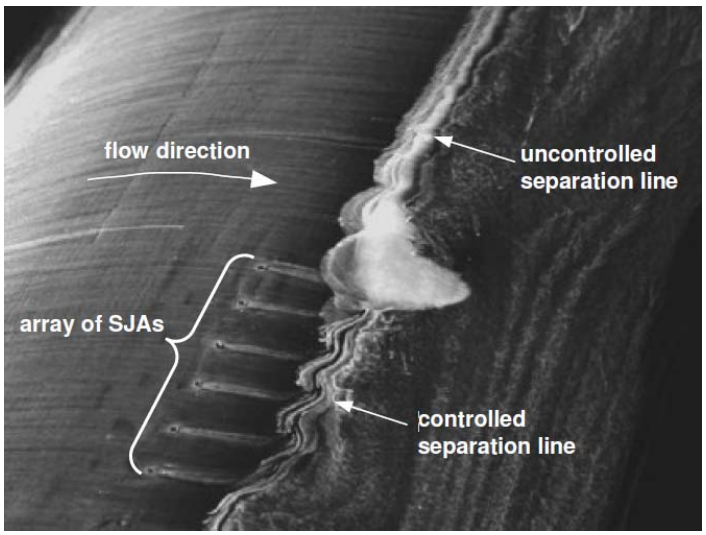

Figure 2.11 Demonstration of flow separation control on a cylinder using an array of synthetic jet actuators (Crook, 2002)

2.4 Synthetic Jets in Quiescent Conditions

2.4.1 Vortex Rings

Vortex motion is a basic and key feature of synthetic jet flows. Counter-rotating vortex pairs are periodically ejected from a '2D' rectangular synthetic jet actuator, and vortex

rings from an axisymmetric actuator. Vortex rings and vortices can be considered as one of the fundamental building blocks of fluid mechanics and acoustics. For a thorough review of vortex rings the reader is referred to the article by Shariff and Leonard (1992) and the books by Saffman (1992).

2.4.1.1 Formation of Vortex Ring

The simplest viscous vortex is the Lamb-Oseen vortex (Lamb, 1997), in which the velocity increases from zero at the centre of the core to a maximum and then decrease asymptotically to zero. Auerbach (1988) suggests that real vortex rings may go through four stages of development as: a) the generation or formation process; b) the stable laminar phase; c) the unstable or wavy phase; d) the turbulent phase. These stages are shown in figure 2.12 (Didden, 1977). It should be noted that a vortex ring may miss some of the stages of development depending on the generating conditions. For very high ejection velocities, a vortex ring may become turbulent immediately, whereas for low ejection velocities, it may only become a stable laminar ring and then decay due to viscosity.

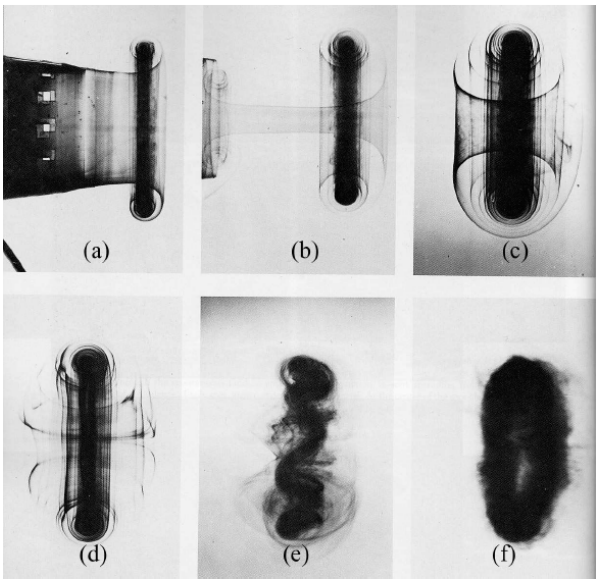

Figure 2.12 Sequence of photographs showing the formation and development of a laminar vortex ring, with azimuthal instability shown in (e) leading to the formation of a turbulent vortex ring in (f) (Didden, 1977)

When fluid is ejected from an orifice or nozzle, a vortex sheet is formed which then proceeds to roll-up into a vortex ring. The velocity across an idealized vortex sheet is discontinuous and consists of a continuous distribution of vortex lines as shown in figure 2.13. Crook (2002) described the roll-up process as follows;

1 The vortex sheet induces a velocity upon itself perpendicular to the plane of the sheet and is a maximum at the leading edge of the sheet
2 The self-induced velocity causes the leading edge of the sheet to curve
3 The curved vortex sheet continues to induce a velocity component on the leading edge, which together with the normal component of the velocity induced by the uncurved sheet, is responsible for the roll-up.

But in reality the velocity jump across the vortex sheet is not discontinuous due to the action of viscosity. The formation and roll-up process of a vortex ring at a nozzle exit using dye visualisation is shown by Didden (1979) in figure 2.14.

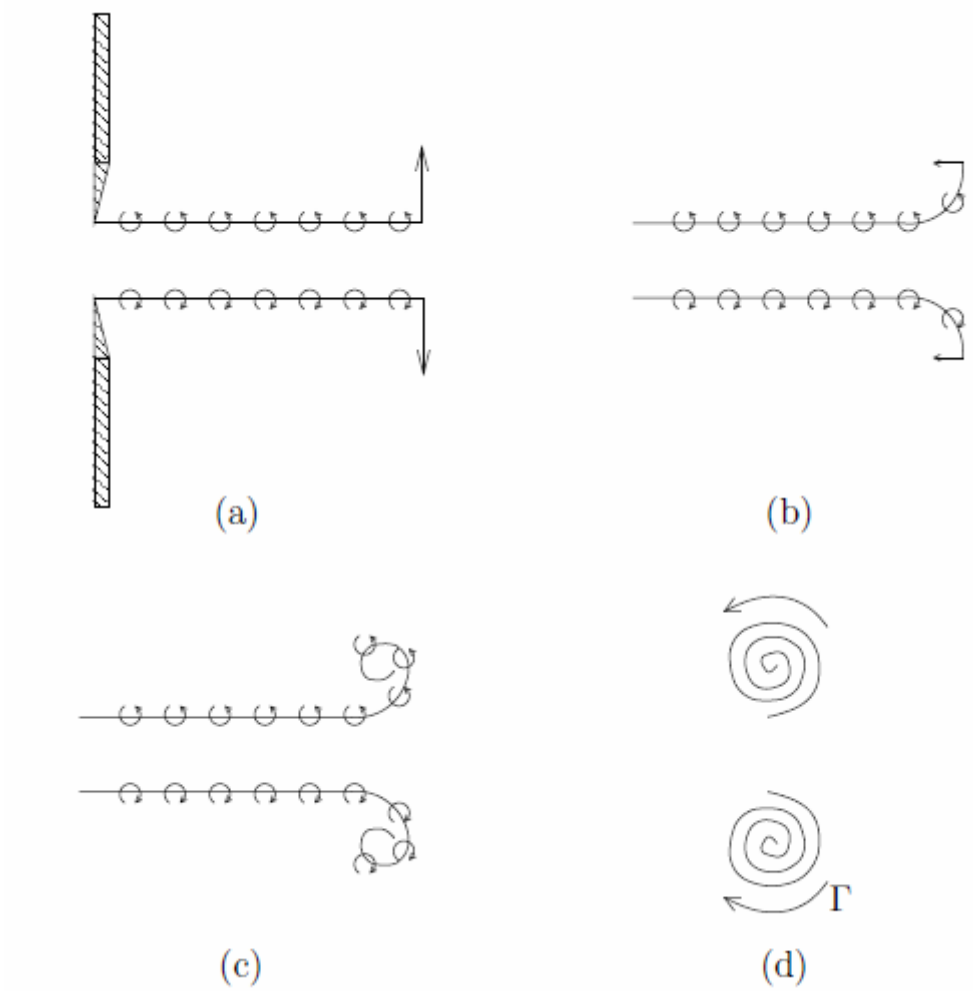

Figure 2.13 Idealised vortex ring formation (a) creation of vortex sheet through an orifice (b) … (d) roll-up; Straight lines represent induced velocity, small curved ones vorticity (Crook, 2002)

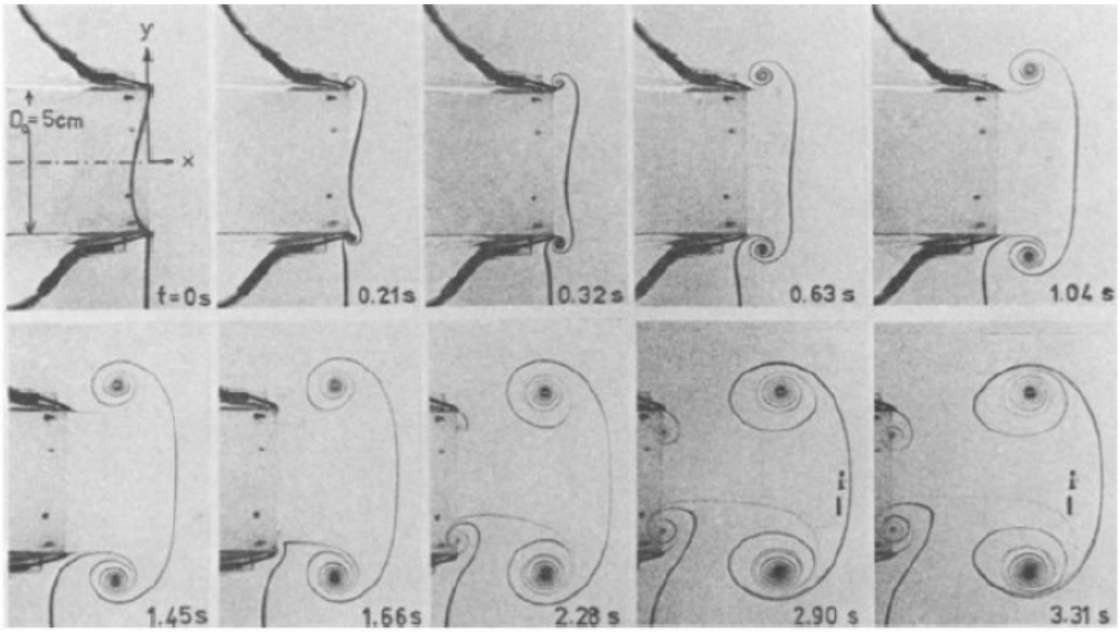

Figure 2.14 Dye visualisation of the roll-up process of a vortex ring at a circular nozzle (Didden, 1979)

2.4.1.2 Vortex Circulation

It is useful to have a method for predicting vortex circulation from commonly measured variable such as velocity. Without hotwire probe or triple wire, or PIV/LDA it is not possible to measure vorticity and hence calculate circulation experimentally. There are two models estimating vortex circulation: Slug-Flow Model and Self-Similar Model (Shariff and Leonard, 1992). In the current investigations, only the Slug-Flow Model is introduced here.

The slug model assumes that the vortex ring is formed from a cylindrical volume ('slug') of fluid that is ejected from an orifice, with diameter D_o, a constant velocity U_o for a time T_o. The length of the fluid slug, or namely the stroke length is therefore

$$L_o = U_o T_o \qquad \textbf{Eq. 2-1}$$

In reality, the velocity U_o is not constant and the history of the velocity is necessary to calculate the vorticity flux across the exit plane. Therefore, a mean velocity is defined as

$$\overline{U_o} = \frac{1}{T_o}\int_o^{T_o} U_o(t)dt \qquad \textbf{Eq. 2-2}$$

where $U_o(t)$ is the instantaneous spatial-averaged velocity over the orifice exit. The stroke length is now defined as

$$L_o = \int_o^{T_0} U_o(t)dt = \overline{U_o} T_o \qquad \textbf{Eq. 2-3}$$

Glezer (1988) defines a velocity program factor, P, to account for a specified variation of U in time

$$P = \int_0^1 \left(\frac{U_o^2}{\overline{U_o}^2} \right) d\left(\frac{t}{T_o} \right) = \frac{\overline{U_o^2}}{\overline{U_o}^2} \qquad \textbf{Eq. 2-4}$$

To calculate the initial total circulation generated in the production of the vortex ring, the flux of vorticity across the plane of the orifice is calculated

$$\frac{d\Gamma_o}{dt} = \int_0^{r_0} \omega_\phi u_x dr \approx \int_0^{r_0} -\frac{\partial u_x}{\partial r} u_x dr = \int_0^{r_0} -\frac{1}{2} \cdot \frac{\partial \left(u_x^2 \right)}{\partial r} dr \approx \frac{1}{2} U_o^2(t) \qquad \textbf{Eq. 2-5}$$

The first approximation sign means boundary layer assumptions are being invoked and the second, that the boundary layer edge velocity is $U_o(t)$. Thus the initial (or total) circulation is

$$\Gamma_o = \int_o^{T_0} \frac{1}{2} U_o^2(t) dt = \frac{\overline{U_o^2} T_o}{2} = \frac{P \overline{U_o}^2 T_o}{2} = \frac{P L_o^2}{2 T_o} \qquad \textbf{Eq. 2-6}$$

It is inherent in the definition (2.4) that $P \geq 1$. Therefore, any departure from a constant-velocity program acts to increase the circulation and the momentum of a vortex ring.

2.4.1.3 Universal Formation Time Scale

Gharib *et al* (1998) addressed the question "for a given geometry, is there an upper limit to the maximum circulation that a vortex ring can acquire?". Using flow visualization, DPIV and a piston/cylinder arrangement, they carried out a series of experiments for large values of non-dimensional piston stroke, L_P/D_P and different piston velocity 'programs' (impulsive, fast ramp and slow ramp).

For L_P/D_P = 14.5, they observe that the leading edge is 'disconnected' or 'pinched-off' from the trailing jet in terms of both the velocity and vorticity fields. Vorticity in the shear layer ceases to flow into the vortex core once the pinch-off process starts, and instead proceeds to roll-up into a series of vortices in a process similar to the Kelvin-Helmholtz instability (figure 2.15). The zero flux of vorticity into the primary ring also implies that there is no further increase in the vortex ring circulation. By measuring the vortex ring circulation for maximum stroke displacements L_P/D_P of 0.5-6.7, it was observed that the circulation ceased to increase beyond L_P/D_P ~ 4-5. In a second set of experiments the total circulation (that produced from the nozzle) and the vortex ring circulation were measured as a function of formation

time, $\overline{U_P}t/D_P = L/D_P$, until the piston was stopped at $L_P/D_P \sim 8$. A plot of Γ versus formation time shows that the total circulation increases as one would expect until the piston is stopped, while the vortex ring circulation levels out at 4. This shows that the maximum circulation that the ring can attain is equal to the total circulation discharged from the nozzle up to $L_P/D_P \sim 4$. If $L_P/D_P \sim 4$ then the ring formed would have no trailing jet.

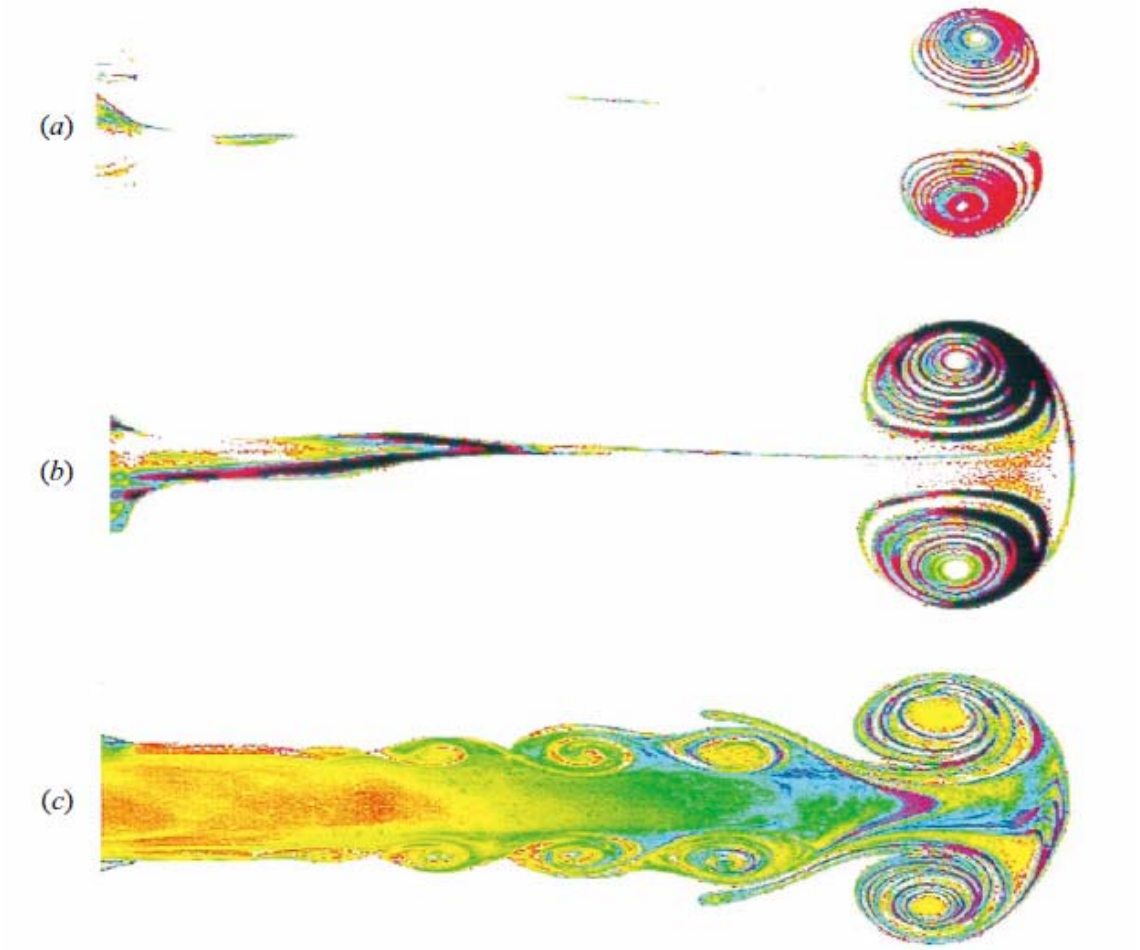

Figure 2.15 Flow Visualisation showing the effect of increasing L_P/D_P at $x_A/D_p \sim 9$ (a) $L_P/D_P = 2$; (b) $L_P/D_P = 3.8$ and (c) $L_P/D_P = 14.5$ (picture taken at $\overline{U_P}t/D_P = L_P/D_P = 8$ before mechanical stroke length reached) (Gharib *et al*, 1998)

The effect of the velocity program on the formation number is also small in the experiment, with a faster ramp tending to increase the formation number. Gharib *et al* (1998) also propose an analytical model to account for the existence of a formation number based upon the variational principle of Kelvin (1880) and Benjamin (1976) for axis-touching rings. From this principle it follows that the pinch-off of the ring from the trailing shear layer occurs when the generating apparatus is no longer able to deliver energy at a rate compatible with the requirement that a steady translating vortex ring

have maximum energy with respect to impulse preserving iso-vortical perturbations i.e. the maximum energy that the ring can contain while preserving the circulation of each fluid element. To apply this principle they compare the energy required for a steady ring, E_R, with the energy provided by the piston, E. As long as $E > E_R$, the formation process is incomplete. For a non-dimensional energy,

$$E_\alpha = \frac{E}{I^{\frac{1}{2}}\Gamma^{\frac{3}{2}}\rho^{\frac{1}{2}}} \qquad \textbf{Eq. 2-7}$$

the formation process is incomplete as long as the value of E_α exceeds a limit, found experimentally by Gharib *et al* (1998) to be 0.33. Using this criteria, they predict the formation numbers for different velocity programs using an analytical expression for $E_{\alpha_{piston}}$ based upon the slug model, that are in good agreement with the experimental values. This work is complimented by the direct numerical simulation of Rosenfield *et al* (1998) and further analytical work are reported by Mohseni and Gharib (1998); Shusser *et al* (1999) and Shusser and Gharib (2000). It is noted that the formation number is actually the dimensionless stroke length. Therefore the finding that the formation number is approximately four indicates that, when the dimensionless stroke length is equal to about four, the circulation of the resulting vortex ring reaches its maximum and will not increase with a further increase of the dimensionless stroke length.

2.4.2 Formation and Evolution of Synthetic Jets

The formation and evolution of synthetic jets in quiescent have been investigated both experimentally (Smith and Glezer 1998; Mallinson *et al*, 1999; Crook *et* a,l 1999, 2001; Muller *et al*, 2001 and Cater and Soria, 2002) and numerically (Kral *et al*, 1997; Rizzetta *et al*, 1998 and Lee and Goldstein, 2002). A very good review on this topic has been made by Glezer and Amitay (2002).

The types of orifice exit for which results are available are circular and rectangular in shape. The structure of the resulting synthetic jets is quite different for the two orifice types, with the flow from a high aspect ratio (150) rectangular jet in the experiments of Smith and Glezer (1998), demonstrating that only one vortex pair is visible at any one time. This contrasts to the idealised picture of a synthetic jet shown in figure 1.3, in which the jet is formed from a train of vortex rings, this being more valid for axisymmetric synthetic jets. The PIV investigation of Zhong *et al* (2004) also

reveals that although plane synthetic jets with a high aspect ratio appear to be two-dimensional when they are just formed, they are highly unstable and experience subsequent "axis swapping" between the major and minor axis of the jet further downstream.

2.4.2.1 Formation of Synthetic Jets

There are several key dimensionless parameters that define the formation and subsequent roll-up of synthetic jets. The formation of synthetic jets is primarily characterised by the dimensionless 'stroke' length. Based on the slug model mentioned in section 2.4.1.2, Smith and Glezer (1998) proposed the following velocity scales to originally facilitate a comparison between synthetic jets and steady jets, which has subsequently been widely adopted in the synthetic jet literature (e.g. Smith and Swift, 2003; Milanovic and Zaman, 2005; Tang and Zhong, 2006 and Mark and Zhong, 2006)

$$\overline{U_o} = \frac{1}{T}\int_0^{T/2} \widetilde{u}_o(t)dt \qquad \textbf{Eq. 2-8}$$

Where $\overline{U_o}$ is the jet blowing velocity averaged over the entire cycle and $\widetilde{u}_o(t)$ is the instantaneous, spatial-averaged velocity at the orifice exit. Note that $\overline{U_o}$ is neither the time average of $\widetilde{u}_o(t)$ over a whole cycle, which should be zero, nor its time average over a time $T/2$ (i.e. the blowing half of a complete cycle), which is $2\overline{U_o}$. The stroke length is now defined as

$$L_o = \int_0^{T/2} \widetilde{u}_o(t)dt = \overline{U}_o T \qquad \textbf{Eq. 2-9}$$

which represents the length of fluid column ejected during the blowing stroke. L_o can be non-dimensionalised by the orifice diameter to give the dimensionless stroke length, L

$$L = \frac{L_o}{D_o} = \frac{\overline{U_o}T}{D_o} = \frac{\overline{U_o}}{fD_o} \qquad \textbf{Eq. 2-10}$$

The distance between consecutive vortices that are periodically formed through an orifice is related to the Strouhal number. It can be shown that the Strouhal number is related to the stroke length by

$$St = \frac{D_o f}{\overline{U_o}} = \frac{1}{L} \qquad \textbf{Eq. 2-11}$$

It has been noticed that a threshold value exist for the dimensionless stroke length for the formation of vortex rings from an impulsively-started piston (Didden, 1979). It was observed that isolated vortex rings could not be produced for $L < 0.4$. Similarly, for synthetic jets, a minimum stroke length is required to ensure propagation of newly formed vortices away from the orifice and therefore jet formation.

For synthetic jets, the stroke length represents the length of the fluid column ejected during the blowing stroke (Equation 2.9). It is also proportional to the distance that a vortex ring travels away from the orifice exit. If the stroke length is too small, the vortex ring can not move sufficiently far away from the orifice before the onset of the next suction stroke. Consequently, the ring will be ingested back into the orifice due to suction. As a result, a synthetic jet will only form when the vortex ring is able to overcome the suction velocity during the ingestion stroke.

Several studies have been undertaken to establish the criterion for synthetic jet formation. The investigation of Smith *et al* (1999) revealed that the formation criterion for round synthetic jets is $L = 1$ (note that the value presented here has been altered to be consistent with the definition given in equation 2.10) and below this value the vortex structure is ingested back into the orifice during the suction stroke hence no jet is formed. Holman *et al* (2005) defined synthetic jet formation as the appearance of a time-averaged outward velocity along the jet axis which corresponds to the generation and subsequent convection of vortex rings. Based on their numerical and experimental studies, a formation criterion for both two-dimensional and axisymmetric synthetic jets was proposed. It was stated that in order for the synthetic jet to form the reciprocal of the Strouhal number $\frac{1}{Str} = \frac{\overline{U}}{2\pi f D_o}$ should be greater than a threshold value K, where the constant K depends on geometric factors such as orifice/slot shape, radius of curvature and aspect ratio of slot. For axisymmetric synthetic jets, K is found to be equal to 0.16, which means the dimensionless stroke length L is about 0.5 taking into account the relationship between the Strouhal number and the dimensionless stroke length. Milanovic and Zaman (2005) obtained yet a smaller criterion of $L = 0.25$. The difference in the threshold is attributed to factors such as the differences in the lip shape of orifice and the diaphragm velocity programme. Fugal *et al* (2004) studied the formation of a plane synthetic jet using numerical simulations and found that the threshold is about $L = 2$ for a sharp lip and about $L = 10$ for a rounded lip.

2.4.2.2 Extent of vortex roll-up

Vortex rings are known for their ability to entrain ambient fluid into their cores which enhances mixing. When a synthetic jet is issued into a boundary layer, the injection of coherent vortices via the initial vortex roll-up results in the formation of a hierarchy of vortical structures, which are capable of delaying flow separation. It is understandable that the strength of vortex rings in terms of the level of circulation will determine the impact of synthetic jets on external flow. A question remains, however, if a synthetic jet which satisfies the aforementioned formation criterion will definitely have a vortex roll-up.

Tang (2006) studies the behaviour of synthetic jet using numerical simulation and demonstrates that roll-up is primarily characterised by the Stokes number, *S*. The Stokes number for an oscillatory pipe flow is defined according to equation 2.12 as

$$S = \sqrt{\frac{2\pi f D_o^2}{\nu}} \qquad \textbf{Eq. 2-12}$$

The strength of a vortex sheet can be measured by the level of vorticity Ω. And the dimensional form of the vorticity can be estimated as

$$\frac{\Omega D_o^2}{\nu} \sim L \cdot S^2 \cdot \frac{D_o}{\varepsilon} \qquad \textbf{Eq. 2-13}$$

where ε is the thickness of the Stokes layer in the orifice, which is defined as the radial distance between the position of the velocity peak and the wall at the orifice exit. The dimensionless vorticity expressed on the LHS of equation 2.13 indicates that, to obtain a similar roll-up, vorticity Ω should be much higher for an actuator with an orifice of small diameter. It is true because the vortex ring of small scale has a higher curvature, which demands a higher vorticity on the vortex sheet. It is found that the normalised thickness of the Stokes layer ε/D_o is to be a function of the Stokes number assuming that the oscillating flow in the orifice is a fully developed laminar flow. Figure 2.16a and 2.16b show the variation of ε/D_o and its inverse against the Stokes number *S* respectively. Figure 2.16a indicates that the velocity peak stays at the centre of the orifice exit when $S < 10$, whereas it gradually retreats towards the orifice wall as *S* increased when $S > 10$. The position of the velocity peak is believed to affect the roll-up of vortex sheet. Imagining that a 'thick' cylindrical vortex sheet dominates the whole the whole orifice duct when $S < 10$, with a maximum velocity at the centre, the leading edge of the vortex sheet is unable to curve due to the axisymmetry and continuum of the

flow. When S is greater than 10, however, a potential core appears at the centre of the orifice, allowing the rollup of vortex rings. In addition, since D_o/ε increases with the Stokes number when $S > 10$ (see figure 2.16b), equation 2.13 reveals that the dimensionless vorticity on the vortex sheet depends more on the Stokes number S than on the dimensionless stoke length L.

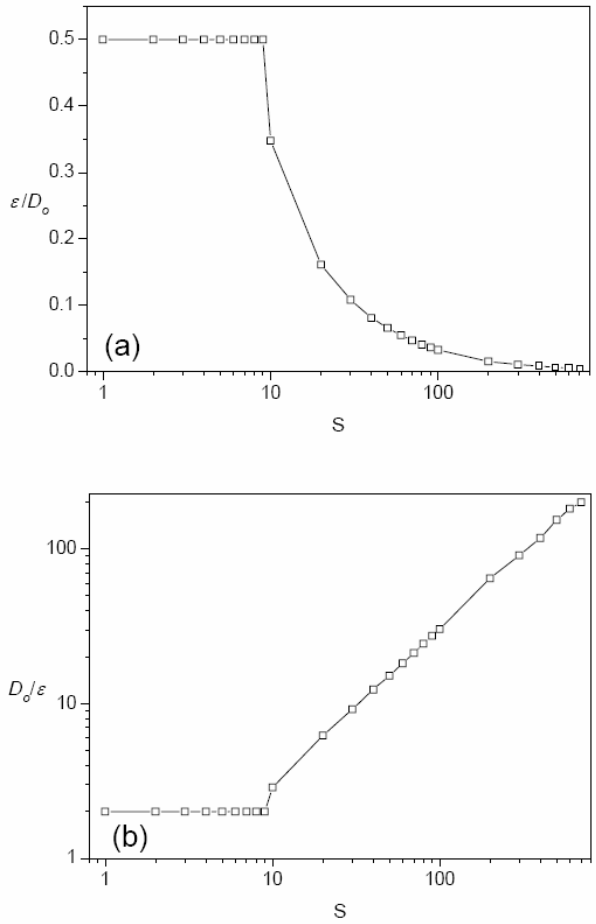

Figure 2.16 Variation of the thickness of the Stokes layer in an oscillating pipe flow (a) ε/D_o vs. S and (b) D_o/ε vs. S (Tang, 2006)

The effect of change S and L on the exit velocity profiles of synthetic jet issued from an orifice with a finite length (h/D_o = 1) is also illustrated using numerical simulation. As shown in figure 2.17a, at the same L the exit velocity profile changes gradually from a near parabolic shape to a top-hat shape as S increases from 7 to 22. The influence of the Stokes number on synthetic jets appears to be similar to what is known of oscillating pipe flow. In figure 2.17b, the normalised velocity profiles at the same Stokes number (S = 14.7) but different L are compared. It is shown that the dimensionless stroke length also affects the shape of the exit velocity profiles considerably, especially the central part of the profile. A lower L produced by the use of

a smaller diaphragm displacement results in a dip in the central region, which stretches itself out as the dimensionless stroke length increases. In comparison, L appears to exert less effect on the exit velocity profile than the Stokes number.

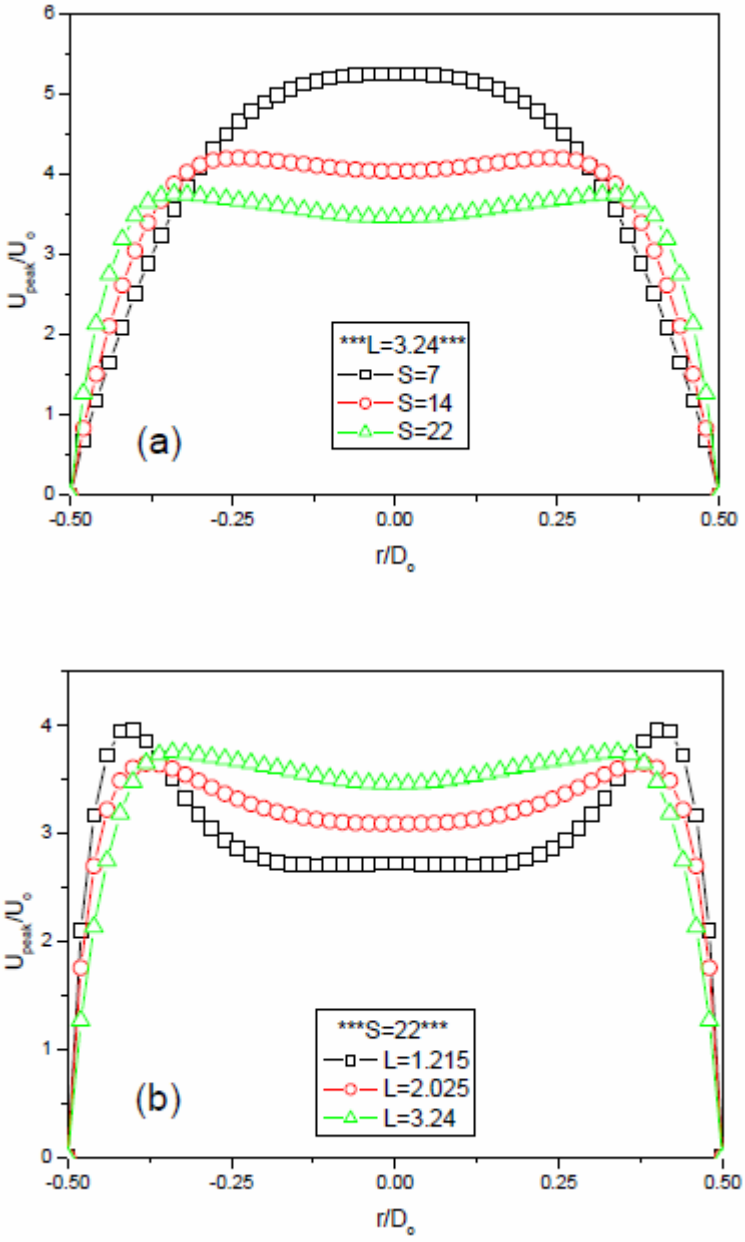

Figure 2.17 Comparison of exit velocity profile (a) at different Stokes numbers and (b) at different dimensionless stroke lengths (Tang, 2006)

Using particle tracking method, Tang (2006) showed the effect of the magnitude of the Stokes number (S = 22, 12 and 7) on the strength of vortex roll-up at fixed dimensionless stroke length (L = 3), as shown in figure 2.18. At S = 22, the timelines on the wings of the jet curl around due to an intense local rotational motion indicating the presence of a strong vortex roll-up. The blank area inside the vortex core is largely

formed of the surrounding fluid that is entrained into the vortex. At S = 7, however, although the timelines one the wings of the jet still curl towards the stem of the jet, rotational motion is barely visible and no vortex rings forms. At S = 12, a moderate level of rotational motion around the vortex core is observed.

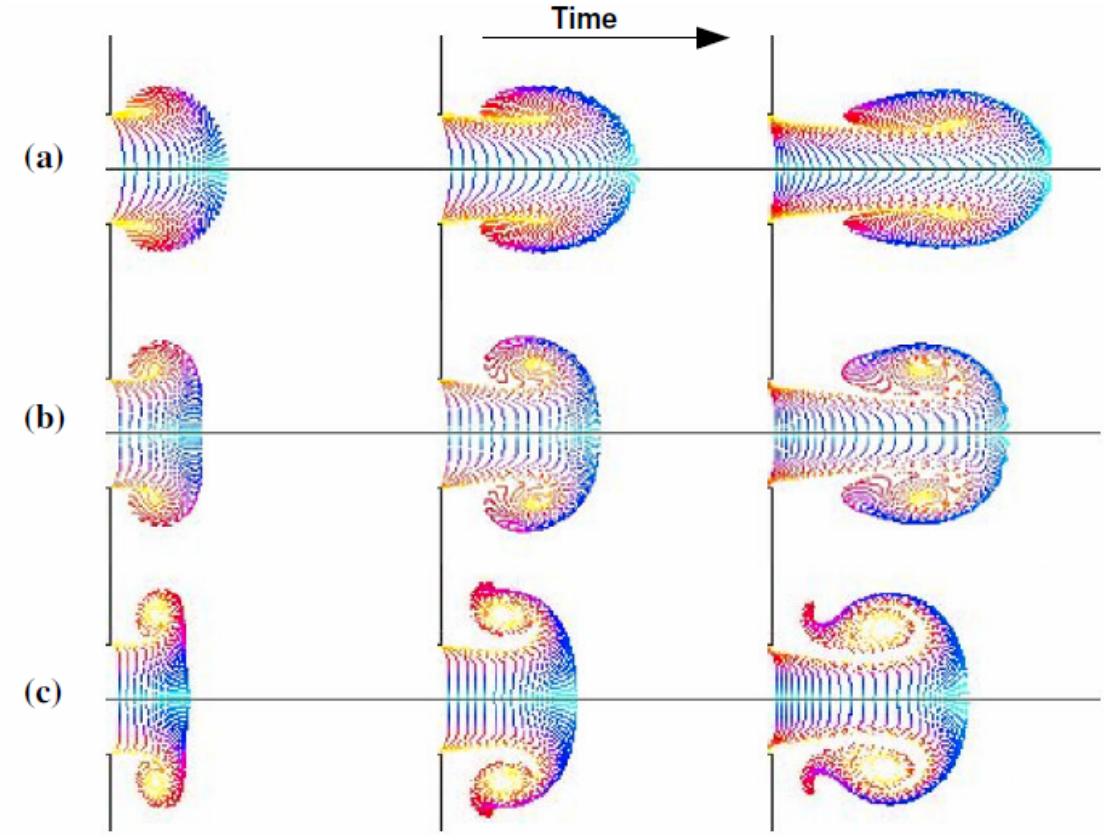

Figure 2.18 Illustration of the extent of vortex roll-up using particle tracking (a) L = 3.24, S = 7; (b) L = 3.24, S = 12.1 and (c) L = 3.24, S = 22.2 (Tang, 2006)

Based on the above visual impressions, Tang proposed that a minimum Stokes number of about 10 is required for an appreciable roll-up to occur within the range of dimensionless stroke length examined. The parabolic exit velocity profile at S = 7 is believed to be the reason that no vortex roll-up is observed in this case since merging of the Stokes layers along the orifice axis inhibits the curling up of vortex sheets that form the vortex rings. The criterion of a minimum Stokes number of 10 is also consistent with the theoretical prediction for fully developed oscillating pipe flows.

2.4.2.3 Strength of Vortex rings of synthetic jets

A synthetic jet issued from circular orifice consists of a train of vortex rings. For flow control purpose, the vortex circulation of vortex rings is the key characteristic, which represents the strength of the vortex ring. Glezer (1988) showed that the circulation of a

vortex ring is directly related to a Reynolds number based on the stroke length, L_o. Substituting equation 2.9 into equation 2.6

$$\frac{2\Gamma_o}{\nu} = \frac{PL_o^2}{2T\nu} = \frac{P\overline{U_o}L_o}{\nu} \qquad \textbf{Eq. 2-14}$$

The term on the RHS of equation 2.14 emerges as a Reynolds number, which allows various vortex-ring flows to be ordered according to their strength. In the present study, this Reynolds number is defined as

$$\mathrm{Re}_L = \overline{U_o}L_o/\nu \qquad \textbf{Eq. 2-15}$$

This is related to the dimensionless circulation on the LHS of equation 2.14. Therefore, for a synthetic jet that satisfies the criteria of jet formation and vortex roll-up, the Reynolds number ultimately determines the strength of the vortex rings.

Smith and Swift (2003) used the Reynolds number based on the time-averaged jet blowing velocity over the entire cycle, $\overline{U_o}$, ($\mathrm{Re} = \overline{U_o}D_o/\nu$) to characterise synthetic jets and compare their behaviour with steady jets of the same Reynolds number. It can be shown that this Reynolds number is related Re_L by

$$\mathrm{Re}_L = \frac{\overline{U_o}L_o}{\nu} = \mathrm{Re}\frac{L_o}{D_o} = \mathrm{Re}\cdot L \qquad \textbf{Eq. 2-16}$$

Also note that the three key dimensionless parameters of synthetic jet in quiescent conditions namely, L, S, Re_L are all related to each other via

$$S = \sqrt{\frac{2\pi\,\mathrm{Re}_L}{L^2}} \qquad \textbf{Eq. 2-17}$$

therefore only two are independent.

Using Reynolds number based on the peak velocity, U_{peak}, ($\mathrm{Re}_{U_{peak}} = U_{peak}D_o/\nu$), Crook and Wood (2000) studied the round synthetic jets at different forcing levels. The smoke visualization experiment revealed a number of different flow patterns of vortex rings of synthetic jets depending on the Reynolds number and stroke length, as shown in figure 2.19.

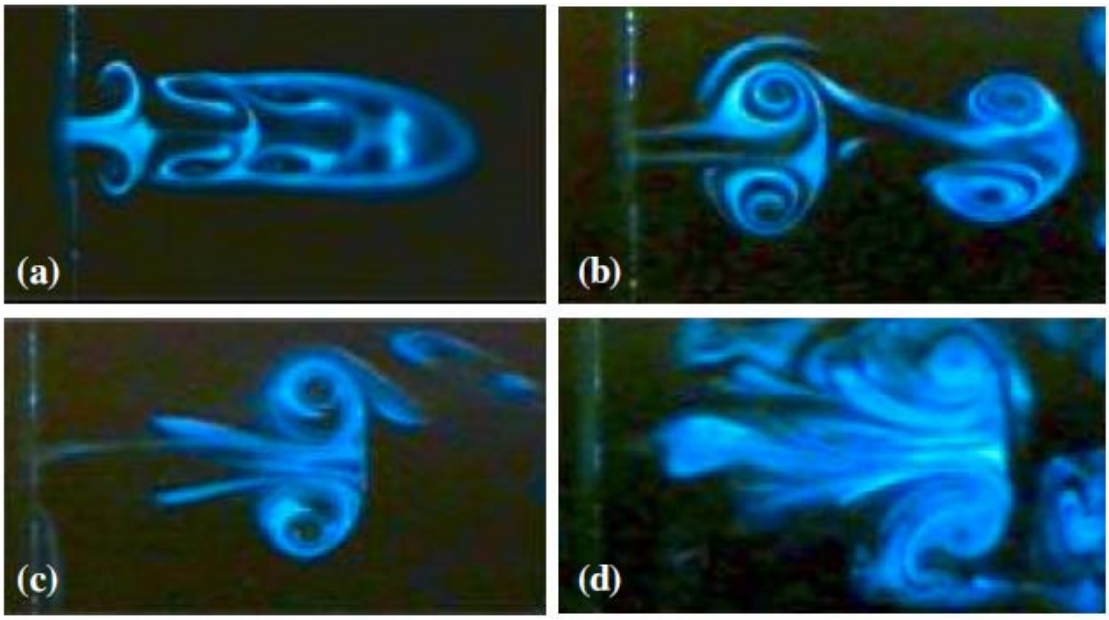

Figure 2.19 Four different flow patterns of vortex rings produced by synthetic jets with D_o = 5mm and f = 50Hz: (a) $\mathrm{Re}_{U_{peak}}$ = 330, L = 1.2; (b) $\mathrm{Re}_{U_{peak}}$ = 660, L = 2.4; (c) $\mathrm{Re}_{U_{peak}}$ = 980, L = 3.6 and (d) $\mathrm{Re}_{U_{peak}}$ = 2300, L = 8.5 (Crook and Wood, 2000)

For the lowest Reynolds number of 330 (figure 2.19a), the vortex rings are of low circulation, as indicated by the small core sizes. The relatively low stroke length for this case (L = 1.2) also means that suction has a dominant effect on the vortices, as seen by the elongation of the rings along the axis of symmetry. Furthermore the interaction between adjacent rings is very strong due to their close proximity to each other, such that they eventually merge together at a few diameters away from the orifice.

For a Reynolds number of 660 (figure 2.19b), the vortex rings have a higher circulation relative to those in figure 2.19a. This is indicated by the core of the rings, which are more defined and larger in diameter due to increased entrainment of fluid. The influence of suction is also diminished due to the higher stroke length (L = 2.4).

As the Reynolds number increases to 980 (figure 2.19c), the vortex ring is still characterised by a well-defined core. And once again, the diameter of the vortex ring has increased from that at the lower Reynolds numbers. The diameter of the ring is an indication of its circulation. The fact that the diameter of the ring does not increase on the appearance of a large wake indicates that the circulation of the vortex ring has reached a limit, which is less than the total circulation produced in the generation process. The reason is the stroke length (L = 3.64) reaches the limit ($L \approx 4$) to the maximum circulation that a vortex ring can acquired, which is consistent with the knowledge of the aforementioned formation number in section 2.4.1.3.

At the highest Reynolds number of 2300 (figure 2.19d), the vortex ring diameter is comparable with that in figure 2.19c. Further increases in Reynolds number do not increase the diameter of the vortex ring, as one would expect with the knowledge that a vortex circulation limit exits. The increase in Reynolds number has resulted in a region of concentrated vorticity in the wake of the ring. This is in fact a secondary vortex ring, which is the result of strong vorticity shed into the tail. The appearance of the secondary vortices is still believed to be due to the fact that a vortex ring can only accommodate a certain level of circulation. Jabbal (2008) observed the variation of total circulation and primary vortex circulation with the dimensionless stroke length. The circulation in the primary vortex increases until L reaches 4. When L exceeds 4, the circulation in the primary vortex remains constant although the circulation in the entire structure continues to increase.

2.4.2.4 Evolution of Synthetic Jets

The near-field evolution of synthetic jets is dominated by the periodic formation, advection, and interactions of discrete vortical structures. Due to the suction flow, the time-averaged static pressure near the exit plane of a synthetic jet is typically lower than the ambient pressure and both the streamwise and cross-stream velocity components reverse their direction during the actuation cycle. The periodical reversal in flow direction along the jet centreline (between the blowing and suction strokes) leads to the formation of a stagnation point on the centreline downstream of the orifice and hence the suction flow is confined within a finite region near the exit plane. The present of saddle point in the near field of synthetic jets has been observed in several studies (e.g. Gilarranz and Rediniotis, 2001; Glezer and Amitay, 2002 and Fugal *et al*, 2005).

The oscillatory nature of the synthetic jet flow in the near field, which is dominated by vortex rings also gives rise to a much greater entrainment of ambient fluid compared with the case of a steady jet, as demonstrated by Mallinson *et al* (2001), Cater and Soria (2002) and Smith and Swift (2003). As a result, synthetic jets grow more rapidly, both in terms of jet width (i.e. increased spreading) and volume flux, thereby establishing more quickly than steady jets. The larger spreading rate of synthetic jets compared to steady jets is shown in terms of fluorescent dye visualisation (Cater and Soria, 2002) in figure 2.20.

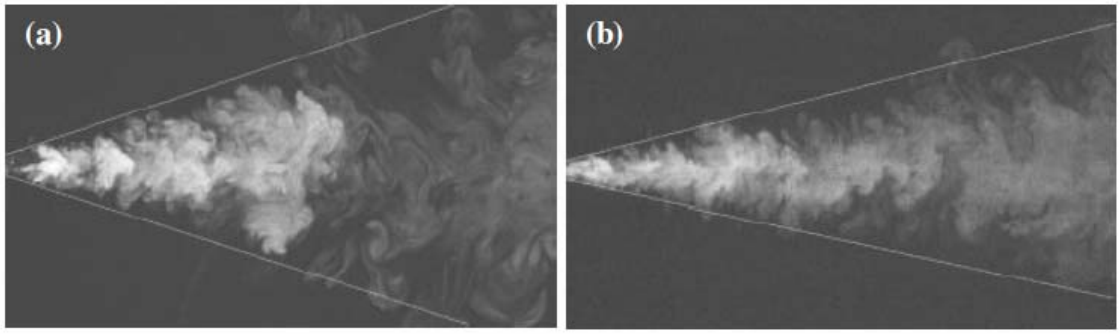

Figure 2.20 Flow visualisation of fluorescent dye marker for (a) a synthetic jet and (b) an equivalent steady jet. The light-coloured lines drawn on the images indicate the mean boundary of the dye flow. The approximate spreading rates are: (a) $Str_b \approx 0.13$ and (b) $Str_b \approx 0.1$ (Cater and Soria, 2002)

In the far field of synthetic jets, the vortex rings eventually become undistinguishable from the jet flow and travel with the jet mean velocity. For the study of 2D synthetic jets in air, Smith and Glezer (1998) found that the vortices decelerate and transition to turbulence within 7 slot widths. Consequently, the far field behaviour of a synthetic jet is similar to that of a conventional (turbulent) steady jet. Self-similarity of a conventional steady jet implies that its characteristic width and the inverse of its centreline velocity increase linearly with distance from the orifice exit. Studies by Smith and Glezer (1998) and Mallinson *et al* (2001) have reported that the streamwise variation of the centreline and cross-stream velocity distributions of synthetic jets appear to collapse when plotted in the usual similarity coordinates, thus confirming their similarity to a steady jet in the far field.

2.4.3 Parameters of Synthetic Jet Actuators

As mentioned previously, for synthetic jet actuators there are four geometric parameters (orifice diameter D_o, cavity diameter D_c, orifice depth h, and cavity height H) and two operating parameters (diaphragm oscillatory frequency f, and diaphragm displacement, Δ). In addition, two independent non-dimensional parameters (stroke length L, and Reynolds number Re_L) characterises the performance of synthetic jets in quiescent conditions. For flow control purposes, the jet velocity, momentum and circulation are amongst the most important performance parameters that determine the impact of synthetic jets on the external flow (Tang and Zhong, 2006). In order to optimise synthetic jets actuators for flow control, an understanding of the relation of the actuator parameters with both the dimensionless jet flow parameters and performance parameters is necessary.

2.4.3.1 Effect of Geometric parameters of SJAs

The orifice diameter D_o (or width h for rectangular orifice) is the most important characteristic length scale for synthetic jet actuators. Given that the process of forming a vortex ring at low frequencies is essentially incompressible, a decrease in orifice diameter increases the jet velocity according to the law of mass conservation. The ratio of surface force to body force, which is proportional to D_o^{-1}, affects the behaviour of the flow in the orifice significantly. This indicates that the surface force, which is essentially the viscous friction, can be negligible for an orifice of large diameter, whereas it becomes dominant in orifices of a small diameter. Experience gathered in MEMS shows that the surface force has a dominant effect in devices with a size smaller than a millimetre (Ho and Tai 1998). In this thesis, therefore, synthetic jet actuators with D_o > 1mm are defined as macro-scale actuators, whereas those with D_o < 1mm are defined as micro-scale actuators. The significant viscous friction in the orifice as a result of a small orifice diameter will lead to the onset of compressibility in the cavity flow and therefore the incompressible assumption is not valid for micro-scale actuators.

The orifice depth h affects the development of the oscillatory flow in the orifice. If h is large enough, the flow in the orifice is fully developed which can be analysed as a classical oscillatory pipe flow. If h is small, however, the separation bubble located at the orifice inlet could affect the flow in the whole orifice duct, making the flow complex. Also, an accelerating region exists at both the inlet and outlet of the orifice, introducing an extra length to the nominal orifice depth. The extra length is a small multiple of the orifice diameter (Rathnasingham and Breuer, 1997), which can make significant changes if the orifice depth is relatively small compared to the orifice diameter. The ratio of orifice depth to orifice diameter, h/D_o, is found to affect the stability of the ejected vortex ring. Crook (2002) concluded that the ratio should be of the order of unity to find a compromise between the stability of the vortex sheet forming the ring and the produced vortex circulation. Crook and Wood (2000) also observed in their smoke visualization experiments that an increase of orifice depth resulted in an increase in the circulation of vortex rings. They explained that a deeper orifice would produce a thicker orifice boundary layer, which creates a larger diameter vortex core, increasing the vorticity and hence the total circulation produced. However, the finding of Crook and Wood is contrary to the numerical simulation results of Tang and Zhong (2005), which showed that vortex strength increased with reducing h. Simulation of the flow through the orifice duct revealed that the extent of the separation zone (bubble) varies

with h, hence affecting the flow characteristics at the orifice exit and ultimately, vortex circulation. The reason for the discrepancy could be method used for the measurement of the vortex circulation, which is based on the size of the vortex ring from images. Comparatively, the results of Tang and Zhong (2005) is obtained from quantitative simulation information and thus more convinced. The PIV measurement results of Jabbal (2008) show that the vortex circulation remains relatively constant when h/D_o is greater than 1 but increases rapidly when h/D_o decreases from 1, reaching a maximum at $h/D_o = 0.5$ across the range of diaphragm.

The cavity also has an effect on the strength of the vortex rings. Crook and Wood (2000) observed that an increase in cavity height, H, resulted in an increase in vortex circulation, as observed in the more defined cores pertaining to the vortex rings. It was suggested that for a larger cavity, the ingested vortex travels further and in doing so, induces more vorticity on the cavity walls, thereby increasing the level of vorticity of a newly formed vortex ring during the blowing stroke. Similarly however, their finding is contrary to the numerical simulation results of Rizzetta *et al* (1999), Lee and Goldstein (2002) and Tang and Zhong (2005). These studies all showed that vortex strength gradually increased with reducing H. Rizzetta *et al* (1999) explained that the reduced vortex circulation could be accounted by the increased penetration of the vortex rings into the cavity, thereby reducing their effect on the flow ejected through the orifice. Lee and Goldstein (2002) believed that the vorticity inside a shallow cavity might be pushed out of the orifice during blowing, thereby enhancing vortex roll-up. For the cavity diameter, Tang and Zhong (2005) showed that when the stroke length is kept the same, variations in the cavity diameter had negligible impact on the strength of the ensuing vortex rings.

Consider a container of air with an orifice. If disturbed, the volume of air in and near the orifice tends to vibrate at a certain frequency due to the 'springiness' of the air inside the container. This resonant frequency is referred to as the Helmholtz frequency and is dependent upon the geometry of the container and orifice as well as the fluid properties of the air. Consisting of a cavity with an orifice and an oscillating diaphragm that provides a continuous source of excitation, a SJA can be regarded as a Helmholtz resonator. If the column of air in the orifice is treated as a dynamic system consisting of a mass suspended on a spring, the Helmholtz frequency, f_H, of a cylindrical SJA with an orifice, as derived by Tang and Zhong (2007) is given by

$$f_H = \frac{a}{2\pi}\frac{D_o}{D_c\sqrt{Hh'}} \qquad \textbf{Eq. 2-18}$$

where a is the speed of sound, D_o and D_c are, respectively, the orifice diameter and cavity diameter, and h' is the effective orifice depth, $h' = h + 0.85D_o$. The effective orifice depth accounts for the accelerated flow region at the two ends of the orifice, which adds an extra length to the geometric length of the orifice, h.

At Helmholtz resonance, the small driving force in the cavity is amplified to produce a large mass flow through the orifice (i.e. relative to the mass displaced by the diaphragm alone), thereby increasing the peak in space-averaged exit velocity. It is anticipated for a SJA operating at or near the Helmholtz frequency, the increase in exit velocity will give rise to a higher velocity gradient between the near wall and core flow through the orifice duct. As a result, the strength of the separating shear layer increases, thereby increasing the circulation of the vortex ring.

2.4.3.2 Effect of Actuating Parameters

The two operating parameters, diaphragm displacement Δ and frequency f, can be tuned to obtain synthetic jets of different strength. It is obvious that increasing Δ for fixed f would result in an increase in the jet velocity according to the law of mass conservation. The stroke length L_o represents the length of air column ejected during an oscillating cycle. Muller *et al* (2001) stated that L_o can be used to characterise the amplitude of the oscillation in the orifice. And Fugal *et al* (2005) concluded that the near-field behaviour of synthetic jets should be scaled on L_o rather than slot width h. As mentioned previously, the formation criterion of a synthetic jet is associated with the dimensionless stroke length, below certain of which no jet is generated. The experimental investigation of Jabbal *et al* (2006) revealed that the formation number for a round synthetic jet is still approximately four, beyond which the circulation of the primary vortex saturates and the excess vorticity sheds into a trail or even forms a secondary vortex structure.

The effect of varying f is more complex. For a given power input, a change in f is usually accompanied by a change in Δ, depending on the mechanical property of the diaphragm (Gallas *et al*, 2003a; Lockerby and Carperter 2004 and Gomes *et al*, 2006b). For synthetic jet actuators, there are two characteristic frequencies which are the frequency of Helmoltz resonance and the frequency of the diaphragm mechanical resonance. The mechanism of Helmholtz Resonance can be found from many acoustics

books (Kinsler *et al*, 1982 and Dowling *et al*, 1983). And usually the diaphragm is made of a metal disc, which is clamped around its edge. The mechanical resonance frequency is dependent on its geometric and material properties. For a given actuation input, the effectiveness of the actuator can be maximised when the diaphragm and cavity are driven at a coupled resonance.

The mechanical property of piezoelectric mechanisms however, is such that the oscillation amplitude is dependent on the oscillation frequency and therefore the sole effect of each cannot be determined. The sole effect of f on jet performance can be studied by keeping Δ fixed while varying the power input to the mechanical system of the diaphragm, e.g. the use of a diaphragm driven by a permanent magnetic shaker (Crook and Wood, 2000 and Jabbal *et al*, 2006).

At the University of Manchester, Tang and Zhong (2006) developed an incompressible, performance prediction model for circular SJAs using both dimensional and quantitative analyses from a theoretically predicted diaphragm deformation. The model provides analytical relations between the performance parameters and the operating parameters of SJAs, in which Δ and f are allowed to vary independently of each other. Tang and Zhong (2006) assumed the diaphragm to be an ideal deformable shell without mechanical and material properties. In this way, Δ and f are decoupled and the input of the system is change from electrical voltage to Δ and f thereby allowing the analysis to be purely mechanics-based. In the first instance, the model was validated via a systematic numerical study with good agreement.

2.5 Synthetic Jets in Cross-Flows

The study of synthetic jets in a cross-flow allows an insight into the behaviour and the interaction between the synthetic jets and a boundary layer. A lot of efforts have been made to investigate the impact of synthetic jets on the boundary layer, which could improve the ability of flow separation control.

2.5.1 Interaction with a Uniform Cross Flow

For a synthetic jet with fixed geometry, the list of parameters on which the behaviour of the synthetic jet will depend should be extended to include the freestream velocity, U_∞, as well as the diaphragm operating conditions. Therefore, in addition to the key dimensionless jet parameters in quiescent conditions (i.e. L and Re_L), the jet-to-

freestream velocity ratio, *VR*, and Strouhal number, *St* (based on U_∞) need to be considered. In current study, *VR* and *St* are defined as

$$VR = \frac{\overline{U_o}}{U_\infty} \qquad St = \frac{fD_o}{U_\infty} \qquad \textbf{Eq. 2-19}$$

where *VR* represents the relative strength between the jet and the freestream velocity. Note that the definition of *VR* may vary according to the jet velocity scale used. For the present synthetic jet actuator, *VR* defined using U_{peak} will be π time of that defined with $\overline{U_o}$ since $U_{peak} = \pi\overline{U_o}$. The use of $\overline{U_o}$ represents a more 'stable' reference jet velocity compared to U_{peak} and it is used in the definition of *VR* in the present study unless otherwise stated. The velocity ratio *VR* ultimately characterises the trajectory of the vortex structures as they propagate downstream (Crook *et al*, 2000). For a synthetic jet in cross flow, it has been shown that at a given streamwise location, the jet penetration height is solely a function of the momentum flux ratio, which is equivalent to the velocity ratio *VR* in the present study (Milanovic and Zaman, 2005). Thus at low values the synthetic jet will reside within the boundary layer for a longer period of time, thereby increasing its potential effectiveness where flow control is ultimately desired.

St in equation 2.19 represents the Strouhal number, which is based on the U_∞. The use of U_∞ instead of $\overline{U_o}$ in defining *St* in a cross flow emphasises the influence of the freestream flow on periodic behaviour of the synthetic jet. When an external flow is present, the vortex rings will be forced to convect with that flow shortly after they emerge from the orifice and hence the use of *St* based on U_∞ is more appropriate in describing the behaviour of synthetic jets in a uniform cross flow or boundary layer.

The dynamics and trajectories of vortex rings formed by the pulsation of a jet in a uniform flow were studied by Chang and Vakili (1995) using flow visualisation and numerical simulation. They observed that the vortex rings formed at low pulsing frequencies penetrated in the cross flow much deeper than for high pulsating frequencies. With an increased frequency, therefore the Strouhal number, the spatial distance between successive vortex rings becomes smaller, thereby producing stronger interactions between vortices that reduces their penetration. They also observed that the penetration of vortex rings into the cross flow was considerably deeper with the increase of vortex strength. It was hypothesised that an increased penetration combined with the discretisation of a jet into vortex rings result in an increased mixing. Furthermore, it was

observed that vortex rings had a tendency to tilt as they moved into the flow by as much as 30˚. Experiment and numerical simulations showed that non-uniform interaction with the cross flow leads to the tilting of the ring as it is formed near the jet exit. This tilting resulted in the downstream portion of the vortex moving farther into the cross flow.

Similar results were reported by Crook (2002) for synthetic jets in a cross flow. Flow visualisation of synthetic jet in a cross flow for different diaphragm displacements, frequencies and freestream velocities were carried out. At lower values of *VR* (based on peak jet velocity) and *St*, larger spacing between vortex rings leads to less interaction, resulting in the vortices retaining their coherency over a larger distance as shown in figure 2.21. At higher values of *St* and *VR*, reduced spacing between adjacent rings increases their mutual interaction and leads to incoherent structures being ejected, shown in figure 2.22. Laminar vortex rings appears in the case of figure 2.21 and a reduction in the diameter of the upstream side of the ring relative to the downstream side was observed. This is due to an asymmetric roll-up, as the downstream side of the ring is effectively shielded from the oncoming flow by the upstream side. For $St \approx 0.1$ and low values of *VR*, the vortical structures were subject to the very thin boundary layer due to the close distance to the wall. Crook suggested that the tilting of the vortex ring, combined with stretching in the presence of shear, presents a mechanism for the formation of a quasi-steady, streamwise longitudinal vortex pairs. It was hypothesised that the coalescence of stretched vortex rings, figure 2.23, was responsible for the cylinder surface flow patterns subject of flow control by synthetic jet actuators as reported by Crook and his co-authors (Crook, 2000).

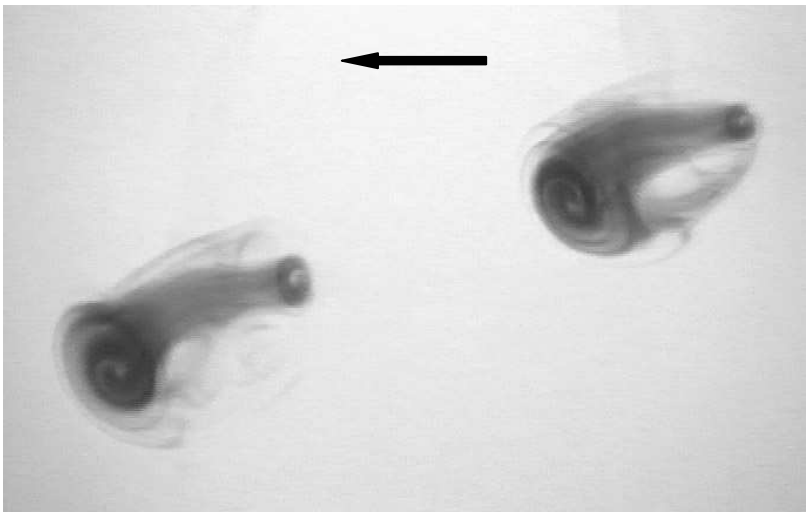

Figure 2.21 Tilting and asymmetry of vortex rings in a synthetic jet in a cross-flow for VR = 2.1 and St = 0.15 at U_∞ = 0.066ms^{-1} (Crook, 2002)

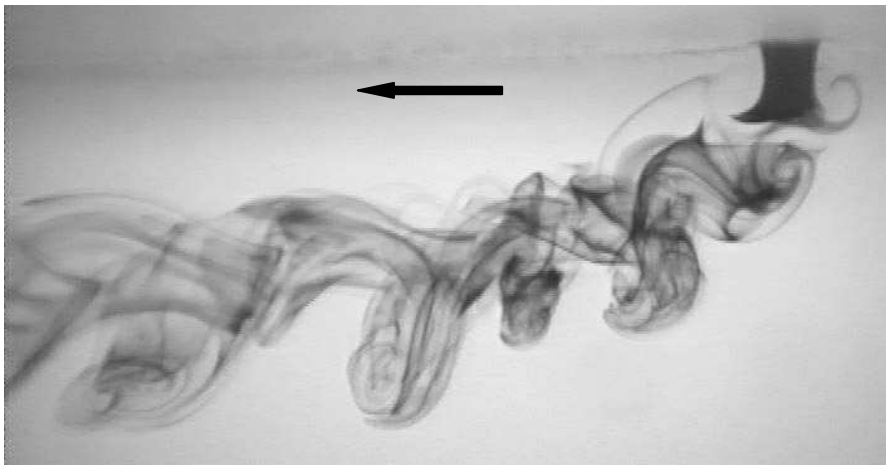

Figure 2.22 Complex linking of the vortex rings of a synthetic jet in a cross flow for VR = 0.33 and St = 0.38 at U_∞ = 0.066ms^{-1} (Crook, 2002)

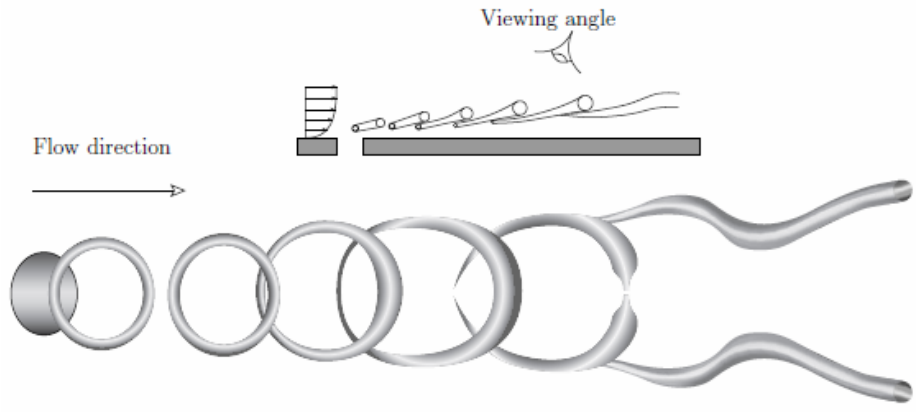

Figure 2.23 Sketch of hypothesised structure of a synthetic jet embedded in a turbulent boundary layer in play view (Crook, 2002)

Milanovic and Zaman (2005) studied the behaviour of a synthetic jet in cross flow using hot-wire anemometry and a numerical simulation and compared it to a steady jet in cross flow. It was observed that for given f and U_∞, the penetration distance of a synthetic jet increased with an increasing L. Furthermore, distributions of mean velocity, streamwise vorticity, as well as turbulence intensity for a synthetic jet were found to be similar to those of a steady jet when the peak exit velocity of a synthetic jet was equal to the mean exit velocity of a steady jet for a given cross flow. A pair of counter-rotating streamwise vortices was also observed in the case of synthetic jet, which corresponded with the bound vortex pair in the steady case. In both cases, the vortex pair gave rise to the lift up of low-momentum fluid near the inboard of each vortex.

2.5.2 Interaction with a Boundary Layer

For a synthetic jet embedded in a boundary layer, the parameters of the boundary layer that affect the behaviour of a synthetic jet should include the boundary thickness δ and wall shear stress τ_w. From the dimensional analysis expressed as non-dimensional parameters, these equate to the ratio of boundary layer thickness to orifice diameter, d, and skin friction coefficient, c_f.

$$d = \frac{\delta}{D_o} \qquad c_f = \frac{\tau_w}{\rho U_\infty^2} \qquad \textbf{Eq. 2-20}$$

Note that in the aforementioned studies of Crook (2002) and Milanovic and Zaman (2005), the ratios of boundary thickness to orifice diameter were small (i.e. $d \leq 1$), such that the boundary thickness was considered not important, as the synthetic jet penetrated the layer quickly without being affected by the shear.

Several studies have been undertaken in larger shear flows (i.e. $d > 1$), typically utilising a synthetic jet actuator embedded in a flat boundary layer to explore some of the fundamental interaction characteristics. Mittal *et al* (2001) simulated the interaction of a synthetic jet from a 2D slot with a laminar boundary layer for three different values of VR, based on U_{peak}. At the lowest $VR \approx 0.3$ (figure 2.24a), the upstream side of the vortex exposed to the oncoming boundary layer is quickly cancelled. Conversely, the downstream component, with a vorticity of the same sense as the boundary layer, remains embedded near the wall and does not entrain any freestream fluid. At $VR \approx 0.67$ (figure 2.24b), an asymmetric vortex still appears, however it penetrates into the boundary layer deeper, which results in entrainment of freestream fluid by the

downstream vortex into the boundary layer. At $VR \approx 3$ (figure 2.24c), the increase of velocity ratio results in the upstream component surviving the onset of shear, with a symmetrical vortex pair ensuring. The vortex pair rapidly penetrates the boundary layer and convects away into the freestream. They also observed that at $VR \approx 3$, the streamline are perturbed to such an extent that a large mean recirculation bubble forms, thereby altering the effective shape of the body. In contrast, no circulation bubbles were found at the lower VR and the streamlines were only slightly perturbed in the near vicinity of the jet exit.

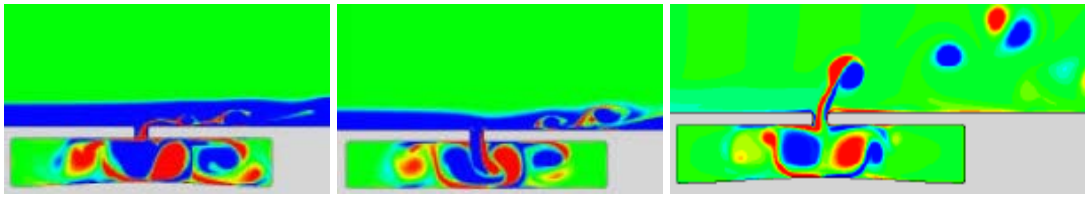

Figure 2.24 Plot of synthetic jet vorticity contours a) $VR \approx 0.3$; b) $VR \approx 0.67$ and c) $VR \approx 3$ (Mittal *et al*, 2001)

Schaeffler (2003) studied the interaction between the round synthetic jets and a turbulent boundary layer, tested at different velocity ratio VR. It was proposed that as the jet pulse develops and moves out into the boundary layer it evolves in a continuously changing fashion that interacts with the boundary layer fluid continuously. The jet and the boundary layer must interact in an unsteady fashion, either seeing the other as a steady feature, even though the operating frequency of the synthetic jet is an order of magnitude higher than the characteristic frequency of the boundary layer. Results showed that for normal synthetic jet, the increase of the Mach number of the outer flow reduced the perturbation, in terms of time-averaged streamline displacement, introduced by the jets. At the maximum VR (based on U_{peak}), $VR \approx 1.35$, the streamline closest to the wall is lifted to a distance of 88% of the undisturbed boundary layer height. At the lowest $VR \approx 0.5$, the streamline is lifted to about 44% of the undisturbed boundary layer height. The results are shown in figure 2.25.

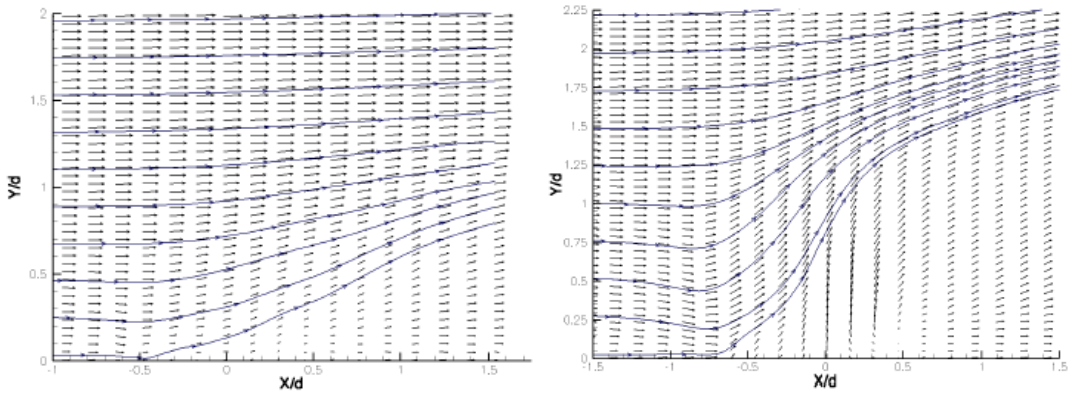

Figure 2.25 Velocity vector map for a SJA operating in a boundary layer at a) *VR* = 0.5 and b) *VR* = 1.35 (Schaeffler, 2003)

Cui *et al* (2003) performed numerical simulation of a synthetic jet actuator embedded in a turbulent boundary layer, highlighting the importance of *VR* relative to the height of the local boundary layer. In the study, the *VR* (based on U_{peak}) was kept identical as 3.9 but *d* changed from 7 to 61. In the case with $d = 7$, the penetration depth into the boundary layer of discrete vortices of the synthetic jet scales with the turbulent boundary layer thickness. The vortices penetrate the boundary layer and their influence is felt to a distance of $\approx 4\delta$ in the freestream direction. At $d = 61$, the discrete vortices of the synthetic jet scale with the inner sublayer. And the vortices have a smaller penetration in the boundary layer ($\approx 0.2\delta$) and their influence is felt to a smaller distance of ≈ 0.8 in the freestream direction.

To the knowledge of the author, many of the studies have been undertaken by setting the actuator operating conditions by trial-and-error. As with other active flow control methods, there is strong evidence to suggest that the separation control effectiveness of synthetic jets depends primarily on the injection parameters. In turn, this effectiveness depends materially on the strength, location and type of vortical structures that form in the boundary layer.

For flow control purposes, the vortical structures formed by the interaction of the synthetic jet with a boundary layer must be considered. At the University of Manchester, Crook and Wood (2001) proposed that the vortex rings produced at the orifice stretched and interacted with the adjacent fluidic structures as they travelled downstream, to finally coalesce into a pair of counter-rotating vortical structures aligned to the main flow direction. Zhong *et al* (2005) examined the behaviour of synthetic jets formed from a round orifice in a flat plate laminar boundary layer using flow visualisation. Experiments ranged in *VR* from 0.06 to 0.7, with Reynolds number Re_L

from 16 to 245, and Strouhal numbers based on the freestream velocity from 0.1 to 0.5. The stroke length normalised by the orifice diameter ranged from 0.56 to 1.4. The typical value of d at the location of the orifice exit was approximately 3.

Zhong *et al* (2005) showed that shear in the boundary layer will have a greater influence on those structures formed at low *VR* causing vortex stretching, as opposed to those formed at high *VR*, which rapidly penetrate the boundary layer. The level of impact of shear is directly related to the ratio of the boundary layer thickness to the orifice diameter *d* and it is therefore an important cross flow characteristic of embedded synthetic jets. Three distinct behaviours were observed, as shown in figure 2.26. At low *VR* and Re_L, the vortical structures produced by synthetic jets appeared as highly stretched hairpin vortices, which are attached to the wall (figure 2.26a). At intermediate *VR* and Re_L, the vortex sheet rolled up into vortex rings, which experienced considerable amount of titling and stretching as they entered the boundary layer (figure 2.26b). At high *VR* and Re_L, the vortex rings appeared to experience a certain amount of tilting but no obvious stretching and penetrate the edge of the boundary layer quickly (figure, 2.26c).

It was explained that the appearance of hairpin vortices through a process of vorticity cancellation. The upstream side of the rolling-up vortex sheet has an opposite sign to that of the oncoming boundary layer and thus a certain degree of vorticity cancellation is expected. If after this cancellation process there is still an amount of vorticity available, the upstream of the vortex sheet rolls up and a vortex ring is formed; if no vorticity is left at the end of the blowing stroke, then the resulting structures has the shape of a hairpin-like vortex. These findings are similar to the aforementioned simulations produced by Mittal *et al* (2001).

It was hypothesised by Zhong *et al* (2005) that due to their long resident time in the boundary layer, hairpin vortices were likely to be the most desirable vortical structures required for effective separation control with minimal power consumption. However no quantitative measurements have been provided to support this hypothesis. Furthermore, it was suggested that the streamwise structures observed by Wood *et al* (2000) on a cylinder were like to be produced by the overlapping legs of hairpin vortices. Similarly however, no surface or off surface measurement have been provided to support this opinion.

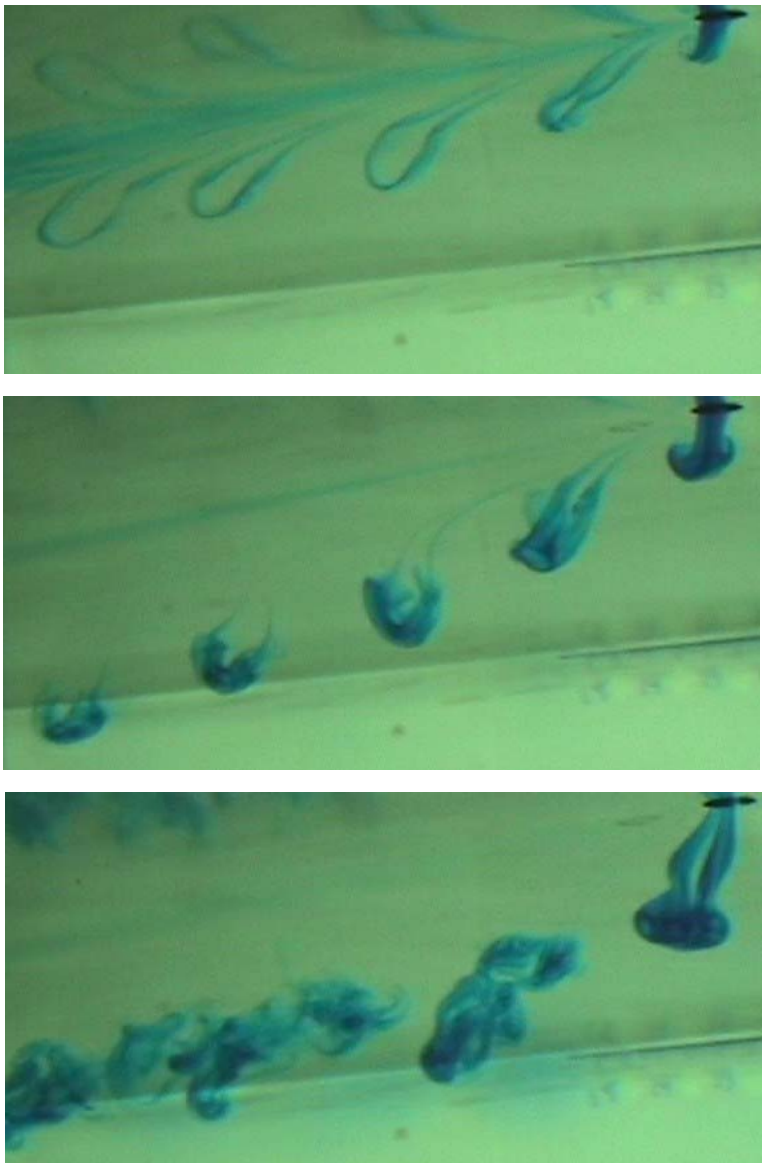

Figure 2.26 Dye visualisation of vortex structures in a laminar boundary layer a) hairpin vortices; b) stretched tilted vortex rings and c) non-stretched vortex rings (Zhong *et al*, 2005)

By comparing the impact of three types of vortex structures along the wall using a thermochromic liquid crystal-based instantaneous convective hear transfer sensing system, Jabbal and Zhong (2006) revealed that both stretched tilted vortex rings and hairpin vortices could be responsible for the streamwise vortex pairs that delayed the flow separation. Furthermore, the authors presented a map of parameter space where the different types of vortical structures were observed based on the velocity ratio VR and the dimensionless stroke length L. As shown in figure 2.27, for hairpin vortices, the range in L and VR required for their formation is approximately $1 < L < 3$ and $0.1 < VR < 0.3$ respectively, and for stretched tilted vortex rings, the range in L and VR is $2 < L < 4$ and $0.2 < VR < 0.45$ respectively.

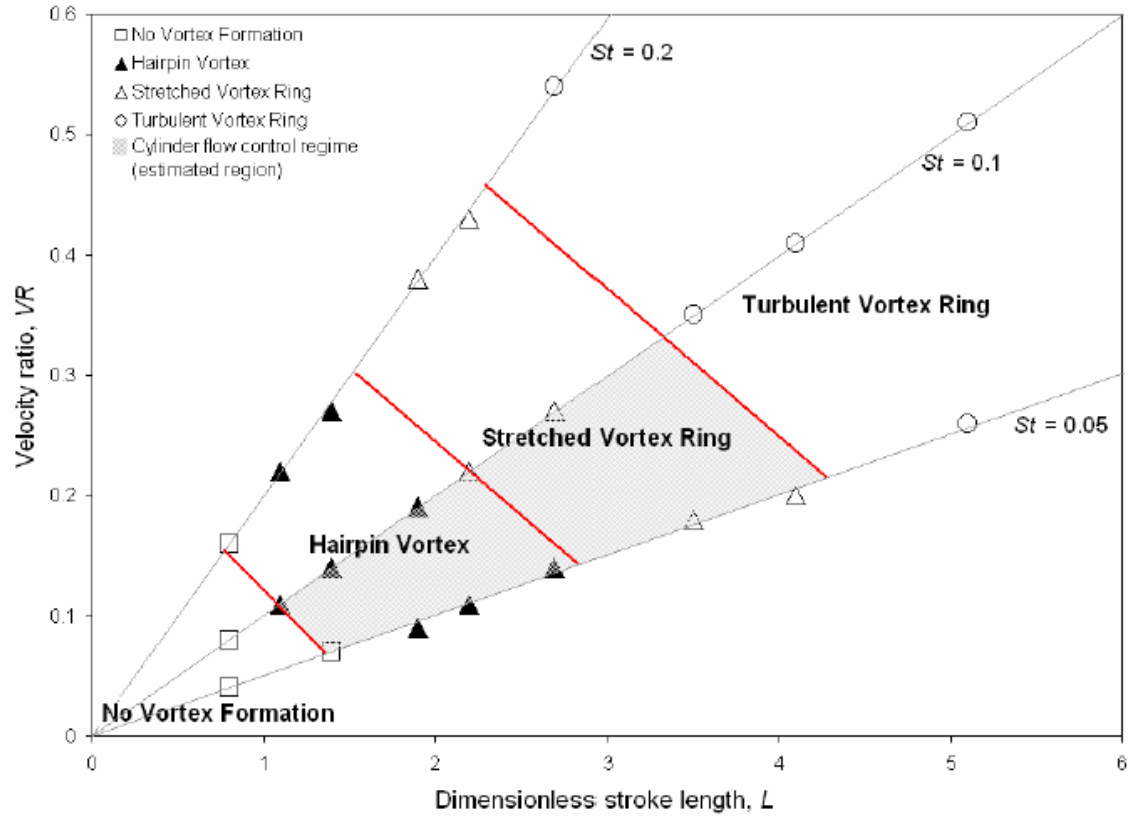

Figure 2.27 Parameter space of the different vortical structures seen as a result of the interaction between synthetic jets and a laminar boundary layer (Jabbal and Zhong, 2006)

2.6 Summary

In this chapter, some research related to the phenomenon of flow separation and its control using various methods have been reviewed, as well as the literature related to synthetic jets and their potential for flow separation control. Although the investigations into synthetic jets have contributed to an improved understanding of their behaviour in quiescent conditions and boundary layers, several issues still remain unresolved. In the author's point of view, these issues are essential to the design of synthetic jets and the selection of their operating conditions for effective flow control in practical settings. As such, these issues form the basis of the research presented in this thesis.

Firstly, in quiescent conditions, there is a need for understanding the effect of non-dimensional parameters, such as L and S on the vortices of synthetic jets, as a confirmation of the findings by Glezer (1988) which were obtained from piston-generated vortex rings. The formation criterion for synthetic jets is needed since the criterion is expected to serve as a useful design guide for synthetic jet formation for flow control purposes. Secondly, since the extent of vortex roll-up determines the

impact of synthetic jets on external flow by entraining ambient fluid into their cores, which enhances mixing, a vortex roll-up criterion is also required to ensure the formation of strong coherent vortices in the boundary layer. Thirdly, as for full-scale flight applications, the boundary layer in which the actuators will be embedded is often very thin such that actuators with an orifice diameter of ten to hundred microns operating at a frequency of a few kilohertz could be used. Performing detailed flow measurements on such devices is often beyond the capability of laboratory instrumentation. Hence the studies have to been undertaken on generic rigs operating at benign conditions unrepresentative of those at which synthetic jet actuators will have to operate. It is expected that at small diameters the viscous effect inside the orifice duct becomes important which can in turn induce the compressibility effect in the cavity. A need of identifying the dimensionless scaling parameters for actuators of different scales therefore arises so as to enable the research finding to become applicable to the actual devices.

It is known that the vortical structures produced as a result of the interaction between the synthetic jet and the boundary layer play an important role in enhancing mixing in the boundary layer hence delaying flow separation. Therefore, finally and most importantly, there is a need to further investigate how these vortical structures alter upon changing in the synthetic jet operating conditions and their flow control effect in delaying flow separation. This information will be useful to choosing the optimal operating conditions for synthetic jets that will produce the best flow control effect with a minimum amount of energy consumption.

3 Experimental Setup and Methods

In this chapter, the information about the facilities and models used in the experiments is provided and then the experimental techniques used for the measurement of the synthetic jet flow are described with the details about the principal, setup and measurement uncertainties given.

3.1 Experimental Facilities and Models

3.1.1 The Quiescent Flow Experiments

3.1.1.1 The Synthetic Jet Actuator

The synthetic jet actuators used in this thesis consist of a diaphragm located at the bottom of a cavity and a circular orifice in the face opposite to the diaphragm. A general view of the actuator is shown in figure 3.1. The purpose of the experiments in the quiescent condition is to investigate the relation between the synthetic jet performance and the operating parameters (frequency and displacement) and geometry parameters. Therefore the synthetic jet actuators is designed and constructed such that the displacement of the diaphragm can be measured easily and the cavity and orifice size can be changed as desired. In this thesis, synthetic jet actuators of two different scales are tested with the dimension as described in table 3.1.

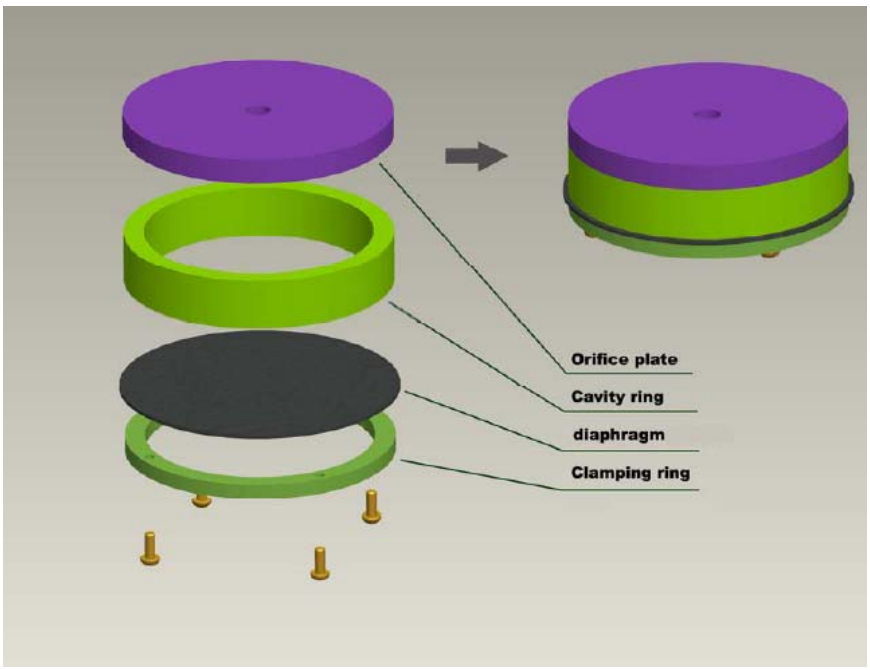

Figure 3.1 Construction of the synthetic jet actuator

Table 3.1 The geometrical parameters of the synthetic jet actuators

Macro Scale		Micro Scale	
Parameter	Value(mm)	Parameter	Value(mm)
D_c	45	D_c	20
H	10	H	10
D_o	2.5, 5, 7.5	D_o	0.5
h	2.5, 5, 7.5	H	0.5

The geometrical parameters of the macro-scale are chosen based on the previous researches carried out in our research group (Crook, 2002; Tang, 2006; Li, 2007 and Jabbal, 2008) in order to simplify the comparison. On the other hand, desirable range of the dimensionless parameters, stroke length (L), Stokes number (S) and Reynolds number (Re_L), can be obtained under the current combination of the geometrical parameters. The orifice diameter of the micro-scale actuators is $1/10^{th}$ of that of macro-scale actuator due to the limit of the mechanical process available in the laboratory. The cavity geometry is chosen as it is impractical to make a scale down version.

These two actuators of different scales share the same rig and the method of assembly. The cavity is created by screwing the diaphragm on the cavity ring using a clamping ring as shown in figure 3.1. And the cavity size can be changed by using a cavity ring with a different size. The cavity is clamped to a U-shape block which is mounted to the same metal base as the LDS permanent magnet electrodynamics shakers is. A general view of the rig is shown in figure 3.2.

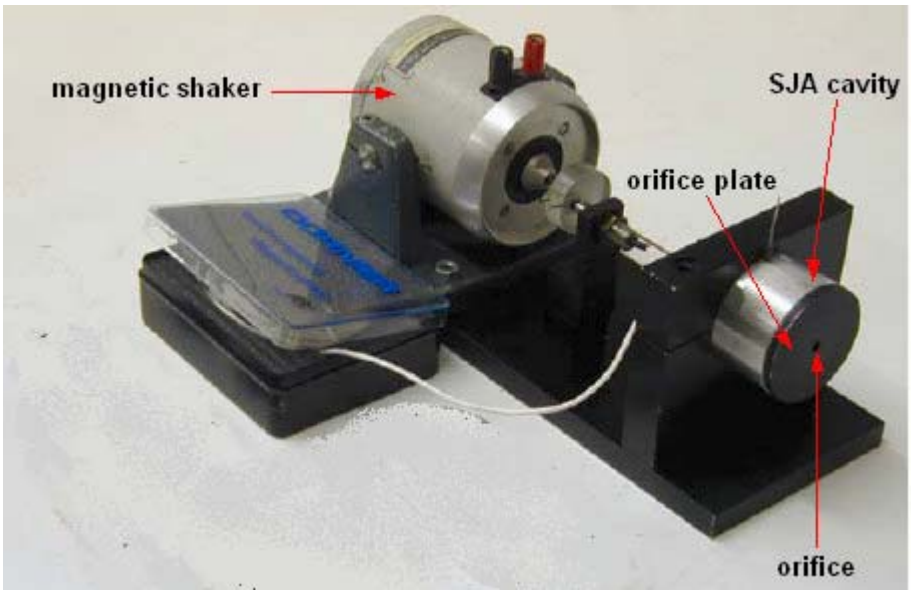

Figure 3.2 Photograph of the synthetic jet actuator

The diaphragm was connected via a steel rod with the shaker. The shaker is driven by an amplifier to which a sinusoidal signal is the input. The sinusoidal signal is generated by either a signal generator or a DAQ (data acquisition) card depending on the experiments to be carried out.

Among all the parts mentioned above, the choice of the diaphragm is most critical because the performance of the diaphragm determines the characteristic of the synthetic jet. In the current thesis, two different diaphragms are used depending on the driving frequency hence two different connection designs. In all the experiments, the operating frequency of the synthetic jet actuators are divided into two frequency bands with the high frequency band ranging from 300Hz to 900Hz and the low frequency band ranging from 1Hz to 150Hz. The high driving frequency is used for the micro-scale synthetic jet actuators to enable a comparison of their performance with that of the macro-scale synthetic jets at similar levels of non-dimension parameters.

For the high driving frequency band, a thin stainless steel membrane with a thickness 0.1mm is chosen to act as the diaphragm to avoid the problem associated with the aging of a rubber diaphragm. In addition, the deformation of the rubber diaphragm is not predictable since the air inside the cavity is regard as compressible due to the small orifice diameter and high jet velocity. For this diaphragm, the method of connecting it to the cavity ring is similar to that used by Li (2007). Firstly, a circular metal sheet with the same diameter as the clamping ring is cut. Screw holes are marked on the metal sheet by placing it on the cavity which has already been machined with thread holes. Once the screws holes on the metal sheet are drilled, it is clamped on the cavity ring tightly by screwing the clamping ring. A 1mm screw is used to connect the diaphragm with the metal rod which is screwed onto the shaker as shown in figure 3.3. The 1mm screw is chosen because it minimizes the contact area between the driving rod and the diaphragm to ensure the proper prediction of the deformation of the diaphragm. A smaller screw has been tried but the pressure on the diaphragm is so high that the diaphragm tends to break at the contact point.

For the low driving frequency band, a rubber diaphragm is used because of its lower stiffness. And due to the difference of the property between the rubber and the metal, some changes are made for the installation and driving. Firstly, the rubber diaphragm needs to be pre-stretched before clamped on the cavity ring so as to keep the tension when it is oscillating. On the other hand, an improved design of connection is applied from the inspiration of the suspension mechanism of the speaker. Instead of

using screw to connect the diaphragm with the driving rod directly, two brass disks with 1mm thickness and 43mm diameter are used to generate a 'sandwich' structure as shown in figure 3.4. Then a screw is used to connect the 'sandwich' diaphragm with the driving rod as shown in figure 3.3. When the diaphragm is fixed to the driving rod two alignment rings with an internal diameter of 43mm and thickness of 1mm are put between the disk and the cavity ring to ensure that the gap between the clamping disk and the cavity ring is evenly distributed as shown in figure 3.5.

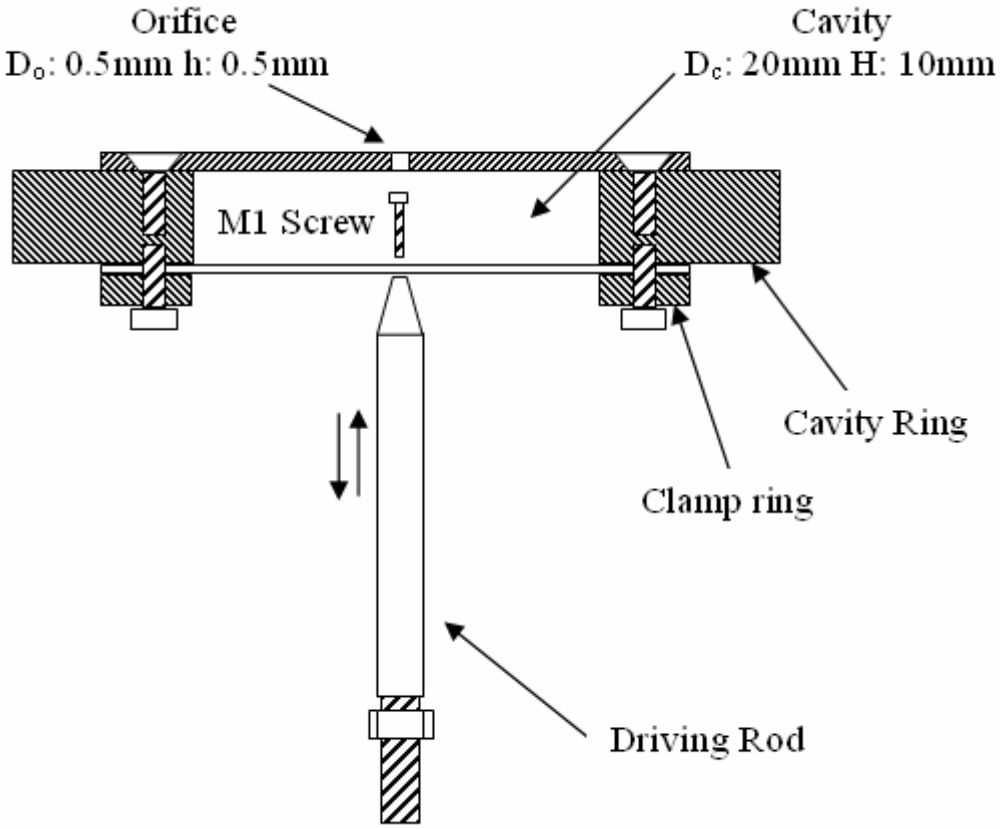

Figure 3.3 Structure of the metal diaphragm connection

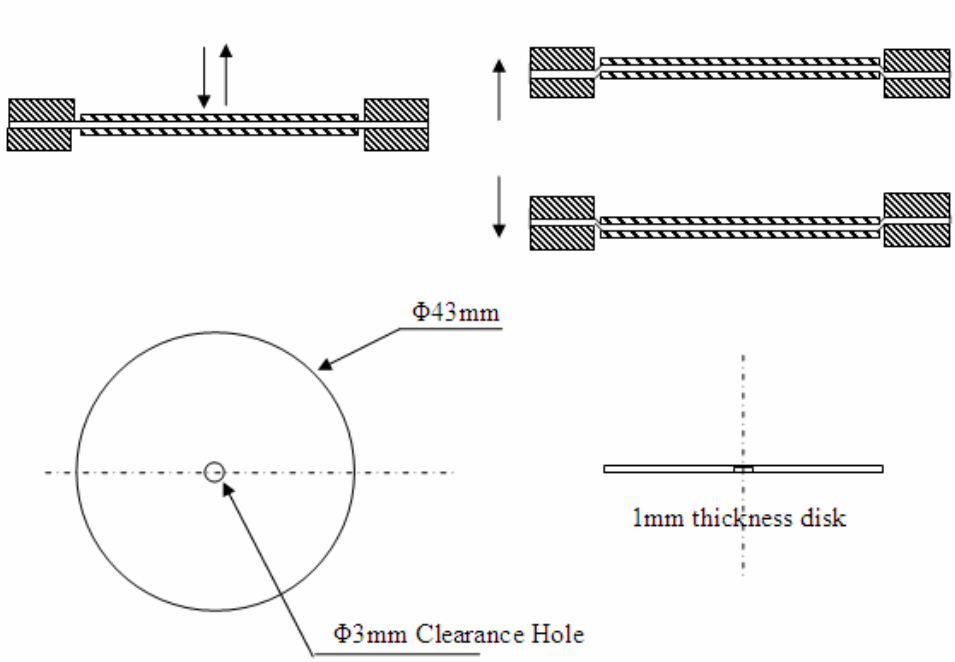

Figure 3.4 'Sandwich' Structure for the rubber diaphragm

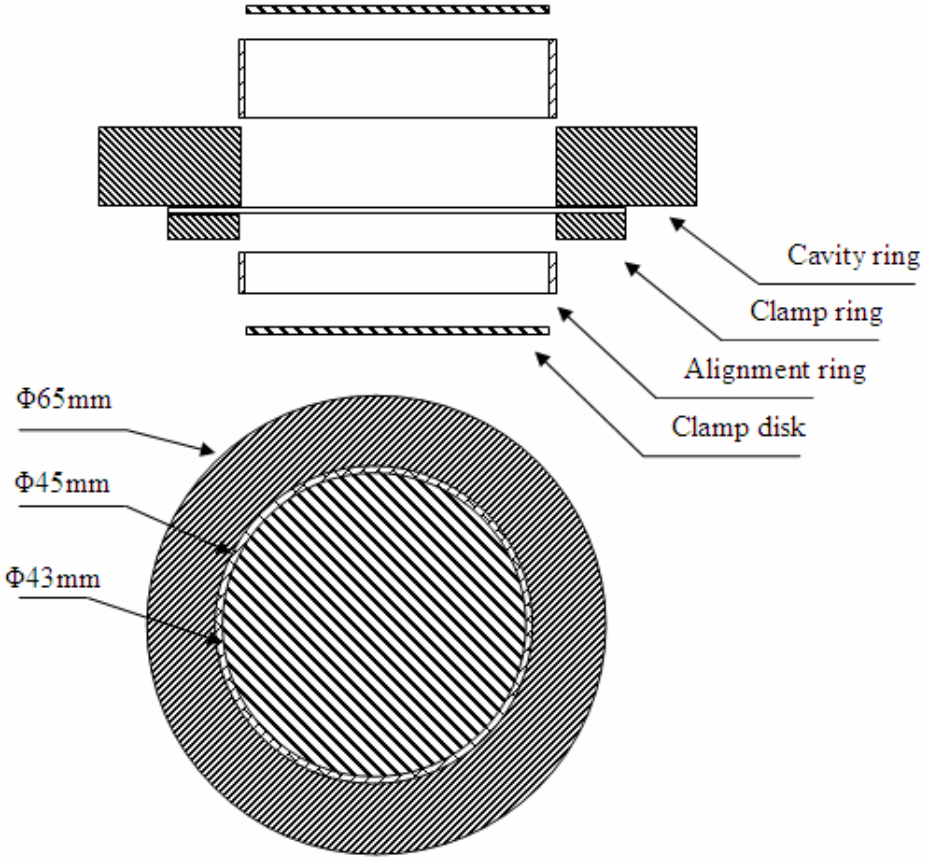

Figure 3.5 Sketch of alignment of the clamp disk

Two operating parameters, i.e. the driving frequency and diaphragm displacement, should be known in order to investigate the characteristics of the

synthetic jet actuator. The driving frequency is a known parameter from the signal generator. The diaphragm displacement is measured by a *PCB PIEZOTRONICS* shear accelerometer for the micro-scale (high frequency) and a Monitran eddy current displacement sensor for the macro-scale (low frequency) experiment respectively.

The reason to use the acceleration sensor for the micro-scale synthetic jet actuators is due to their relative small displacements which range from 2μm to 20 μm. In this case, a special glue came with the sensor from the manufacturer is used to attach the sensor onto a Perspex disk which is fix on the driving rod. The movement of the driving rod, the Perspex disk and the centre of the diaphragm should be identical. Since the output voltage signal from the acceleration sensor is related to the acceleration but not the displacement of the diaphragm, the relation between the acceleration and the displacement should be calculated.

When a sinusoidal signal from a signal generator is applied to the shaker through an amplifier, the instantaneous diaphragm displacement at the centre of the diaphragm is described as:

$$\delta = \frac{\Delta}{2}\cos(2\pi ft) \qquad \textbf{Eq. 3-1}$$

where Δ is the peak-to-peak displacement at the centre of the diaphragm and f is the driving frequency. The derivative of equation 3.1 with time gives the moving velocity of the diaphragm

$$v = \pi f \Delta \sin(2\pi ft) \qquad \textbf{Eq. 3-2}$$

The derivative of the equation 3.2 with time gives the acceleration of the diaphragm,

$$a = 2\pi^2 f^2 \Delta \sin(2\pi ft) \qquad \textbf{Eq. 3-3}$$

Therefore, the relation between the displacement and acceleration is described as:

$$\delta = a / 4\pi^2 f^2 \qquad \textbf{Eq. 3-4}$$

The relation between the output voltage and the acceleration is linear and is determined in the factory.

For the low frequency experiment, a Monitran eddy current displacement sensor which works in conjunction with a metallic target is used to measure the displacement at the centre of the diaphragm. In this case, a stainless steel disk with 5 mm diameter is fixed onto the Perspex disk. The relationship between the displacement and the voltage from the sensor is calibrated by moving the sensor through a known distance from the

target and measuring the voltage. To achieve this, a lathe and a digital multimeter are used to read the distance and voltage respectively. Within the range of interest, the relation between the voltage (V) and the displacement (Δ) is linear as shown in figure 3.6 and it can be expressed as:

$$V = 7.5476\Delta + 0.1272 \qquad \textbf{Eq. 3-5}$$

The actuator introduced above is for the study of the synthetic jet issued into quiescent air. In order to investigate the interaction between the adjacent jets of a synthetic jet array in quiescent condition, experiments are also carried out in a water tank on the synthetic jet actuator with five orifices. This actuator has the same cavity diameter of 45mm and a similar configuration as the synthetic jet actuator used in air. However, several changes are made. Firstly, since the study of the jet array is to be carried out both at quiescent and cross-flow conditions, in order to minimize the effect of geometry change, the same design of the actuator is used at both conditions. Therefore the flat plate forms a part of the actuator even without the cross-flow as shown in figure 3.7. Secondly, the cavity and the orifice plate of the actuator are made as a single piece which is mounted flush with the flat plate. Thirdly, a cavity ring is used to fix the actuator on the flat plate. Finally, to generate the orifice array the diameter of the orifice is reduced from 5mm to 2mm with a 6mm spacing.

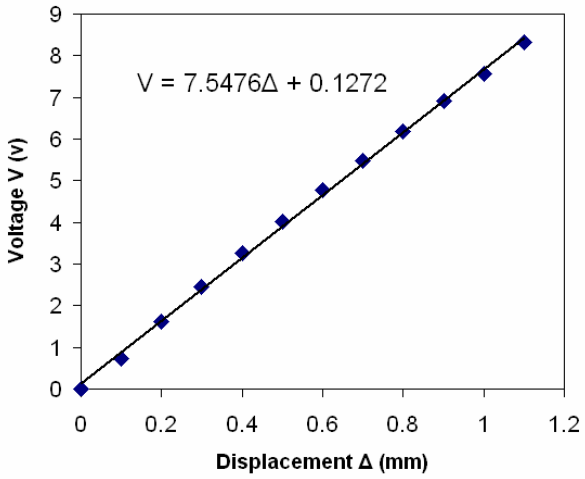

Figure 3.6 Calibration curve of the displacement sensor

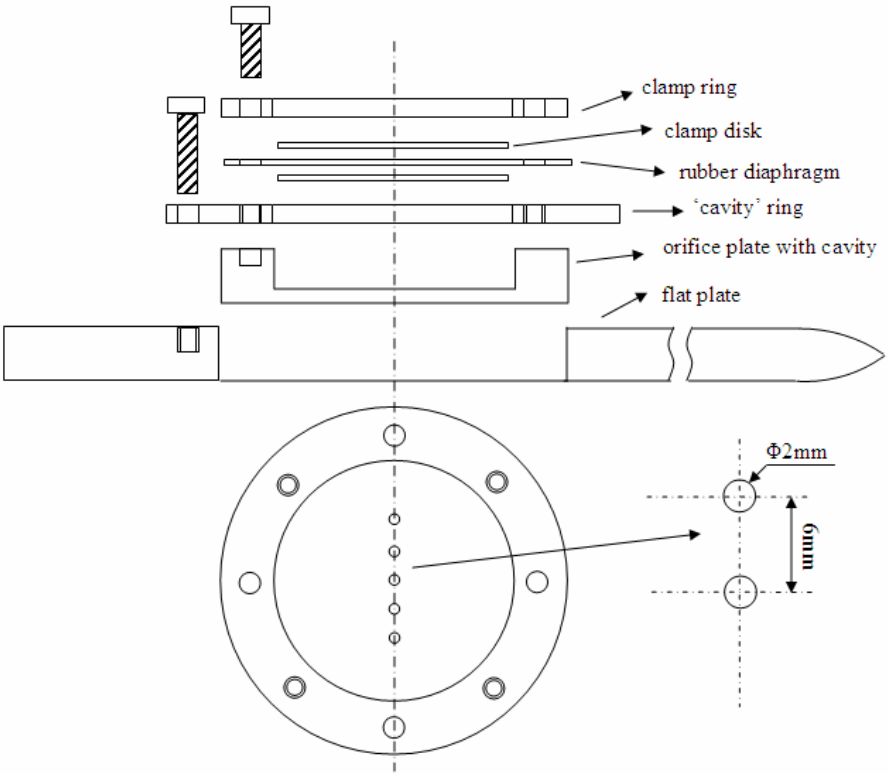

Figure 3.7 Sketch of the Synthetic jet actuator in water tank

3.1.1.2 The experimental setup

In this part, the experimental setup for four experiments carried out at the quiescent condition will be introduced, including the PIV measurement for macro-scale synthetic jet, the PIV measurement for micro-scale synthetic jet, the smoke-wire visualization of the vortex roll-up of synthetic jet, fluorescent visualization and PIV measurement in the cross flow.

The experiment setup for the PIV measurement of macro-scale and micro-scale synthetic jet is essentially the same. A general view image of the PIV set-up is shown in figure 3.8. In order to minimize the reflection of the laser light from the orifice plate, the rig shown in figure 3.2 is turned 90° up into the vertical position as shown in figure 3.9. In this set-up, the laser light goes over the orifice plate surface tangentially rather than 'crash' on it directly. The orifice plate surface is also painted into black to decrease the reflection further. All these efforts help to obtain PIV images of better quality hence more trustable velocity vectors near the orifice.

In order to keep the seeding particles used for tracking the flow at the interested area, the actuator is placed inside a 400mm cubic box with a glass window for light access and image acquisition. And to minimise the effect of the flow disturbance caused

by the vibration of the shaker and the driving rod, the box only covers the top part from the U-shape block, instead covering the complete rig as shown in figure 3.8.

A small smoke-wire device fixed at the roof of the cubic box is used to generate the particle tracer to follow the flow. This device consists of a glass cylinder, a nichrome wire and a power supply. The nichrome wire is wrapped around the glass cylinder and heated with an electric current. Paraffin oil is dripped on the heated glass cylinder and vaporized into smoke particles with about 1μm in diameter (Melling, 1997). The smoke particles have a density very close to the density of air and they are small enough to minimize the velocity differences across their dimension.

For the smoke-wire visualization experiment, the similar rig setup shown in figure 3.10 is used except that an orifice plate with a bigger size is used in order to connect the weight with the wire, which will be described in section 3.2.2.1. The cubic box is still used in this experiment in order to minimize the atmospheric disturbance. The top surface of the box is made removable in order to enable an easy access to the actuator to paint the wire with paraffin oil.

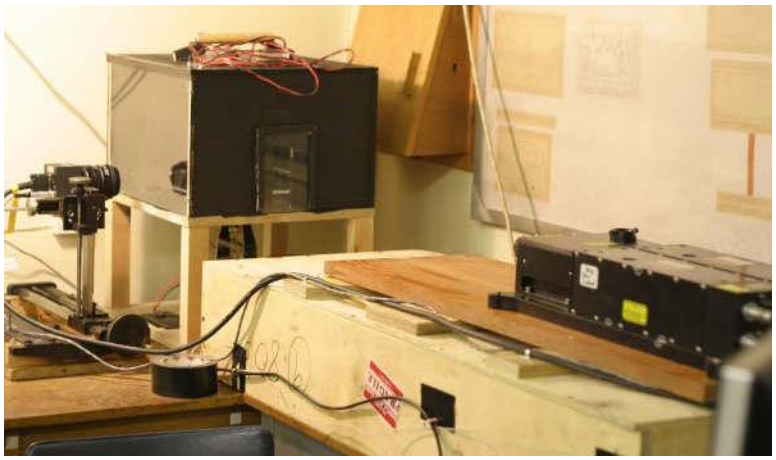

Figure 3.8 The PIV system at quiescent condition

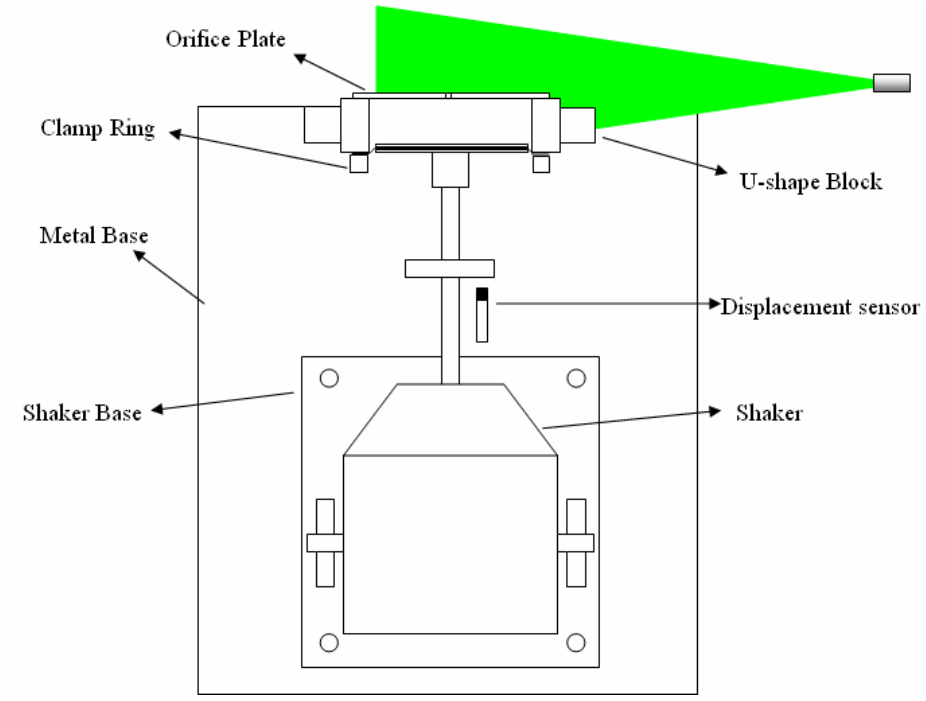

Figure 3.9 Schematic of the vertical set-up of the rig for PIV measurement

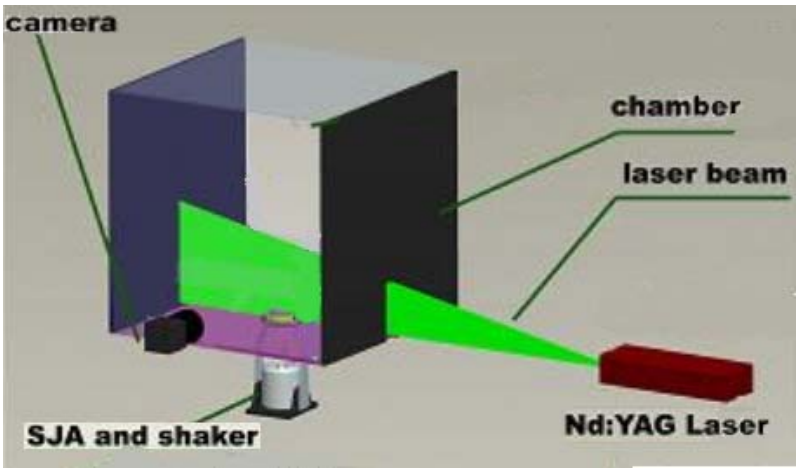

Figure 3.10 Schematic of the smoke wire setup

The florescent visualization of the synthetic jet actuator array are conducted in a glass tank measuring 700mm(L) ×310mm (W) ×400mm (H) full of water. A general view of the rig is shown in figure 3.11. In this case, the test surface is facing downwards to allow for an easy setup.

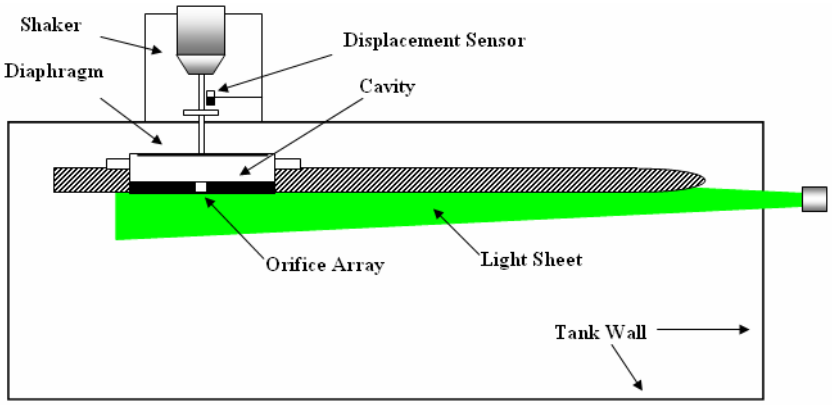

Figure 3.11 Schematic diagram of the setup of actuator in water tank

For all the experiments mentioned above, the camera is fixed on a three-dimensional traverse in order to locate precisely the interested area. And the rigs and the camera are levelled by an electrical inclinometer.

3.1.2 The Boundary Layer Experiments

3.1.2.1 The Tilting Flume

The investigations of the interaction of synthetic jets with a laminar boundary layer and the separation flow control experiment are carried out in the tilting water flume at the University of Manchester Goldstein Research Laboratory. Photograph of the tilting flume are shown in figure 3.12 and a schematic layout of the flume is given in figure 3.13.

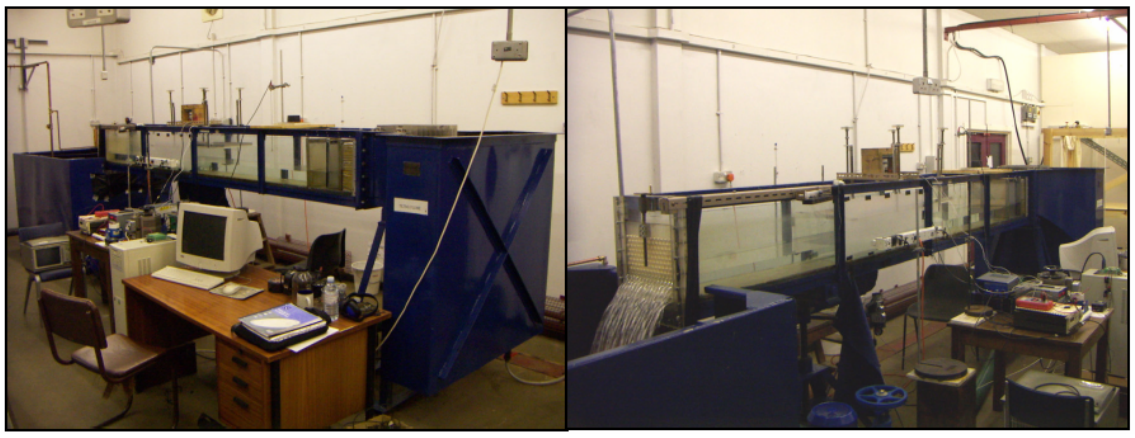

Figure 3.12 The tilting water flume facility

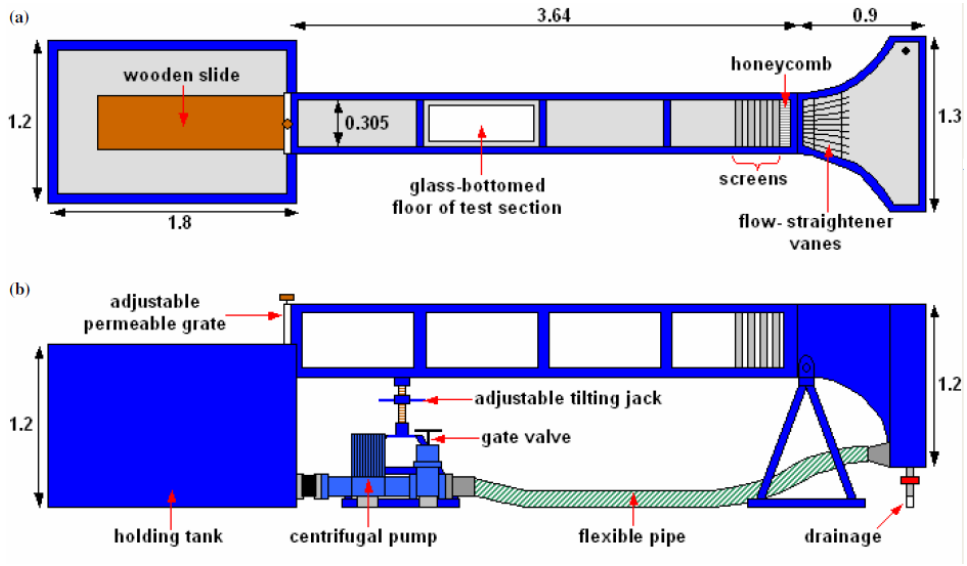

Figure 3.13 Schematic layout of the tilting water flume from (a) plan view and (b) side view (all dimensions in metres)

Water is primarily stored in a holding tank at the end of the flume section. A vertical centrifugal pump draws water out of the tank and through a flexible pipe return section (with an outer diameter of 0.1m) to a smaller entry tank upstream of the flume. The water then passes through a series of flow-straightener vanes and honeycomb to provide a streamlined, two-dimensional flow. A series of four increasingly fine screens are also installed at the upstream entrance of the flume to reduce any turbulent eddies before it enters the test section. The dimension of the working section is 1000mm(L) ×310(W) ×500mm(H). Three sides of the working section are made of glass for optical access. Finally, the water passes through the flume channel and comes out at the end through a permeable gate into the main holding tank. To prevent water falling directly over the entrance to the pump and thereby forming bubbles which may inadvertently be drawn into the flow, a wooden slide is fixed at the flume exit to carry the falling water to the opposite end of the tank.

For the present experiments, the flume is set in the horizontal position using a digital inclinometer. The water speed and height of water surface are controlled by the speed of the pump and the opening of the permeable gate at the end of the horizontal channel. The speed of the pump is controlled by the *ABB* inverter, rather than the mechanical gate valve, which is fully opened during the experiments. As such the vibration of the system is reduced and the flow quality is improved.

The velocity of cross flow is measured by dye visualization method. The details will be given in section 3.2.1.1. In the current thesis, the freestream velocity is fixed at 0.1m/s. The accuracy of this method is confirmed later by the PIV measurement.

3.1.2.2 The Test Plate

To study the interaction between the synthetic jet and the boundary layer, the synthetic jet actuator is mounted to the back of the test plate that forms the ceiling of the test sections, as shown in figure 3.14. The test surface faces downwards to allow the synthetic jets actuator to be mounted above the free surface of water. The test plate consists of three 10 mm thick aluminium flat plates which are connected with each other sequentially using hinges. The three plates have a total length of 880 mm and they are mounted horizontally across the whole width of the test section. The most upstream plate is 530 mm in length and is manufactured with a 1:5 (nose thickness-to-length ratio) super-elliptical leading edge. According to Narasimha and Prasad (1994), this design helps to avoid flow separation and premature transition at the leading edge of the plate. The middle and third plate remain undeflected for the zero-pressure gradient tests.

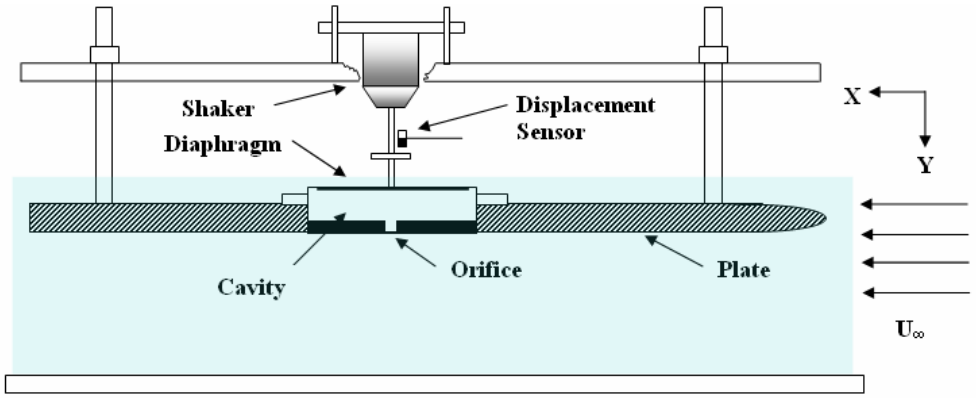

Figure 3.14 Schematic of test plate for interaction study

To investigate the effect of the synthetic jet array on the flow separation control, the middle plate, which is 200 mm in length, is inclined 5° upwards relative to the horizontal plane to generate a separation region, show in figure 3.15. A rubber sheet is used to provide a smooth transition from the first plate to the middle plate. The arrangement is shown in the inset figure in figure 3.15. The rubber sheet is fixed on the plates when both of them are in horizontal position and is uniformly pre-stretched. When the middle plate is angled at 5 degree, the middle part of the rubber sheet is stretched to form a straight shape since rubber can only sustain normal stresses. After a series of initial test, 5 degrees is chosen as the angle because desirable size and location

of the separation region are observed under this angle. The boundary layer developing along the horizontal plate will separate at some point along the inclined plate, creating a separated boundary layer to which flow control with synthetic jets can be applied. The third plate with a 150 mm in length is attached to the end of the inclined plate. The incidence angle of this plate can be altered to ensure that the flow is attached at the leading edge of the horizontal plate.

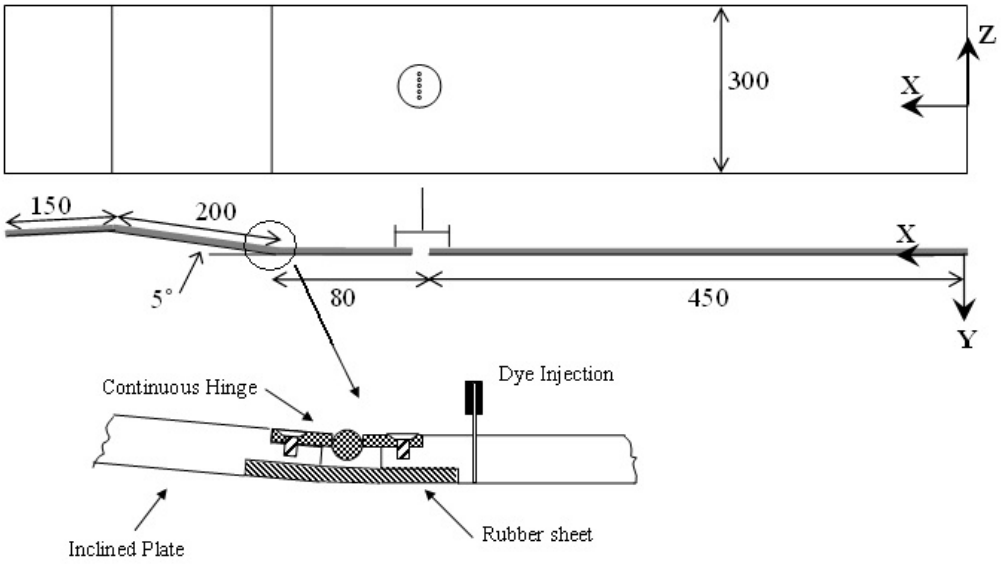

Figure 3.15 Schematic drawing of the test plate for separation control and the coordinate system (units in mm)

3.1.2.3 The Synthetic Jet Actuator

The synthetic jet actuator used in cross flow experiment has already been shown in figure 3.7 and it is used for experiments in the quiescent condition as well. The cavity has a diameter, D_c = 45 mm and height, H = 10 mm. The actuator has five orifices, which has a depth, h = 2 mm and a diameter D_o = 2 mm, and they are spaced 6mm ($3D_o$) apart. The orifices were flush to the test surface of the plate and aligned normally to the freestream direction, see figure 3.15. The centres of the orifices were located at 450 mm downstream of the leading edge of the horizontal plate, leaving a distance of 80 mm to the start of the inclined plate. During testing, the plate and synthetic jet actuator cavity were fully submerged in water.

For the study of the vortical structures produced as a result of the interaction of synthetic jets with a zero-pressure gradient boundary layer, four orifices were blocked using blue tacks and only the middle orifice was left open. For the separation control effect investigation, all five orifices were left open to generate an orifice array, through which five jets were issued.

3.2 Experimental Methods

In this part, the experimental techniques implemented in this thesis are introduced. These methods include both qualitative experimental techniques such as dye visualization, smoke-wire visualization and fluorescent visualization, and a quantitative technique which is Particle Image Velocimetry (PIV).

3.2.1 Dye Visualisation

Dye visualisation is one of the oldest experimental techniques used to observe the fluid motion which is dated back to the time of Leonardo da Vinci. This technique is inexpensive and very easy to implement.

In the current experiment, food dye is used because it is safe to handle and easily available. Red dye is chosen as a personal preference because it generally produces better picture contrast. Because the food dye comes in a concentrated solution and it has a specific gravity greater than one, a small quantity of acetone is added to the dye solution to make the dye naturally buoyant. To test the buoyancy of the mixture, the mixture is injected into a cup of water at a minimum velocity. If the mixture moves downwards, it means the gravity is over one and more acetone needs to be added. On the contrary, more food dye is needed if the mixture moves upwards. The exact amount of acetone added entails some degrees of trial and error because the concentration and gravity of the food dye vary for different bottles (25ml) and the commercial grade acetone does not all come with the same degree of purity. After the dye/acetone mixture is made neutrally buoyant, it is then diluted with the water from the flume to ensure the temperature difference between the mixture and the water is kept to a minimum. The method of the dye injection depends on the applications as it will be explained in the following sections.

3.2.1.1 Freestream Velocity Measurement

One of the applications of dye visualization is to measure the freestream velocity in the flume before the more accurate technique (PIV) is available. In this case, the dye is released through a dye probe which is fabricated using a stainless steel tube of 1.1 mm in diameter. The probe is mounted on a small three-dimensional traverse which is fixed on the test section of the water flume. The location of the release is at the central plane of the flume and 100 cm upstream of the leading edge of the flat plate. The dye is supplied to the probe by a gravity-feed reservoir. In order to minimize the effect of the

change of height of the dye level, a large reservoir of 25 cm in diameter is used so as to maintain at a relative stable level for a long time. The reservoir is mounted on a jack which is adjustable to so as to vary the dye injection velocity. By observing the structure formed at the exit of dye probe, it can be told if a correct velocity is reached or not. When the exit velocity is too high, a jet flow is produced, which generates 'mushroom-like' structures. Conversely, when the exit velocity is too low, wake structures are formed, which appear as a series of interconnecting vortex loops. A smooth filament indicates a correct exit velocity.

The movement of the dye is captured using a Canon digital video camcorder XL1S, which has a frame rate of 25Hz, a wide-view lens, a very good low light capability and adjustable shutter speed from 1/10 to 1/10000. A stainless steel ruler with resolution 1mm is recorded in the same view field as shown in figure 3.16. This camcorder is connected with a desktop computer through a firewire cable. The Adobe software is used to record and display the motion of the dye trace. The Matlab software is used to analyse the recorded images and calculate the velocity of the dye trace. By measuring the distance that distinct features in the dye trace travel in a known time interval, the velocity of the cross flow can be calculated. In the current measurement as shown in figure 3.16, the distinct feature marked by the arrow travels 100mm in one second, which means the flow velocity is 0.1m/s.

The shutter speed used is 1/2000 second. Therefore a spot light is powerful enough to provide the illumination. To enhance the contrast, a white paper is attached to the far-side wall of the test section to generate a white background. It should be noted that the measurement of the freestream velocity was carried out without the synthetic jet actuator operating.

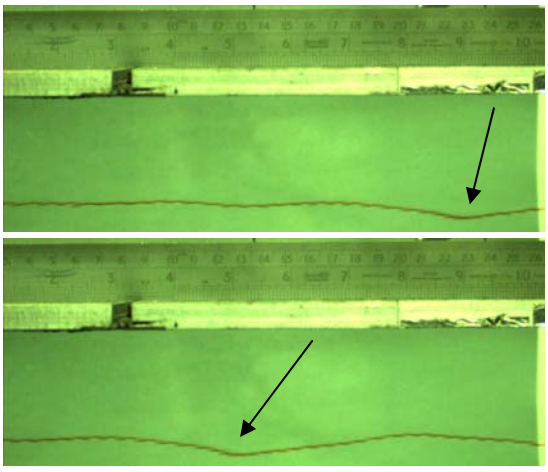

Figure 3.16 Measurement of cross-flow speed using dye visualisation

3.2.1.2 Synthetic Jet Structure Visualization

In order to visualize the structure produced by the interaction between synthetic jet and the boundary layer, dye is released into the cavity of the synthetic jets actuators. In order to ensure a good mixing inside the cavity, the dye is injected into the cavity through four stainless steel tubes which are evenly distributed around the cavity ring as shown in figure 3.17. The velocity at which the dye enters the cavity is kept to minimum so as to minimize the disturbance to the formation of the synthetic jet.

Since the actuator is sealed during the test, the exit velocity of the tubes can not be judged by the flow structure at the exit. Therefore a small intermediate reservoir as shown in figure 3.18 is added between the injection tubes and the main reservoir. Dye is introduced into this intermediate reservoir through a stainless steel tube that goes through the rubber stopper on the top. By counting the number of dye drops, the exit velocity of the injection tube can be estimated. At the bottom of the small reservoir, four stainless steel tubes are used to connect the small reservoir with the injection tubes through plastic tubes with the same length.

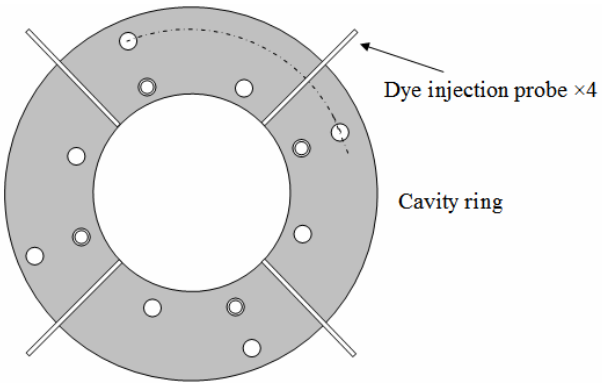

Figure 3.17 Sketch of dye injection tubes on cavity ring

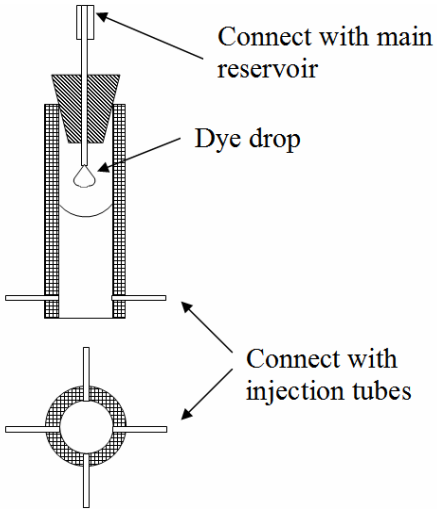

Figure 3.18 Sketch of the small reservoir

Due to the lack of a high-speed camera, a Hitachi KP-F120 black and white CCD camera is used to record the dye images. It is capable of a frame rate of 30Hz at a maximum resolution of 1260 × 512 pixels. A high shutter speed of 1/10000sec is used to capture well-defined images of flow structures. As such a high shutter speed, a great deal of illumination is required which is provided by a strobe light. The light source is operated at the trigger model and is triggered by the same signal which is sent to the camera.

In the dye visualization experiment, the oscillating frequency of the synthetic jet actuator ranges from 1 to 16Hz. Although the frame rate of the CCD camera can be increased to 60Hz when operated at the partial scan model, the frame rate is still not fast enough to capture enough number of image frames in one cycle of the synthetic jet operated at 16Hz. However, periodic repeatability of synthetic jets makes it possible to reconstruct the continuous motion of the synthetic jet structure in one cycle by using the images obtained at certain phase points from different cycles. Images at the same phase point from different cycles are examined and identical flow patterns are obtained. The same measurement technique has been used by Crook (2002) and Jabbal (2008).

To achieve this, the camera is configured to take images when an external trigger signal is received. For a given driving signal input to the actuator, the trigger signal is chosen such that it progressively scans through a whole range of different actuation phases after a certain number of cycles, then the process repeats itself until the stop button is pressed. For example as shown in figure 3.19, the frequency of the driving signal and the trigger signal is 5 Hz and 4 Hz respectively. These two signals have the same start time. Using the driving signal as reference, these two signals overlap at phase point 0°, 90°, 180°, 270° and 360° (0°) in the 1^{st} ,2^{nd} , 3^{rd} and 4^{th} cycle respectively. For different driving signals, the trigger signals are varied accordingly to ensure sufficient number phases are captured in the record. The combination of the driving frequency and trigger frequency for the range of driving frequencies covered in the tests are shown in table 3.2.

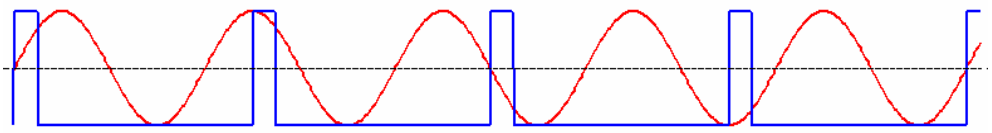

Figure 3.19 Relation between the driving signal and trigger signal

These two signals, named trigger signal and driving signal, are generated from a National Instrument PCI-6221 data acquisition card which is configured and programmed by Labview software. The form for the driving signal is sinusoidal, which is input to the shaker to drive the diaphragm after amplified through an amplifier. The trigger signal is a 10% duty cycle square wave. These two signals are synchronized by the build-in clock on the data card and this ensures that the two signals have the same sample rate and time base.

Table 3.2 Signal frequency configuration

Driving Frequency	Trigger Frequency	Phase Difference	Points per cycle
1	30	0	30
2	60	0	30
4	3.9	360/39	39
6	5.8	360/29	29
8	7.8	360/39	39
12	11.6	360/29	29
14	13.8	360/69	69
16	15.6	360/39	39

3.2.2 Smoke-wire Visualization

3.2.2.1 Smoke-wire Setup

To investigate the vortex roll-up phenomena at the exit of the orifice, smoke-wire visualization is applied. In this technique, the smoke is produced by oil vaporized from a fine wire heated by an electric current. In principle, this technique requires only a fine metal wire, mineral oil and a power source. In the current experiment, a nichrome wire is used due to its good strength and high electrical resistivity. Two factors are considered when choosing the wire diameter. To some extents, the size of the wire is dictated by the flow speed. For low-speed applications, smaller diameter wires are preferred because a thinner wire produces shaper smoke filaments. At higher speeds, a larger diameter wire is more desirable because the larger surface area can maintain a higher smoking rate and the wire is more able to stand up the required tension at a higher temperature. Another factor which is considered when deciding the wire size is the Reynolds number. To minimize the flow disturbance, the Reynolds number based

on the wire diameter should be less than 20. Based on the considerations above, wires with 0.1 mm in diameter are chosen in the current experiment and they yield a maximum Reynolds number of 10 for all the cases.

The schematic of the smoke-wire system is shown in figure 3.20. A larger size orifice plate is made for the connection of the weight and the power supply system. The orifice plate is made of synthetic material which is insulated from the electricity. The weight is to keep the wire stretch taut when heated. To minimize the effect of deformation of the wire when heated, only a small part of the wire covering the orifice plate is connected within the circuit as show in figure 3.20. The wire is attached on to the orifice plate by conductive copper tapes through which the current is applied to the wire. This setup ensures that the wire is kept close to the orifice plate with no gap. On the other hand, the influence of this connection method to the flow near the orifice is negligible because the thickness of the tape is only 0.05mm.

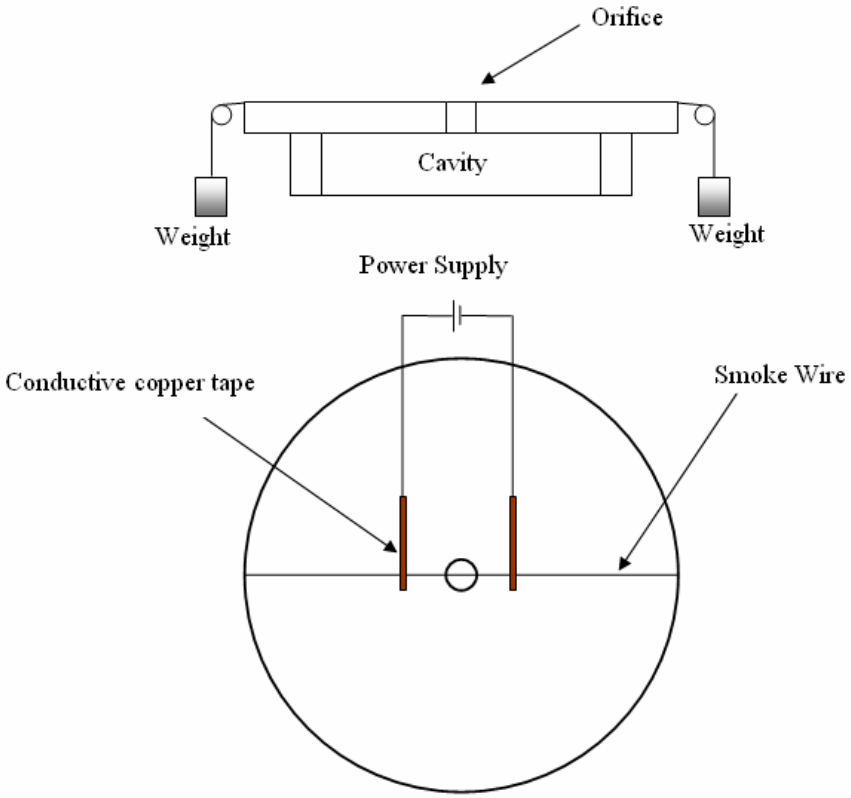

Figure 3.20 Schematic of the smoke-wire setup

Paraffin oil is used to produce the smoke filaments. To ensure that the smoke is produced uniformly along the length of the wire, it is essential the wire is coated evenly with the oil. In this experiment, a pen brush is used to apply the coating on the wire

manually. The manual technique is easy to implement and allows better control of the oil thickness.

The amount of smoke produced and its duration depends to a great extent on the voltage and current applied to the wire. In the present experiment, a DC power supply with maximum voltage 24V and current 1 amp is used to heat the wire. The current and voltage applied on the wire for different cases entails some degrees of trial and error because the flow speed at the orifice exit varies for different cases. And it is adjusted through a variable resistor connected to the power supply circuit. The value of the variable resistor ranges from 0 to 30 ohm. As shown in figure 3.21, a solenoid valve is connected in the circuit in order to synchronize the power supply system with the light source and the camera. This circuit will be switched on when the solenoid valve receives the trigger signal.

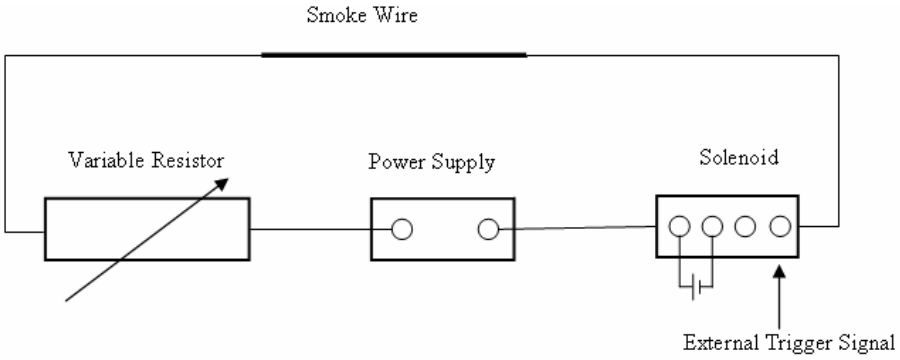

Figure 3.21 Schematic of the Power Supply Circuit

3.2.2.2 Illumination and Camera System

Because the flow speed is relatively high (few meters per second) for certain cases, the shutter speed of the still camera is too slow to capture sharp images. In order to arrest the high speed fluid motion, a commercial PIV system from TSI is utilized due to the advantage of the pulse light sheet which has a flash duration of 40 ns. This system consists of two Nd:YAG lasers, a digital CCD camera and a synchroniser, as shown in figure 3.22. The laser light has a wavelength of 532 nm and a maximum pulse energy of 185 mJ.

The light sheet is formed using a combination of cylindrical and spherical lens as show in figure 3.23. The digital CCD camera (Powerview Plus4MP) used is a high-resolution, high performance camera for scientific applications. Each image contains 2048 × 2048 pixels and renders a special resolution of 10 μm/pixel in the present setup. The laser and the camera are connected with the synchroniser which makes the laser and

camera work at a controlled time order. The timing diagram of the laser and camera system is shown in figure 3.24. The time separation of the two laser pulse is adjustable and with accuracy up to 1μs. The camera and the synchroniser are connected with the computer which displays and saves the images from the camera and configures the whole system using software named Insight 3G developed by TSI.

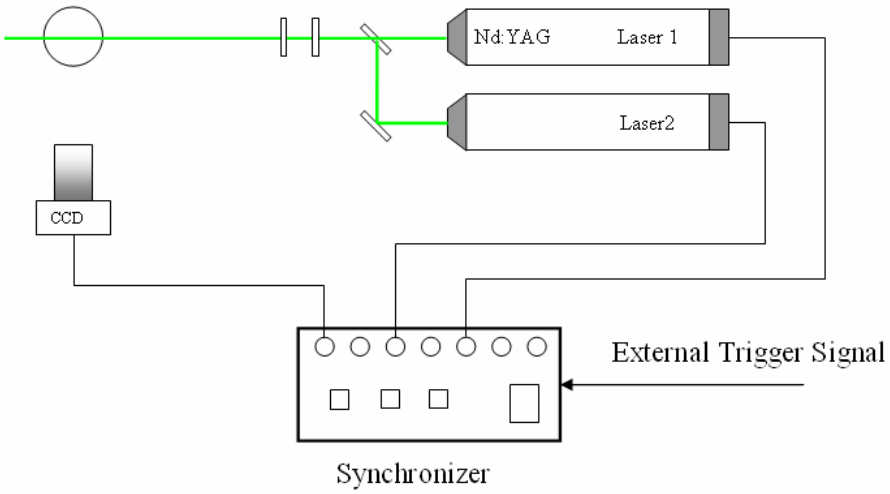

Figure 3.22 Schematic of the illumination and camera system

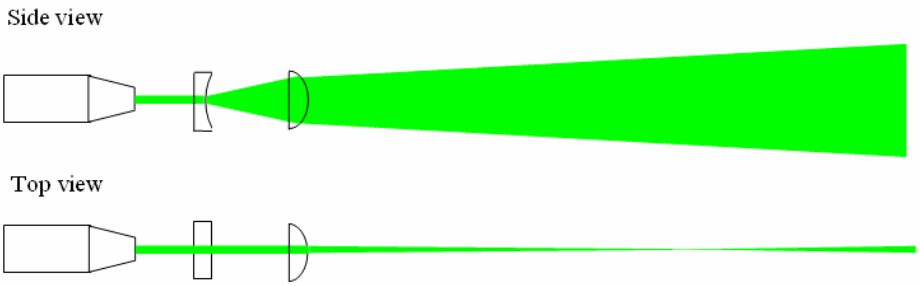

Figure 3.23 Laser optics configurations for laser sheet generation

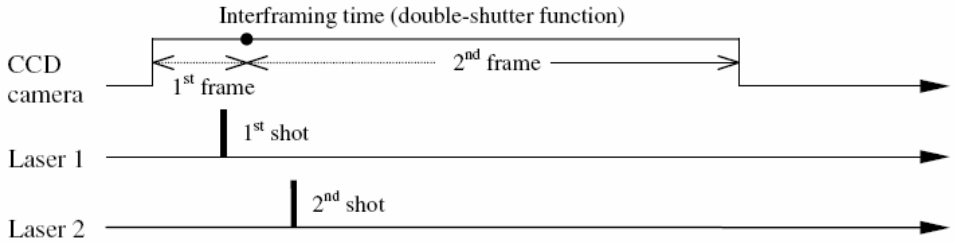

Figure 3.24 Timing diagram of the laser and camera system

3.2.2.3 Synchronization System

In order to capture the motion of the fluid from the orifice at a certain phase point, the power supply system, the illumination and camera system and the actuator should be triggered to work at a controlled time order. In this case, the same signal generation method as mentioned in the dye visualization section is used to generate the driving signal and the trigger signal. The driving signal is amplified and input to the shaker. The trigger signal is divided into two by a BNC T adaptor; one is connected to the solenoid to trigger the power supply system and the other is connected to the synchroniser to trigger the illumination and camera system. The time diaphragm of the synchronization system in an ideal condition is shown in figure 3.25.

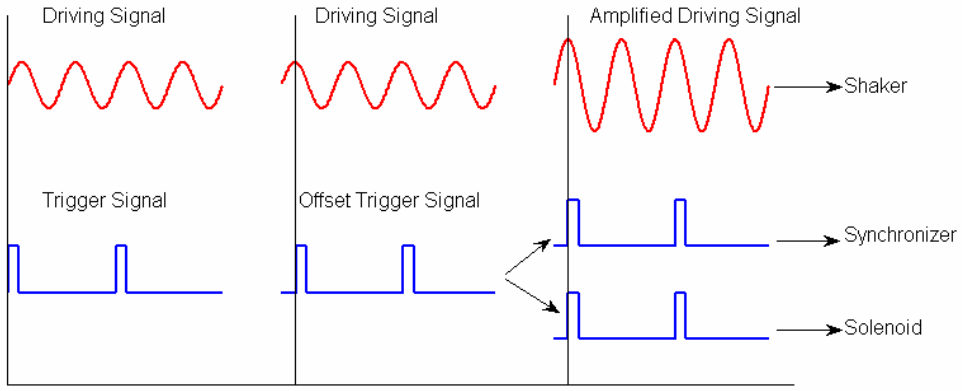

Figure 3.25 Synchronisation of the smoke-wire system

3.2.2.4 Operation of the Smoke-wire System

The purpose of the smoke visualisation experiments is to study the vortex roll-up structure in the near field of the orifice exit. Therefore, in order to compare the fluid motion at different parameters, the smoke should be generated at the same phase point for all the cases, which is the start of the blowing cycle in this present experiment. At this phase, the diaphragm is located furthest away from its neutral position. As shown in figure 3.25, in an ideal condition, the smoke is generated at the start of the blowing cycle when the trigger signal is configured to offset 90° relative to the driving signal. However, a certain level of time delay exists in all the three systems in the real world. For the driving signal, the delay happens when the signal is amplified through the amplifier and the signal passes through the shaker. For the trigger signal to the solenoid, a delay is the reaction time for the device to change position from ‘off’ to ‘on’. For the trigger signal to the synchroniser, a delay occurs in the lasers generate pulse as shown in figure 3.24.

Among the three delays, only the delay for the laser pulse generation is known, which can be configured in the TSI software Insight 3G. To minimize the impact of the time difference between the driving signal and diaphragm motion, the driving signal is replaced by the displacement signal from the diaphragm whose phase is coordinated with that of the incompressible fluid motion at the orifice exit. To reduce the delay associated with the solenoid, the voltage applied on the wire is measured and referred as the start of the smoke generation.

To ensure the smoke is generated at the chosen phase point, the displacement signal from the diaphragm and the voltage signal on the smoke wire are collected using the same PCI card and are displayed and analysed to get the phase difference $\Delta\Phi$ first. Since the voltage applied on the wire lasts a certain time from t1 to t2 which depends on the duty cycle of the trigger signal, the middle of the t1 and t2 is used as the reference for the smoke generation. Suitable duty cycle of the trigger signal is made as short as possible as long as the smoke can be generated and this entails some degrees of trial and error. Then an offset equal to $\Delta\Phi$ is configured on the trigger signal to the smoke-wire system. Finally, the start point of the diaphragm and the smoke generation point are overlapped.

As the signal shows in figure 3.25, the signals to the solenoid (smoke-wire generation system) and the synchroniser (the image capture system) are the same one. If no delay exists on the synchroniser, the smoke generation point will be captured by the camera. In order to capture the smoke motion at a certain position downstream of the orifice, a time delay is configured between the trigger signal to the synchroniser and the laser and camera system. The time separation between the pulse laser 1 and 2 is also set to get continuous images in one cycle, which depends on the required distance that the smoke moves downstream.

3.2.3 Laser Induced Fluorescent (LIF) Visualization

Under normal lighting, a dilute fluorescent dye solution appears almost transparent, but when illuminated with a laser light source of an appropriate wavelength the dye fluoresces strongly. This unique property allows it to be used to visualize the structures of fluid flow by illuminating it with a thin sheet of laser light. The fluorescent dye used in this current experiment is fluorescein. When it is illuminated with an argon ion laser, fluorescein displays a green colour. Pure disodium salt in a powder form is used as fluorescein. The disodium salt is resolved with water first and then diluted to the

required concentration. The diluted dye is delivered into the cavity of the actuator using the same way as that used in the dye visualization. This technique is used in two different experiments in this thesis. Therefore different illumination and recording methods have been applied.

In the study of separation control effect of the synthetic jet, a 5W Argon-Ion continuous laser was used for the illumination purpose. A thin sheet of laser light is generated by three cylindrical lenses with configuration shown in figure 3.26. In this experiment, the light sheet is perpendicular to the flat plate and illuminates the central plane of the separation area along the streamwise direction as shown in figure 3.27. A colour CCD camera is used with a full resolution 1008 × 1008pixels. In this case, the dye is injected into the separation region through a 1.0 mm tube which is located at the start of the flap and mounted flush with the plate surface, shown in figure 3.27.

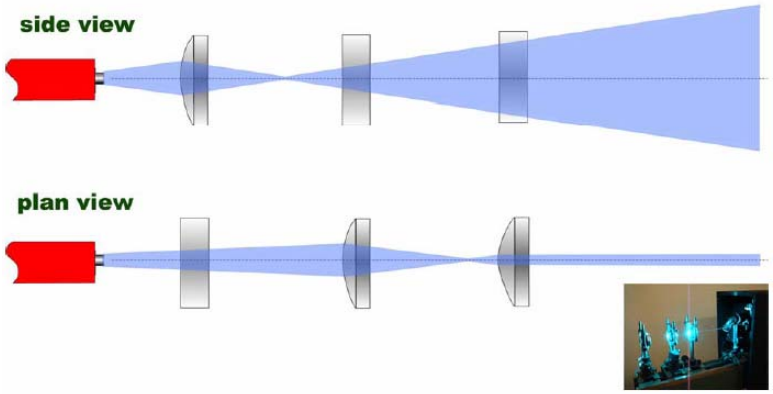

Figure 3.26 Configuration of lenses for light sheet generation

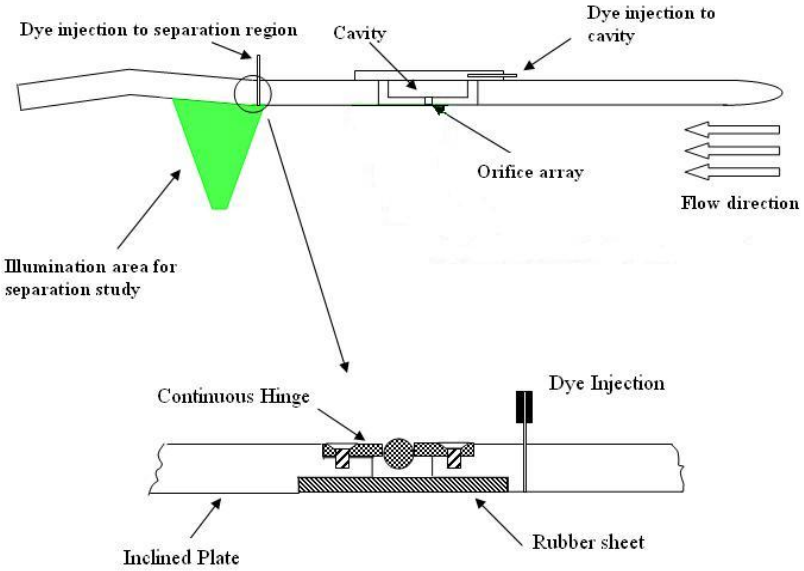

Figure 3.27 Sketch of dye injection and illumination area with zoom in view of the injection to the separation region

The second experiment is for the visualization of a synthetic jet array in a water tank, as shown in figure 3.11. In this experiment, a TSI PIV system was used for the illumination and the images acquisition similar as in the smoke-wire visualisation experiment. Since the maximum acquisition rate of the PIV images, dictated by the laser pulse repetition rate is 15 Hz, which is not fast enough to capture continuous frames in one cycle of the synthetic jet movement, the PIV system is configured to run at the trigger mode, i.e. the system takes images when a trigger signal is received. A similar signal system as used in the dye visualisation mention in section 3.2.1.2 is used. And since the same actuator is used in both the boundary layer experiment and the water tank experiment, the same dye delivery system as mentioned in section 3.2.1.2 is used.

3.2.4 Particle Image Velocimetry

Particle Image Velocimetry (PIV) technique is used in this thesis to examine the characteristics synthetic jets in quiescent conditions and to evaluate the separation control effect of a synthetic jet array.

3.2.4.1 Basic Principle of PIV

PIV is a technique that enables instantaneous measurement of the flow velocity in a plane. The working principle is quite simple: the flow is seeded with light reflecting particles (smoke in air and glass beads in water), a light sheet illuminates the particles in the measurement plane and a camera is used to take two exposures of the illuminated plane. The two exposures should be taken within a short interval, so that the same particles are caught in two different images. Then the distance that the particle has moved during the inter image time is found and translated into a velocity measure. The relation between velocities, u, and particle displacement in the corresponding direction, d, is simply

$$u = \frac{d}{M\Delta t} \qquad \textbf{Eq. 3-6}$$

where M is the magnification and Δt is the inter image time.

Each image pair is discretised into a large number of individual regions known as interrogation areas. Each interrogation area is typically 32 × 32 pixels, which for a typical image size of 1280 × 1024 pixels means that the fluid velocity is sampled at more than 1000 locations within the flow field. A velocity vector is obtained for each

interrogation area by the application of a cross-correlation analysis between the two constituent images in an image pair.

Cross-correlation provides a means for measuring the similarity of two functions. In the analysis of PIV image pairs, it is used to calculate the optimum spatial displacement of the second image, such that there is a maximal overlap of common pixels with the first image. The underlying process is statistical pattern matching. The analysis is performed separately for each interrogation area, which leads to a full-field set of fluid displacements.

Consider an interrogation area measuring $M \times N$ pixels. Each pixel in the interrogation area may be described by a coordinate (m, n), where m and n run from [1: M] and [1: N] respectively. The pixel intensities from the first image can be defined by I1(m, n), and those from the second image by I2(m; n). The cross-correlation may thus be written as (Keane and Adrian, 1992)

$$R_{I_1 \cdot I}(i,j) = \sum_{m=1}^{m=M} \sum_{n=1}^{n=N} I_1(m,n) \cdot I_2(m+i, n+j) \qquad \textbf{Eq. 3-7}$$

where i and j represent pixel shifts between the two interrogation areas.

$R_{I_1 \cdot I}(i,j)$ is obtained by shifting the second interrogation area by i pixels along the M axis, and j pixels along the N axis, and calculating the shared pixels. This is performed for all values of i and j such that there is at least one overlapping pixel between the two interrogation areas. i and j thus run from -(M - 1) to (M - 1), and -(N - 1) to (N - 1) respectively. The two interrogation areas completely overlap when i = 0 and j = 0. $R_{I_1 \cdot I}(i,j)$ has a large value when there are many shared pixels. The optimum shift of the second interrogation area, such that there are a maximum number of shared pixels, produces a pronounced peak in the correlation function. The correlation function may be represented graphically as a three-dimensional correlation plane. An example of the cross-correlation between two interrogation areas, and the resulting correlation plane, is shown in figure 3.28. The main peak in the correlation plane may be trivially located at (-1, 3), which provides a first order estimate for the optimum displacement vector. An estimate of the mean fluid velocity between the interrogation areas is thus $(-1/\Delta t, 3/\Delta t)$. It is possible to calculate this velocity to sub-pixel accuracy using more sophisticated peak finding algorithms, described below.

Equation 3.7 describes a convolution in the spatial domain. The convolution theorem states that such a convolution can be evaluated in the Fourier domain using a

multiplication of the Fourier transforms of I_1 and I_2. In PIV this relationship is known as the Wiener-Kinchin theorem (Raffel *et al*., 1998), and may be written mathematically as

$$\widetilde{R} = \widetilde{I}_1 \times \widetilde{I}_2 \Rightarrow R = \hat{f}^{-1}(\widetilde{R}) \qquad \textbf{Eq. 3-8}$$

where $\widetilde{I}_1$ is the Fourier transform of I_1, $\times$ indicates a multiplication and $\hat{f}$ indicates a Fourier transform. It is common practice to calculate the cross-correlation using the Fourier domain representation. The use of fast Fourier transforms allows for a significant computational advantage over a direct convolution-based evaluation.

In most implementations of PIV, including that in this work, the displacement vector is calculated by fitting a Gaussian curve to the largest correlation peak. The curve takes into account the two nearest neighbours along both the *M* and *N* axes. This allows an estimate of the optimum displacement to be made to an accuracy of 0.1 pixels (Raffel et al., 1998).

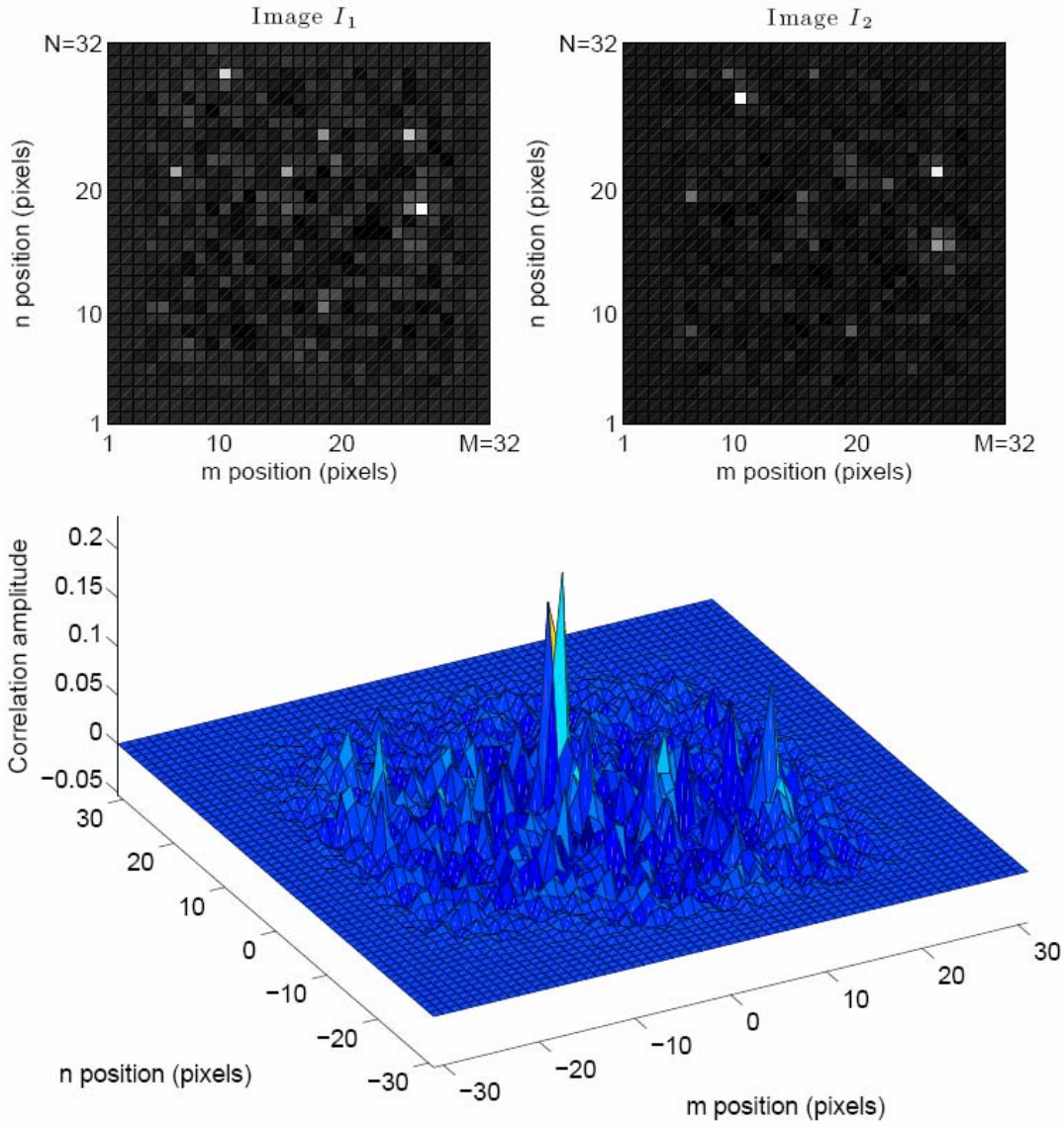

Figure 3.28 An example of a cross-correlation calculation for a single interrogation area. At top are the two raw interrogation areas, with the lighter coloured pixels marking the position of seeding particles. At bottom is the correlation plane representation of the cross-correlation function between the two interrogation areas

A careful selection of three key parameters, the seeding density, the pulse interval and the size of interrogation area, determines the quality of PIV images. The values of these parameters vary with individual experiments. Usually, they are selected initially according to some basic rules and then refined by trial and error.

The seeding density, i.e. the number of particles per unit area in an image, must be sufficiently high to ensure that there are enough particles in an interrogation area for cross-correlation algorithm to produce reliable velocity vectors. In addition, the particles

have to be big enough to scatter a sufficient amount of light from the laser sheet so as to be registered by the camera. On the other hand, they should be small enough to follow the flow and not to affect the flow that is to be measured. The density of the seeding needs to be as close as possible to the density of the fluid so as to minimise the errors due to the gravitational effects. For further discussions regarding the size, type and density of particles as well as the error analysis associated with the particle motion, refer to Merzkirch (1987), Adrian (1986, 1991, 2005) and Melling (1997).

The size of the interrogation area, d_{IA} is chosen as a compromise between the desired spatial resolution and the minimum number of particles contained in the interrogation area required for obtaining a reliable velocity vector. The bigger the area, the more particles are in it. This tends to increase the reliability of the vector found, but degrade of the spatial resolution of the measurement. This issue is particularly in vortical flows where the velocity gradient is large. Thus it is necessary to select an interrogation area which contains enough particles pairs but small enough to minimise errors due to velocity gradient. As a rule of thumb, an interrogation area should contain at least ten pairs of particles.

The time separation Δt is chosen accordingly with the size of the interrogation area. To obtain reliable velocity vectors, most particles captured in the first image should be inside the interrogation when the second image is shot. As the cross-correlation is statistical process, a rule of thumb is that the maximum particle displacement allowed between the two pulses must not be bigger than a quarter of the interrogation area. A ratio between the distance measured in pixel on the CCD and the physical distance measured in the area of interest is required to translate velocities in pixels per second on the CCD chip to metres per second in the plane of measurement. This ratio, also know as the magnification factor, M, is obtained from a calibration process. The relation relationship between the pulse separation and the maximum velocity, V_{max}, in the interrogation area is given as:

$$\frac{M \cdot V_{\max} \cdot \Delta t}{d_{IA}} < \frac{1}{4} \qquad \textbf{Eq. 3-9}$$

Equation 3.9 indicates that once the length of the interrogation area, d_{IA}, is selected, the time separation imposes a constraint on the maximum velocity in the flow that can be measured.

The process of selecting the time separation and the size of the interrogation area is interactive and it depends greatly on the characteristics of the flow to be measured. It is recommended to start with a relatively big interrogation area of, for example, 64 × 64 pixels, and a relatively long time separation. Depending on the application, either a short time separation or a small area could be preferred. In the case of vortical flows, due to the large spatial velocity gradients that are present, a small interrogation area should be selected in order to capture sufficient details in the vortices. Once the size of the interrogation area is fixed, the maximum value of the time separation can be calculated by substituting the value of the maximum velocity expected in the flow into equation 3.9. The minimum value of time separation is imposed by the error introduced by the cross-correlation algorithm and also by the specification of the PIV system. The latter is related to the physical characteristics of the camera-laser configuration which in modern system can be as low as 1μs. The former has a typical value of $\left|\varepsilon\overline{X}\right|$ ~ 0.05 pixels although values as small as 0.01 pixels have been reported (Martin Hyde, TSI). As this value is a function of the quality of seeding and the cross-correlation engine but not of the velocities in the flow, the magnitude of the error increases as the particle displacement decreases.

Denoting the value of the velocity in the flow by V_r and the displacement of the tracked particles in the interrogation area in pixels by $\left|\Delta\overline{X}\right|$, the value of the measured velocity V_m can be expressed as:

$$V_m = \frac{\left(\left|\Delta\overline{X}\right| + \left|\varepsilon\overline{X}\right|\right)\cdot M}{\Delta t} \quad V_r = \frac{\left|\Delta\overline{X}\right|\cdot M}{\Delta t} \qquad \textbf{Eq. 3-10}$$

Substituting the second expression of equation 3.9 into the first one gives

$$V_m - V_r = \frac{\left|\varepsilon\overline{X}\right|\cdot M}{\Delta t} \qquad \textbf{Eq. 3-11}$$

from equation 3.12 the dependence of the absolute error on Δt is clear. The relative error obtained by dividing the absolute error by the velocity magnitude:

$$\frac{V_m - V_r}{V_r} = \frac{\left|\varepsilon\overline{X}\right|\cdot M}{V_r\cdot\Delta t} = \frac{\left|\varepsilon\overline{X}\right|}{\left|\Delta\overline{X}\right|} \qquad \textbf{Eq. 3-12}$$

the value of d_{IA} and Δt should be selected according to V_m so as to maximise the displacement $\left|\Delta\overline{X}\right|$ since the measurement errors diminish with increasing displacements as shown in figure 3.29. The final interrogation area used in this thesis is 32 × 32 for all the PIV experiments and the Δt are selected to maximise the displacement $\left|\Delta\overline{X}\right|$, which is about 8 pixels. Therefore, the accuracy is 0.5% of the maximum velocity measured in the whole field according to figure 3.29.

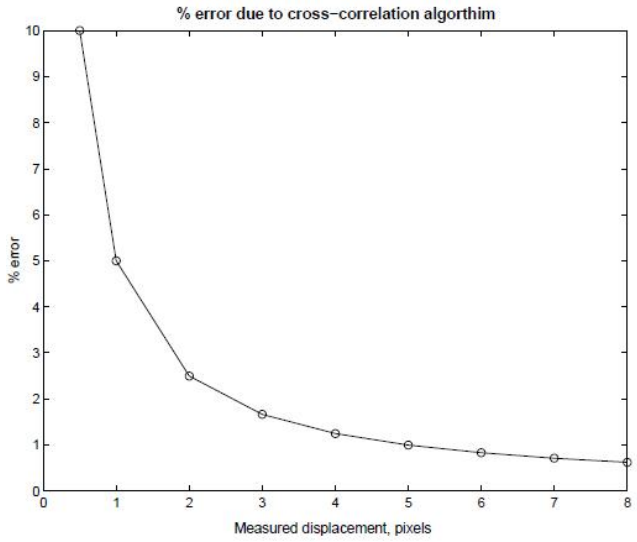

Figure 3.29 Error in the measured velocity for a typical correlation error of 0.05 pixel with an interrogation area of 32 pixels (Melling, 1997)

3.2.4.2 PIV System Used in Experiments

The PIV system used in this thesis is a commercial system from TSI. It consists of two Nd:YAG pulse lasers, a TSI Powerview Plus4MP CCD camera with Nikon high standard micro AF 28mm, 60mm and 105mm focal length lenses and a TSI synchroniser. The laser has a maximum power of 135mJ and repetition rate up to 15Hz and the laser pulse width is 3 ~ 5ns. The CCD camera has a resolution of 2048×2048 pixels, 12-bit intensity dynamic range and a frame rate up to 16 per second.

The synchroniser generates a series of timing controls which is required for each image pair acquisition as show in figure 3.30. The trigger is activated with an external signal for phase lock measurements. The first flash lamp is initiated with the trigger and the Q-switch is activated to release the laser energy after 250μs. The user-controlled time delay (shown 80μs) initiates the second lamp/Q-switch. The aperture of the camera opens up for 255μs twice in succession to record the images.

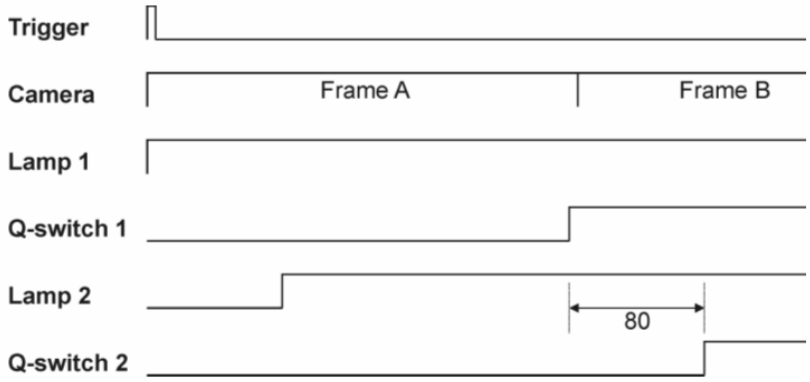

Figure 3.30 Timing of the PIV system

In this thesis, the PIV measurement technique is applied in four different experiments, including the measurement of the macro-scale and the micro-scale synthetic jets in quiescent condition, and the evaluation of the flow separation delay over a flap in both streamwise and spanwise directions. In general the set up for all the cases is the same as shown in figure 3.8. In all the cases, the camera is fixed on a 3D traverse in order to locate the view field precisely. The size of view field varies depending on the interested characteristic ranging from 6mm × 6 mm for the first case to 160mm × 160mm for the last case. The seeding particle for the first two cases is generated from a smoke generator and the size is about 1μm. For the last two cases, the glass particles with a diameter of 5μm and a density of 1.005kg/m^3 are used since the experiments are conducted in water.

The PIV technique requires a two-dimensional velocity calibration to be conducted prior to testing with a target of a known size. In the present experiments, the calibration process is described as follows. Firstly, according to the required field of view (i.e. 6 mm × 6 mm) and the resolution of the camera (2048 × 2048 pixels), the ratio of the pixel to distance can be calculated. A gauge with a known size is then mounted perpendicularly to the camera and positioned in the plane bisecting the synthetic jet actuator orifice along its centreline. The camera was then re-positioned and focused on the gauge to obtain the pixel/mm ratio calculated earlier.

In the present study, the waveform of the diaphragm displacement (measured by the displacement sensor) has a phase delay relative to the sine waveform input (sent to the shaker via the signal generator), similar to that observed by Yao *et al* (2004). For the first three experiments, to implement PIV measurement at a given phase point of the actual diaphragm oscillation cycle rather than to the input signal, the signal generator with two output channels is used. The first channel generates a sine waveform to drive

the diaphragm while the other generates a TTL signal to trigger the PIV system with a time offset relative to the first channel. By monitoring the waveforms on a multi-channel oscilloscope, the TTL signal can be adjusted such that the PIV system is triggered at any phase point according to the diaphragm waveform.

The system is set up so that during the experiments, measurements were taken at 36 phases equally spaced across the diaphragm cycle, giving a temporal resolution of 10°. For a given phase point, phase-average flow field were obtained by recording and averaging 100 instantaneous image pairs. For the separation region measurement, 500 instantaneous image pairs were recorded to produce the time-averaged flow field for each operating condition, since the structure of synthetic jets in the separation region is no longer repeatable after having travelled a long distance travel from the orifice. A summary of the parameters for all four PIV experiments is shown in table 3.3.

Table 3.3 Summary of configuration for the PIV experiments

Experiment	Micro-scale SJA	Macro-scale SJA	Cross-flow (streamwise)	Cross-flow (spanwise)
Size of View (mm)	6 × 6	27.9 × 27.9	152 × 152	160×160
Camera Resolution (pixel)	2048 × 2048	2048 × 2048	2048 × 2048	2048 × 2048
Magnification Factor (mm/pixel)	0.0029	0.0136	0.0742	0.0781
Time Separation (μs)	1 ~ 20	10 ~ 100	5000	10000
Error	± 0.5%	± 0.5%	± 0.5%	± 0.5%
Interrogation Size (pixel)	32 × 32	32 × 32	32 × 32	32 × 32
Spatial Resolution (mm)	0.094	0.436	2.375	2.5
Overlap	50%	50%	50%	50%
Number of images for averaging	100	100	500	500
Phase Lock	Yes	Yes	No	No
Seeding Particle	Glycerol	Glycerol	Hollow glass	Hollow glass

3.2.5 Test Conditions

A boundary layer profile at a distance of 5 mm upstream of the synthetic jets is exacted from the velocity field obtained by averaging 500 consecutive frames of PIV images, as shown in figure 3.31. The boundary profile is close to the Blasius profile,

which confirms the zero-pressure gradient nature of the laminar boundary layer at the current freestream velocity. The local boundary thickness is about 10mm.

The freestream turbulence intensity for the flat plate flow is also evaluated at appoint on the edge of the boundary layer from the PIV data used to calculate the undisturbed boundary layer velocity profile. 500 pairs of images are recorded at 5Hz and total date recording time is 100 seconds, which is sufficiently long to accurately resolve the turbulence intensity. Bernard and Wallace (2002) have shown that towards the boundary layer edge ($y/\delta \geq 0.8$), the turbulence in a flat plate flow becomes isotropic, that is, the average fluctuation velocity is the same for all three components. As such, only the streamwise, *u*-velocity component is considered. For the present experiments, the turbulence intensity is found to be about 1.0%, which, according to Tachie *et al* (2001), is typical of water tunnel experiments.

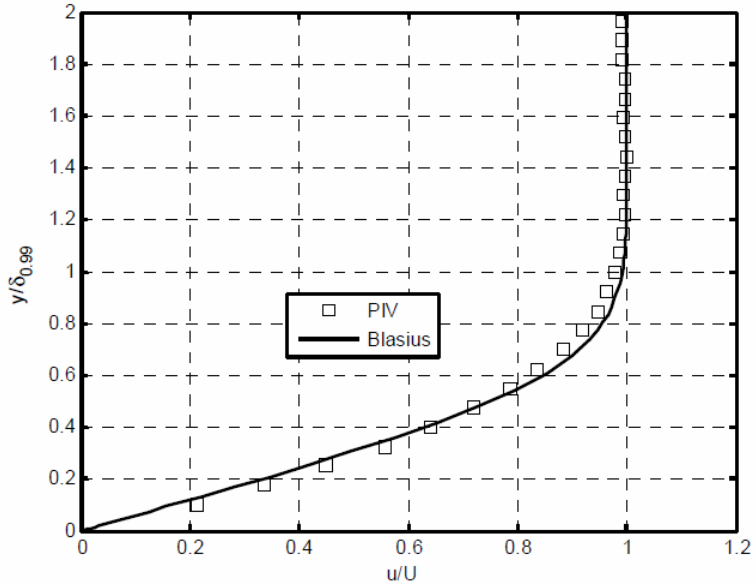

Figure 3.31 Undisturbed boundary layer velocity profiles along a streamwise centreline location at $x/D_o = -5$

4 The behaviour of Synthetic Jets in Quiescent Flows

In this chapter, the behaviour of synthetic jets issued from an orifice 5mm in diameter in quiescent flow will be studied and the dimensionless parameters that determine the behaviour of the synthetic jet will be examined with the quantitative information obtained from PIV measurements. Then the PIV results and smoke-wire visualization technique are used to study the vortex roll-up of synthetic jets. At last, the behaviour of micro-scale synthetic jets issued from an orifice 0.5mm in diameter is presented and compared with that of macro-scale synthetic jets issued from a 5mm orifice.

4.1 The Characteristics of Macro-scale Synthetic Jets

4.1.1 Test Conditions

The actuator and the experimental setup used in this experiment are described in section 3.1.1. The macro-scale synthetic jet actuator consists of a cylindrical cavity with a diameter D_c = 45mm and height H = 10mm. The cavity is capped on one end with a thin rubber diaphragm, which is sandwiched between two metal disks. The diaphragm is attached via a steel rod to a permanent magnetic shaker, which oscillates the diaphragm in a sinusoidal manner. The other end of the cavity is enclosed by an orifice plate of thickness, h = 5 mm. The diameter of the orifice is D_o = 5 mm. In the experiment, the geometry of the actuator is fixed and the characteristics of the synthetic jets are altered by varying the diaphragm oscillating displacement (Δ) and frequency (f). For this actuator, with the diaphragm displacement varying from 0.056 to 0.247mm and the frequency from 5 to 50Hz, the range of the Reynolds number defined based on the stroke length is Re_L = 11 to 1018, the Stokes number S = 7.2 to 22 and the dimensionless stroke length L = 0.9 to 4.0.

4.1.2 The Effect of Dimensionless Stroke Length *L*

The vorticity contours of a typical synthetic jet in a diaphragm oscillation cycle are shown in a sequence of frames in figure 4.1, with velocity vector being superimposed for clarity. The data of each frame are phase-averaged flow field which are obtained by averaging 100 instantaneous velocity field obtained with PIV. And these instantaneous velocity fields are taken phase-locked to the actuator driving signal at 36 equally spaced phases in a diaphragm oscillation cycle. The sequence begins with the upward motion

of the actuator diaphragm at the phase corresponding to the maximum cavity volume ($t/T = 0$) which results in the injection of the fluid from the jet cavity. At $t/T = 3/6$ which corresponds to the phase of the minimum cavity volume, the blowing cycle finishes and the suction cycle starts with the downwards motion of the diaphragm. Within the PIV measurement area, it can be observed that two vortical structures appear on some frames. The one nearer to the orifice is produced by the present cycle and the one further downstream by the previous cycle.

As shown in figure 4.1b, at $t/T = 1/6$ as the front end of the fluid slug that is ejected out of the orifice two small areas of opposite vorticity near the orifice exit are observed, with one on each side of the orifice exit. The cylindrical vortex sheet separates at the edge of the orifice and rolls up to form a vortex pair at $t/T = 2/6$, entraining ambient fluid in the process. At the end of the blowing part of the cycle, $t/T = 3/6$, the vortex ring has formed and separates from the orifice immediately afterwards.

As the vortex ring propagates downstream from the orifice after formed, it is affected by the negative pressure gradient produced at the exit of the orifice by the suction cycle. This pressure gradient induces an area of reverse velocity near the orifice, which creates a saddle point that can be seen at $t/T = 4/6$ near $z/D_o \approx 0.4$ and remains present for the rest of the suction part of the cycle. The location of the saddle point moves downstream from the orifice as the suction cycle progresses which can be seen at $z/D_o = 0.7$ at $t/T \approx 5/6$. As explained by Smith and Glezer (1998), the streamlines converging into the saddle point divide the flow field outside of the cavity in the regions where the fluid is entrained by the vortex ring (above the saddle point), and the suction flow (toward the jet orifice). The suction flow is restricted to the domain that is also bounded by the exit plane of the jet and is nominally axisymmetric with respect to the jet centre.

Comparing the shape of the vortex ring at $t/T = 4/6$ and $t/T = 5/6$, one can be seen that the vortex ring is slightly more elongated at the latter instant. It is believed that this is caused by the fact that the vortex ring is affected by the presence of suction flow in the neighbour of the orifice. It is seen that the size of the vortex ring increases as it moves further away from the orifice and at the same time the magnitude of vorticity of the vortex structures decreases as a result of the entrainment of ambient fluid into the vortex core.

The development of the synthetic jet formed at a lower dimensionless stroke length of $L = 1.56$ but at the same Stokes number of $S = 22$ is shown in figure 4.2. In

comparison to the vortex ring shown in figure 4.1, the strength of vortex at L = 1.56 appears to be weaker as a result of a lower Reynolds number, Re_L. In addition, due to its lower dimensionless stroke length, the vortex ring has not moved far away enough from the orifice at the start of the suction cycle. Consequently, it is affected strongly by the presence of the inverse flow formed during the suction cycle as seen in figure 4.2e and 4.2f. As such, the vortex ring has only convected downstream by a small distance downstream by the time the next cycle begins and the strength of the ring is also weaken considerably, see figure 4.2a.

Figure 4.3 shows the development of synthetic jets during a cycle formed at the lowest dimensionless stroke length of L = 0.9 and S = 15.4. It can be seen that a weak vortex pair appears at the orifice exit during the blowing cycle at t/T = 3/6. However, beginning at t/T = 4/6, the vortices are ingested into the cavity during the suction cycle leaving no distinct vortical structure in the jet flow and eventually disappear. It can be imagined that, if the vortex ring formed in this case is issued into a boundary layer, the suction will have strong impact on the upstream branch of the ring, resulting in the formation of a highly asymmetric vortical structure.

The time-averaged streamwise velocity contours for the above three cases are shown in figure 4.4. It can be seen that the magnitude of mean velocity decays rapidly at lowest dimensionless stroke length of L = 0.9. For a comparison, the results from Holman *et al* (2005) are shown in figure 4.5. The case shown in figure 4.5b is classified by Holman *et al* (2005) as a transitional case between no jet formation and with jet formation. The contours in figure 4.4c are similar to those shown in figure 4.5b. Therefore, the case of L = 0.9 and S = 15.4 may also be regarded as a transitional case for the present experiment.

Based on the results from the present experiment, it is found that the ability of the vortex to survive the influence of suction depends on the dimensionless stroke length. It appears the dimensionless stroke length has to be large enough to ensure jet formation. This result is consistent with the finding by Holman *et al* (2005). Taking into account the relationship between the Strouhal number and the dimensionless stroke length, the jet formation criterion established by Holman *et al* (2005) can be translated into a dimensionless stroke length of about 0.5 for axisymmetric synthetic jets. The result from the present study is also in line with their criterion with a possible difference in the exact threshold which could be attributed to factors such as the difference in the orifice geometry and diaphragm velocity programme.

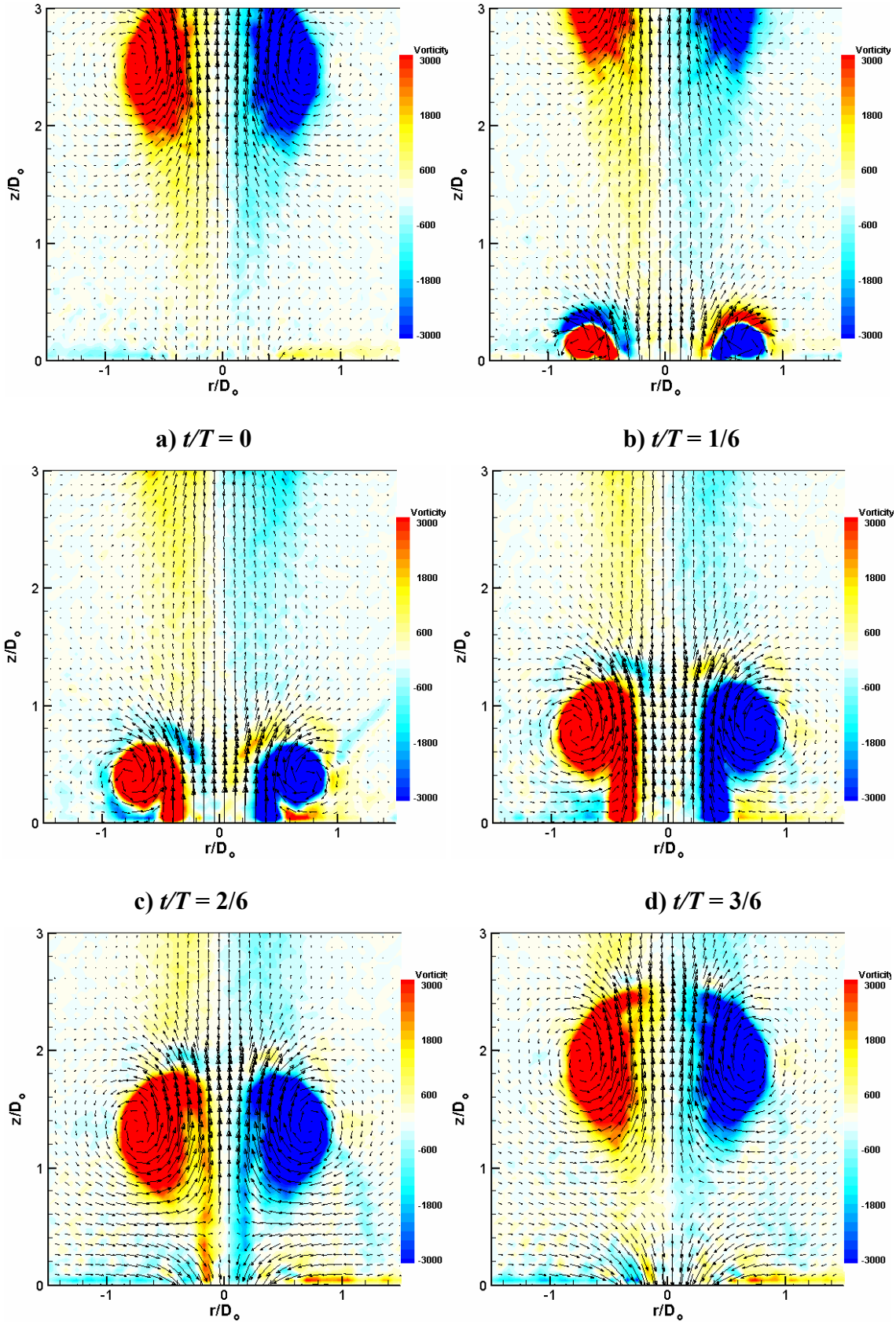

a) $t/T = 0$ b) $t/T = 1/6$

c) $t/T = 2/6$ d) $t/T = 3/6$

e) $t/T = 4/6$ f) $t/T = 5/6$

Figure 4.1 Velocity vector fields with overlaid vorticity contour of synthetic jets at six equal intervals during a cycle ($L = 3$, $S = 22$, $Re_L = 756.8$) (vorticity units: s^{-1})

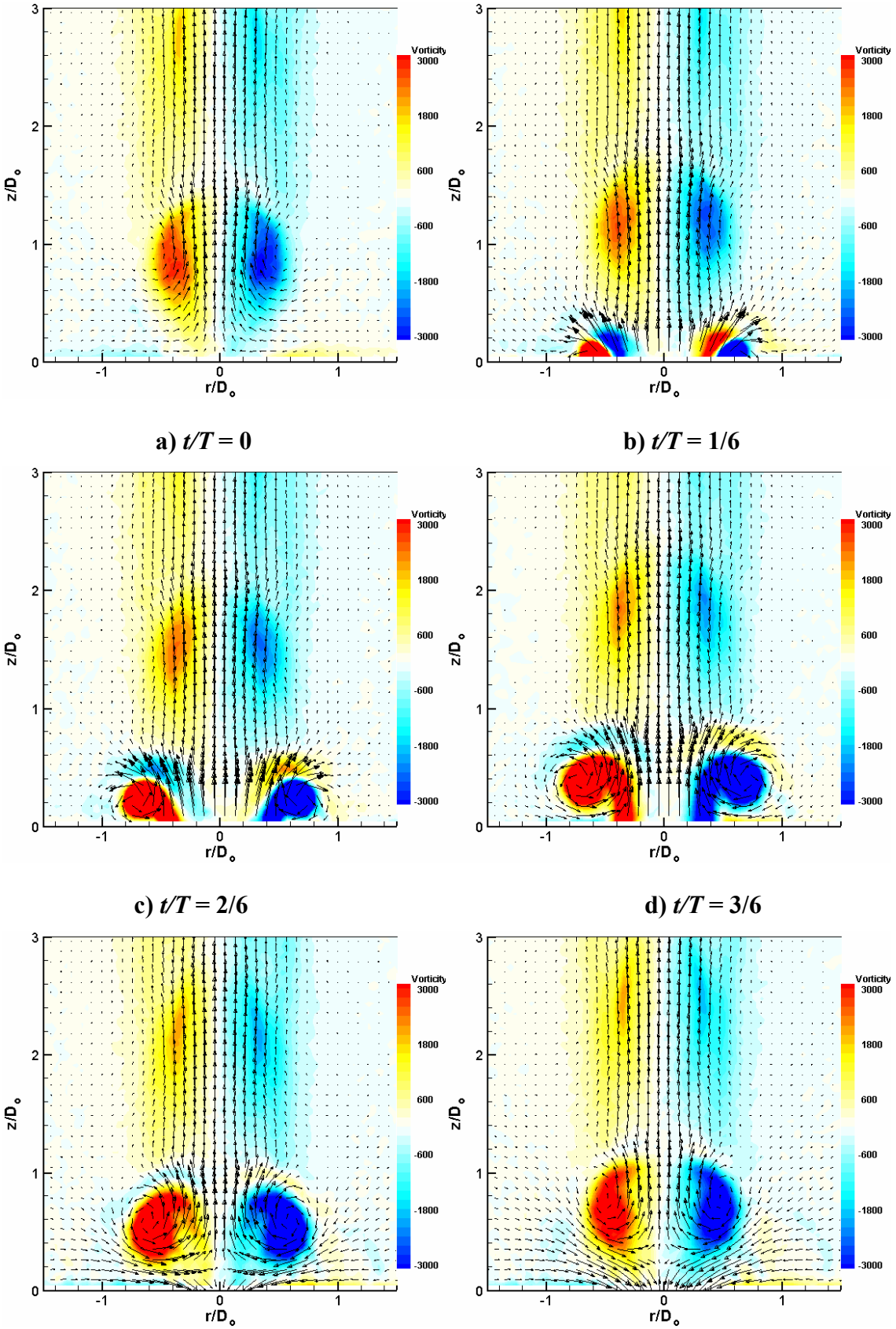

a) $t/T = 0$ b) $t/T = 1/6$

c) $t/T = 2/6$ d) $t/T = 3/6$

e) $t/T = 4/6$ f) $t/T = 5/6$

Figure 4.2 Velocity vector fields with overlaid vorticity contour of synthetic jets at six equal intervals during a cycle (L = 1.68, S = 22, Re_L = 237) (vorticity units: s^{-1})

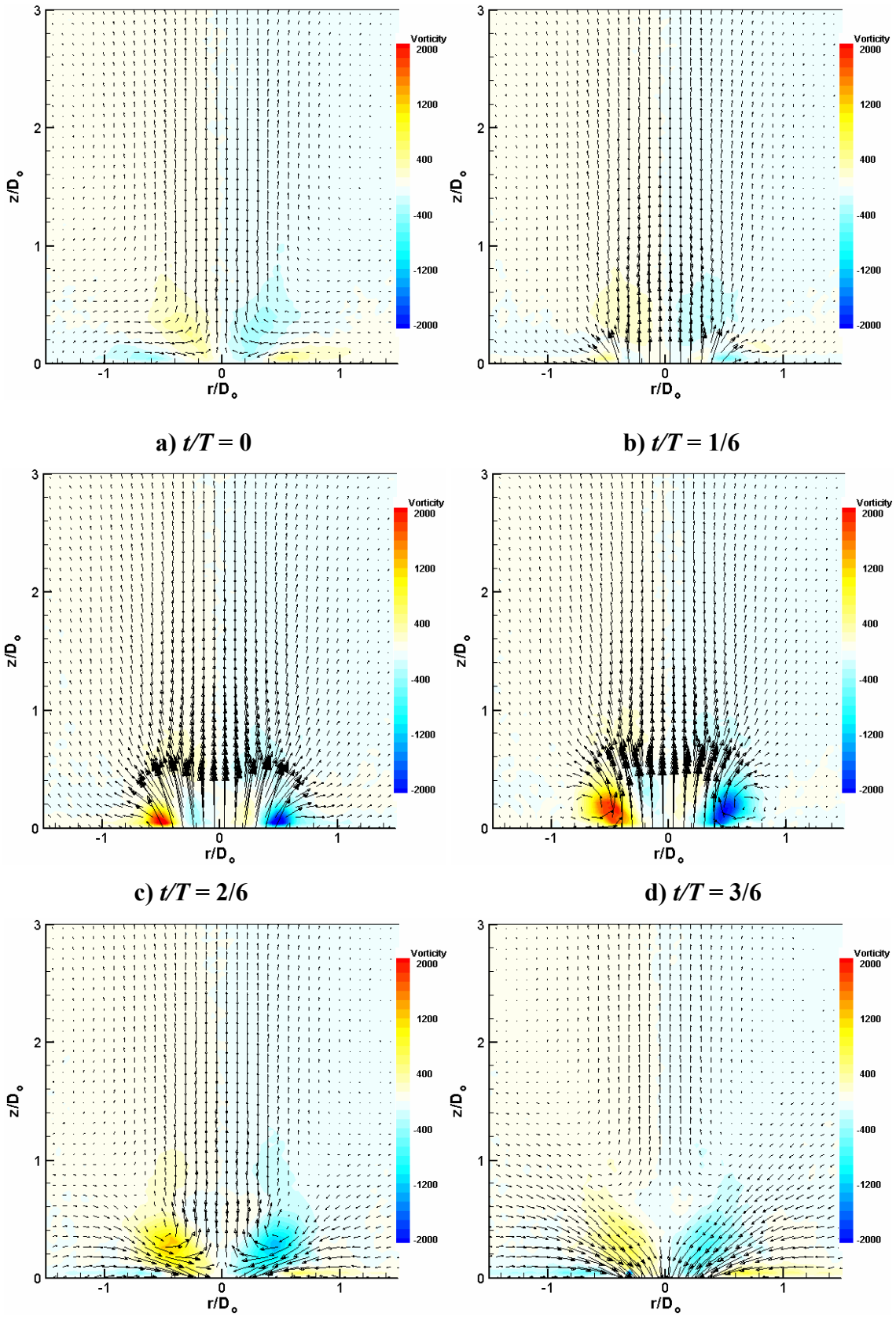

a) $t/T = 0$ b) $t/T = 1/6$

c) $t/T = 2/6$ d) $t/T = 3/6$

e) $t/T = 4/6$ f) $t/T = 5/6$

Figure 4.3 Velocity vector fields with overlaid vorticity contour of synthetic jets at six equal intervals during a cycle ($L = 0.9$, $S = 15.4$, $Re_L = 32$) (vorticity units: s^{-1})

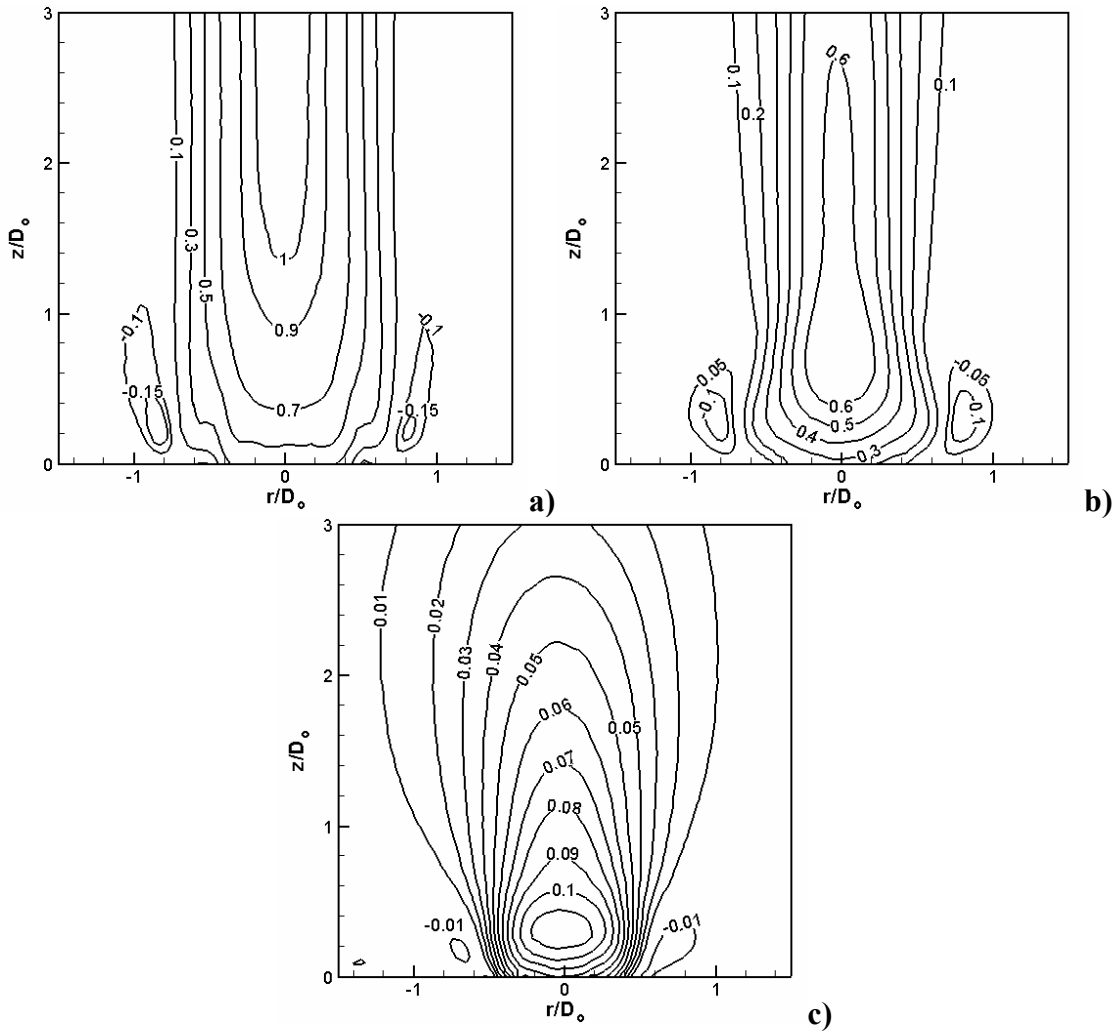

Figure 4.4 U-component velocity contours corresponding to figure 4.1, figure 4.2 and figure 4.3 (Note that the increment between lines is different for clarity and the units is m/s) a) $L = 3$, $S = 22$, $Re_L = 756.8$; b) $L = 1.68$, $S = 22$, $Re_L = 237$ and c) $L = 0.9$, $S = 15.4$, $Re_L = 32$

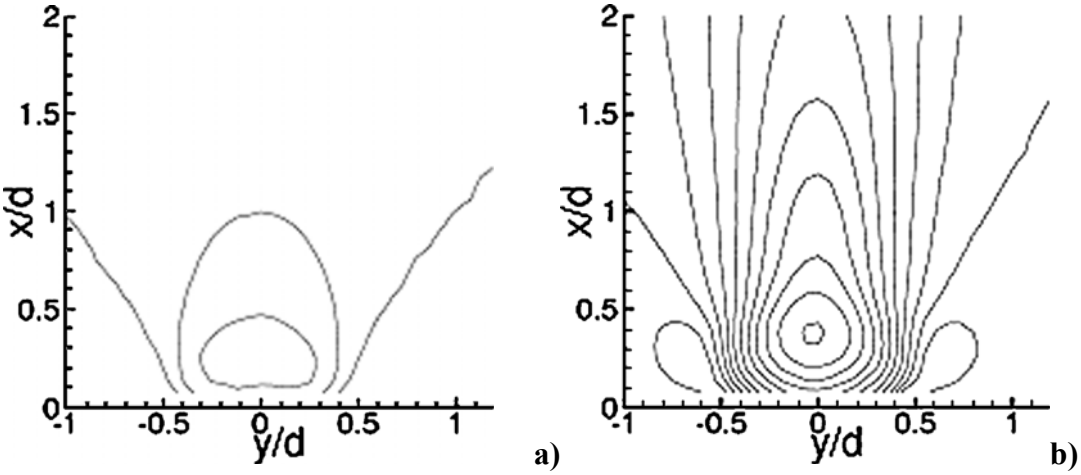

Figure 4.5 U-component velocity contours, increment between contour lines is 0.05 m/s, $S = 18$, circular orifice: a) no jet ($Re/S^2 = 0.14$) and b) transition ($Re/S^2 = 0.25$) (Holman *et al*, 2005)

4.1.3 Effects of Orifice Diameter D_o

In this section, PIV results obtained using different orifice diameters D_o which are 2.5mm, 5mm and 7.5mm are examined. Since the ratio of orifice depth to diameter is an important parameter that determines the strength of the vortex roll-up of the synthetic jet (Tang and Zhong, 2005 and Jabbal *et al*, 2006), it is kept the same as $D_o/h = 1$ for the current test since Crook (2002) recommended that the ratio should be of order unity in order to find a compromise between the stability of the vortex sheet forming the ring and the produced vortex circulation. For the real application to the aerofoils, the ratio could increase in order to make the device robust due to the requirement for the small orifice size (10 ~ 100 μm). And it is believed the development of new materials and technologies will improve the robustness as well. The cavity geometry is fixed for all cases with $D_c = 45$ and $H = 10$mm. Four groups of selected cases are compared in which the operating parameters L and Re_L are made the same by using different combinations of diaphragm displacement and driving frequencies.

The velocity vectors maps of synthetic jets superimposed onto the vorticity contours at six phase points during the blowing cycle are shown in figure 4.6 for orifices with different diameters. The unit of vorticity is s^{-1}. It can be seen the appearance of the synthetic jet in terms of velocity vectors and vorticity content are identical although the jets are issued from different D_o.

Figure 4.7 shows a comparison of the velocity distributions across the orifice exit at the blowing phase normalized by the averaged blowing velocity in the whole cycle at four different actuator operating conditions. It can be seen that for each case with the same dimensionless parameters, the dimensionless exit velocity profile is almost identical for the three different orifice diameters. The above results indicate that the performance of the macro-scale synthetic jet is dependent only on the dimensionless operating parameters L and Re_L within the range of the orifice diameters examined here.

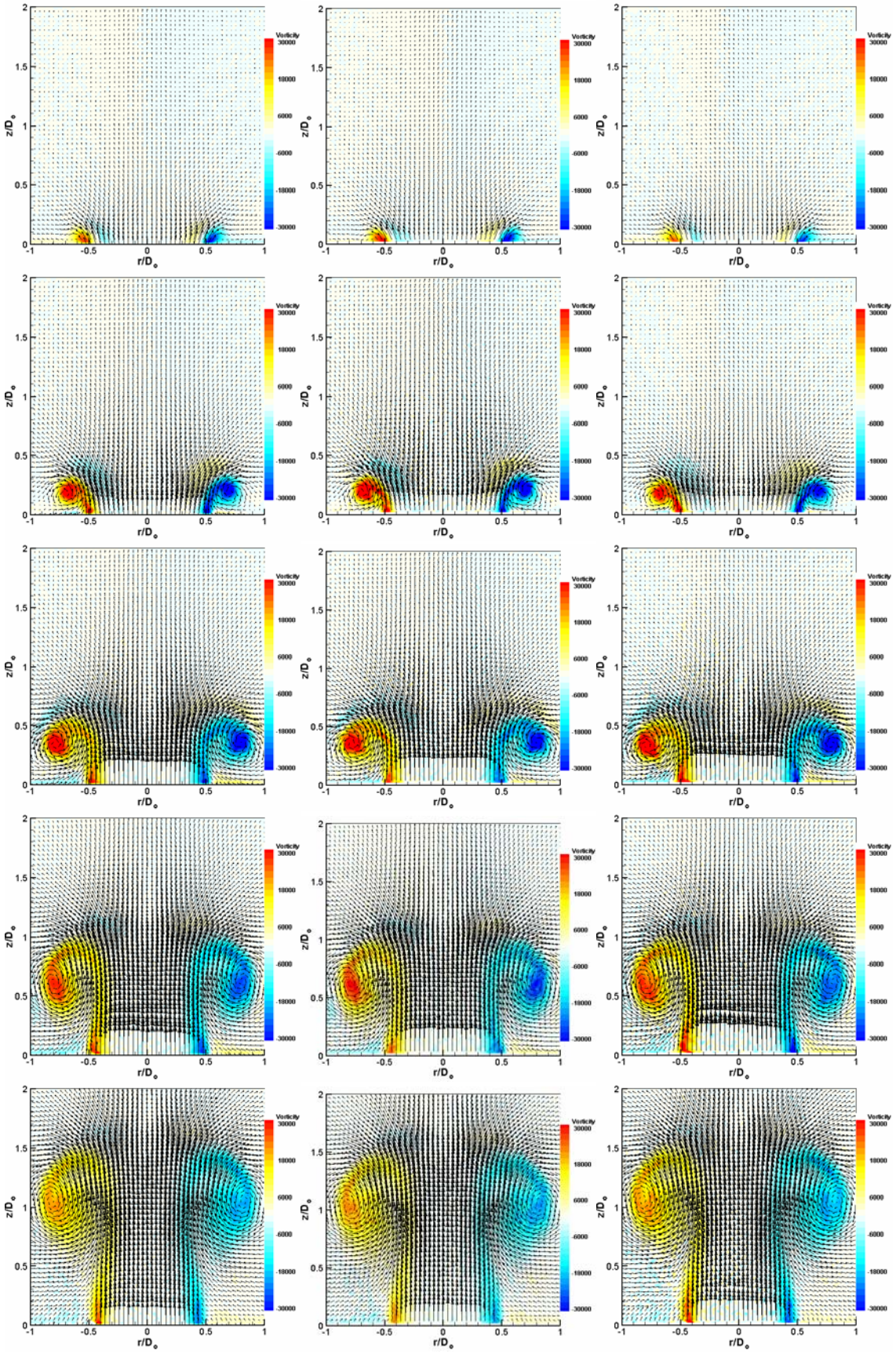

a) D_o = 2.5mm b) D_o = 5.0mm c) D_o = 7.5mm

Figure 4.6 Comparison of synthetic jets issued from orifices of different diameters at the same dimensionless parameter (L = 4, S = 19.4, Re_L = 1018.6)

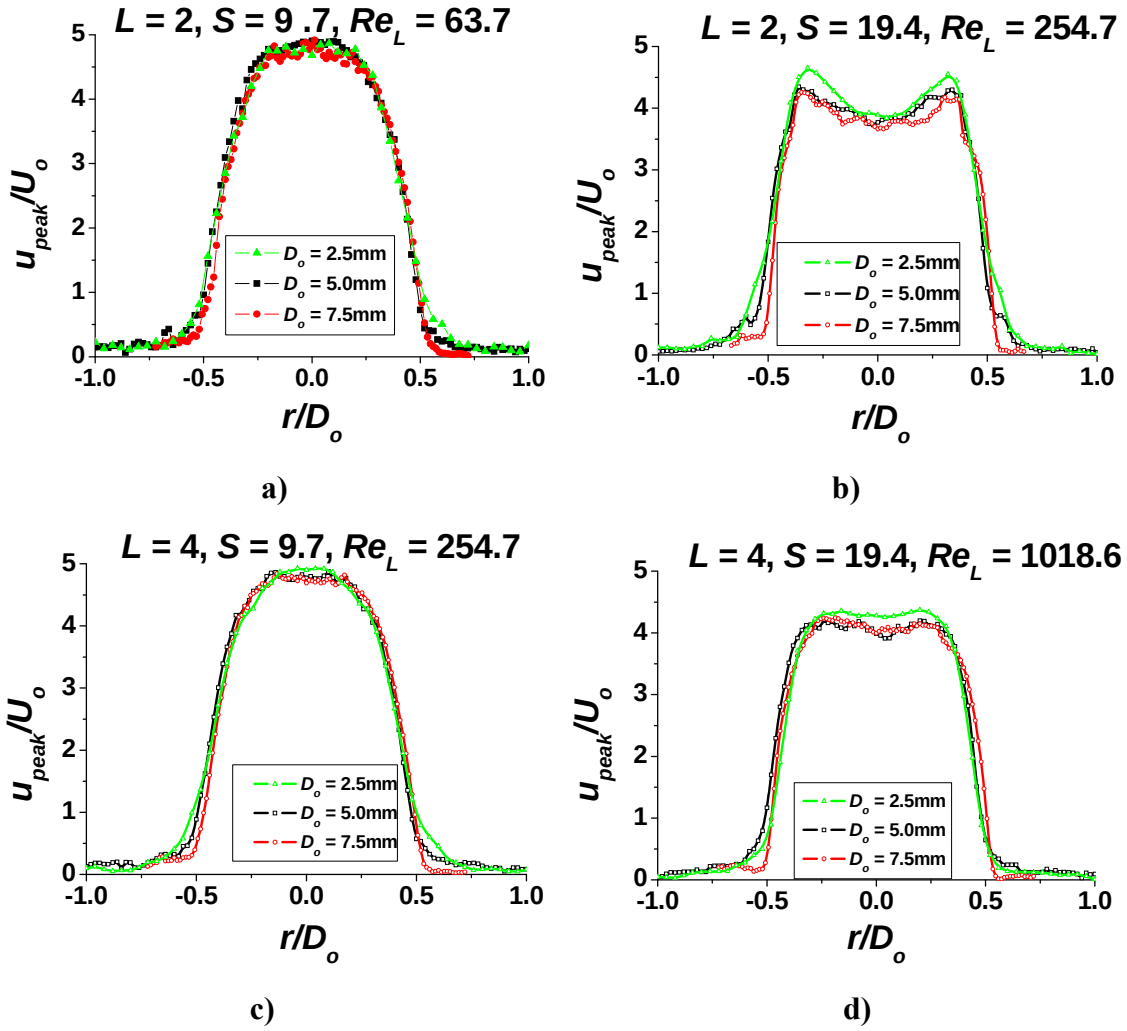

Figure 4.7 Comparison of orifice exit velocity profiles at the same dimensionless operating parameters for different orifice diameters

4.2 Criterion for Vortex Roll-up for Synthetic Jets

In this section, a further PIV experiment and a smoke-wire visualization experiment have been carried out to study the condition for vortex roll-up and the parameters of synthetic jet which affect the vortex roll-up at the orifice exit. The result can provide a more in depth understanding of the behaviour of synthetic jets in quiescent conditions, which will be useful for the design of more effective synthetic jet actuators for flow separation control.

4.2.1 Test Conditions

The actuator used in this work has been described in section 3.1.1.1. It consists of a cylindrical cavity with a diameter D_c = 45mm and depth H = 10mm. And the orifice has a circular exit opening with a diameter D_o = 5mm and depth h = 5mm. The

diaphragm displacement ranges from 0.124mm to 0.37mm and the frequency from 5 to 50Hz. The corresponding dimensionless stroke length (L) varies from 2 to 6, the Stokes number (S) from 7.2 to 22.9 and the Reynolds number defined based on the stroke length (Re_L) is from 44 to 2290.

4.2.2 Effects of Stokes Number on Jet Exit Velocity and Vortex Roll-up

It has been shown by the numerical simulations of Tang and Zhong (2006) that both the Stoke number and dimensionless stroke length affect the strength of vortex roll-up. They also show that for a fully developed oscillating orifice flow, the Stokes number plays an important role in determining the exit velocity profile hence the tendency and strength of vortex roll-up. In this thesis, further evidence from experiments is provided to verify their finding.

In order to distinguish the influence of the Stokes number and the dimensionless stroke length (or the Reynolds number), these two parameters have to be varied independently. Note that in all cases in this section, the dimensionless parameters S, L and Re_L are calculated using equation 2.12, 2.10 and 2.14. This relationship has been proved by both the simulation (Tang and Zhong, 2006) and the experiment (Jabbal, Wu and Zhong, 2006) respectively.

The normalised time-averaged jet exit velocity profiles $u_{peak}/\overline{U_o}$ for a wide range of dimensionless stroke length are compared as shown in figure 4.8. Here u_{peak} is the exit velocity profile at the maximum blowing phase (corresponding to the diaphragm at the neutral position in the blowing cycle). $\overline{U_o}$ is calculated by

$$\overline{U_o} = \frac{1}{T}\int_0^{T/2}\left[\frac{1}{A}\int_0^{D_o/2} u(r,t)2\pi dr\right]dt = \Delta f\left(\frac{D_c}{D_o}\right)^2 \qquad \textbf{Eq. 4-1}$$

It can be seen in figure 4.8a that at the same Stokes number of 7.2, the shape of the exit velocity profile only changes slightly as the dimensionless stroke length increases from 2 to 6. It indicates the dimensionless stroke length has a little effect on the exit velocity profile. As shown in figure 4.8b, at a higher Stokes number (S = 22.9) the effect of the dimensionless stroke length is more pronounced, especially the central part of the profile. A lower L produced by the use of a smaller diaphragm displacement results in a

dip in the central region, which stretches itself out as the dimensionless stroke length increases.

In figure 4.9, the shape of the exit velocity profiles at the same stroke length (L = 3) but different Stokes numbers is compared. It is shown that the exit velocity profile changes gradually from a near parabolic shape to a top-hat shape as S increases from 7.2 to 22.9. The influence of the Stokes number on the exit velocity profile of synthetic jets appears to be similar to what is known of fully oscillating flows. Being so called a kinetic Reynolds number, the Stokes number is a measure of the ratio between the unsteady force and viscous force in an oscillating flow (White, 1991). Rathnasingham and Breuer (1997) stated that the viscous effects in an orifice of a finite length are characterised by the Stokes number. At a small S the oscillating boundary layer dominates the entire orifice duct, the flow is 'chocked' hence the jet velocity is proportional to the area of the orifice. In this case, the velocity profile exhibits a parabolic shape. At a large S the boundary layer is restricted close to the orifice wall, the flow in the orifice may be considered to be inviscid hence the jet velocity is inversely proportional to the area of the orifice. In this case, the velocity profile exhibits a top hat shape.

To illustrate how the strength of vortex roll-up is affected by the magnitude of the Stokes number, the particles tracking method is used to examine the extent of roll-up for the three cases shown in figure 4.9. Timelines containing lines of particle that were emitted from the orifice exit plane at different phases of the actuation cycle are shown in figure 4.10. At S = 22, the timelines on the wings of the jet appear to curl around the vortex core due to a strong rotational motion in the core. The blank area inside the vortex is largely formed of the surrounding fluid that is entrained into the vortex. At S = 7, however, although the timelines on the wings of the jet still curl towards the stem of the jet, the rotational motion inside the vortex core is barely visible, an indication of lack of entrainment capability. At S = 12, a moderate level of entrainment activity in the vortex ring is observed. The elongated appearance in the vortex ring at the last phase is caused by the fact that some of the ejected fluid is inhaled into the orifice at the onset of the suction cycle due to the relative low stroke length of this case. Based on the above visual impressions, it appears that a minimum Stokes number of about 10 is required for any identifiable roll-up to be observed within the range of stroke lengths examined here.

Contours of axial velocity with superimposed velocity vectors for the corresponding cases are shown in figure 4.11. The PIV results also illustrate how the extent of vortex roll-up is related to the magnitude of the Stokes number. Figure 4.11 shows that at $S = 22$ there is a distinct roll-up at the orifice exit, whereas at $S = 7$ only a weak vortex is formed at a small distance away from the orifice exit plane. The contour of axial velocity superimposed on the velocity vectors also indicates the velocity profiles of the jet which is consistent with what is shown in figure 4.9.

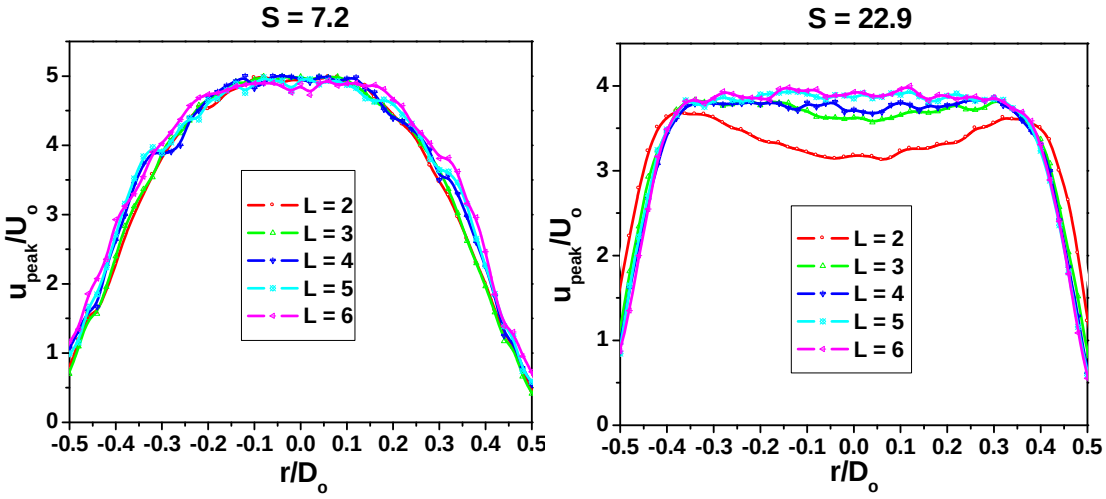

Figure 4.8 Comparison of exit velocity profiles at different dimensionless stroke length but the same Stokes number a) $S = 7.2$ and b) $S = 22.9$

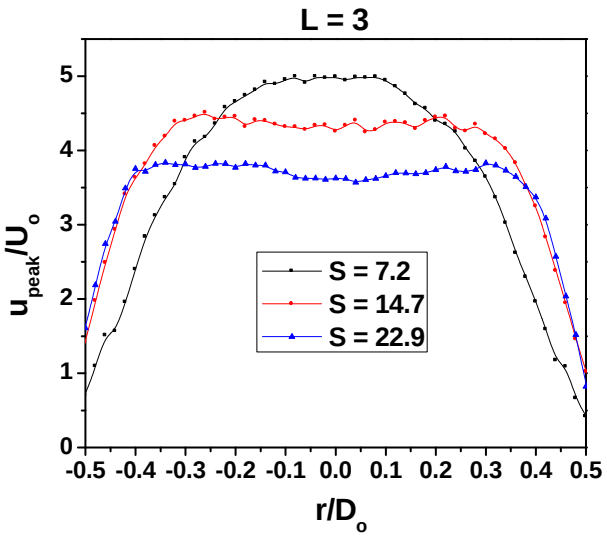

Figure 4.9 Comparison of exit velocity profiles at different Stokes number at $L = 3$

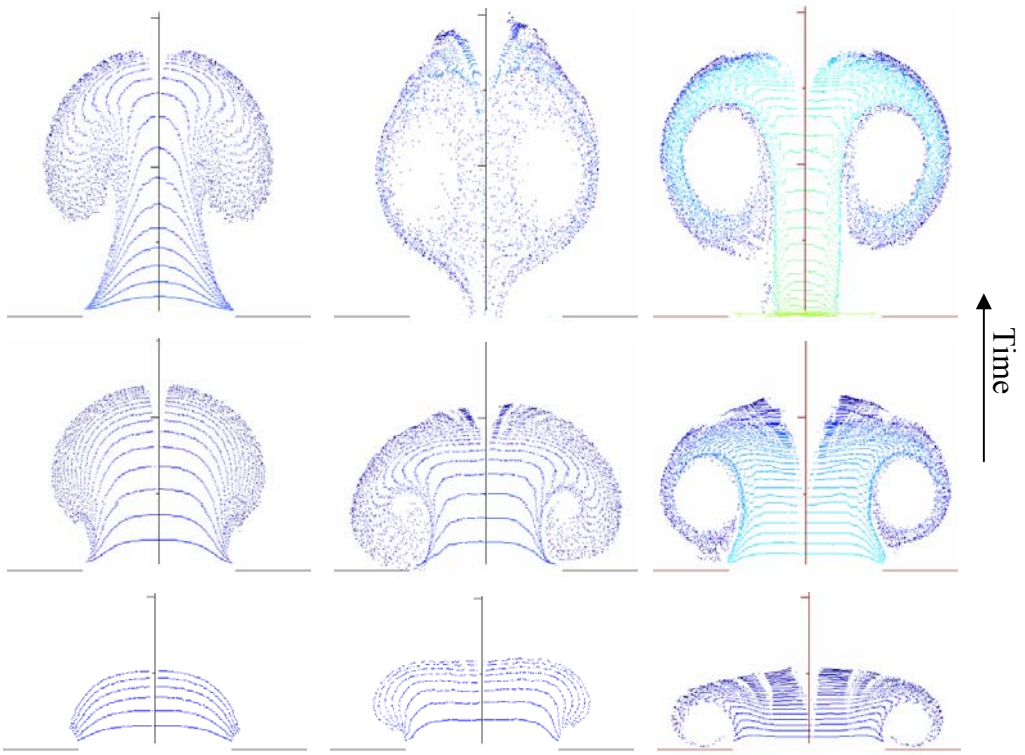

a) b) c)

Figure 4.10 Illustration of the extent of vortex roll-up using the particle tracking method (D_o = 5 mm) a) S = 7, L = 2.9, Re_L = 71; b) S = 12, L = 2.9, Re_L = 209 and c) S = 22, L = 3, Re_L = 756

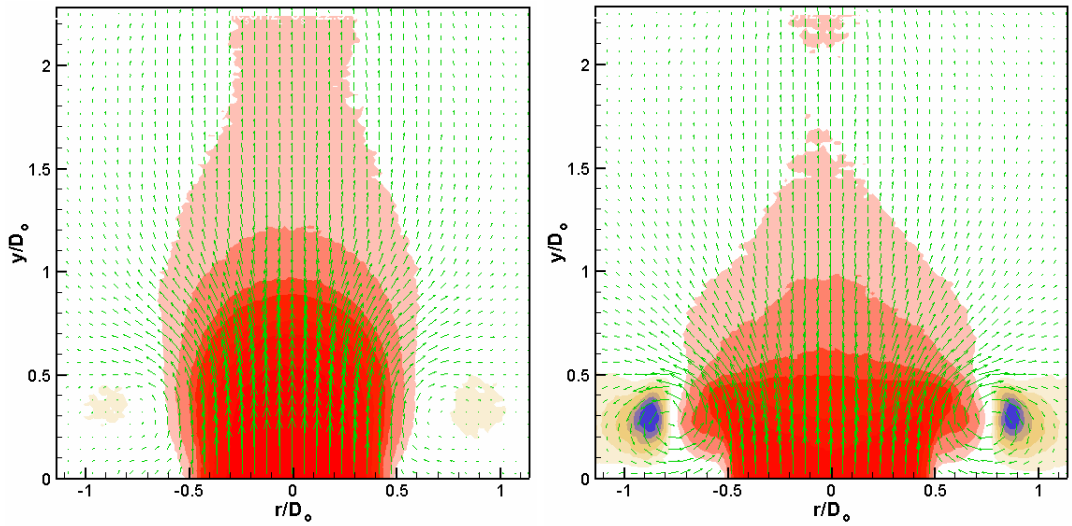

a) b)

Figure 4.11 Comparison of synthetic jets at the same L showing the Stokes number affects the vortex roll-up. Velocity vectors are superimposed by the contour of axial velocity. One of three vectors is shown for clearance a) L = 3, S = 7.2 and b) L = 3, S = 22.9

4.2.3 Criterion for Vortex Roll-up

To illustrate further how the extent of vortex roll-up is affected by the magnitude of the Stokes number and stroke length, a series of smoke-wire visualization experiments are conducted. With the smoke released right at the orifice exit, the smoke trace gives a clear indication of the extent vortex roll-up.

The sequence of smoke images at six time instants at S = 22.9 is shown in figure 4.12. The smoke is released into the flow at the orifice exit at the start of the blowing cycle (corresponding to the diaphragm at the furthest position where the cavity has the maximum volume). It can be seen clearly that smoke filament at the wings of the smoke plum produced by the ejected fluid curls upstream due to the intense local rotational motion (see figure 4.12b). As the blowing cycle proceeds, the number of swirls near the wings increases. The surrounding fluid near the orifice exit is seen to be entrained into the wing of the structure, which is indicated by the black area inside the vortex structure. This structure is believed to be associated with a vortex ring since it behaves in the way one would expect from a vortex ring. The centre of the swirling motion is believed to coincide with the location of the vortex centre. This case is considered to be a typical case where a strong vortex roll-up is present.

As the Stokes number reduces to 12.5, a vortex ring similar to that observed at S = 22.9 also appears, although it is less well defined indicating that its strength is weaker as shown in figure 4.13f. Although the amount of the entrained ambient fluid is small, entrainment still takes place as the wings of the structure roll-up (see figure 4.13a to 4.13f). Therefore, this case is still considered to be a vortex roll-up case.

As the Stokes number reduces further to 9.1, the wings of the structure still curl towards the stem of the jet as shown in figure. 4.14. But the amount of entrainment is only marginal. Hence, this case is considered to be a transitional case for vortex roll-up.

At the strokes number reduces to 7.2 which is the limit the current rig can achieve, the rotational motion is barely visible with the smoke filament exhibits a "Ω" shape at the end of the time sequence as shown in figure 4.15f. No entrainment of ambient fluid is observed from these images. As the jet does appears to advance downstream during the cycle as shown by the smoke, this case is considered to be the case which has jet formation but no vortex roll-up.

Based on the above visual impressions and discussion of the four cases, it appears that when the dimensionless stroke length is kept constant (L = 2), as the Stokes

number increases from 7.2 to 22.9 the formation of synthetic jets undergoes transition from jet without vortex roll-up to jet with vortex roll-up. The near parabolic exit velocity profile at S = 7.2 is believed to be the reason that no vortex roll-up is observed in this Stokes number since a thick Stokes layer inhibits the curling up of vortex sheets that form the vortex rings. Base on the above visual impressions, it is confirmed that a minimum Stokes number about 9 is required for an appreciable roll-up occur within the range of dimensionless stroke lengths examined here.

Another two groups of selected cases are examined to illustrate the effect of the dimensionless stroke length when the Stokes number is fixed. In these groups, only the images at two time instants are captured. The two time instants are selected to frozen the image of the vortical structure at the same downstream positions near the orifice exit so as to aid the comparison between different cases. As shown in figure 4.16, at S = 7.2 the structures at different stroke lengths are similar and no vortex roll-up is observed for all cases due to the associated low Stokes number. However, at S = 22.9 a distinct vortex roll-up appears in all the cases shown in figure 4.17 as the Stokes number is high enough. Based on these two groups of images, it is confirmed that the dimensionless stroke lengths has little effect on the occurrence of vortex roll-up.

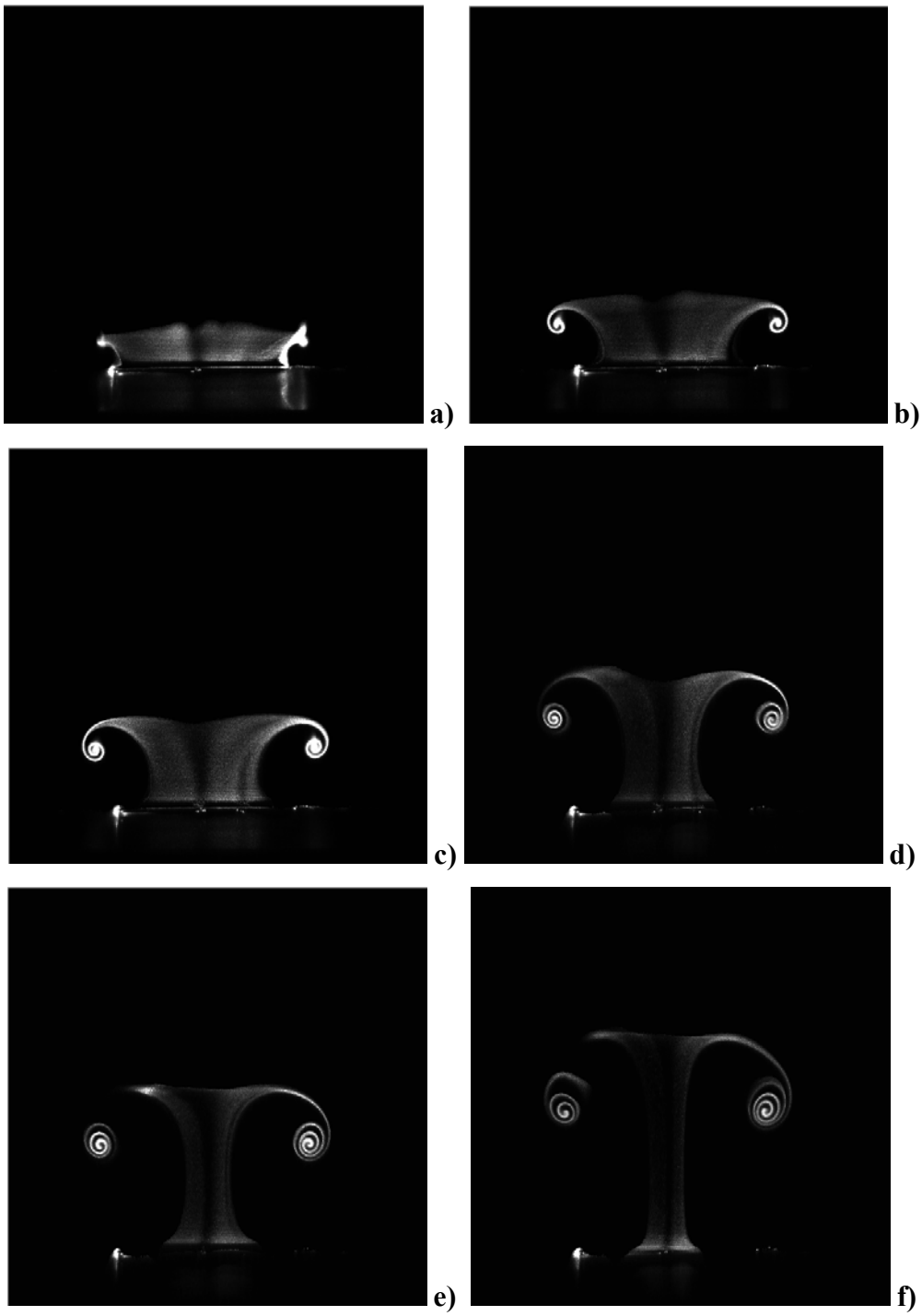

Figure 4.12 A time sequence of the development of vortex at S = 22.9 (f = 50Hz) and L = 2

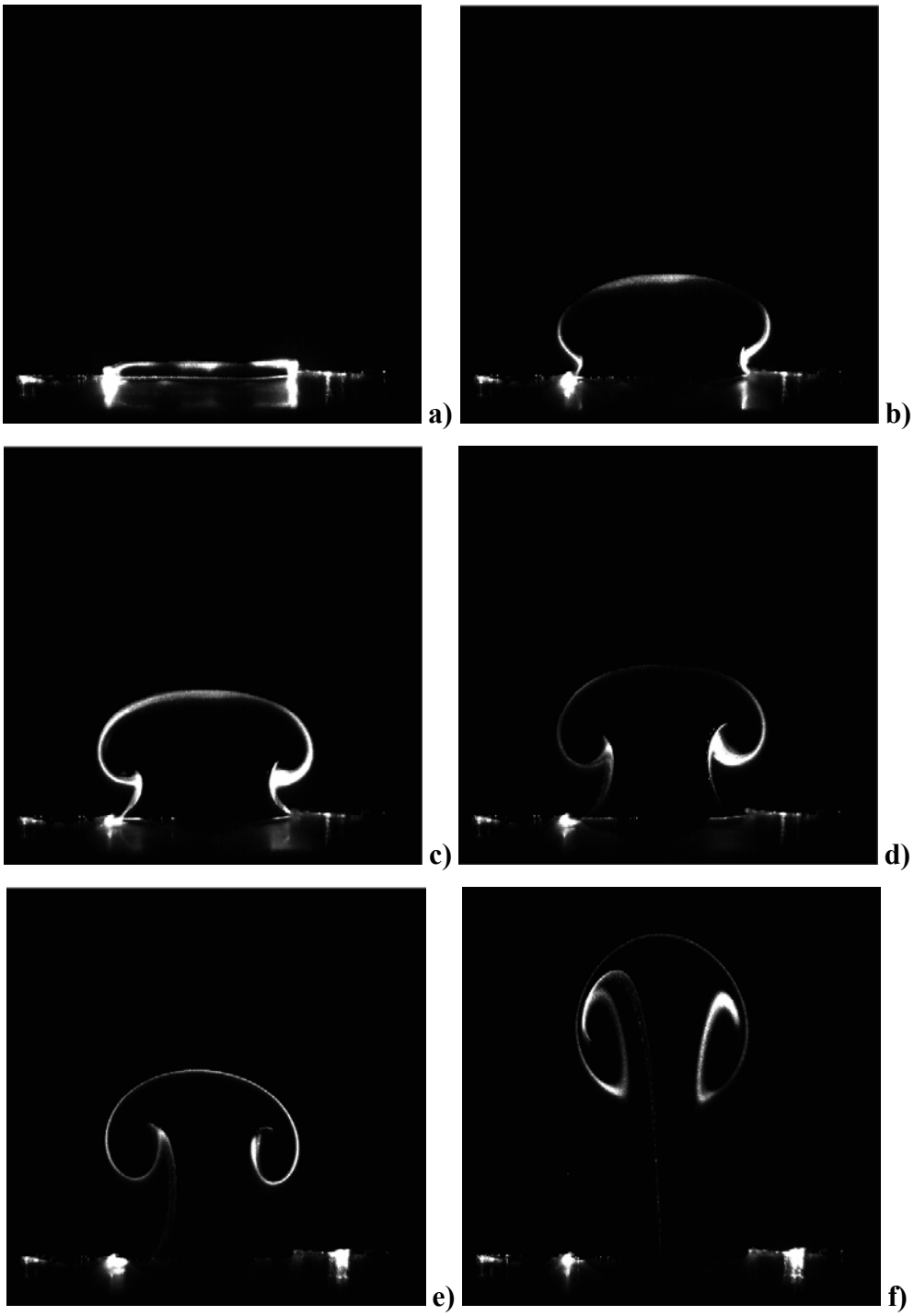

Figure 4.13 A time sequence of the development of vortex at S = 12.5 (f = 15Hz) and L = 2

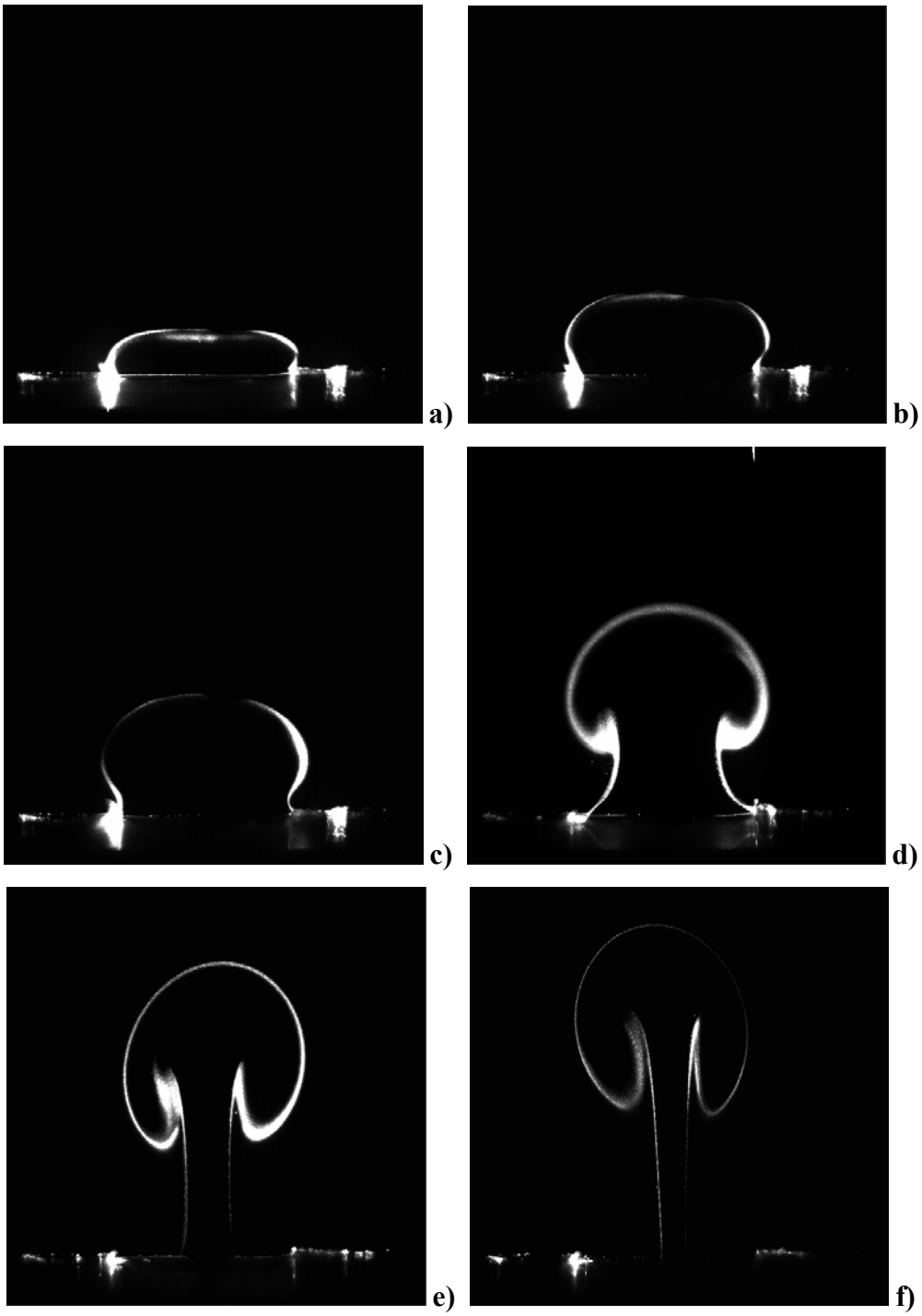

Figure 4.14 A time sequence of the development of vortex at S = 9.1 (f = 8Hz) and L = 2

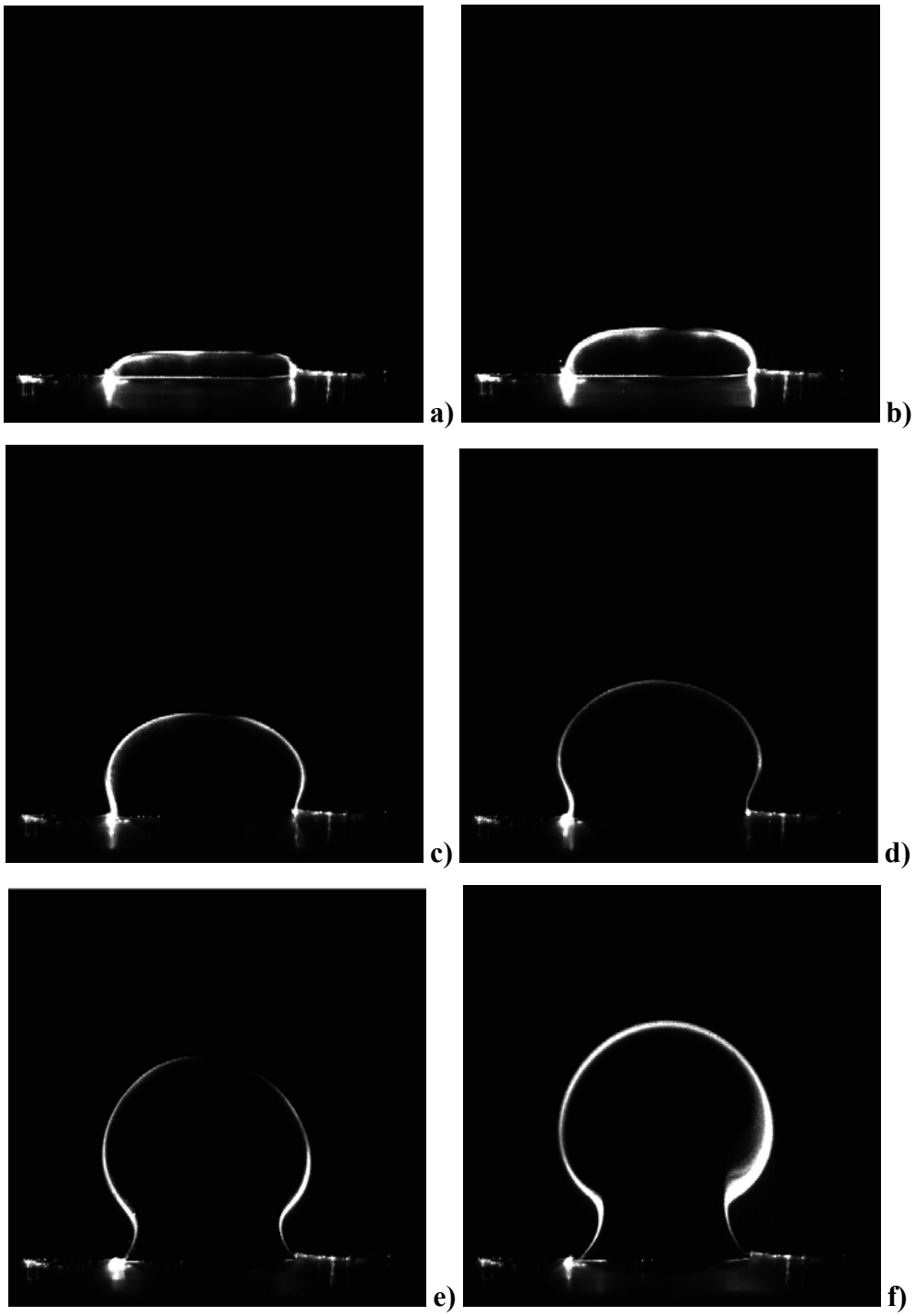

Figure 4.15 A time sequence of the development of vortex at S = 7.2 (f = 5Hz) and L = 2

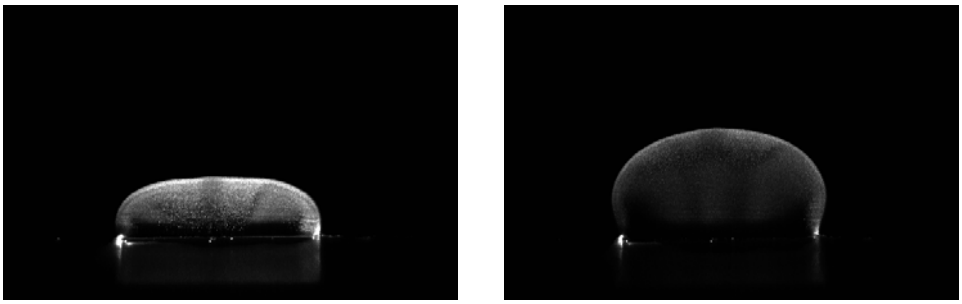

***L* = 2**

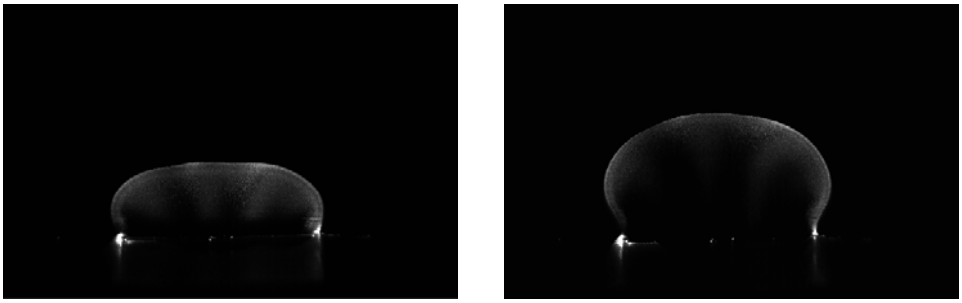

***L* = 3**

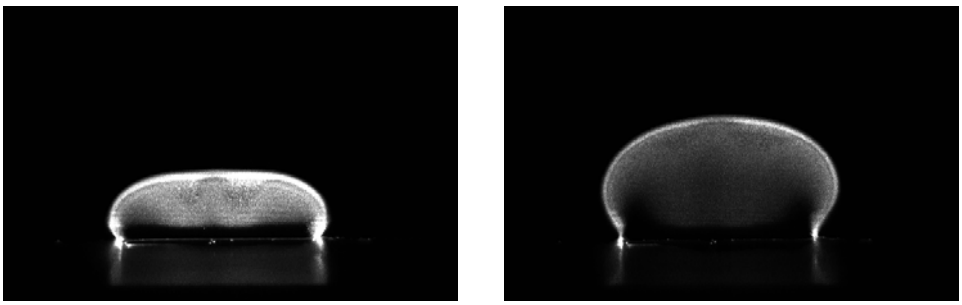

***L* = 4**

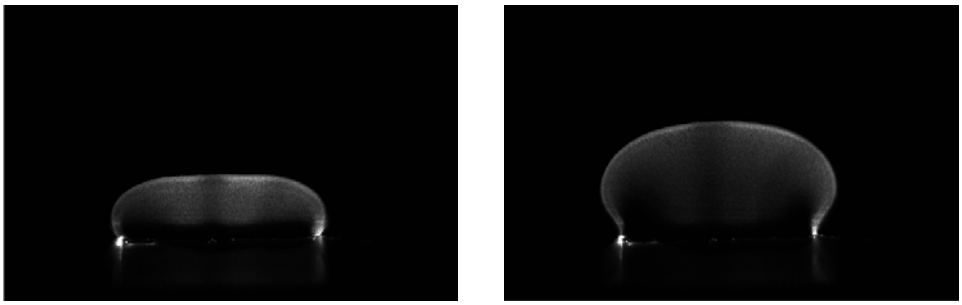

***L* = 5**

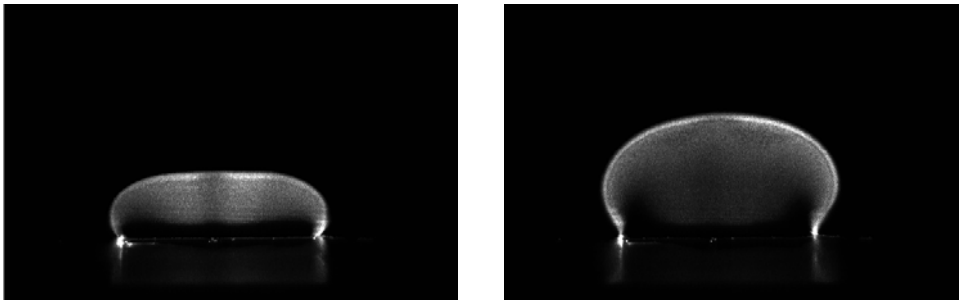

***L* = 6**

Figure 4.16 Development of vortex ring at *S* = 7.2 for different stroke lengths

***L* = 2**

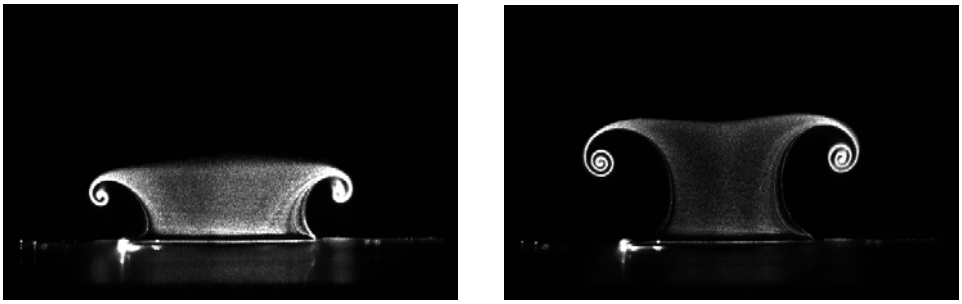

***L* = 3**

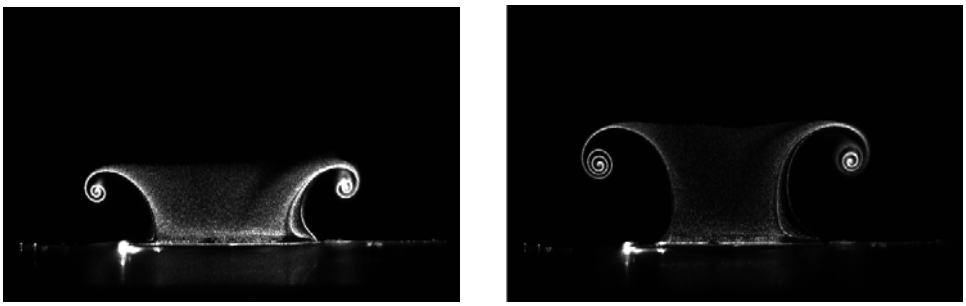

***L* = 4**

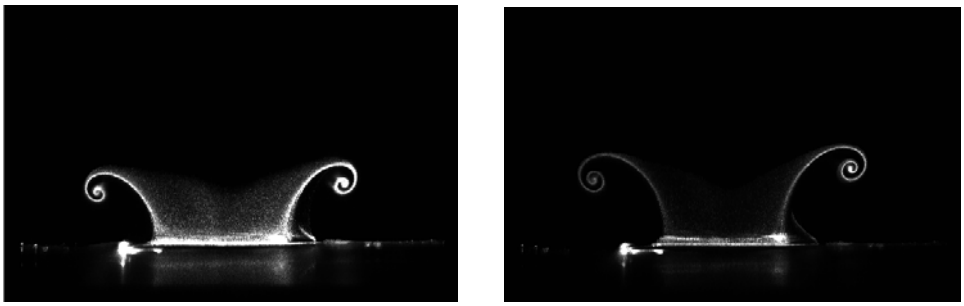

***L* = 5**

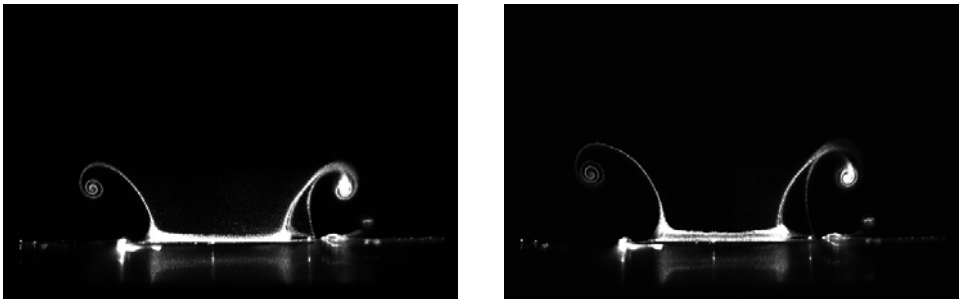

***L* = 6**

Figure 4.17 Development of vortex ring at *S* = 22.9 for different stroke lengths

4.2.4 Comment on the Effect of Re_L and S

The Reynolds number based on the stroke length Re_L is commonly believed to determine the strength of vortex rings. This is in line with the theoretical formula showing that Re_L is proportional to the total circulation ejected through the orifice during the blowing cycle. This study suggests that there is an exception when the Stokes number is low. Figure 4.18 shows the vorticity contours superimposed on the velocity vector field for two test cases which have the same Re_L but different Stokes numbers hence two distinctly difference exit velocity profiles. As S = 12, the exit velocity profile exhibits a potential core which is surrounded by a shear layer adjacent to the orifice wall. In this case, the location of the core of the roll-up vortex appears to almost coincide with the centre of vorticity in the shear layer. Since the potential core is irrotational, most of the circulation produced by the blowing part of the cycle is likely to be contained in the vortex ring. However, at S = 7, the exit velocity profile has a near parabolic shape and the roll-up, if any, is very weak. At this Stokes number, there is an offset between the core of the roll-up vortex and the centre of vorticity in the shear layer. It appears that only a small portion of the total circulation is accumulated in the vortex and the rest is deposited in the shear layer which extends to the jet centreline. This seems to suggest that although Re_L determines the total circulation ejected through the orifice during the blowing cycle, the Stokes number moderates the proportion that will be collected in the initial roll-up. Nevertheless, when the Stokes number is sufficiently high such that a predominant potential core is present in the jet flow, it may become more adequate to state that the Reynolds number determines the strength of roll-up since a majority of the total circulation is pumped into the vortex ring.

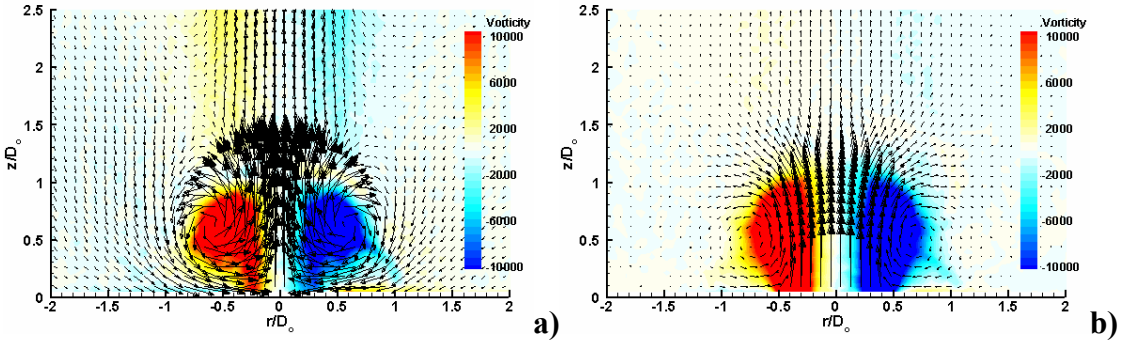

Figure 4.18 Velocity vector field and vorticity contour of D_o = 5 mm jet a) S = 12, L = 1.6, Re_L = 71 and b) S = 7, L = 2.7, Re_L = 71

Further evidence can also be found in the smoke visualisation images shown in figure 4.19. Two groups of images are shown with the two cases in each group having a similar Re_L. Within the same group, the total circulation ejected through the orifice during the blowing cycle is the same due to the same Re_L. However, a comparison between figure 4.19(a1) and (a2) or figure 4.19(b1) and (b2) reveals that the strength of vortex roll-up is different as a result of the difference in the Stokes number. Only the case with a higher S within the group has an appreciate vortex roll up.

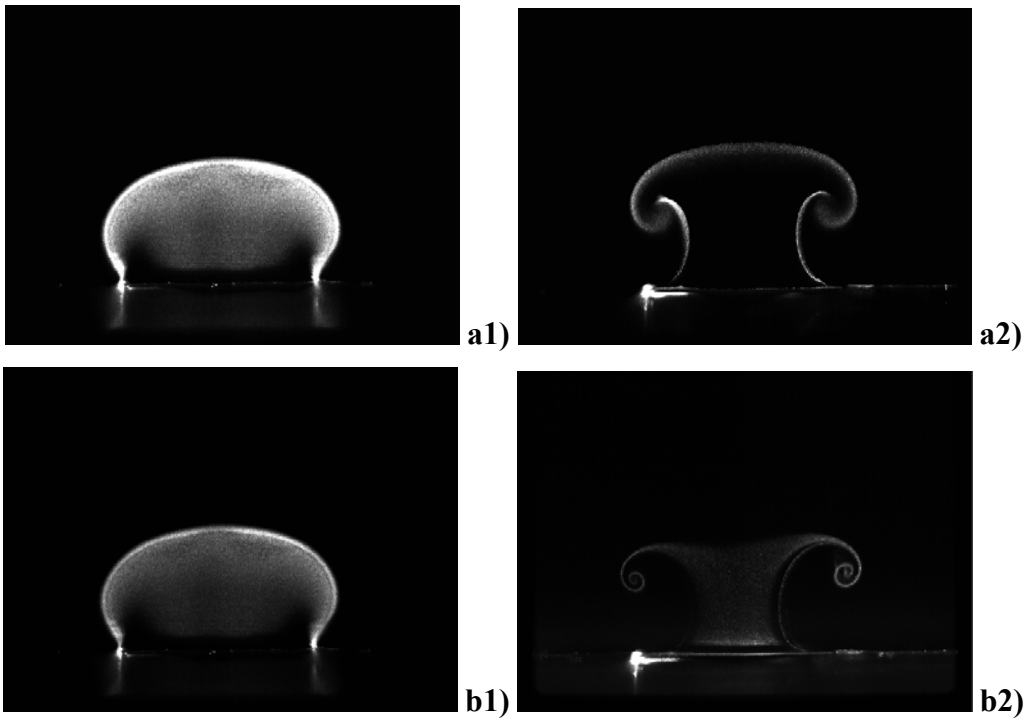

Figure 4.19 Comparison of synthetic jets at the same Re_L showing the effect of Stokes number on vortex roll-up
a1) L = 4, S = 7.2 (Re_L = 137); a2) L = 2, S = 14.4 (Re_L = 137);
b1) L = 6, S = 7.2 (Re_L = 297); b2) L = 2, S = 22.9 (Re_L = 334)

4.2.5 Parameter Map for Vortex Roll-up

From the above discussion, it has become clear that the Stokes number plays an important role in determining the strength of vortex roll-up of a synthetic jet since it affects the shape of the jet exit velocity profile significantly. In order to appreciate the effect of both Stokes number and dimensionless stroke length on the state of a synthetic jet, it is useful to establish a parameter space in which the difference regimes of synthetic jets classified as jet without roll-up and jet with vortex roll-up are identified for the present actuator.

In the current thesis, smoke-wire visualization of thirty cases have been undertaken using different combination of diaphragm displacements and frequencies

which cover the range of $1 \leq L \leq 6$ and $7.2 \leq S \leq 25.1$. Whether a vortex roll-up has occurred is judged based on observation of the smoke visualization images. The results are shown in the form of a parameter map shown in figure 4.20. The parameters map can be divided into jet without vortex roll-up and jet with vortex roll-up. The transitions boundaries between them are also shown.

From this graph, it can be seen that there is a transitional boundary separating the jets with and without vortex roll-up. For $L < 2$, the threshold of S for vortex roll-up increases as the dimensionless stroke length decreases. The transitional boundary has an expression of $S = 21.3L^{-1.1}$. For $L > 2$, the transitional boundary is asymptotic to a nearly horizontal line at about $S = 9.4$, suggesting that the threshold of S for vortex roll-up remains constants at large L. Hence at large dimensionless stroke lengths, the Stokes number is the only parameter which determines if a vortex roll-up will occur. The need to have a sufficiently high Stokes number for vortex roll-up to occur in a synthetic jet is consistent with the finding from the theoretical analysis of a fully developed oscillating orifice flow (Tang and Zhong, 2006). The slightly lower threshold value than the theoretical predicted value of 10 is believed to be caused by the short length of the orifice duct which encourages the exit velocity profile to acquire a top-hat shape. It should be noted that the threshold value of $S = 9.4$ for vortex roll-up is obtained specifically for the synthetic jet actuator studied in this paper. Hence this value is expected to alter for actuators which have a different orifice lip shape, orifice depth to the diameter ratio and velocity programme.

According to its definition, the Stokes number decreases significantly as the orifice diameter decreases. Since the orifice diameter is expected to be in the rang of a few tenths or hundredths of a millimetre for flow control purposes in aerospace applications, the Stokes number can become undesirably small resulting in no vortex roll-up. Based on the finding from this study, to ensure the flow control effectiveness of synthetic jets in practical settings, as the scale of the actuator reduces, the actuator operating frequency has to increase substantially in order to satisfy the conditions for vortex roll-up.

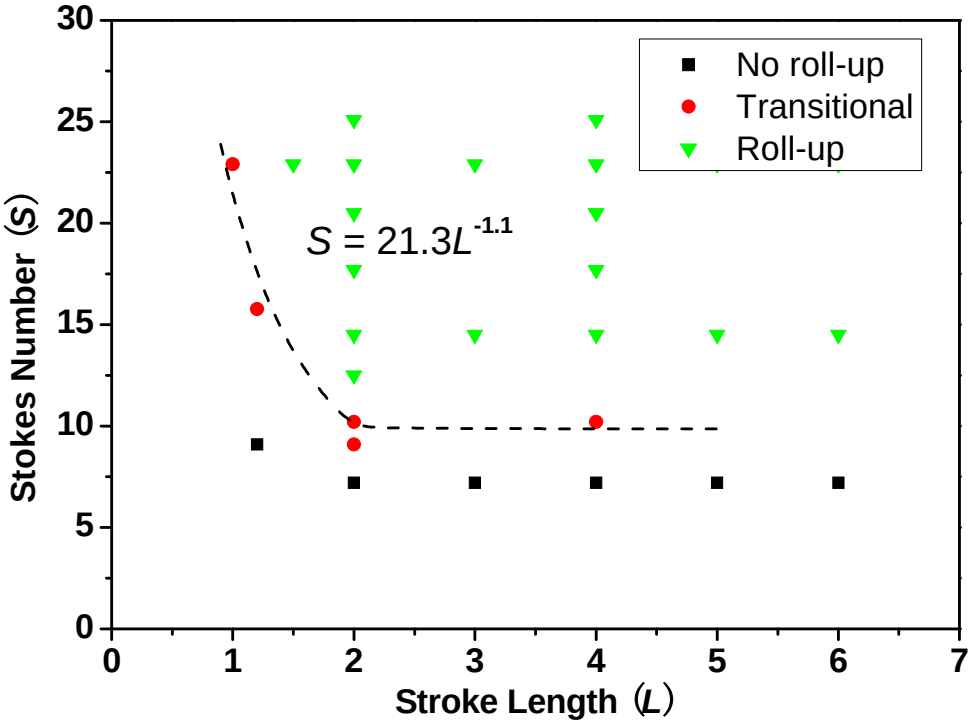

Figure 4.20 Parametric map showing the regimes of roll-up formation of synthetic jet

4.3 Characteristics of Micro-scale Synthetic Jets

In this section, the PIV study of the characteristics of synthetic jets issued into quiescent air from micro-scale orifice of 0.5mm diameter is undertaken and the results are compared to that of synthetic jets from a macro-scale orifice of 5.0mm diameter.

4.3.1 Test Condition

For the micro-scale actuator, it has an orifice diameter D_o = 0.5mm which is 1/10th of that of the macro-scale actuator. Since the ratio orifice depth to diameter is an important parameter that determines the strength of the vortex roll-up of the synthetic jet (Tang and Zhong 2005), it is kept the same as for the macro-scale actuator, i.e. D_o/h = 1 or h = 0.5mm. The cavity geometry is chosen as D_c = 20mm and H = 10mm as it is impractical to make a scale down version. In order to control the diaphragm displacement and frequency, the diaphragm driving mechanism is kept the same as for the macro-scale synthetic jet actuator. The diaphragm displacement is deduced from the reading from an accelerometer and is varying in the range of 2μm to 20μm. The diaphragm oscillation frequency is varied between 300Hz and 900Hz. Due to the small dimension, the micro-scale synthetic jet tend to have smaller Reynolds numbers (Re_L = 22 to 217) compared to their macro-scale counterparts. The Stokes number is also smaller unless the

actuation frequency is increased substantially. The maximum frequency that can be obtained from the rig is 900Hz which restricts the maximum Stokes number to 8.9. A similar range of stroke length as that of the macro-scale actuator can still be obtained.

4.3.2 Comparison of the Characteristics of D_o = 5mm and D_o = 0.5mm Synthetic Jets

A sequence of the phase averaged velocity field for D_o = 5mm synthetic jet at L = 2.9, S = 22, Re_L = 756 is shown in figure 4.21. A pronounced vortex roll-up occurs at the orifice exit and the strength of the vortex ring appears to persist downstream. This is what one would expect to see in a typical macro-scale synthetic jet.

The sequence of phase-averaged velocity field of D_o = 0.5mm synthetic jet at the same dimensionless stroke length is illustrated in figure 4.22. The Reynolds number and Stokes number for this case are much smaller (Re_L = 76, S = 7) due to the small diameter of the orifice. In comparison to the appearance of D_o = 5mm jet, a clear difference is found to exist: only a weak vortex occurs at the orifice exit and it becomes dissipated quickly downstream. Best efforts have been made on the orifice manufacturing process, but it is very hard to guarantee that the orifice has a sharp edge along the circumference, which could be the reason for the asymmetry in the velocity vector data. The size of the orifice was measured using the PIV camera with micro-scale lens with the resolution of 2.5μm/pixel.

The distributions of the normalized time-average axial velocity during the blowing cycle at the orifice exit are then examined at the corresponding test condition in figure 4.21 and 4.22. It is found that the velocity profiles are quite different for synthetic jets issued from orifices of different scales as shown in figure 4.23. For the D_o = 5mm jet, a region with a constant velocity exists near the centre of the orifice exit, which is an evidence of the presence of a potential core. However, for the D_o = 0.5mm jet, the velocity profile is close to parabolic shape, indicating that the boundary layers developing along the orifice duct have merged at the centre of the orifice and the viscous effect becomes dominant. No doubt, the difference in the shape of the exit velocity profile attributes to the significant difference in the strength of vortex roll-up observed in figure 4.21 and 4.22. This confirms the findings of the effect of Stokes number S on the vortex roll-up discussed in section 4.2.

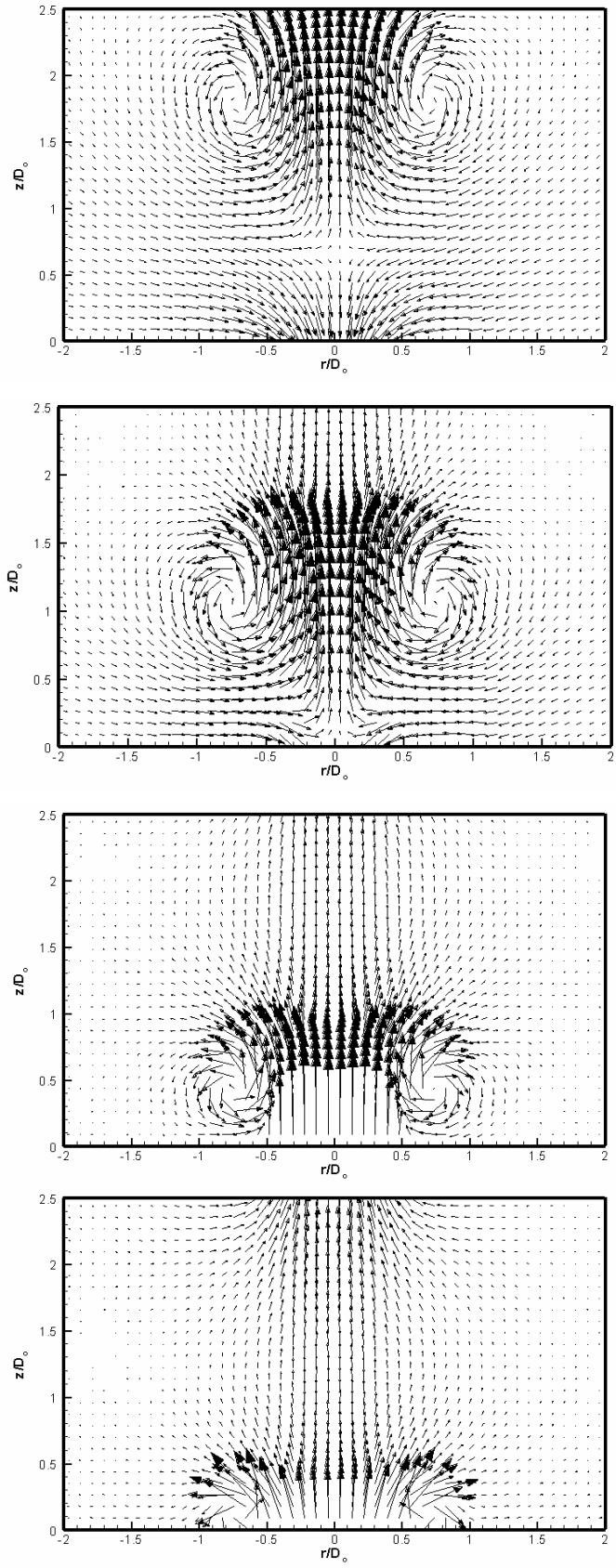

Figure 4.21 Phase-averaged velocity vector field for D_o = 5mm synthetic jet at L = 2.9, S = 22, Re_L = 756

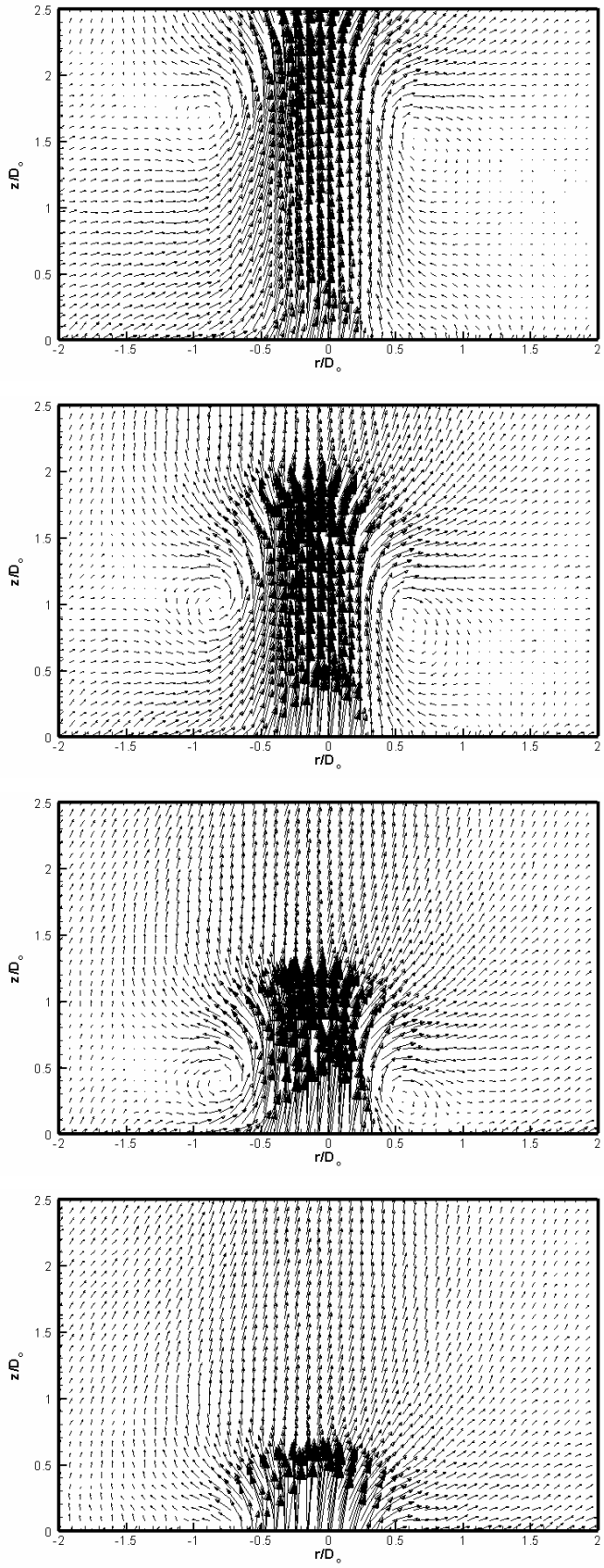

Figure 4.22 Phase-averaged velocity vector field for D_o = 0.5mm synthetic jet at L = 2.9, S = 7, Re_L = 71

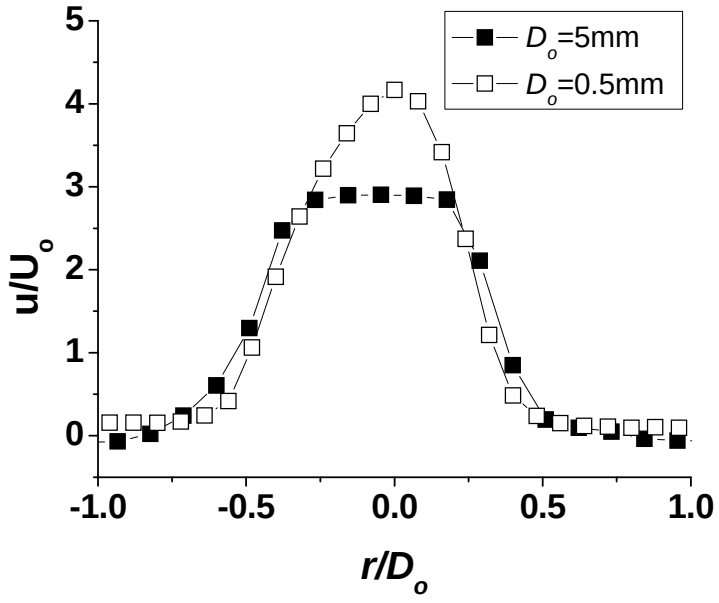

Figure 4.23 Normalized time-averaged exit velocity profiles for synthetic jets shown in figure 4.21 and 4.22

4.3.3 Dimensionless Scaling Parameters for Synthetic Jets of Different Scales

In the previous section, the differences between typical macro-scale and micro-scale synthetic jets are identified and are attributed to the difference in the magnitude of Stokes number which results in jet exit velocity profiles of different shape. In this section, the characteristics of synthetic jets of different scales with similar level of dimensionless parameters (Re_L, L and S) are examined for the purpose of identifying the dimensionless scaling parameters.

The normalised exit velocity profiles of D_o = 0.5mm jet and D_o = 5mm jet are shown in figure 4.24. It is seen that the jet exit velocity profiles have very similar shape within the scatter of PIV data when the jets with different scales have similar Re_L, L and S. Figure 4.25 compares the synthetic jets of two different scales. In both cases, only a weak vortex is observed due to the low Stokes number (S = 7). The small difference in appearance between the velocity vector fields for these two cases are believed to be due to the small difference in L and Re_L since it is difficult to keep these parameters identical in two separate experiments. The fact that two jets of significantly different scales are observed to have similar structural appearance and vorticity strength suggests that the dimensionless stoke length and the Reynolds number (or the Stokes number) are the scaling parameters for synthetic jet actuators of different scales in the near field. And the synthetic jets have identical appearance when any two of the three

dimensionless parameters (S, L and Re_L) are the same On the basis of these scaling of these scaling parameters, the finding acquired from the studies on macro-scale actuators can be applicable to micro-scale actuators, which are more difficult to measure.

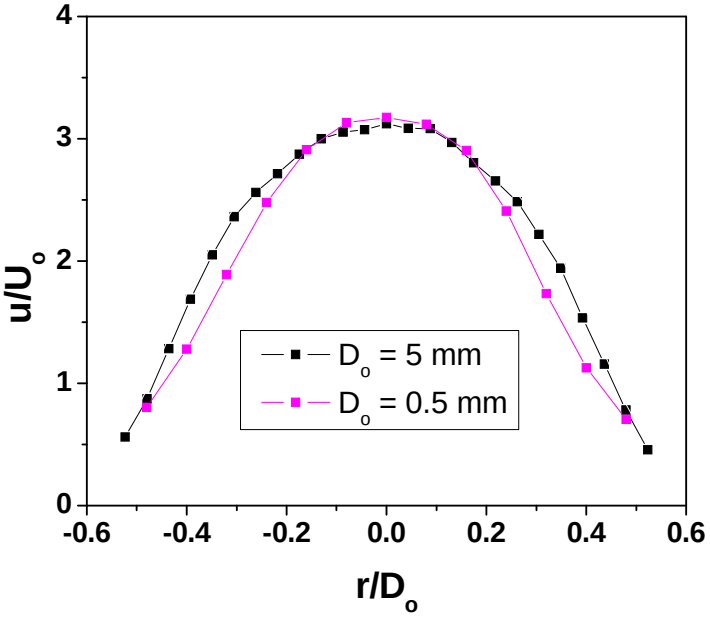

Figure 4.24 Jet exit velocity profiles for the D_o = 5mm (f = 8Hz, S = 8.9, L= 1.7 Re_L = 38.7) and D_o = 0.5mm (f = 800Hz, S = 8.9, L = 1.6, Re_L = 32.6)

It has now become clear that the weak roll-up observed in the D_o = 0.5 mm jet is in fact due to the low Stokes number which results in a near parabolic exit velocity profile. For a given actuator, to ensure the formation of vortex rings the operating frequency should be chosen accordingly in order to satisfy the requirement on the minimum Stokes number. Based on the definition of Stokes number, as the scale of actuator reduces, the actuator operating frequency has to be increased substantially in order to maintain the magnitude of Stokes number. To the best knowledge of the author, such a criterion was initially established by Tang (2006) and it is the first time that it is verified in experiments.

The question that remains if the formation of vortex ring is essential to the flow control capability of synthetic jets. The delay of separation on a 2D circular cylinder by an array of synthetic jets has been investigated by Crook and Wood (2001) and is linked to the downstream formation of pairs of counter rotating vortices within the boundary layer, not dissimilar to those formed by more conventional vane devices (Lin, 1999). According to the subsequent experiments by Zhong *et al* (2005) and Jabbal and Zhong (2006), these streamwise vortices are formed as the result of the interaction of vortex rings produced by the synthetic jet with the boundary layer at moderate stroke lengths

and jet-to-freestream velocity ratios. Vortex roll-up is hence the perquisite for the formation of the desired vortical structures that are capable of delaying flow separation. Furthermore, in the author's opinion, injection of coherent vortices, which stay near to the wall and are capable of entraining fast moving fluids in the outer part of the boundary layer to the near-wall region, is likely to be an effective mechanism of delaying flow separation. This mechanism could be more energy efficient than the mechanism of momentum injection which energises the boundary layer via vorticity diffusion and often requires the use of high jet-to-freestream velocity ratios. However, this hypothesis still requires an experimental validation.

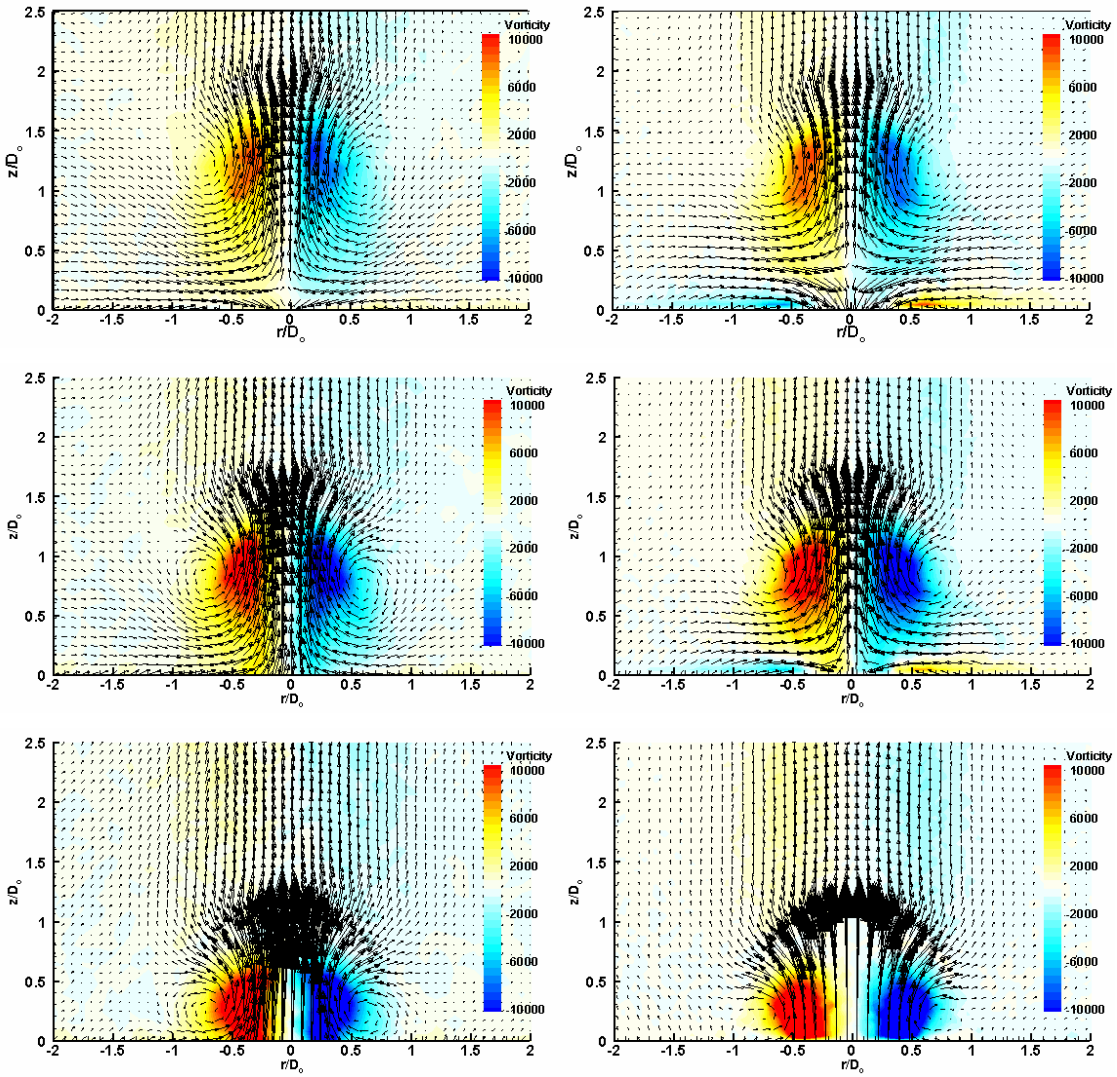

a) **b)**

Figure 4.25 PIV velocity vector maps of synthetic jets with a) D_o = 5mm, f = 8Hz, S = 8.9, L = 1.7, Re_L = 38.7 and b) D_o = 0.5mm, f = 800Hz, S = 8.9, L = 1.6, Re_L = 32.6

4.3.4 Relationships between Actuator Performance Parameters (f, Δ) and (L, Re_L)

As mentioned above, S, L or Re_L are the dimensionless parameters which characterise the behaviour of synthetic jets. Among them L and Re_L depend on the time-averaged jet velocity $\overline{U_o}$. According to the theoretical incompressible model, $\overline{U_o}$ is proportional to the diaphragm displacement Δ and the oscillation frequency f, whereas L is proportional to Δ but independent of f, as

$$\overline{U_o} = \frac{1}{T}\int_0^{T/2} \tilde{u}_o(t)dt = \frac{1}{4}\Delta f\left(\frac{D_c}{D_o}\right)^2 \qquad \textbf{Eq. 4-2}$$

$$L = \frac{1}{4}\left(\frac{\Delta}{D_o}\right)\left(\frac{D_c}{D_o}\right)^2 \qquad \textbf{Eq. 4-3}$$

The variations of the time-averaged exit velocity with the diaphragm displacement Δ and the oscillation frequency f are shown in figure 4.26. Due to the limited PIV cases measured, the results from CFD simulations using Fluent (Tang, 2006) are included in the figure to illustrate a more discernable trend. It can be seen from figure 4.26a that for D_o = 0.5mm jets, the magnitude of $\overline{U_o}$ is smaller than that predicted by equation 4.2 and the linear relationship between $\overline{U_o}$ and Δ is no longer valid due to the presence of the viscosity and compressibility effect inside the actuator. The variation of $\overline{U_o}$ with frequency f is effected by the Helmholtz resonance as shown in figure 4.26b. The Helmholtz resonance frequency is estimated to be around 450Hz where a peak jet velocity is observed. Nevertheless the magnitude of $\overline{U_o}$ is still smaller than that predicted by equation 4.2.

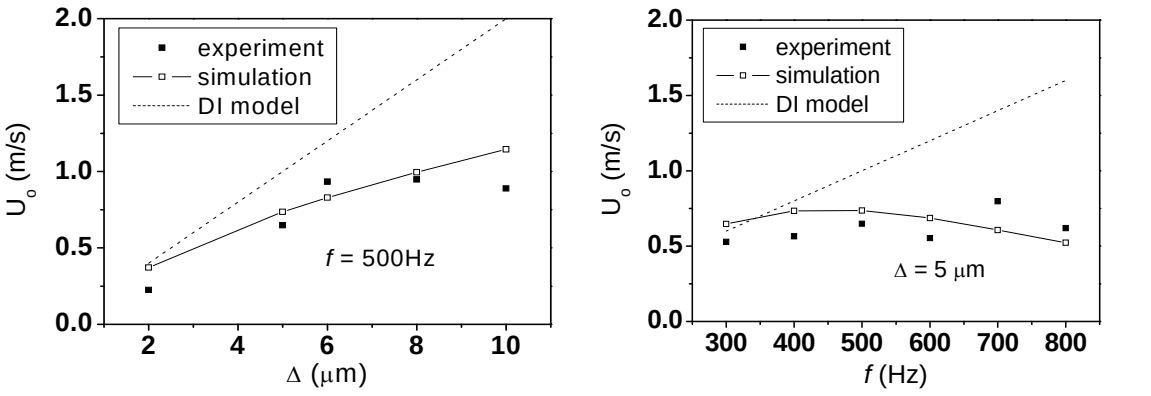

Figure 4.26 Variations of time-averaged velocity with a) Δ and b) f

The variation of the stroke length with the displacement exhibits a similar trend as that of $\overline{U_o}$ with Δ and is also nonlinear. Since the jet velocity does not increase proportionally with the frequency, the stroke length decreases with the frequency as shown in figure 4.27b instead of being independent of frequency. The variations of Re_L with displacement and frequency are similar hence will not be shown here. Because of the complicated relationship between (L, Re_L) and (Δ, f), analytical expressions can not be easily found for micro-scale synthetic jets.

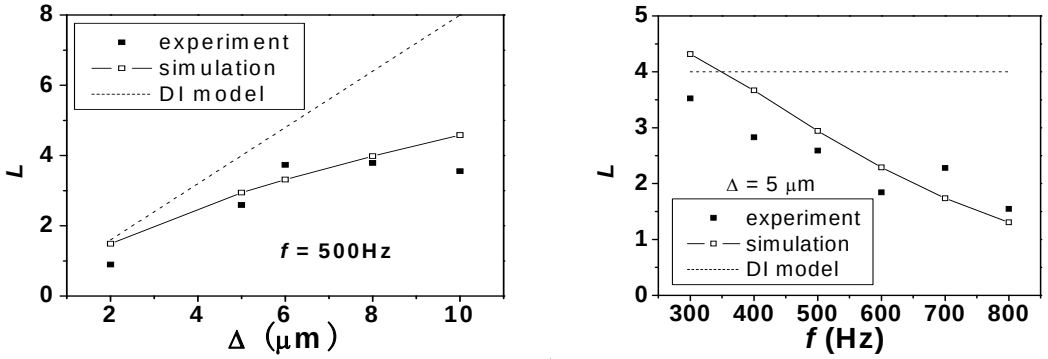

a) b)

Figure 4.27 Variations of dimensionless stroke length with a) Δ and b) *f*

The performance of synthetic jet can be described in terms of the time-averaged mass flow rate $\overline{\dot{Q}}$, the time-averaged momentum flux $\overline{\dot{M}}$ and the total circulation Γ_{total}, where

$$\overline{\dot{Q}} = \frac{1}{T}\int_0^{T/2} \rho \int_0^{D_o/2} u(r,t)\cdot 2\pi r dr \qquad \textbf{Eq. 4-4}$$

$$\overline{\dot{M}} = \frac{1}{T}\int_0^{T/2} \rho \int_0^{D_o/2} u^2(r,t)\cdot 2\pi r dr \qquad \textbf{Eq. 4-5}$$

$$\Gamma_{total} = \int_0^{T/2} \frac{u^2(0,t)}{2} dt \qquad \textbf{Eq. 4-6}$$

When the flow in the synthetic jet actuator can be regarded as incompressible, $\overline{\dot{Q}}$, $\overline{\dot{M}}$ and Γ_{total} are found to be related to L and Re_L according to Tang and Zhong (2005)

$$\frac{\overline{\dot{Q}_o}}{\rho f D_o^3} = K_Q L \qquad \textbf{Eq. 4-7}$$

$$\frac{\overline{\dot{M}_o}}{\rho f^2 D_o^4} = K_M L^2 \qquad \textbf{Eq. 4-8}$$

$$\frac{\Gamma_o}{\nu} = K_\Gamma \,\mathrm{Re}_L \qquad \textbf{Eq. 4-9}$$

where K_Q, K_M and K_Γ are coefficients determined by the waveform and boundary conditions of the oscillating diaphragm.

With the PIV data, $\overline{\dot{Q}}$, $\overline{\dot{M}}$ and Γ_{total} can be obtained by integrating the temporal velocity variations over the orifice exit. From figure 4.28, it is seen that although the relationships between (L and Re_L) and actuator operating condition are intricate, the linear relationships between the dimensionless mass flow rate, momentum flux and total circulation and the two dimensionless operating parameters found for macro-scale synthetic jet is still appear to exist for micro-scale synthetic jets. This finding is encouraging for modelling the performance of micro-scale synthetic jet actuators. At the present, an actuator performance prediction model using the lumped-element model has become available by Tang and Zhong (2006). It can be used to predict the jet exit velocity hence L and Re_L for given actuator geometry and operating conditions quite reliably. Given that a simple linear relationship between the actuator performance parameters and (L and Re_L) exists, the actuator performance parameter can then be predicted.

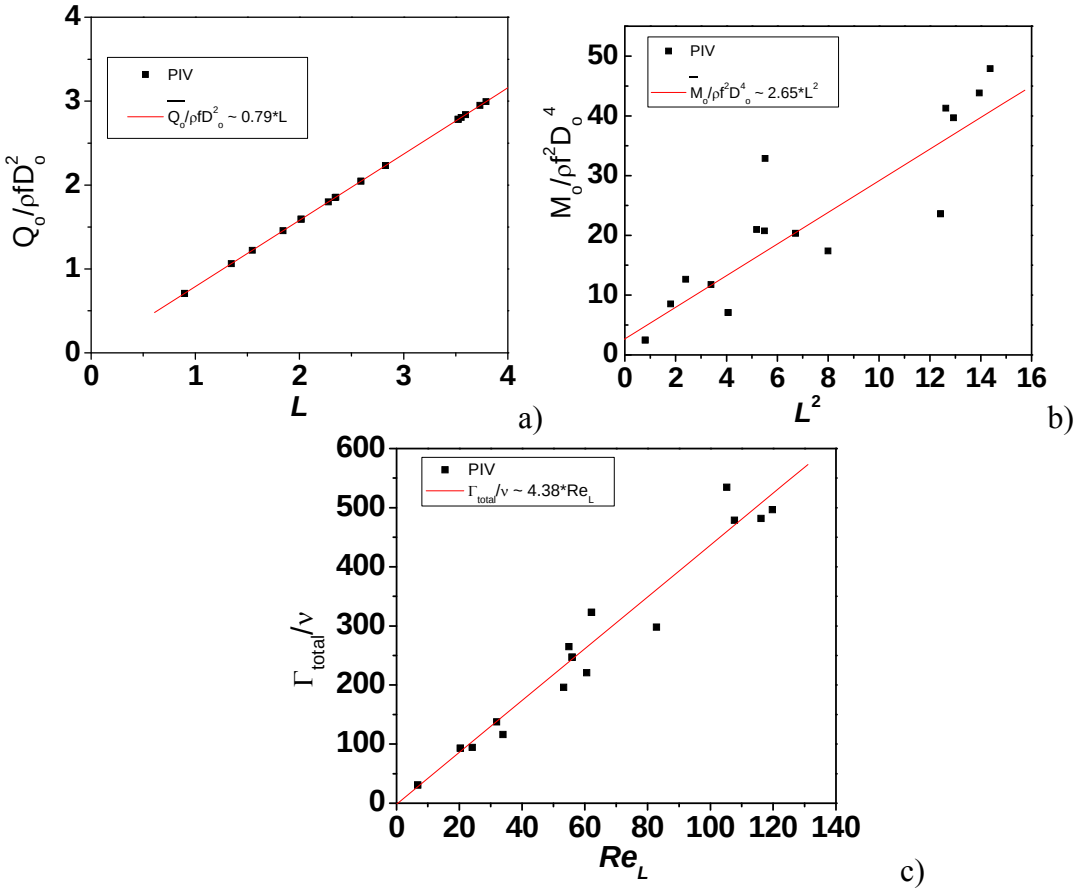

Figure 4.28 Correction between dimensionless performance parameter and (L and Re_L) a) $\overline{\dot{Q}_o}$ and L ; b) $\overline{\dot{M}_o}$ and L^2 and c) Γ_{total} and Re_L (note that the horizontal axis label for a) is L and that for b) is L squared)

4.4 Summary of Findings

In this chapter, the behaviour of synthetic jets issued from an orifice 5mm in diameter in quiescent flow are studied and the dimensionless parameters that determine the behaviour of the synthetic jet are examined with the quantitative information obtained from PIV measurements. The PIV and smoke-wire visualization technique are then used to study the vortex roll-up of synthetic jets. Finally, the behaviour of micro-scale synthetic jets issued from an orifice 0.5mm in diameter is compared with that of macro-scale synthetic jets issued from a 5mm orifice.

The key findings from this work are listed below. They represent a more in-depth understanding of the behaviour of synthetic jets in quiescent conditions, which will be useful for designing more effective synthetic jet actuators for flow control.

- In this study, the role that the dimensionless stroke length L plays in the formation of synthetic jets is confirmed. It is found that L determines the extent of the effect of the onset of suction cycle on the vortex ring and at a low L the vortex ring will be severely weaken by the suction cycle. As a result, if the vortex ring formed is issued into a boundary layer, the suction will have strong impact on the upstream branch of the ring, resulting in the formation of a highly asymmetric vortical structure.
- It is also shown that the Stokes number plays an important role in determining the strength of vortex roll-up as it affects the thickness of the Stokes layer inside the orifice duct hence the shape of the exit velocity profile from the orifice. For the synthetic jet actuator used in the current thesis, a minimum Stokes number of about 9.4 is required to ensure the occurrence of an appreciable vortex roll-up for a dimensionless stroke length greater than 2. The implication of this finding is that to ensure an appreciable vortex roll-up that is desire for effective flow control, a micro-scale synthetic jet actuator has to be operated at a much higher frequency so as to exceed the threshold value of S.
- The study shows that the characteristic of synthetic jets of different scales will be identical when the dimensionless stroke length (L), Stokes number (S) and Reynolds number (Re_L) are the same. On the bases of these scaling parameters, the finding acquired from the studies on macro-scale actuators can be applicable to micro-scale actuators, which are more difficult to be measured.

- Although the linear relationships between (L and Re_L) and actuator operating conditions observed for macro-scale synthetic jets are no longer valid for micro-scale synthetic jets, the linear relationships between the dimensionless jet performance parameters and (L and Re_L) still exist for micro-scale synthetic jets. This finding enables the performance modelling of micro-scale synthetic jet actuators to be simplified.

5 Behaviour of Synthetic Jets in a Cross Flow

The aim of this chapter is to describe the typical vortical structures that arise from the interaction of a synthetic jet with a boundary layer and to assess the level of interaction between adjacent synthetic jets in a jet array.

5.1 The Interaction between Synthetic Jets and a Boundary Layer

5.1.1 Test Conditions

Dye flow visualizations of circular synthetic jets were carried out in a laminar boundary layer developing over a flat plate. The test plate and the synthetic jet actuator used for the flow visualisation tests have been described in Section 3.1.2. The actuator consists of a cylindrical cavity with a diameter, D_c = 45mm and height, H = 10mm. There are five orifices each of which has a diameter D_o = 2mm and a depth h = 2mm on the orifice plate as shown in figure 3.14. In this experiment, the interaction of a single synthetic jet with the boundary layer is studied. Therefore the jets only are issued from the middle orifice with the other four orifices blocked with silicon.

In the present experiments, the geometry of the synthetic jet actuator was fixed. The characteristics of the jet were varied by changing the diaphragm operating conditions (oscillation frequency, f and the diaphragm peak to peak amplitude, Δ). For synthetic jets in a uniform cross flow, it has been established that their behaviour is dictated by three non-dimensional flow parameters, i.e. the Reynolds number, the velocity ratio and the Strouhal number (Crook, 2005). For synthetic jets that are released into a laminar boundary layer, they are also expected to be affected by the relative size of the boundary layer thickness to orifice diameter as well as the level of shear in the boundary layer. In the current experiments, the free stream velocity is fixed at 0.1m/s, therefore the ratio between the boundary layer thickness and orifice diameter as well as the level of shear in the boundary layer are fixed.

Table 5.1 lists the parameters of all the test cases. In the experiments, with the diaphragm frequency f ranges from 2Hz to 16Hz and diaphragm displacement Δ from 0.004mm to 0.024mm. The corresponding range of dimensionless stroke length is $1.27 \leq L \leq 3.8$, the range of Reynolds number based on jet mean velocity ($\mathrm{Re}_L = \overline{U_o} L_o / \nu$) is

$11.3 \leq Re_L \leq 562$, the range of jet-to-freestream velocity ratio is $0.051 \leq VR \leq 0.912$ and the range of Strouhal number is $0.04 \leq St \leq 0.32$. Under the current range of Reynolds number, the vortical structures generated are stable and laminar.

The good agreement between the undisturbed boundary layer velocity profiles and the Blasius solution at U_∞ = 0.1m/s was confirmed in figure 3.31 (section 3.2.5). The Reynolds number based on the local momentum thickness is approximately 113, which is less than the indifference Reynolds number = 520 for a zero-pressure gradient, flat plate boundary layer (Schlichting and Gersten, 2000). Thus the boundary layers in the present study may be considered stable, given that they are below the critical Reynolds number above which the boundary layer will be receptible to disturbances.

Table 5.1 Case Summary for flow visualisation tests

	St = 0.04 f = 2 Hz	St = 0.12 f = 6 Hz	St = 0.32 f = 16 Hz
L = 1.27	Re_L = 11.3 VR = 0.051	33.8 0.152	90.1 0.405
L = 1.58	17.6 0.063	52.8 0.19	140.7 0.507
L = 1.9	25.3 0.076	76.0 0.228	202.6 0.608
L = 2.22	34.5 0.089	103.4 0.266	275.8 0.709
L = 2.53	45.0 0.101	135.1 0.304	360.3 0.811
L = 2.85	57.0 0.114	171.0 0.342	456.0 0.912
L = 3.17	70.4 0.127	211.1 0.380	562.9 1.013
L = 3.48	85.1 0.139	255.4 0.418	
L = 3.80	101.3 0.152	304.0 0.456	

The interaction of synthetic jets with a boundary layer presented in this section are illustrated by the dye patterns captured from two orthogonal views, as described in

section 3.2.1. For each case, the images consist of a side (upper portion) and a plane (lower portion) view of the wall. It should be noted that the structures in the two views are generated at the same condition but not taken simultaneously due to a lack of suitable orthogonal lenses. However, as the image sequences at the two views are taken from the same phase of an actuation cycle, the images can be matched manually by aligning the positions of the orifice in two views. For the images in the plane view, a shadow of the structure is observed due to the set up of the light source as shown in section 3.2.1. The flow direction is from right to left and the dash line marked on the side view indicates the edge of the boundary layer. The Phase of the images shown is arbitrarily chosen to illustrate the main flow features. For simplicity, the cases presented are grouped according to *St* and are shown in the order of increasing *L*, Re_L and *VR*, as a result of an increasing diaphragm displacement.

5.1.2 *St* = 0.04 Synthetic Jets

Figure 5.1 shows the dye flow visualisation patterns at *St* = 0.04 with *L* ranging from 1.27 to 3.8. The formation of a hairpin vortex is observed about the centreline region, with the (spanwise) vortex head located at various x/D_o from 5 to 7 for different *L*. Due to the small *St* (large streamwise spacing), only one hairpin vortex is observed in the measurement area. Due to the low *VR* for all the cases, the hairpin vortex resides in the boundary layer with the trailing portion of its counter-rotating legs attached to the wall, which are thus subject to strong streamwise stretching under the influence of shear in the boundary layer. With an increase of *VR* from 0.051 (figure 5.1a) to 0.152 (figure 5.1d), the distance that the vortex penetrates into the boundary layer increases from $1D_o$ to $2D_o$. And from the side view, as Re_L increases the vortex head becomes stronger which is indicated by the vortex head being visibly larger and the rotation behaviour of the vortex head becoming more obvious. This in turns results in a stronger induced velocity produced by the vortex head which gives rise to an evident lift-up of both vortex head and the leading portion of the legs.

In addition to the hairpin vortex, the plane view shows the development of two dye concentrations. These appear laterally to either side of the darker concentration of dye entrained into the hairpin legs and appear to persist far downstream. The dye concentrations are secondary longitudinal vortex pair, which formed inboard of the hairpin legs due to the initial large lateral displacement of the hairpin legs. Fluid upwash that is induced from the wall inboard of the counter-rotating legs of the hairpin vortices

and fluid downwash towards the wall due to continuity (to replace fluid that is lifted-up from the wall) combine to cause the formation of saddle point in the middle of the hairpin vortex. The flow pattern of the upwash and downwash is represented from a spanwise (y-z) perspective, illustrated by the schematic in figure 5.2. For the present study, the central regions devoid of dye in the plane view of figure 5.1 are believed to correspond to the saddle point.

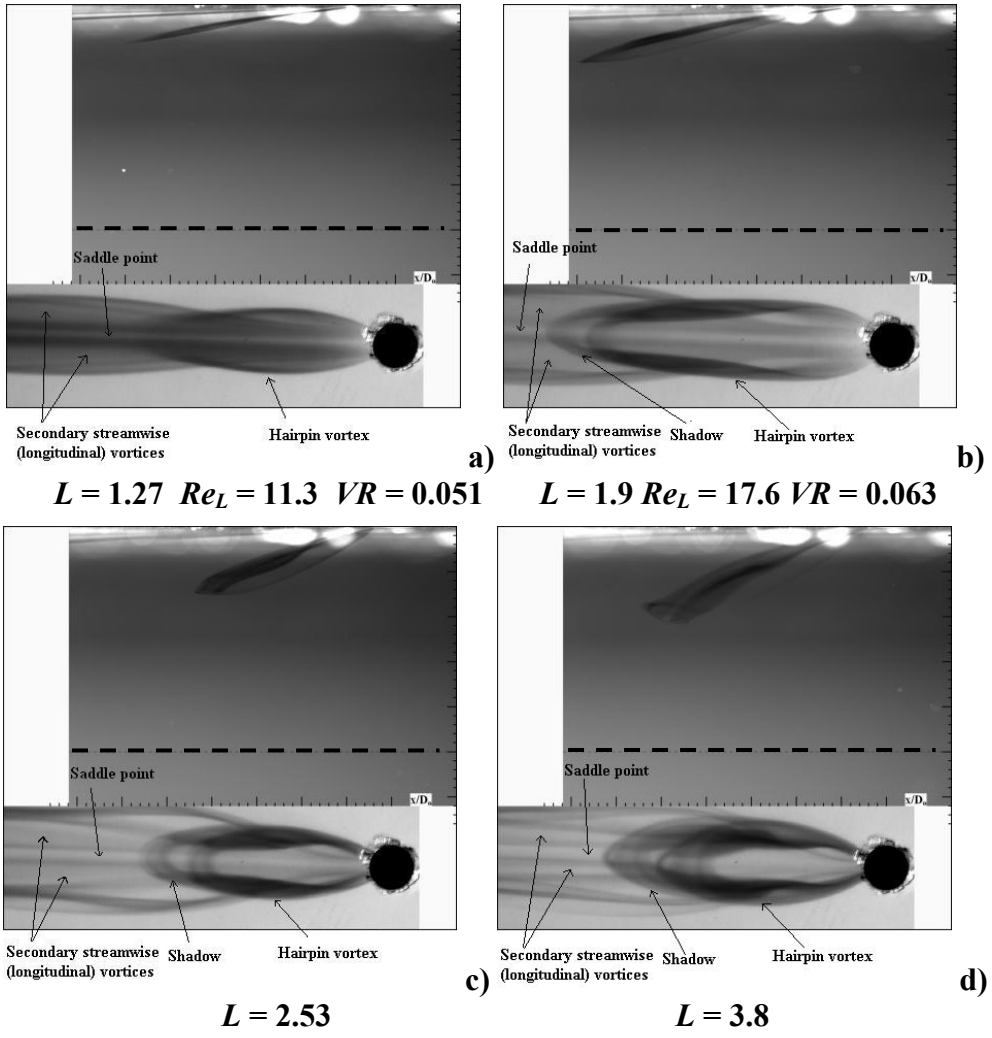

Figure 5.1 Jet formation at $St = 0.04$ and various dimensionless stroke length a) $L = 1.27$; b) $L = 1.9$; c) $L = 2.53$ and d) $L = 3.8$

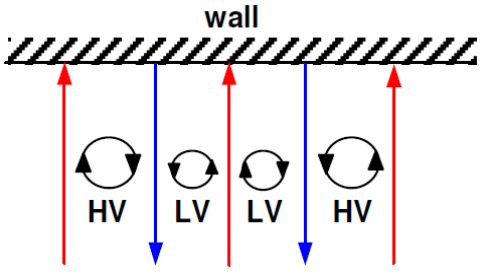

Figure 5.2 Schematic showing regions of downwash (red arrow) and upwash (blue arrow) associated with a hairpin vortex (HV) and longitudinal vortex (LV) pair

5.1.3 St = 0.12 Synthetic Jets

Figure 5.3 shows the synthetic jets formed at St = 0.12. In these cases, both Re_L and VR = 0.152 are higher than those at the corresponding L due to the higher diaphragm oscillation frequency used.

For L = 1.27, Re_L = 33.8 and VR = 0.152 (figure 5.3a), the synthetic jet consists of an agglomeration of hair vortices that remain embedded close to the wall. The close connection of these structures due to the increase in St is analogous to a quasi-steady, streamwise vortex pair created near to the wall. The relative low strength of these vortices is evident by the insignificant lift up of the vortex heads, caused by the relative dominance of the mean shear over self-induction (note that the inclination of the vortex heads form the wall is approximately the same as the inclination pertaining to the legs). Consequently, the high local shear impedes the evolution of the tip of the hairpins such that they appear to be parabolic in shape. As St Increases, the spatial distance between successive vortex rings becomes small, thereby producing strong interactions between vortices that reduce their penetration into the boundary layer. Compared with the cases at the same VR (0.152) and St = 0.04 (figure 5.1d), the jet penetration is reduced from for the case in is $2D_o$ to $1.2D_o$

Unlike the cases shown in figure 5.1, it is believed that the dye concentrations, appeared in between the hairpin vortices in the surface view in figure 5.3a and 5.3b, are not longitudinal vortices. By examining the whole cycle of the development of the jet, it is found the dye concentrations are in fact the counter-rotating legs of the hairpin vortex structures downstream. Jabbal (2008) explained the longitudinal vortices may not be seen at a higher VR since there is no dye near the wall due to the increased penetration of the hairpins vortices. Since the penetration of the hairpins into the boundary layer for the case in figure 5.3a and 5.3b is smaller than that in figure 5.1d, it is believed that there may be some dye near the wall. Therefore, the longitudinal vortices may be non-existent or too weak to entrain any dye from the orifice in the case.

Figure 5.3c shows the propagation of hairpin vortices, which undergo intense stretching as they propagate downstream. The hairpin vortex is a three-dimensional structure characterised by two streamwise components (counter-rotating legs) and a spanwise component (vortex head) of vorticity, which bridges the legs at the tip. The upstream branch is suppressed by a combination of the resident vorticity in the boundary layer and the suction stroke since L is relatively low. The mutual induction

effects caused the forward portion of the legs and the head of the hairpin to move away from the wall as the vortex convect downstream. In doing so, the upper portions of the legs migrate across the boundary layer and as the trailing portions of the legs connect back to the wall, the latter undergo extreme stretching by the local velocity gradient. This stretching process increases the concentration of the vorticity in the core of the legs, which causes the legs to move rapidly together due to image-vortex effects, as illustrated in figure 5.4.

The different rates of migration and stretching of different portions of the hairpin are due to the presence of the boundary and its varying velocity gradient. Consequently, the vortex head and the leading portions of the legs continue to migrate through the boundary layer owing to mutual induction, while the trailing portions of the legs remain attached to the wall and thus subject to extreme stretching by the local velocity gradient pertaining to a high level of shear.

The inclination of the hairpin vortices (shown in figure 5.5 for zoom-out view) from the wall is due to the opposing effects of self-induced velocity that moves the leading portion of the hairpins away from the wall and the shear in the boundary layer, which tends to rotate them back to the wall. Head and Bandyopadhyay (1981) in their studies of hairpin vortices in fully turbulent boundary layers suggest that the angle at which the hairpin reaches equilibrium will be the result of the interaction between these two opposing effects. For the third hairpin vortex in figure 5.5, the tilt angles various from approximately 13° at the trailing portion of the legs to approximately 60° at the tip of the vortex head. This is consistent with the variations in tilt reported by Haidari and Smith (1994) for hairpin vortices in laminar flow (6° and 67° variation between the trailing legs and vortex head) and by Zhou *et al* (1999) for hairpin vortices in turbulent flow (8° to 75° variation between the trailing legs and vortex head).

Figure 5.3d shows vortex formation at $L = 2.22$, $Re_L = 103.4$ and $VR = 0.27$. The vortical structures exhibit several differences to the hairpin structures observed in figure 5.3c. Due to the increase in Re_L, the cores of the vortex heads are visibly larger and exhibit a more well defined roll-up than those pertaining to the previous hairpin vortices. Due to the increase in VR, the structures penetrate deeper into the boundary layer while the counter-rotating legs still reside within the boundary layer and thus remain subject to streamwise stretching. Since VR gives an indication of the relative strength between jet and the incoming freestream flow in terms of velocity, an increase in VR will result in a vortical structure which is less affected by the freestream. For this reason, it was

shown, for the first time, the initial appearance of the upstream branch pertaining to the forming vortical structure, which was suppressed in the previous three cases. Nevertheless, the upstream branch is eventually suppressed due to the resident shear, as well as the effect of suction since the structure does not move sufficiently far from the orifice during the blowing cycle before the onset of the suction due to the low L for this case. The formation process is shown in figure 5.6, which is a close-up view of the vortical structure. Consequently, this results in an asymmetric structure (a hairpin vortex) albeit over a longer formation timescale than the previous cases.

Figure 5.3e similarly shows the appearance of the upstream branch pertaining to the vortical structure forming at L = 2.53, Re_L = 135.1 and VR = 0.304. This upstream branch appears stronger than that observed in figure 5.3d and consequently persists for a longer time period. Partly, this is due to the higher Re_L hence increasing the strength of the vortex relative to that in figure 5.3d, which is evidently captured in a stronger vortex head. It is also due to the larger L, which ensures the structure moves further from the orifice during the blowing stroke such that the effect of suction on vortex formation is expected to be negligible. As a result, the upstream branch is weakened only by the resident boundary layer vorticity and not suction, as shown in figure 5.7. As the structure convects downstream, the upstream branch is cancelled out by the resident boundary layer vorticity since the structure remains in the boundary layer.

It is believed that the presence of these trailing structures could be due to the fluid that has not been entrained into the leading vortex ring as it is formed. At the onset of blowing cycle, the shear layers along the orifice walls separate at the orifice exit and begin to roll up. A vortex ring is formed by the maximum blowing phase. Consequently, trailing fluid cannot be further entrained into the vortex ring due to its relatively slower moving velocity than the ring itself. It is therefore believed that the trailing jet shear layers pushed out of the orifice during the remainder of the blowing stroke are bent into the freestream to form a pair of streamwise, counter-rotating vortices. It is also evident from this case that the trailing streamwise vortices remain attached to the vortex ring and extend back to the near wall region during the entirety of their propagation through the boundary layer.

Figure 5.3f shows the structures formed at L = 3.8, Re_L = 101.3 and VR = 0.152. It can be seen from the side view that a symmetrical vortical structure is formed under this condition, in which the upstream branch is retained and remains comparable in strength to the downstream branch. The reason can be attributed to the increase of VR,

which results in increased jet velocity strength, making it more resistance to the freestream flow. The greater resistance ensures a steeper penetration into and subsequently out of the boundary layer. It is also observed that the increase in Re_L results in the development of prevalent vortex rollers. Consequently the vortex ring, unlike the hairpin vortices, is not subject to significant stretching by shear due to its relatively short resident time in the boundary layer. However, the exception happens to the trailing streamwise vortices, as shown in figure 5.8. The column of dye trailing the vortex ring represents the jet shear layers that are pushed out of the orifice, from T1 to T3. And it is confirmed from the instant T4 to T6 that the trailing jet fluid is bent into the freestream direction, which combines with streamwise stretching, forms streamwise vortices that are similar in appearance to the previously observed hairpin legs.

The arbitrary instants T4 to T6 in figure 5.8 show the extent of anticlockwise vortex tilting of the leading vortex as the structure convects downstream. Due to the large extent of tilting observed for this vortex ring, it is duly referred to as a tilted vortex ring. The phenomenon of vortex tilting has previously been observed for pulsed jets (Chang and Vakili, 1995) and synthetic jets (Zhong *et al*, 2005). A vortex model to explain the mechanism of vortex tilting was described by Zhong *et al* (2005) and for clarity is reproduced in figure 5.9 and 5.10.

When a vortex ring fully emerges from the orifice, it has a vertical velocity component U_y, which is essentially the jet velocity and a very small streamwise velocity component U_x, which can be approximated as zero, shown in figure 5.9a. The upstream and downstream part of this ring can be modelled as a pair of vortex rollers placed in a parallel stream. The velocity of this parallel stream U_r is the resultant velocity of U_y and the local velocity U in the boundary layer, shown in figure 5.9b. Due to its circulation, each roller will be subject to a Magnus force, as illustrated in figure 5.9b. The Magnus effect is the phenomenon whereby a spinning object flying in a fluid creates a whirlpool of fluid around itself, and experiences a force perpendicular to the line of motion. The overall behaviour is similar to that around an aerofoil with a circulation which is generated by the mechanical rotation, rather than by aerofoil action. The Magnus force produces a rotational moment around the centre of the vortex ring causing the ring to tilt in an anti-clockwise direction.

At the same time, there is a strong interaction between the vortex ring and the surrounding fluid flow such that the vortex ring accelerates in the streamwise direction and loses its initial momentum in the vertical direction. As a result, the magnitude of the

Magnus force will reduce accordingly. Tilting stops when the Magnus force that exerts on the upstream and downstream rollers lies in the plane of the ring, figure 5.10b. The whole process occurs within a streamwise distance of about ten orifice diameters.

Further downstream, the vortex ring will remain at a constant inclination angle as it propagates with the freestream flow under the influence of its own self induced velocity, figure 5.9a. This agrees with the present observation of tilted vortex rings shown in figure 5.3f and figure 5.8.

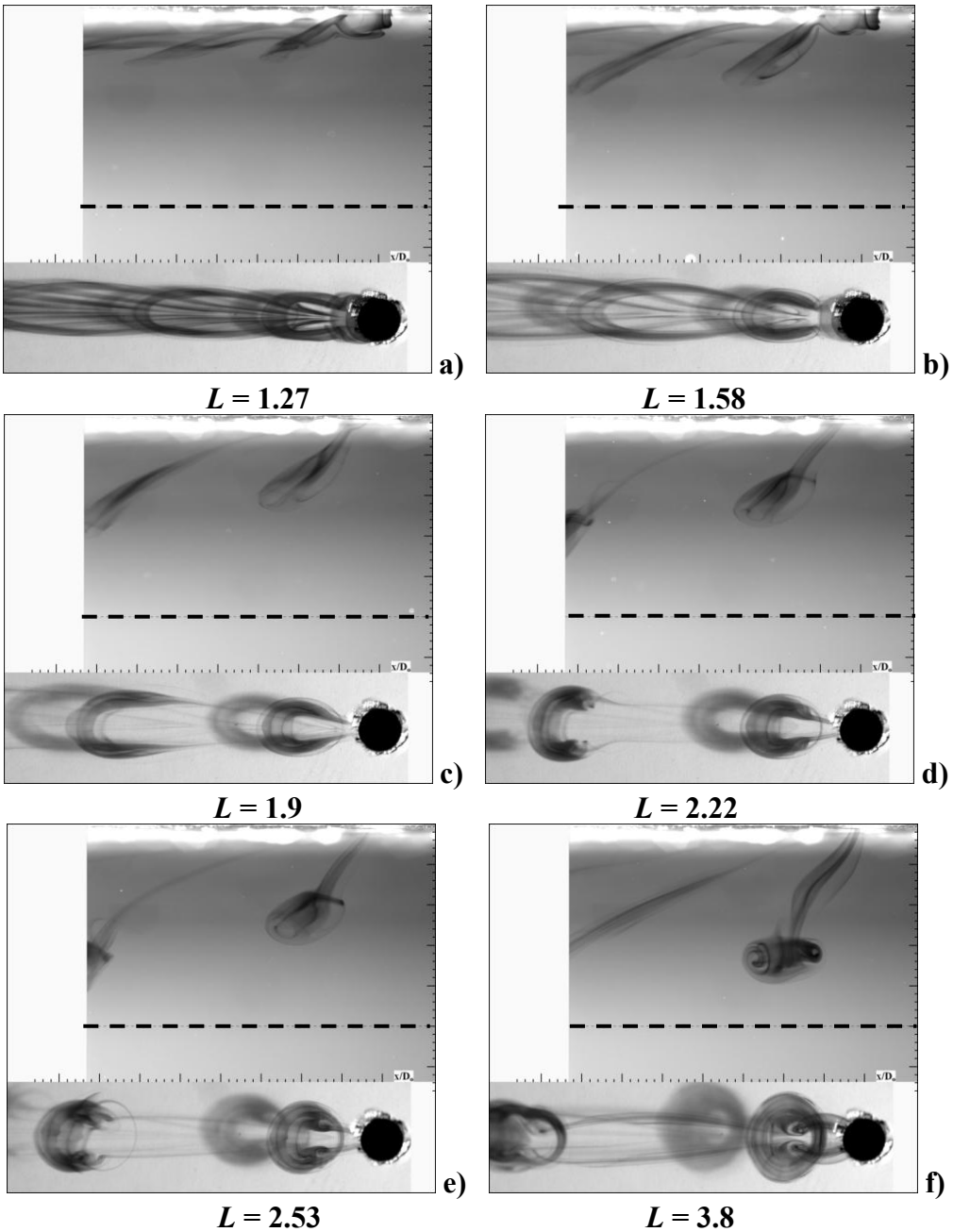

Figure 5.3 Jet formation at *St* = 0.12 and various dimensionless stroke length a) *L* = 1.27 to f) *L* = 3.8

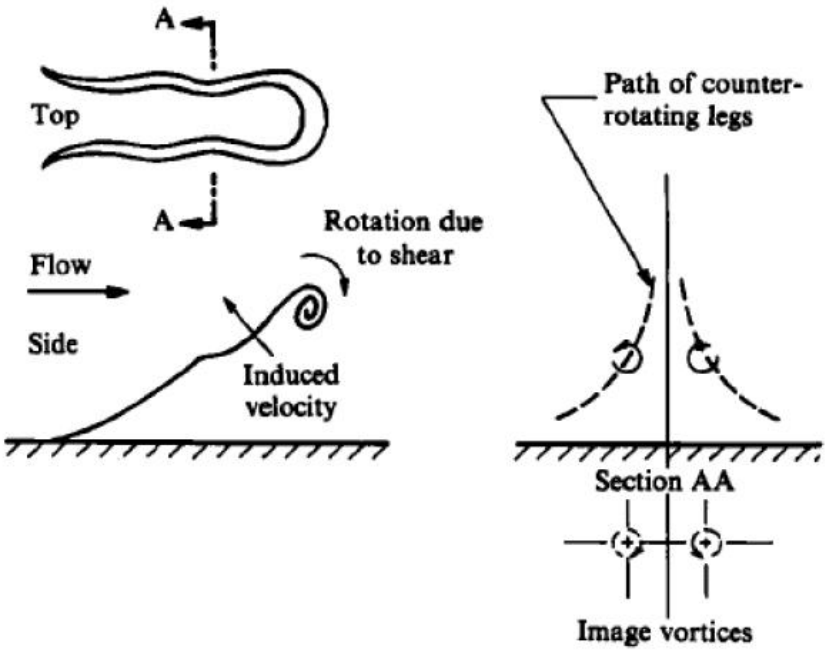

Figure 5.4 Schematic of the portion of the legs migrating together as they lift-up from the surface (Acarlar and Smith, 1987)

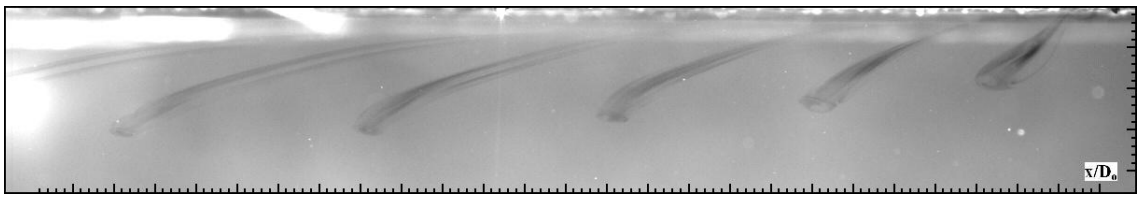

Figure 5.5 Zoom-out view of the jet formation shown in figure 5.3c

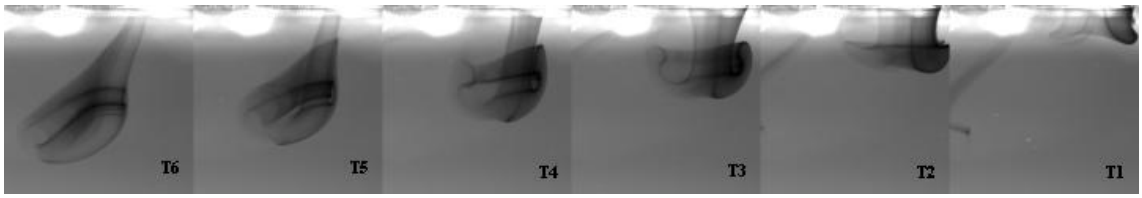

Figure 5.6 Close-up view of development of vortical structure shown in figure 5.3d

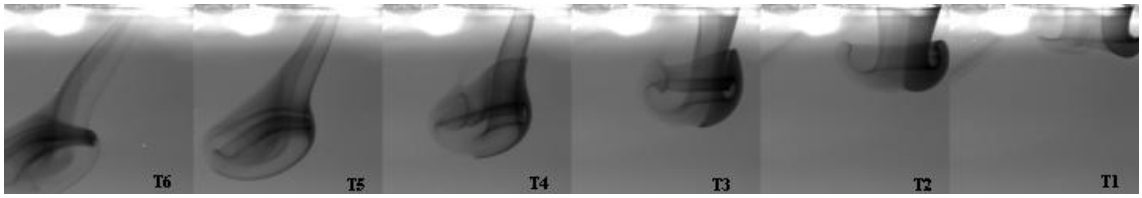

Figure 5.7 Close-up view of development of vortical structure shown in figure 5.3e

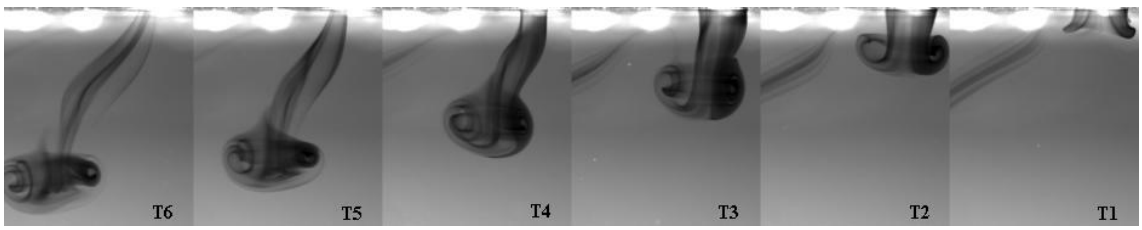

Figure 5.8 Close-up view of development of vortical structure shown in figure 5.3f

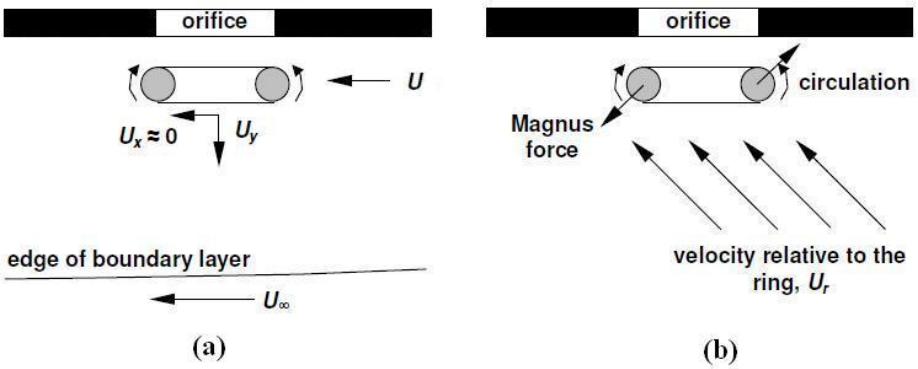

Figure 5.9 A vortex ring as it emerges from the orifice. a) Velocity components in stationary coordinates; b) Flow velocity relative to the ring and Magnus forces acting on it (Modified from Zhong *et al*, 2005)

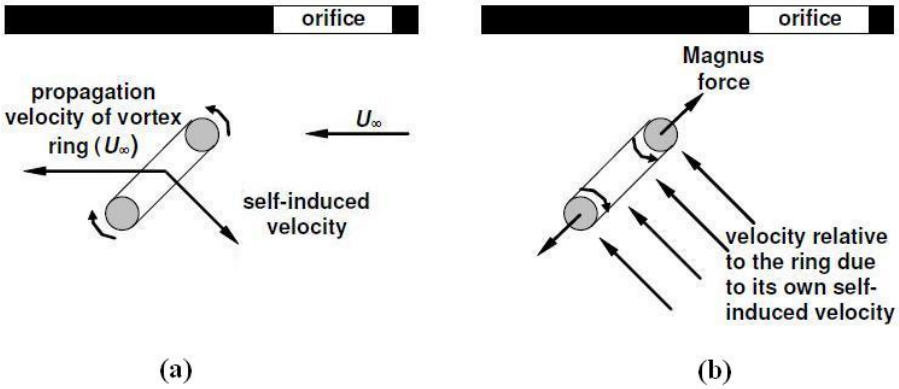

Figure 5.10 A vortex ring as it reaches its stable orientation. a) Velocity components in stationary coordinates; b) Flow velocity relative to the ring and Magnus forces acting on it (Modified from Zhong *et al*, 2005)

5.1.4 *St* = 0.32 Synthetic Jets

Figure 5.11 shows the vortical structures generated at St = 0.32 with a stroke length L varying from 1.58 to 3.17. For L = 1.58, Re_L = 140.7 and VR = 0.507 (figure 5.11a), these vortices penetrate the boundary layer at a short distance downstream ($x/D_o \approx 6$) and as a consequence are not subject to streamwise stretching due to the short resident time in the boundary layer. There is also evidence of anti-clockwise vortex tilting as the structures convect downstream, with a mean vortex inclination of approximately 45°. The mechanism of the vortex tilting has been discussed in section 5.1.3, as shown in figure 5.9 and 5.10. From the surface view, it can be seen that these structures are closed vortex rings. The vortex rings are connected at their trailing legs by two, highly stretched, leg-like structures, which are entrained into the adjacent upstream vortex rings, unlike the vortex rings in figure 5.3f, which extend back into the near wall region. The presence of the trailing structures could be due to the fluid that has not been

entrained into the leading vortex ring as it is formed, like those structures shown in figure 5.3e.

The development of the vortical structures is shown in figure 5.12. At T1, a symmetrical vortical structure is forming. And it can be seen that the trailing structures from the previous cycle are just underneath of the forming vortical structure and are highly stretched due to the resident shear. At T2, the trailing structures moves to underneath the downstream branch of the forming vortical structures, which has an induced velocity toward to the wall. The instant T3 to T6 confirms that the trailing structures are entrained inside the downstream branch of the forming vortical structures.

At L = 1.9, Re_L = 202.6 and VR = 0.608 (figure 5.11b), the distance between adjacent vortical structures increases due to the increase of L. Those vortices penetrate the boundary layer at a shorter distance downstream ($x/D_o \approx 3.5$) due to the increased VR. It can be seen that the trailing structures are still entrained into the adjacent downstream vortical structures. As L increases further to 2.53 and 3.17, it can be seen that the distance between the adjacent vortical structures increases.

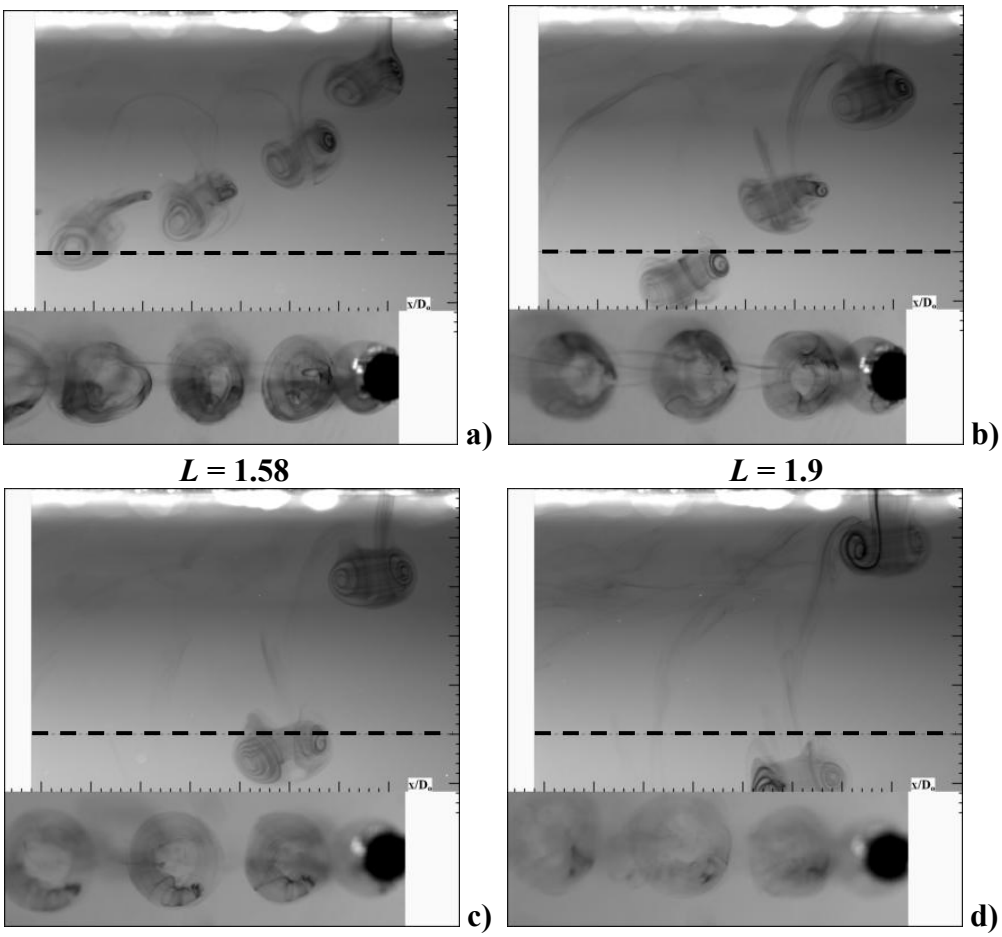

a) ***L*** **= 1.58** **b)** ***L*** **= 1.9**

c) ***L*** **= 2.53** **d)** ***L*** **= 3.17**

Figure 5.11 Jet formation at *St* = 0.32 and various dimensionless stroke length from a) *L* = 1.58 to d) *L* = 3.17

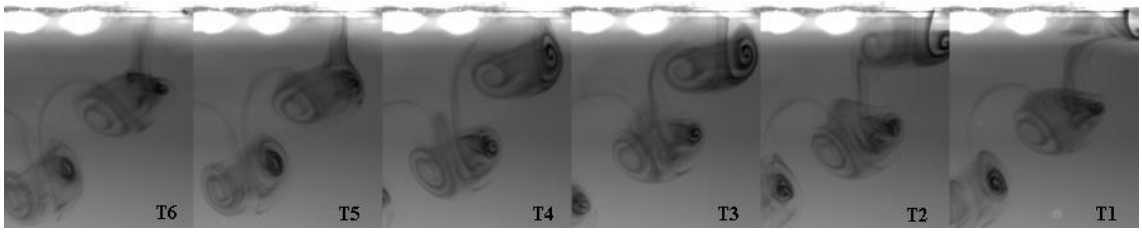

Figure 5.12 Close-up view of development of vortical structure shown in figure 5.11a

5.2 Interaction between Adjacent Synthetic Jets in an Array

In this part, in order to assess the level of interaction between the jets in a synthetic jet array with jet spacing $3D_o$, the development of the jet array in the quiescent flow is first examined. Then the performance of a single synthetic jet and a synthetic jet array with the same dimensionless parameters, namely Stroke length L and Strouhal Number St, is compared under different actuation conditions. Finally, the trajectory of the jet array in the boundary layer is also studied. Laser induced florescence flow visualization technique was used to reveal the general characteristics of the vortical structures produced by the synthetic jet and the jet array.

5.2.1 Interaction between Synthetic Jets in Quiescent Flow

Figure 5.13 shows the whole cycle of the development of synthetic jet array at S = 11.6 and L = 3.0. Within the visualisation area, six structures are observed in one column, which are generated from the same orifice. The one nearer the orifice (at the top of the image) is produced by the present cycle and the others further downstream are produced by the previous cycles. The phase points are chosen with the same intervals, starting from the instant when the jets just emerge from the orifice. It can be seen that the five structures in the same row are similar to each other at the start of the formation at instant t1. Vortex roll-up is observed at t2. And the distance that the structures propagate downstream from the orifice is almost the same for all of the structures. At t3, the vortex rings are fully formed, each having identical shape and size. This indicates the vortex rings have similar performance characteristics. After the start of the suction cycle at t4, the vortical structures propagate downstream with the induced velocity. And the structures are not affected by the suction cycle and still have the identical shape and size at t5. When the whole cycle finishes at t6, the vortical structures are still identical.

The above discussion is based on the structures generated in the present cycle. From the structures produced in the previous cycle, it can be seen that the three vortical

structures in the middle are identical with each other, but the vortical structures at both sides are slightly titled. It is believed that it is caused by the velocity difference between the inner side and the outer side. The followed discussion is based on the vortical structure on the left of the image (Note that for the vortical structure on the left of the image, the inner side means the right side of the structure and the outer side means the left side of the structure). The half vortical ring on the outside is slowed down due to the viscous effect of the fluid on the left at still. This behaviour causes an asymmetrical pattern of the series of vortex rings. Similar phenomenon is observed for the vortex rings on the rightmost side.

Figure 5.14 shows the comparison of the vortical structures produced at various operating parameters from the synthetic jet arrays. The Stokes number S ranges from 10.0 to 16.4, and dimensionless stroke length L from 2 to 4. In general, the five vortical structures on the first row in every image are identical with each other despite of the difference in the operating parameters. At L = 2, the pattern of the series of vortical structures on both sides inclines towards the middle, which is believed to be caused by the asymmetric induced velocity field that they are subject to, as discussed above. At L = 3, the vortical structures at further downstream become unstable due to the strong interaction with the increase of the Stokes number (S) at 14.2 and 16.4. And similar turbulent vortical structures are observed for all the cases at L = 4.

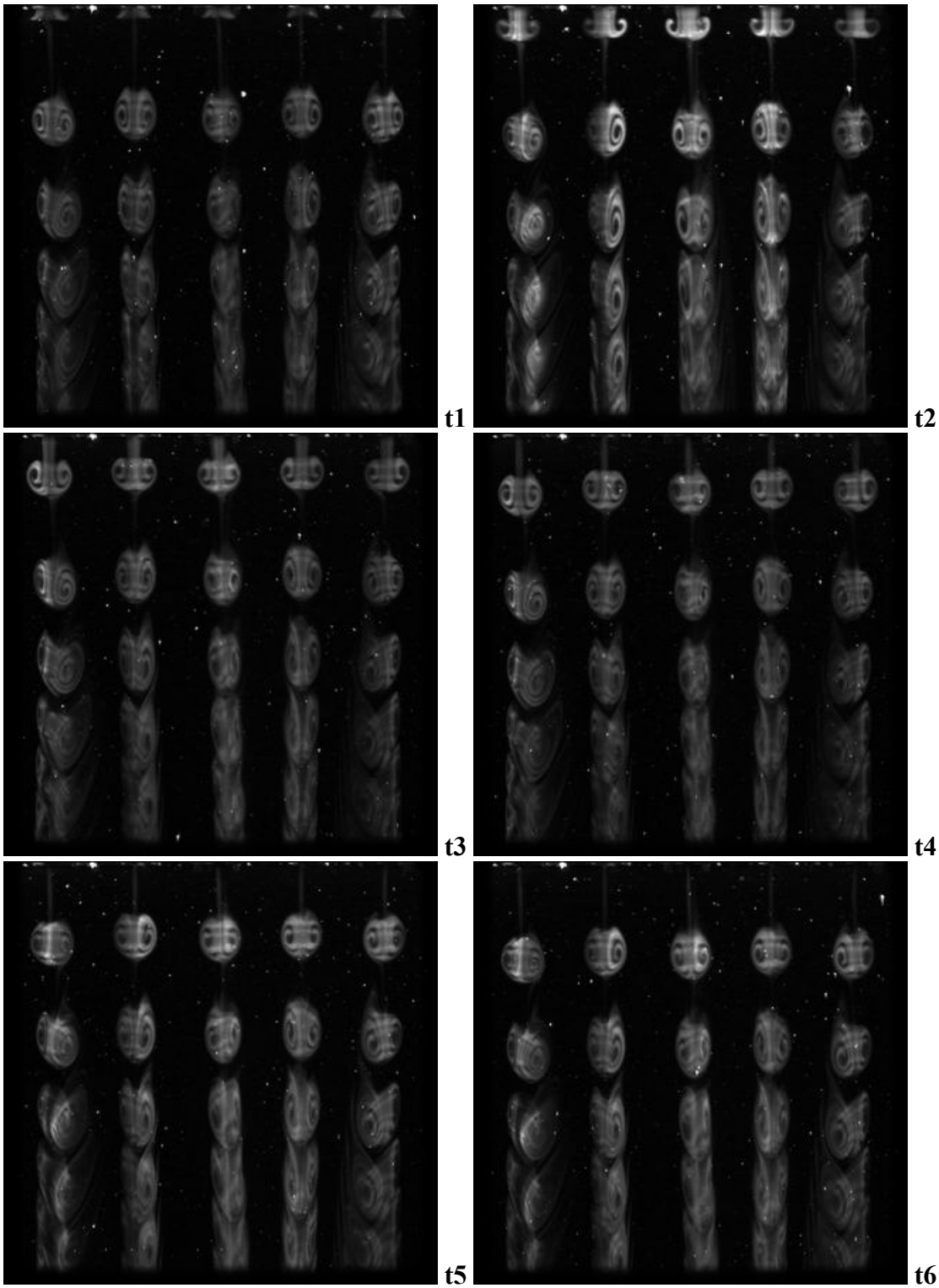

Figure 5.13 Development of synthetic jets array at six phase points at S = 11.6 and L = 3.0

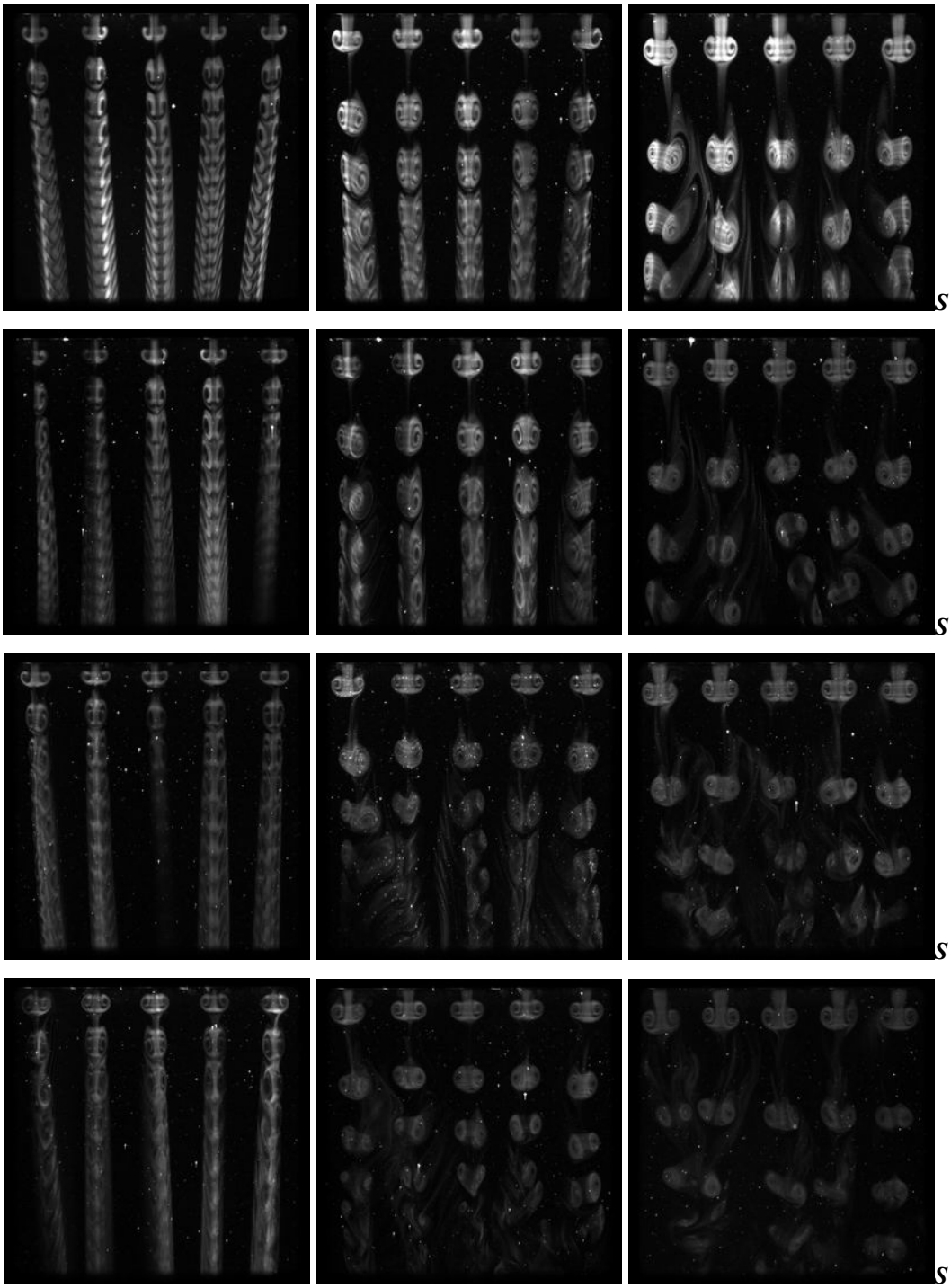

Figure 5.14 Comparison of synthetic jets from jet array at various operation conditions

5.2.2 Comparison of a Single Synthetic Jet and a Synthetic Jet Array in Quiescent Flow

Figure 5.15 shows the comparison of the whole cycle of the development of a single jet and a synthetic jet array. The images are not captured simultaneous in the experiment and are combined together by post-processing. The structures on the left side of the white line are produced by the single jet and those on the right from the synthetic jet array. Only three of five jets in the array are captured and shown in order to get the close-view of the structures. The jet nearest to the white line is the middle one of the five jets. The structures near the orifice (at the top of the image) are produced by the current cycle and the others are produced by the previous cycle.

At t1, the structures are just produced from the orifice and there is no difference observed. At t2, structures with roll-up are observe with no obvious difference between these from the single jet and jet array. And the distance the structures travel from the orifice are almost the same. With the development of the structures, it can be seen that the structure from the single jet travels slightly further downstream than these from the jet array at t3. This becomes more and more obvious as the structures travel downstream (see in t4 and t5), indicating that the single jet moves a bit faster than the jet in the jet array. At the end of the current cycle at t6, the structure from the single jet has travelled about $0.5D_o$ further downstream than those from the jet array. It is believed that each vortex ring in the array will experience an induced velocity which is produced by the adjacent rings. Since this induced velocity is pointing towards to the orifice exits, it will slow down the vortex rings.

Figure 5.16 shows the comparison between the single structure and array structures produced at various operation parameters. It can be seen for $L = 4$ that the structure from the single jet travels farther than the structures from the array do at both $S = 11.6$ and $S = 11.4$. However, for the smaller dimensionless stroke length $L = 2$, there is no obvious difference between the structure from the single jet and the structures from jet array for both $S = 11.6$ and $S = 11.4$. As discussed in section 4.1.3, the dimensionless stroke length has a great effect on the formation of the synthetic jet. The elongated structures shown in figure 5.38 for $L = 2$ indicates that the structures are effected by the presence of the inverse flow formed during the suction cycle. Since the structures are elongated, the distance between the side of each vortex ring and the

nearest side of an adjacent ring increase, which is likely to result in less interaction between the adjacent rings.

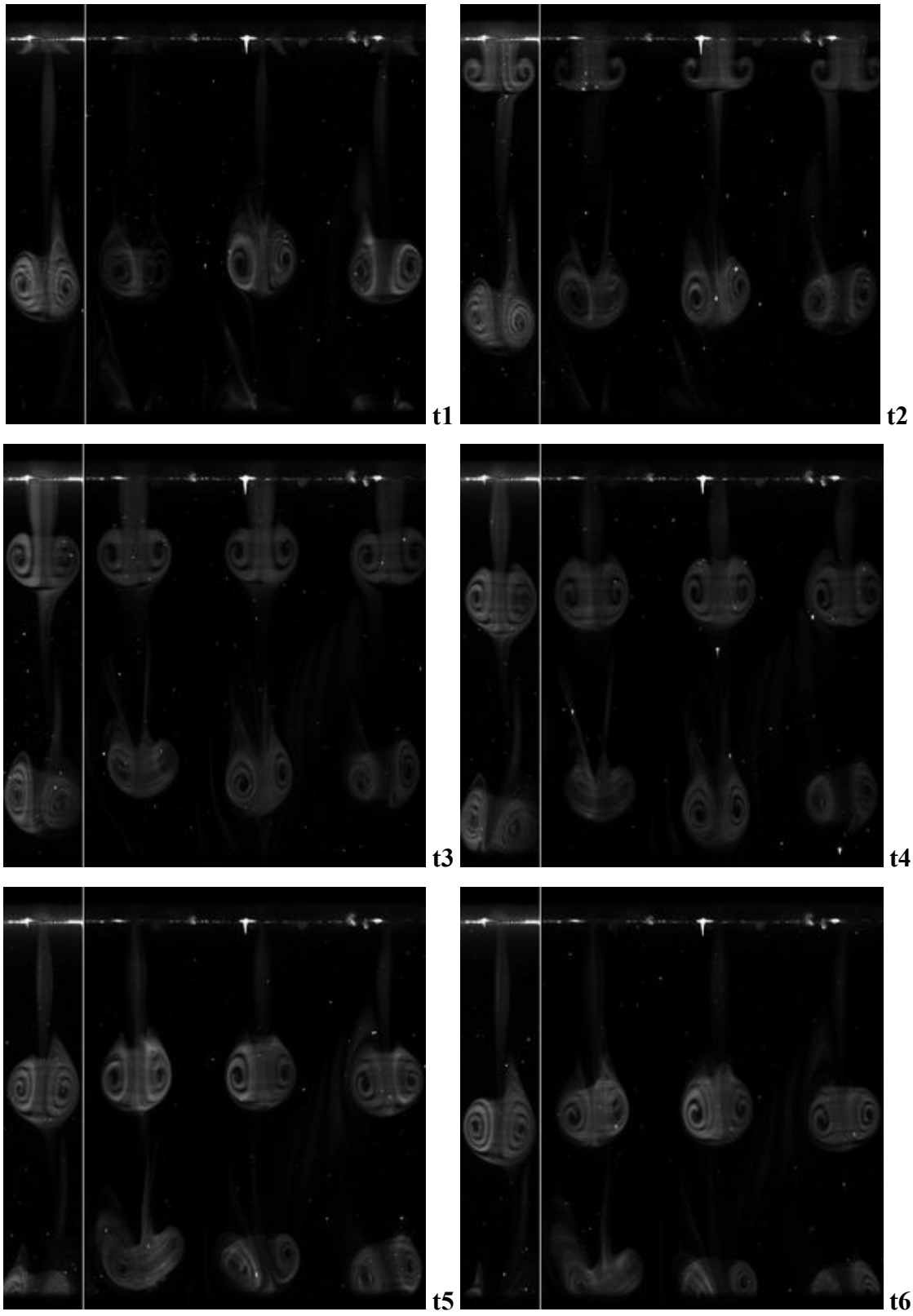

Figure 5.15 Comparison between one orifice and five orifices at S = 11.6 and L = 4

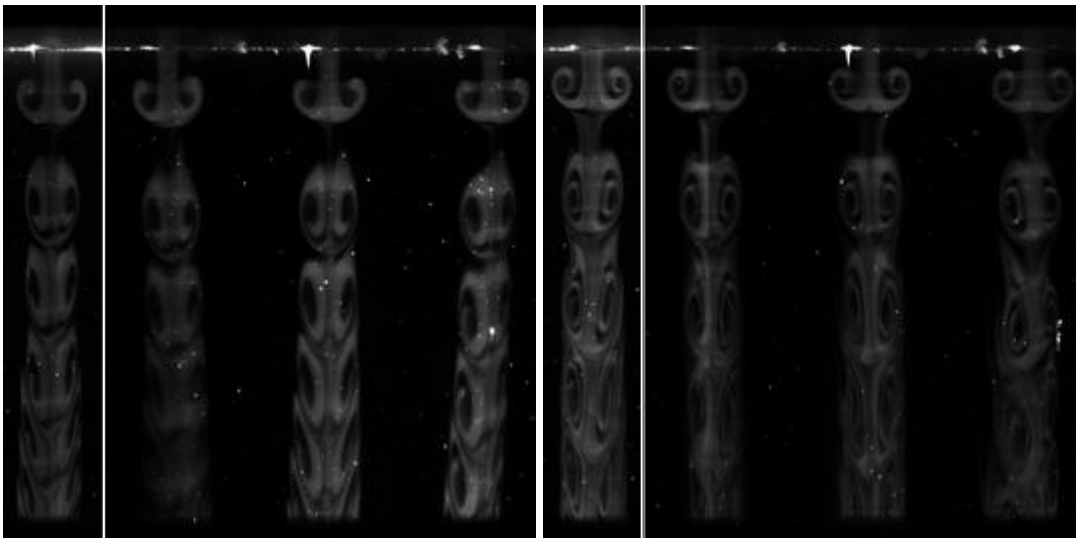

***L* = 2 *S* = 11.6** **$L = 2$ $S = 16.4$**

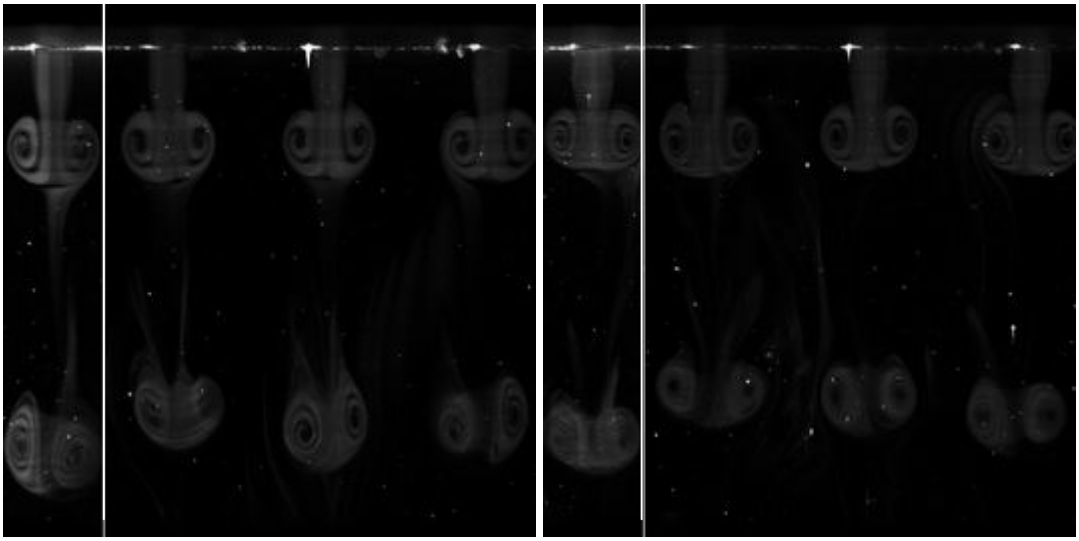

***L* = 4 *S* = 11.6** **$L = 4$ $S = 16.4$**

Figure 5.16 Comparison of single structure and array structures produced at various operating parameters

5.2.3 Trajectory of Vortical Structures in a Boundary Layer

In this part, the trajectory of vortical structures produced by the single jet and the jet array in a boundary layer is studied. The velocity of the cross flow is fixed at 0.1m/s and the frequency of the synthetic jet is set at 6 and 12Hz and the corresponding Strouhal number (*St*) is 0.12 and 0.24. The non-dimensional stroke length ranges from 2 to 4 and the corresponding velocity ratio varies from 0.24 to 0.96. Since the velocity of the cross flow is fixed, an increase in the dimensionless stroke length will results in an increases in the velocity ratio for the current tests.

Figure 5.17 shows the comparison between the trajectory of the structures from the single jet and the jet array in a boundary layer at various dimensionless stroke lengths at $St = 0.12$. For each case, four images are shown: the two images in the first row are from the single jet and those on the second row are from the five-jet array; the two images on the left side are the averaged images over two cycles, which are used to analysis the trajectory of the structures, and the image on the right side are the instantaneous images, used to compare the structures. Scales in D_o are shown in each image in both the streamwise and the transverse direction. The dash line marked at 5 D_o indicates the edge of the boundary layer.

From the trajectory shown in the averaged images at $L = 2.5$, it can be seen that the structure from the single jet moves out the observed region at about $4.5D_o$ and those from the jet array at $4.3D_o$ (note that the dye trajectory close to the test surface is from the wake of the structures). The small difference in the trajectory indicates there is little interaction between the vortical structures issued from the jet array at this condition. Hairpin vortical structures are observed for both cases on the instantaneous image, although the structures are more like stretched vortex ring in the first cycle. And it can be seen from the left most structures on the instantaneous image that the structures of jet array travel further downstream than that of the single jet, which are $22D_o$ and $20.5D_o$ respectively. It indicates that the structures from the jet array moves faster than those from the single jet. As the trajectory of the structures from both the single jet and jet array is very similar, the structures would be expect to propagate downstream at a similar velocity if the boundary layer velocity is identical in these two cases. The difference in the convection velocity of the structures implies that the vortical structures have affected the velocity distribution of the boundary layer to different degrees in these two cases. It is very likely that due to the larger number of jets in the jet array, the structures produced from the jet array have more capability to bring high-momentum fluid from the outer boundary layer to the inner boundary layer, which results in a higher local velocity.

As the L increases to 3.0, the trajectory becomes steeper for both the single jet and the jet array. The distance from the wall when the jet exits the measurement window on the left increases to $6.5D_o$ for the single jet and $6D_o$ for the jet array. For the same reason mentioned above, the structures from the jet array moves faster in the streamwise direction than those from the single jet. At $L = 3.5$, distance from the wall when the jet exits the measurement window on the left increases to $7.0D_o$ for the single

jet, however, the exit position of the jet array drops a little to $5.5D_o$ for the jet array. It is likely that this decrease is caused by the interaction between the adjacent vortical structures, under which the induced velocity pushes the vortical structures closer to the wall. Although the vortical structures from the jet array still move faster in the streamwise direction than these from the single jet, it can be seen the difference is smaller at this case. It is assumed that to bring the fluid closer to the boundary consumes more momentum, therefore less momentum for the vortical structures to travel in the streamwise direction. At $L = 4.0$, the trajectory becomes steeper as the jet exit position increases to $8D_o$ for the single jet as expected. However, the trajectory for the jet array increases to $7.5D_o$ rather than drop further, although the interaction between adjacent structures is supposed to enhance. As a result, the difference of travel distance in the streamwise direction becomes bigger between the single jet and the jet array.

Interestingly, the trajectories of the wake of the structures appear similar for the single jet or jet array with the exit position is fixed at about $2D_o$ for all the cases shown in figure 5.17. The reason behind this behaviour could be the relatively weak strength of the wake of the structures.

Figure 5.18 shows the comparison of trajectory at $St = 0.24$. Due to the high velocity ratio, the jet exit position reaches $6D_o$ for the single jet and $5D_o$ for the jet array at $L = 2$. Comparing with the same velocity ratio at $St = 0.12$ and $L = 4$ with the jet exit point at $8D_o$ and $7.5D_o$ respectively, the trajectory is less steep for high Strouhal number $St = 0.24$ for both the single jet and the jet array. A higher Strouhal number produces smaller streamwise spacing between consecutive structures, therefore increasing the interaction between them, resulting in reduced penetration. At the same time, the structures produced at a higher Strouhal number have more ability for generation of roll-up, increasing the interaction with the boundary layer, resulting in reduced penetration as well. This is supported by Chang and Vakili (1995) in their studies of vortex rings formed by the pulsed jet in a uniform cross flow. As L increases further up to 3.5, the trajectories go steeper and steeper with the jet exit point moving beyond the test region and $10D_o$ for the single jet and the jet array respectively. Unlike what happened at $St = 0.12$ that the jet exit point drops at $L = 3.5$, the jet exit point for all the cases at $St = 0.24$ keeps going further from the wall. The behaviour that the structures from the jet array stay closer to the wall but move faster in the streamwise direction than those from the single jet is also observed for all the cases in figure 5.18.

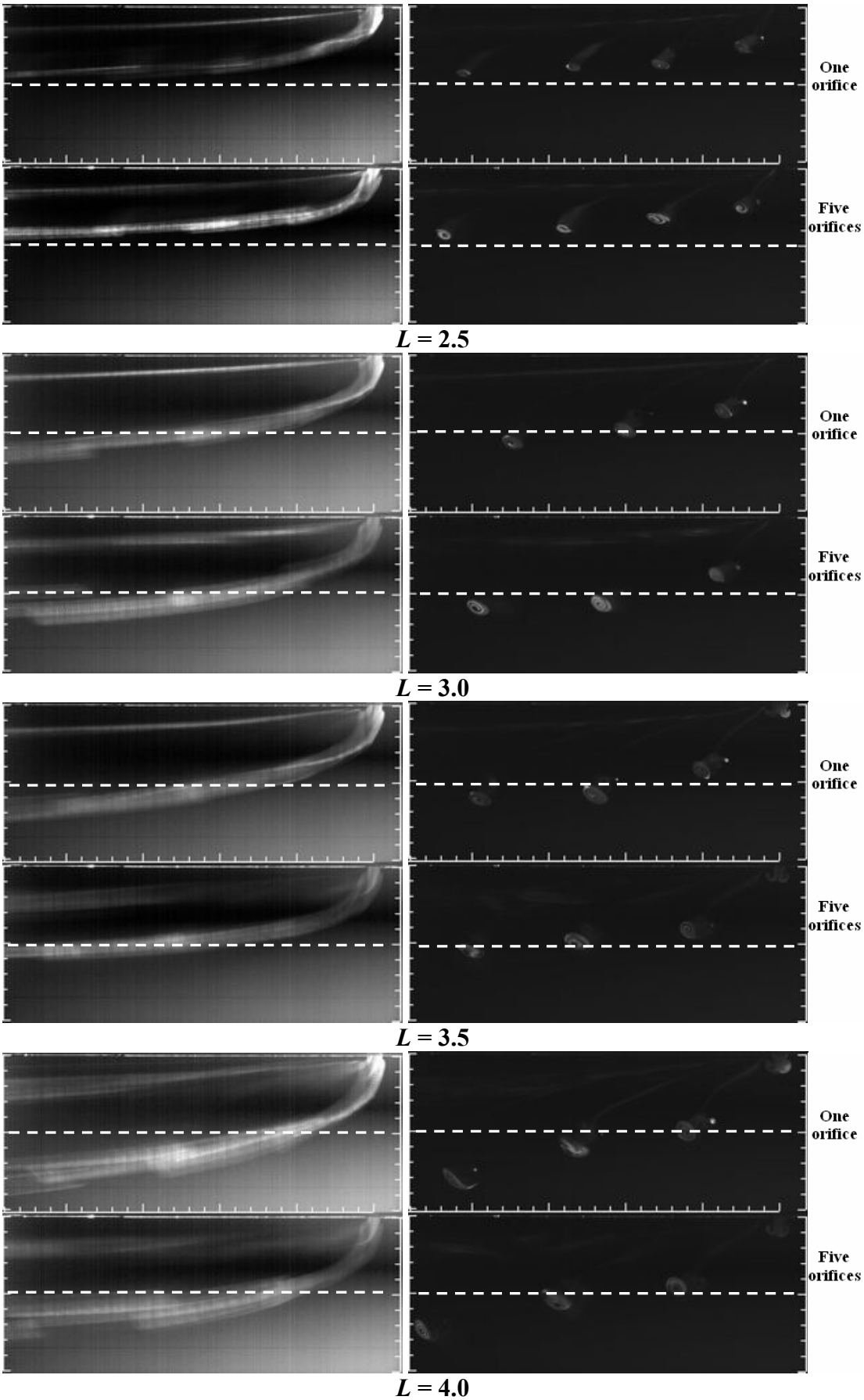

Figure 5.17 Comparison of trajectory and vortical structures produced at St = 0.12

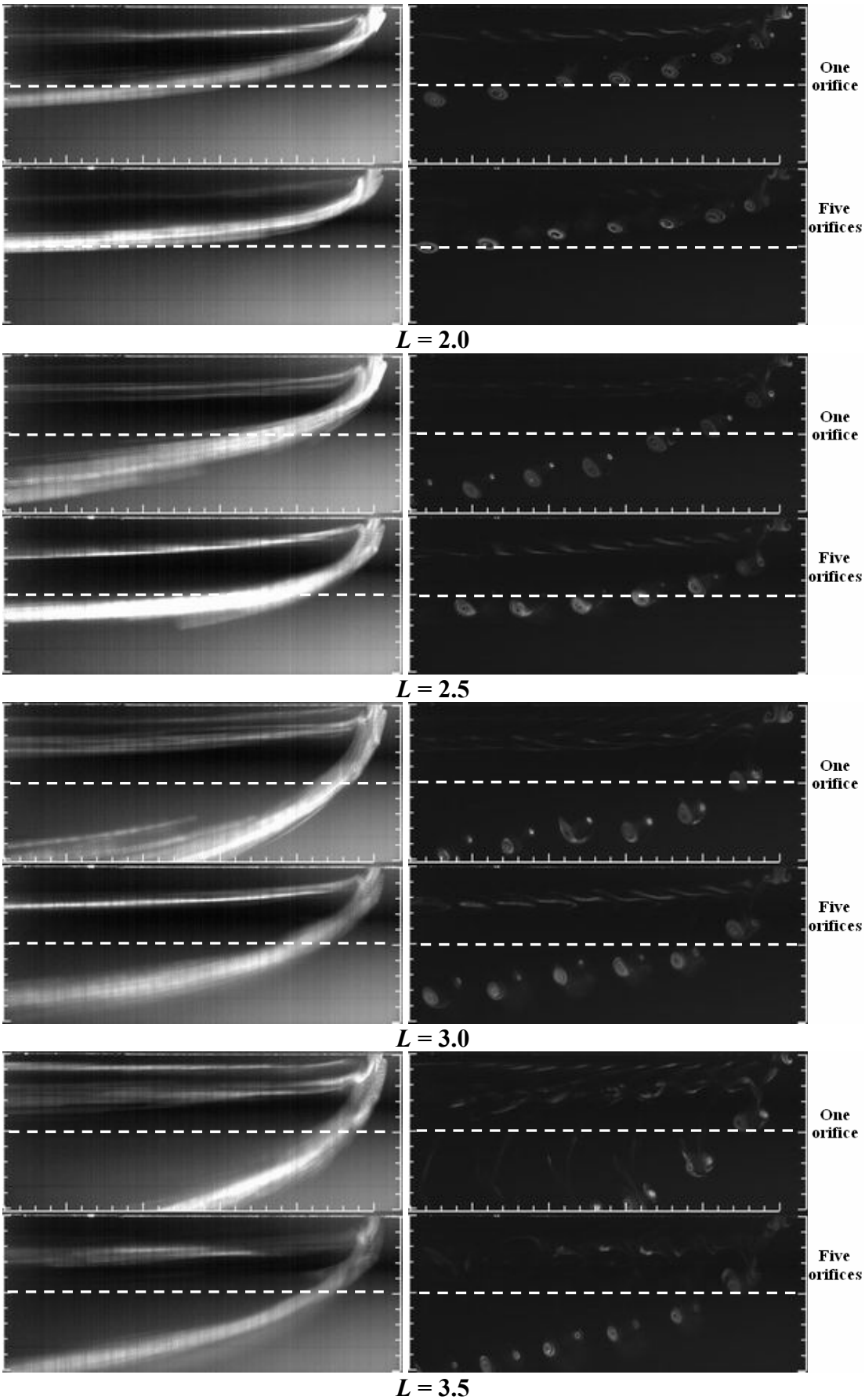

Figure 5.18 Comparison of trajectory and vortical structures produced at St = 0.24

5.3 Summary of Finding

As described herein, flow visualisation of synthetic jets utilising dye in a flat plate laminar boundary layer, and flow visualisation of synthetic jets utilising florescent dye in both quiescent and cross flow, have been undertaken for a rang of synthetic operating parameters. The purpose of this work was to study the nature of the vortical structures produced as a result of the interaction with a zero-pressure gradient laminar boundary layer, and to assess the level of interaction between the jets in a synthetic jet array. To summarise the findings from the investigation, it has been found that

- It has been identified that three types of vortical structures are produced as a result of the interaction of a synthetic jet with a laminar boundary layer, which are hairpin vortices, stretched vortex rings and tilted vortex rings.
- Hairpin vortices and stretched vortex rings experience an asymmetric development, as the upstream branches of the vortices are weakened by the vorticity in the boundary layer. Conversely, tilted and distorted vortex rings experience a symmetrical development due to increased jet strength.
- The experiment in quiescent condition shows that the interaction between adjacent synthetic jets is negligible for the first cycle, but become more obvious as the structures move downstream.
- Comparing with structures from the single jet under the same dimensionless operating parameters, those from the jet array travel slower due to the induced velocity produced by the adjacent rings, which on certain degree depends on the dimensionless stroke length.
- It has been shown that the trajectory of vortical structures from single jet and jet array is different due to the interaction between the adjacent synthetic jets and the interaction between the jets and the boundary layer.

6 Control Effect of Flow Separation over a Flap

The aim of this chapter is to investigate the effect of a synthetic jet array in delaying flow separation in a laminar flow over a flap in water. Three experiments have been carried out. The LIF visualisation experiment allows the flow control effect on the central plane of the middle synthetic jet to be assessed. The PIV measurements on the same plane provide quantitative information of the velocity field in the separated flow. Finally, PIV measurements on a spanwise plane parallel to the flap are undertaken to resolve the 3D interaction between the synthetic jet array and the separated flow.

6.1 General Test Condition

The test plate and the synthetic jet array have been described in section 3.1.2.2 and 3.1.2.3 respectively. The actuator consists of a cylindrical cavity with diameter, D_c = 45 mm and height, H = 10 mm. The synthetic jet array consists of five orifices aligned normally to the flow direction, each with a diameter of D_o = 2 mm and a depth of 2 mm, spaced 6mm ($3D_o$) apart.

All the tests are performed in the tilting flume at a freestream velocity of 0.1m/s. The freestream turbulent intensity was about 1%. A boundary layer profile at a distance of 5 mm upstream of the synthetic jets was extracted from the velocity field, as shown in figure 3.31. The behaviour of synthetic jets issued into the boundary layer is determined by the Reynolds number defined based on the stroke length (Re_L), the dimensionless stroke length L and the velocity ratio VR. To investigate the effectiveness of the synthetic jets at various operational conditions, the oscillating frequency (f) of the diaphragm is varied from 2 to 16 Hz with an increment of 2 Hz and the displacement is varied independently from the frequency to yield a dimensionless stroke length (L) from 2 to 9. These settings result in a velocity ratio (VR) ranges from 0.08 to 1.28, a Reynolds number (Re_L) ranges from 28 to 898 and a Strouhal number ranges from 0.04 to 0.32 .

In the present setup, the frequency of T-S wave is estimated to be 0.6Hz. Since the minimum actuator operating frequency is about two times higher (except at 1Hz), the synthetic jets are not expected to trigger the boundary layer instability. The dimensionless actuation frequency $\overline{f} = fc/U_\infty$ based on the length of the inclined plate c is in the range of 2 to 32.

6.2 Flow Visualisation Results

6.2.1 The Baseline Flow

In the present setup, a rubber sheet is used to provide a smooth transition from the horizontal plane to the 5° inclined plate. Dye was injected from a 1 mm diameter port located on the central plane of the inclined plate and at 20mm upstream to start of the inclined plate, to reveal the location of the separation region in the baseline case without actuation of the synthetic jets. The injection speed of the dye is kept to minimum to ensure the dye follows the separation line where the speed is zero. A typical LIF visualisation image is shown in figure 6.1. It can be seen that the inclined plate and the dye line, which extends from upstream, forms an envelope of the separated region. Therefore, the angle of the dye line formed with the plate surface can be taken as a measure of the effect of separation control which indicates the approximate height of the separation region.

An angle α is defined as the angle formed between the dye line at the baseline condition and the horizontal direction indicated in white, as shown in figure 6.1. Only one image is used since the separation region revealed by the sequence of image appears quite stable at the baseline condition. In this experiment, α is constant and equal to 1.5° for all the cases.

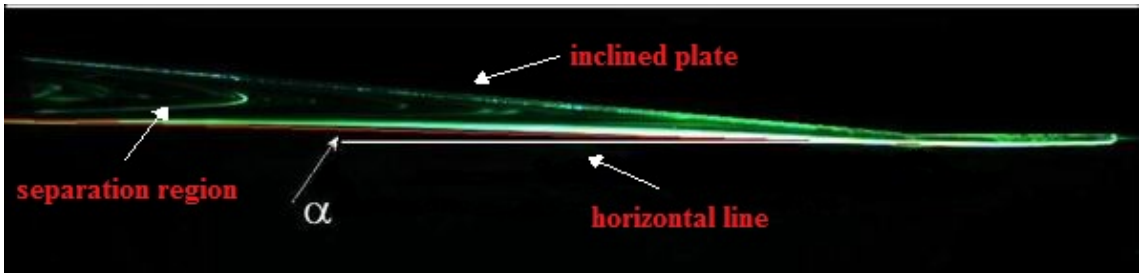

Figure 6.1 LIF visualisation of the flow separation region over the inclined plate in the baseline case (The flow is from right to left)

6.2.2 Controlled Cases

In order to evaluate the control effectiveness of synthetic jets operating at different conditions, the inclined angle of the dye line in the controlled cases is examined. When the synthetic jet array is running, the dyeline fluctuates as the vortical structures pass by. Therefore the images of the separation region are time-averaged to determine the angle of the dye line. Figure 6.2 shows an instantaneous image and the time-averaged image of a typical controlled case. In the controlled cases, dye is also injected into the

synthetic jet cavity, allowing the vortical structures of the synthetic jet to be visualised. These vortical structures can be seen clearly in the instantaneous image. In the time-averaged image, the vortical structures at different phases during the actuation cycle are superimposed with each other, showing the trajectory of their motion.

The dye line marking the boundary of the separated flow region still appears well defined in the time-averaged image. An angle β is defined as the angle formed between the dye line under the controlled conditions and the horizontal direction, see figure 6.2. Therefore, the effectiveness of the control effect can be evaluated by the percentage ratio between the change in the inclined angle of the dye line and the included angle of the separated region in the baseline case,

$$C_e = \frac{\beta - \alpha}{\gamma - \alpha} \times 100\% \qquad \textbf{Eq. 6-1}$$

Here all angles are in degrees. As the inclined angle of the flap $\gamma = 5°$ and the inclined angle in the baseline case $\alpha = 1.5°$, Equation 6.1 can be expressed as:

$$C_e = (\frac{\beta - 1.5}{3.5}) \times 100\% \qquad \textbf{Eq. 6-2}$$

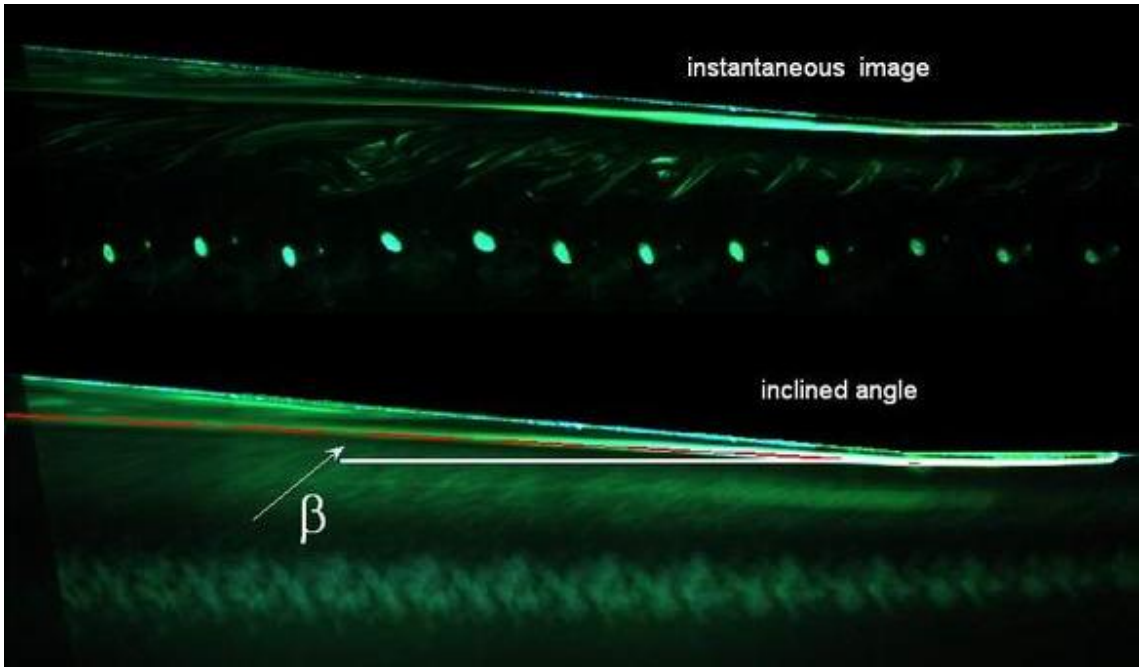

Figure 6.2 Indication of the inclined angle at the controlled condition

Figures 6.3 to 6.7 show the images at different dimensionless stroke lengths for Strouhal number *St* = 0.04, 0.08, 0.16, 0.24 and 0.32. At each dimensionless stroke length, two images are shown； the top one is the instantaneous image revealing the vortical structures which are responsible for the separation delay whereas the bottom

one is the time-averaged image from which the inclined angle of the dye line is determined. The dye line marks the boundary of the separated flow region is indicated by red line. To aid the qualitative comparison of the flow control effect, the location of the boundary in the baseline case is shown as a blue line.

From figure 6.3, it can be seen that at St = 0.04, there is no obvious control effect with L = 2.0, 2.5, 3.0 and 4.0 since the location of the separated flow boundary indicated by the dye line almost coincides with that in the baseline case. The flow control effectiveness is found to be 5.7%, 8.6%, 8.6% and 11.7% respectively based on the value of β = 1.7°, 1.8°, 1.8° and 2.1°. The low VR (from 0.08 to 0.16) in these cases are believed to be the main reason for the weak control effect. As L increases from 5 to 8 and VR from 0.2 to 0.32, the control effect becomes more obvious and the inclined angle of the separation line increases from 2.3° to 3.4°, with an increase in the control effectiveness from 22.9% to 71.4%. From the instantaneous images, it can be seen that the vortical structures at L < 5 are weak and highly stretched streamwise features. As L increases beyond 5, the head of these structures becomes pronounced and these structures appear to be stronger and rise further into the incoming flow. These structures are believed to hairpin vortices which are typically observed at low velocity ratios. As the freestream velocity is fixed in this experiment, at a given diaphragm actuation frequency, a higher L corresponds to a higher VR. As L and VR increases, the vortical stronger structures become stronger, which consequently push the separation line closer to the inclined plate.

At St = 0.08 Hz, there is no obvious control effect at L = 2 and VR = 0.16, as shown in figure 6.4. As L increases from 3 to 5 (VR from 0.24 to 0.4), the separation region becomes smaller and the control effect effectiveness increases from 28.6% to 74.3%. Interestingly, as L increases from 5 to 6, the effectiveness reduces from 74.3% to 68.6%. From the instantaneous images, it can be seen that compared with the vortical structures at St = 0.04, at St = 0.08 the strength of the structures increases quicker as L increases. This is because at the same L the jet velocity hence the velocity ratio is higher at a higher actuation frequency. Nevertheless, the vortical structures observed at St = 0.04 are still hairpin type of structures. The reason that the flow control effectiveness decreases as L increases from 5 to 6, is believed to be caused by a reduced impact due to an increased distance of the vortical structures to the near wall region. This indicates that in order to get a good control effect, the vortical structure needs to stay reasonably close to the wall.

At St = 0.16, a visible control effect is seen at L = 2 (VR = 0.32) as shown in figure 6.5 with a control effectiveness of C_e = 34.3%. As L increases, the control effectiveness firstly decreases at L = 3 (C_e = 28.6%). It then increases to C_e = 51.4% as L increases further to 5 and stays almost constant when L increases to 6. From the instantaneous images, it is seen that at L = 2 the vortical structures produced by the synthetic jets are typical hairpin vortices. These structures are transformed into typical tilted vortex ring type structures as L increases to 3 with the vortex rings within these structures clearly visible. These structures remain to be tilted vortex rings as L increases to 6, although these structures become more distorted. It is believed that the slight decrease in the flow control effectiveness at L is caused by the switching between the type of vortical structures from hairpin vortices to tilted vortex rings and the relatively weak strength of the tilted vortex rings at a low L. As L increases, the tilted vortex ring type of structures gains strength hence produces strong flow control effect. It is worth noting the considerable flow control effect of the tilted vortex ring type structures despite of the large distance between the vortex rings and the separated flow region, Based on the CFD simulation results of Zhou and Zhong (2009), these type of structures also have their own secondary and tertiary structures which are trailing behind the vortex ring and located nearer to the wall. It is the tertiary structures which are in the form of streamwise counter-rotating vortices that entrain fast moving fluid to the near-wall region and are responsible for the delay of flow separation.

At St = 0.24, the vortical structures also are seen to experience a switching from hairpin vortex to tilted vortex rings type of structures at L = 3, shown in figure 6.6. The flow control effectiveness is observed to be the highest L = 2 (C_e = 45.7%) and deduces to C_e =28.6% at L = 3 and 4. The drop in C_e at L = 3 and 4 despite of the structures being stronger is believed to be caused by the further distance of these structures to the separated flow region as a result of a higher VR.

Similar to the case at St = 0.24, at St = 0.32, a pronounced control effect is observed at L = 2 and VR = 0.48 (C_e = 45.67%), as shown in figure 6.7. The control effectiveness reduces at L = 3 (C_e = 28.6%) and stays unchanged at L = 4.

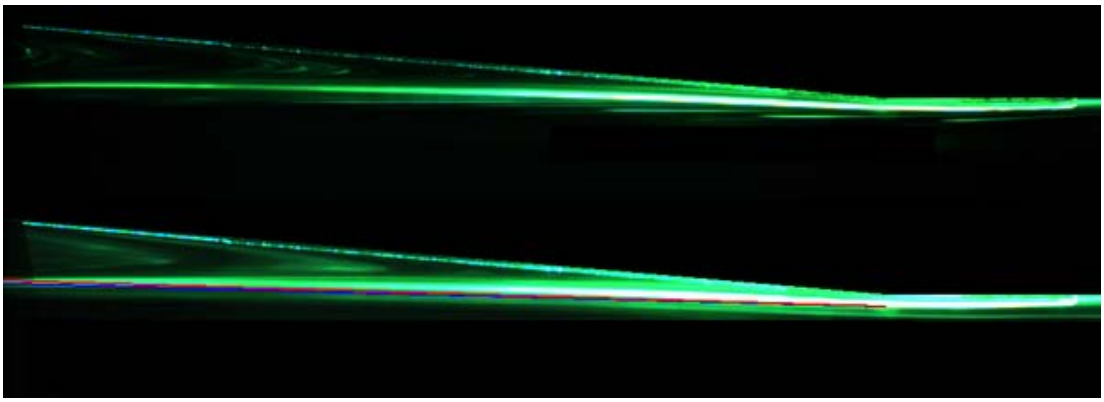

a)

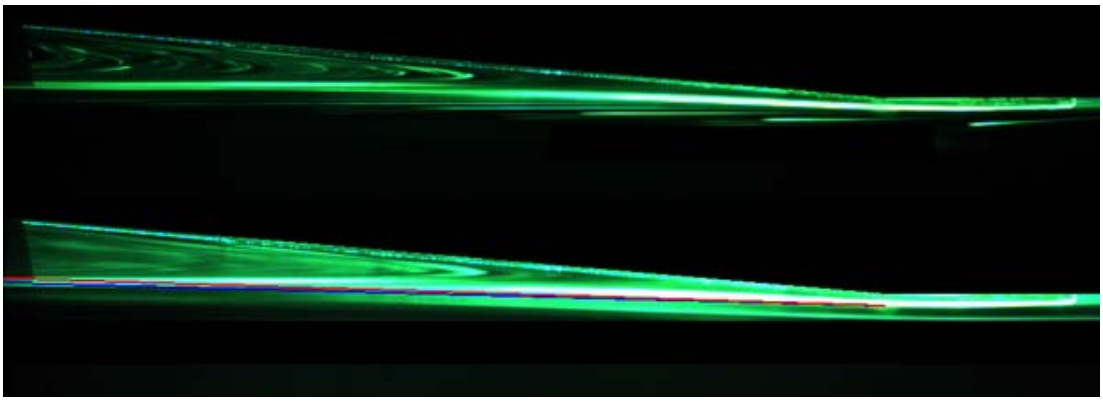

b)

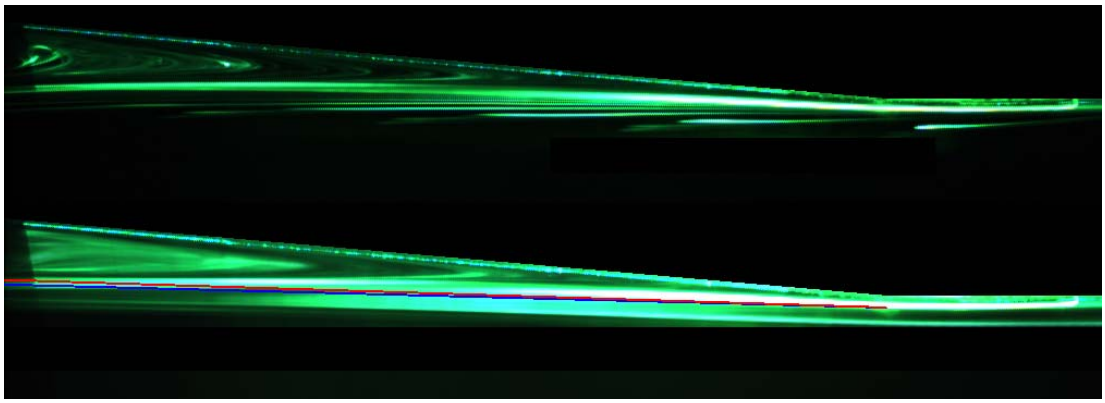

c)

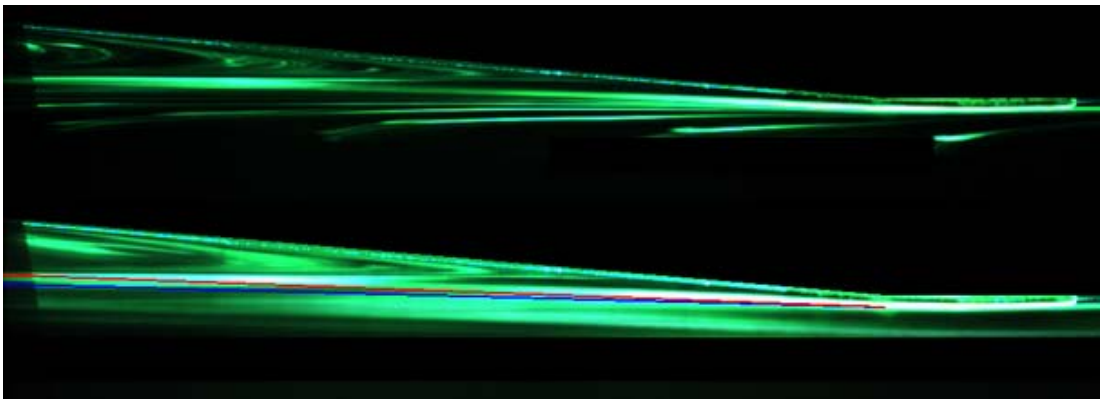

d)

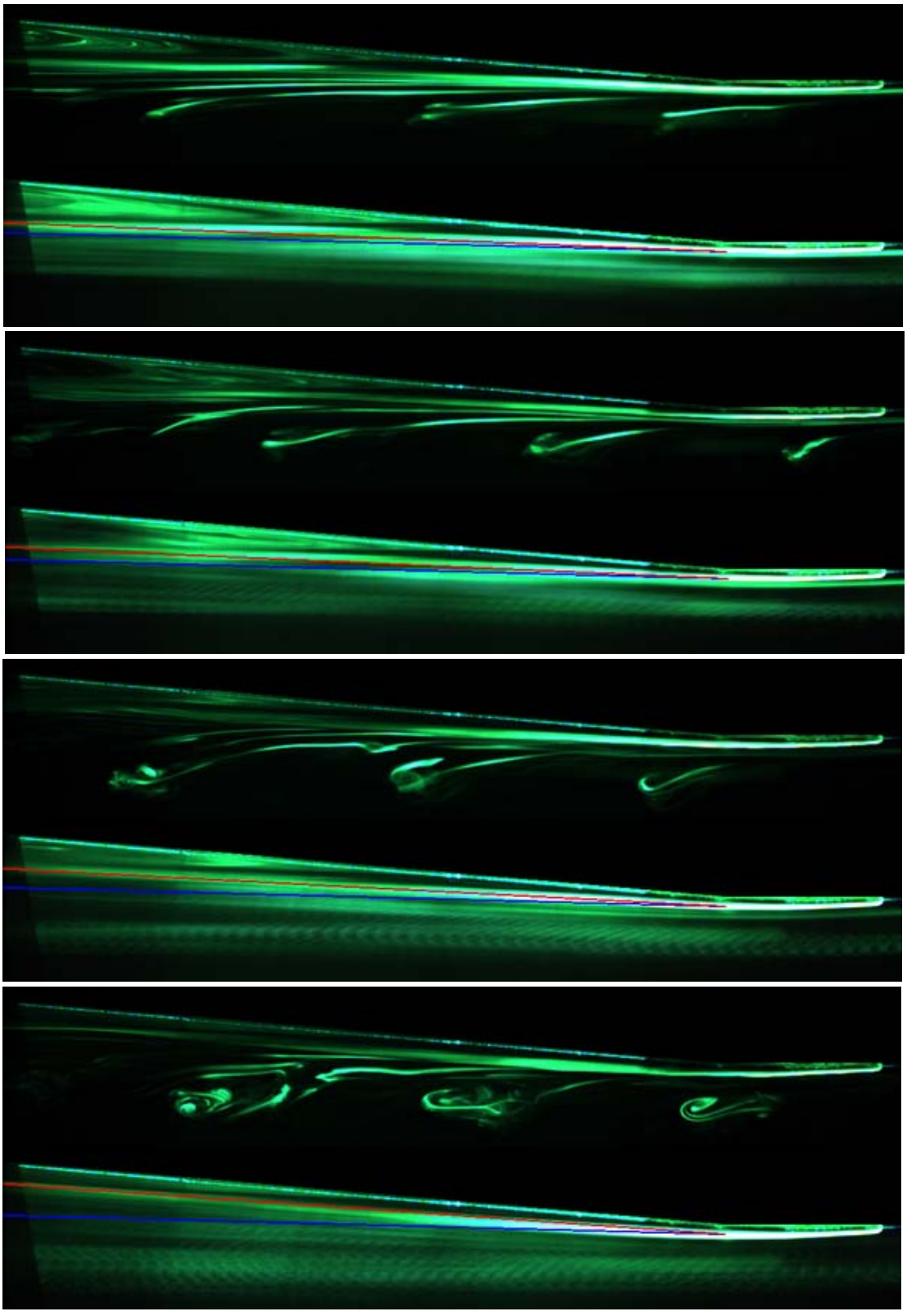

Figure 6.3 Control effect at *St* = 0.04 a) *L* = 2.0, *VR* = 0.08; b) *L* = 2.5, *VR* = 0.1; c) *L* = 3.0, *VR* = 0.12; d) *L* = 4.0, *VR* = 0.16; e) *L* = 5.0, *VR* = 0.2; f) *L* = 6.0, *VR* = 0.24; g) *L* = 7.0, *VR* = 0.28 and h) *L* = 9.0. *VR* = 0.36

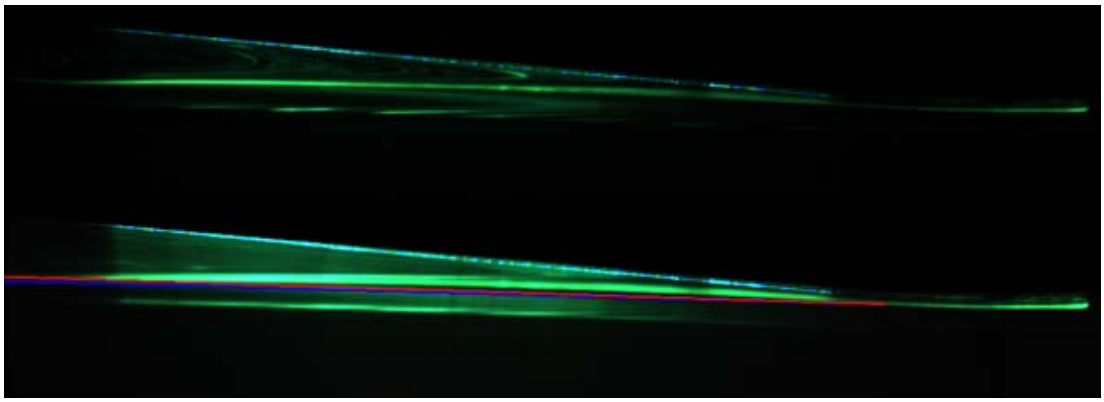

a)

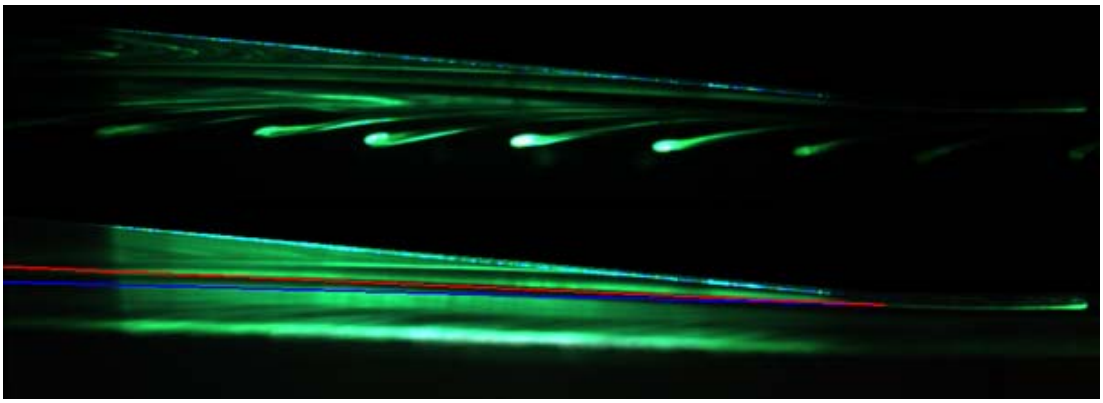

b)

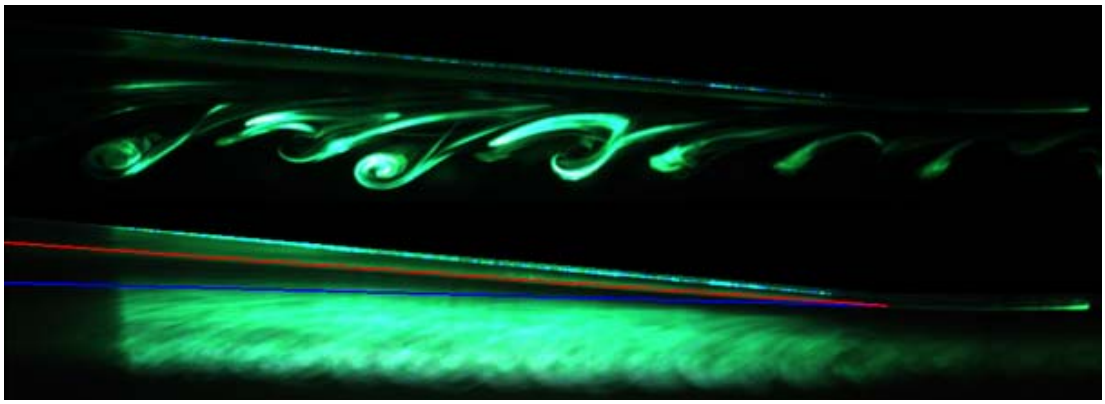

c)

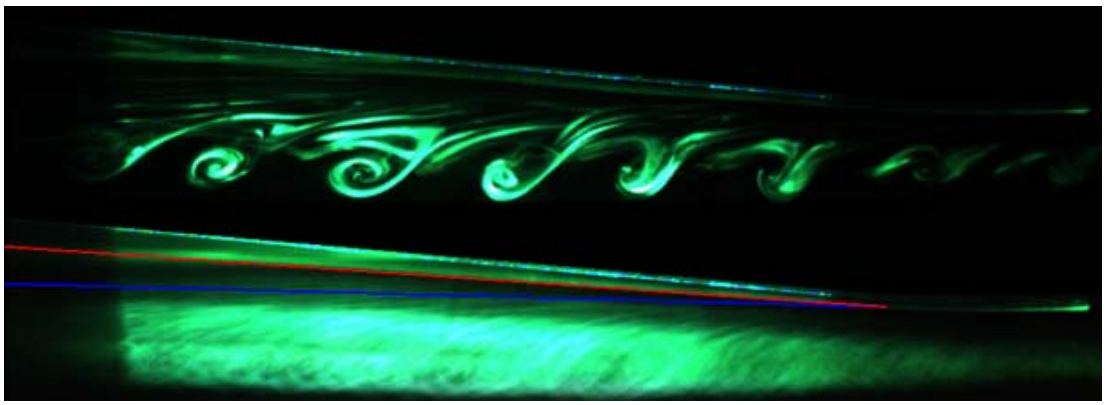

(d)

Figure 6.4 Control effect at condition St = 0.08 with a) L = 2.0 VR = 0.16; b) L = 3.0 VR = 0.24; c) L = 5.0 VR = 0.4 and d) L = 6.0 VR = 0.48

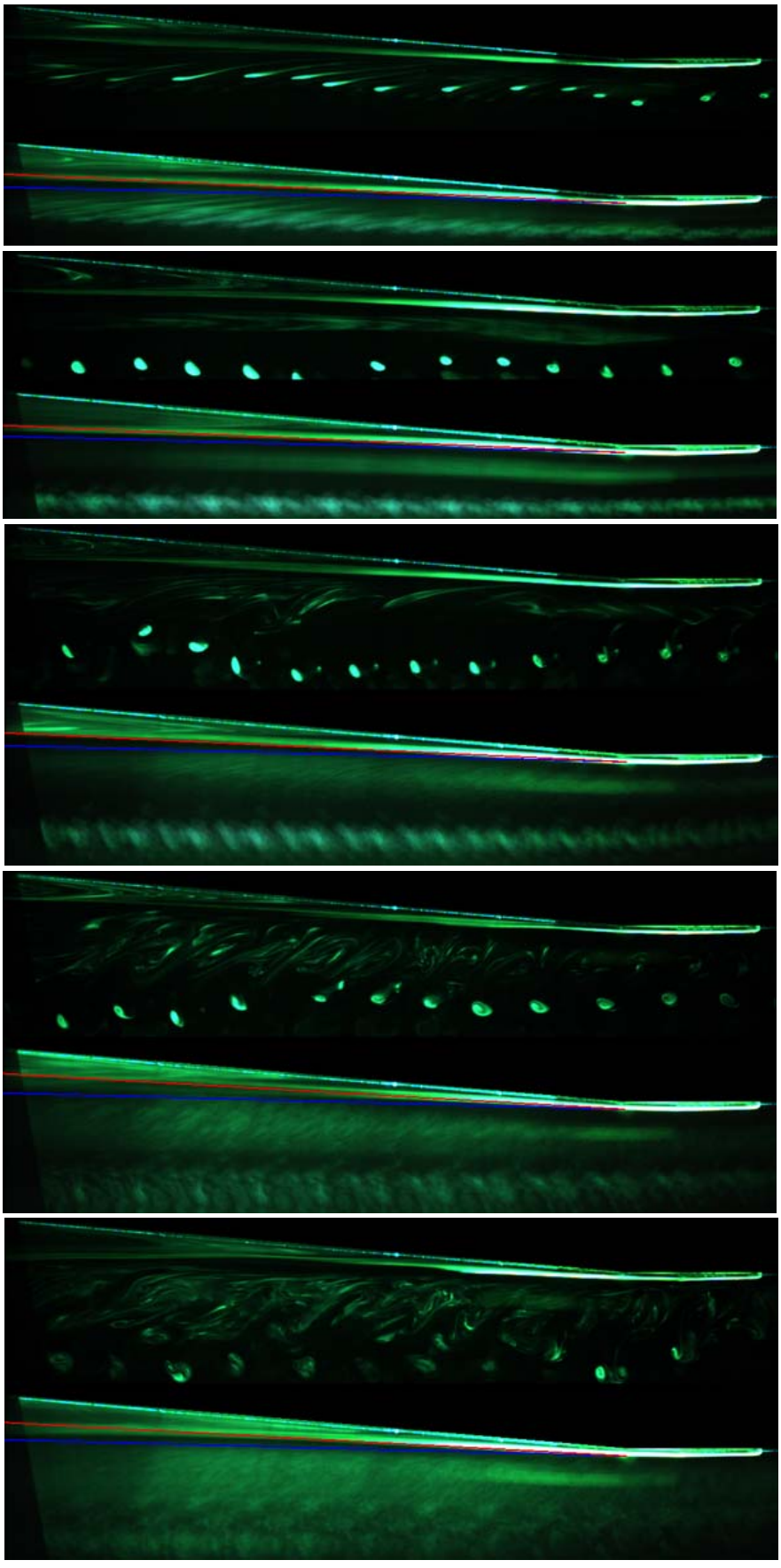

Figure 6.5 Control effect at condition *St* = 0.16 with a) *L* = 2.0 *VR* = 0.32; b) *L* = 3.0 *VR* = 0.48; c) *L* = 4.0 *VR* = 0.64; d) *L* = 5.0 *VR* = 0.8 and e) *L* = 6.0 *VR* = 0.96

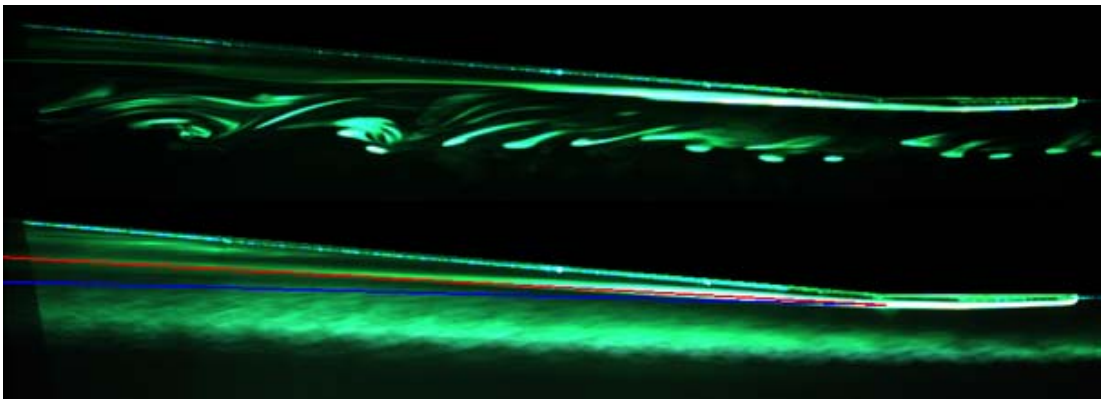

a)

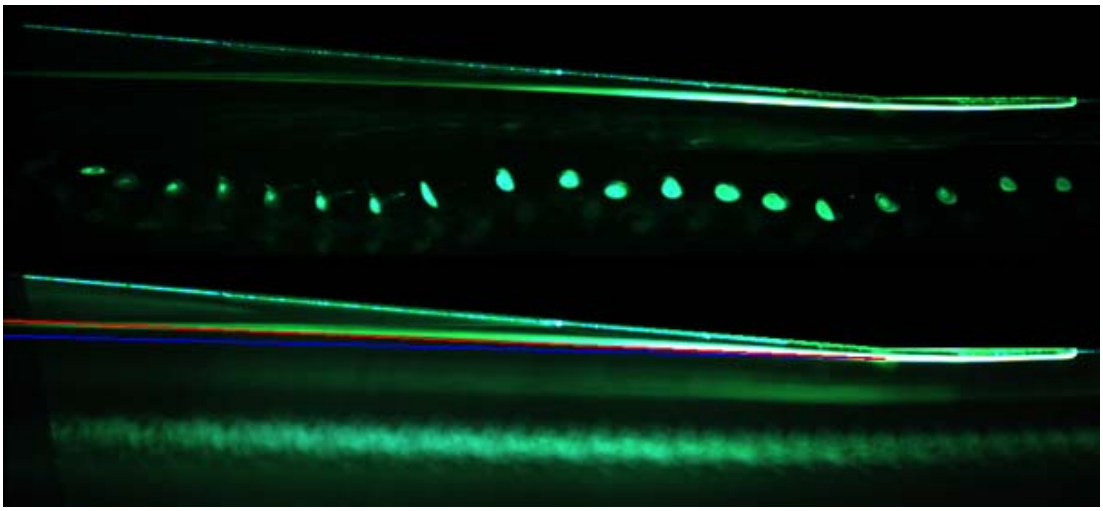

b)

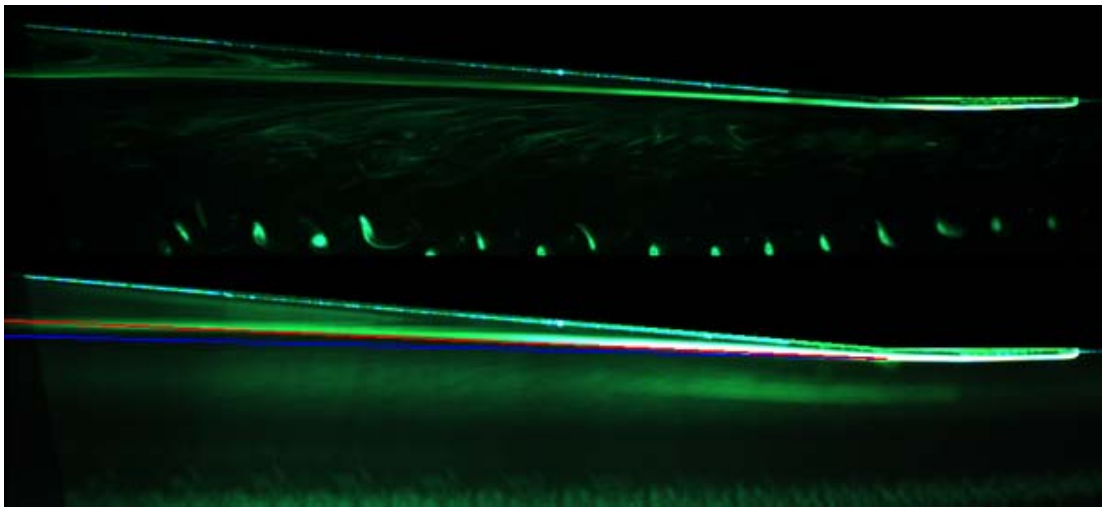

c)

Figure 6.6 Control effect at condition *St* = 0.24 with a) *L* = 2.0 *VR* = 0.48; b) *L* = 3.0 *VR* = 0.72 and c) *L* = 4.0 *VR* = 0.96

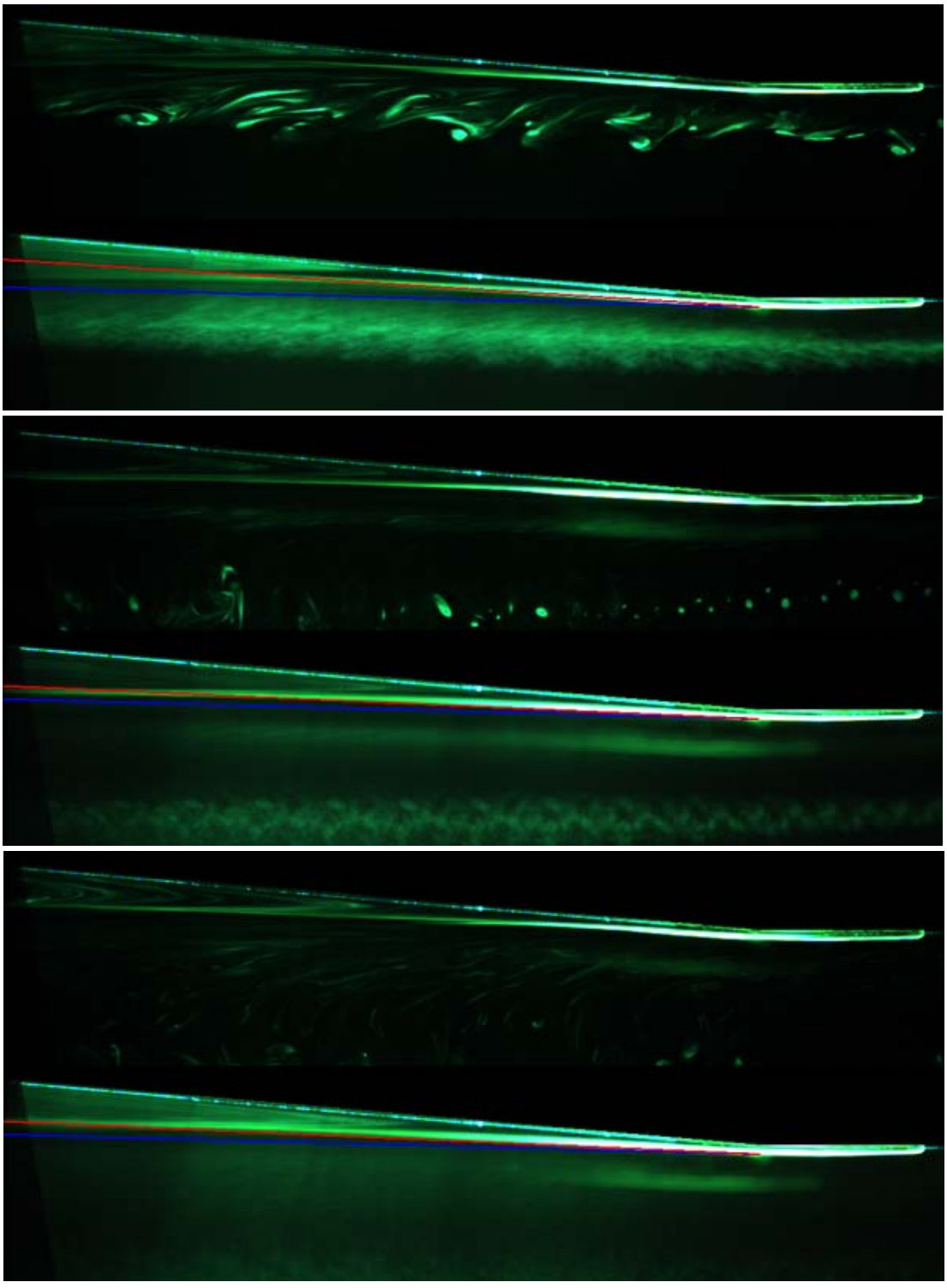

Figure 6.7 Control effect at condition *St* = 0.32 with a) *L* = 2.0 *VR* = 0.64; b) *L* = 3.0 *VR* = 0.96 and c) *L* = 4.0 *VR* = 1.28

In figure 6.8, the effectiveness for all operating conditions is presented as a contour in the space of dimensionless stroke length and diaphragm frequency. Five constant *VR* lines are added to assist the interpretation of results. It is seen that overall good control effects are achieved in a 'strap' region with *VR* valued between 0.3 and 0.7.

For the region where the *VR* is less 0.3, the strength of the vortical structures is too weak to generate appreciable control effect. For the region where the *VR* is higher than 1, the synthetic jets are expected to become turbulent either at the outlet of the orifice or some distance downstream (Crook, 2000) hence trigger the transition of laminar boundary layer into turbulent. Therefore the region with $VR > 1$ is not of interest in this work as its focus is to study the control of laminar separation.

Three isolated regions with a good flow control effect can be identified in figure 6.8; the first one is a region centred around $St = 0.04$ and $L = 9$, the second one a region centred around a $St = 0.08$, $L = 5$, the third one a region centred around $St = 0.32$ and $L = 2$. It is very likely that the first and the second region are parts of a single region which appears as two regions due to data interpolation for intermediate Strouhal number. At $St = 0.04$ and 0.08, the vortical structures are hairpin vortices even at very high L. Beginning at $St = 0.16$, the structures experience a switching from hairpin vortex to tilted vortex ring type of structures hence a good flow control effect is obtained at low L where hairpin vortices are observed then a second peak at a higher L when the tilted vortex ring type of structures has gained a sufficient strength. The third region with good flow control effect occurs around $St = 0.32$ and $L = 2$. Compared the vortical structures which deliver good flow control effect at $St = 0.04$ with those at $St = 0.32$, the structures at low Strouhal number are stronger due to their higher L and are spaced further apart. In contrast, the structures at high Strouhal number are weak due to a lower L but are spaced much closer together. Assuming that these structures propagate downstream at the freestream velocity, the spacing between consecutive structures at $St = 0.04$ and 0.32 is 5 and 0.6 times of the local boundary layer thickness at the synthetic jet orifices. Based on the finding from the present experiment, having weaker structures which are close together (though not too close to cause strong mutual interaction) can be advantageous for producing a good flow control effect.

Overall, it is found that a good control effect is associated with the presence of hairpin type of structures and a *VR* in the range of 0.3 to 0.7 which ensures vortical the structures produced by the synthetic jets have a desirable strength and are close to the wall. These hairpin vortices are formed as the result of the upstream branch of the vortex ring being firstly weakened by the suction cycle as it passes over the orifice and then subsequently being cancelled out by the residential vorticity of the opposite sign as it propagates downstream. The legs of the hairpins are trailing along the wall which can also induce a pair of longitudinal vortices of the opposite sign outboard, as shown in

figure 6.9a. The legs of the hairpins and their induced longitudinal vortices together create a downwash which brings high-speed fluid from the outer part of the boundary layer to the wall, leaving footprints of high-speed streaks which convect downstream (figure 6.9b). However, since the strength of the synthetic jets is relatively weak at lower dimensionless stroke length due to the low Reynolds number, they do not produce a noticeable separation delay. With the increased Reynolds number, the impact of those structures on the separated flow becomes more pronounced.

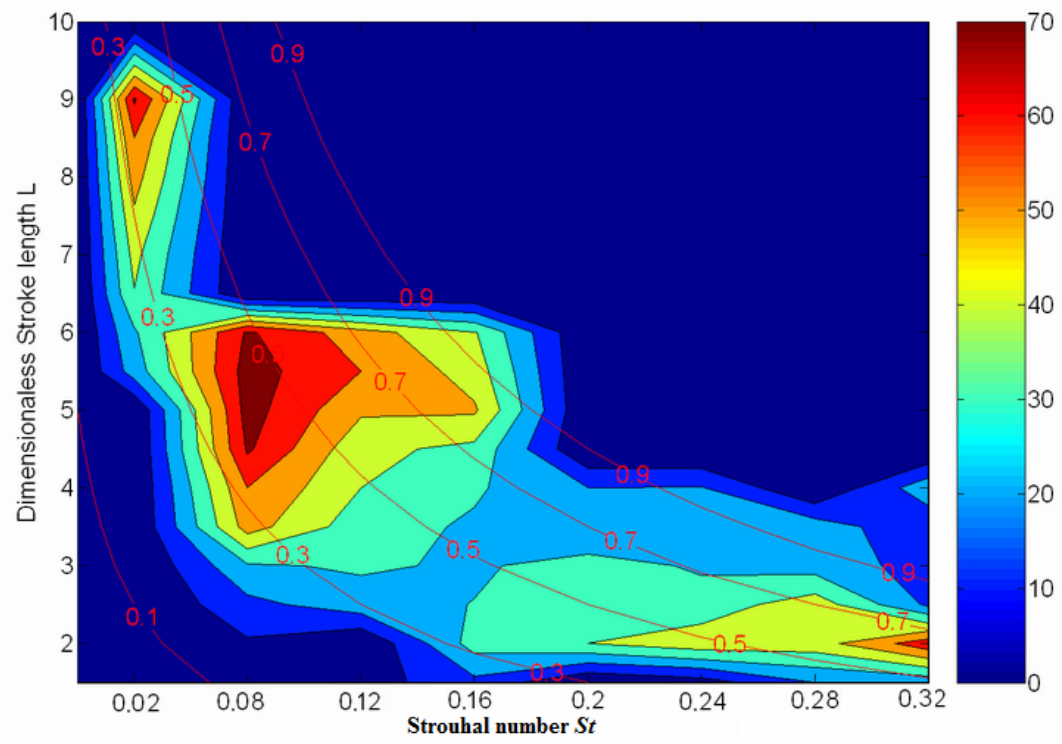

Figure 6.8 Contours of separation control effects for various Strouhal number and dimensionless stroke lengths (red lines are lines of constant *VR*)

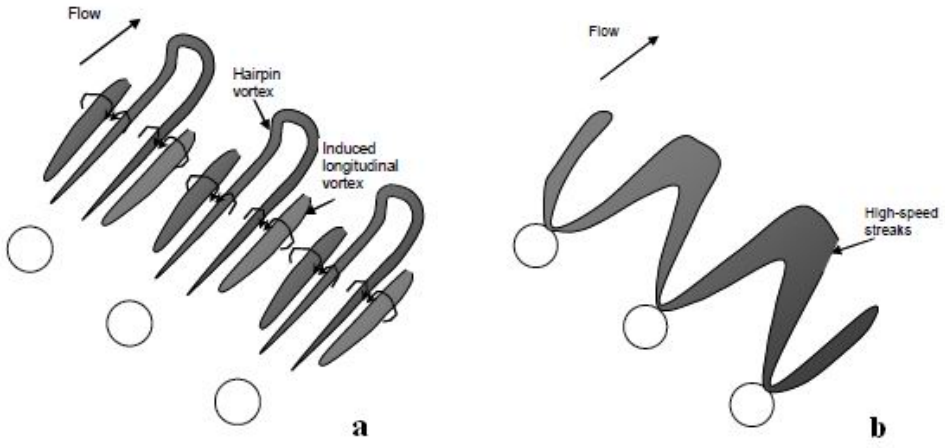

Figure 6.9 Schematic drawing of a) hairpin vortices and their induced vortices and b) production of high speed streaks in the near wall region (three orifices are shown for clarification)

6.3 PIV Measurement on Streamwise Central Planes

In order to achieve a better understanding of the impact of synthetic jets on the separated flow, PIV measurements are undertaken to obtain the velocity distribution on the central streamwise plane across the middle jet of the synthetic jet array in the separation area.

6.3.1 The Baseline Case

Figure 6.10 shows the time-averaged velocity contour across the separated flow region without active control. The flow is from right to left. The origin of the x-y coordinate is located at the start of the inclined plate. It can be seen that a separation region appears from about 50 mm downstream of the start of the inclined plate with a reverse flow occurring further downstream. A small pocket of reverse flow can be clearly seen in the velocity profile along the vertical direction at 143mm downstream of the start of the inclined plate for the baseline case (see figure 6.11).

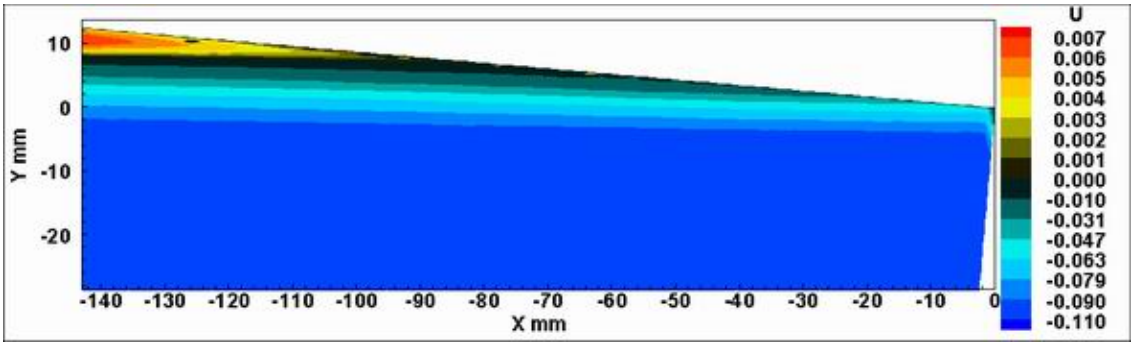

Figure 6.10 Contour of velocity in streamwise direction at the baseline condition (origin at the start of the inclined plate, flow from right to left) (U: m/s)

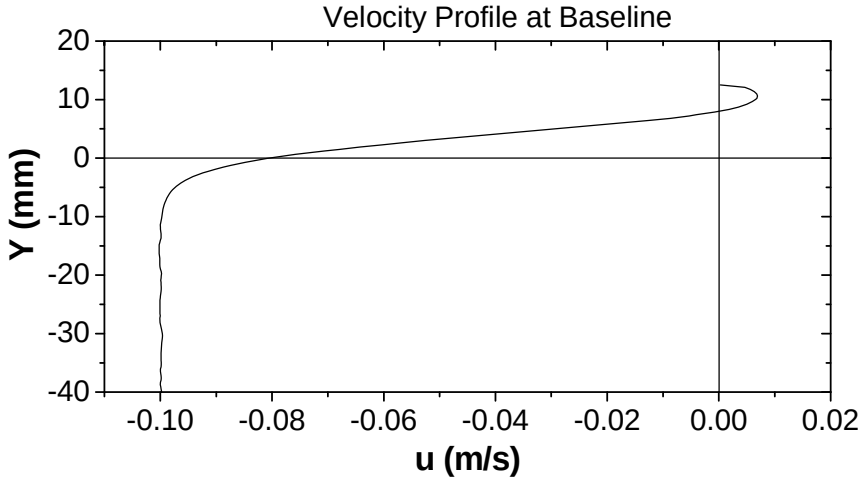

Figure 6.11 Velocity profile along the vertical direction at 143mm downstream of the start of the inclined plate at the baseline condition

6.3.2 Controlled Cases

At St = 0.04 and L = 2, shown in figure 6.12a, the velocity contours looks almost identical to that at baseline condition indicating that there is no visible control effect under this condition, which is consistent with the LIF results. As L increases to 4, it can be seen from the velocity contour the size of the separation region becomes visibly smaller (see figure 6.12c). At L = 5, the control effect improves greatly and only a very small area with reverse flow near to the wall is observed. With L increase further to 7 and 9, the separation region seems to become fully reattached up to the most downstream station of the measurement areas (see figure 6.12d and 6.12e). The above finding is also confirmed by the velocity profiles shown in figure 6.13. At L = 9, there is a velocity dip in outer part of the velocity profile between y = -10 and 0 mm which is believed to be caused by the head of the hairpin vortices reaching out into that region.

Compared with the LIF results, it is noted that at L = 7 and 9 the flow does not appear fully attached as indicated by the dye trace in figure 6.3g and 6.3h,. The discrepancy between the PIV and LIF is likely to be caused by two factors. Firstly, as the dye was injected along the horizontal plate upstream of the inclined plate, a slight non-zero-velocity injection of the dye may cause the dye to depart from the inclined wall. Secondly, due to the relative large velocity gradient in the separation region, the resulting velocity is bigger than the lower velocity in the PIV integration area. Nevertheless, for the purpose of indicating the control effect of synthetic jet operated at different conditions, this is not an issue as the PIV results obtained with the same process parameters will be compared.

At St = 0.08, again there is no visible control effect at L = 2 and VR = 0.16 as shown in figure 6.14a. The separation region appears to decrease steadily as L increases to 5 and remain almost unchanged at L = 6. The velocity profiles at x = 143mm confirms that a separated flow region exists with L up to 4. The velocity profile at L = 2 shows no difference from the baseline case (seen in figure 6.15). As L increases to 3, the velocity at the reverse flow area decreases and the maximum speed in this area is between 0.004m/s and 0.005m/s, indicated by the contour colour. And size of separation becomes smaller, as the start position of the reverse flow moves from 8mm to 9.5mm as seen from the velocity profile in figure 6.15. It can be seen that the overall velocity from 0mm to 12.5mm increases. At L = 4, a good control effect appears as no reverse flow is seen in the separation region from the velocity profile. As the stroke length increases to

L = 5 and L = 6, the control effect improves further as it can be seen that the velocity increases further from the velocity profile. At L = 5 and 6, a reduction in velocity in the region between 0mm and -10mm indicates that the vortical structures have moved out the boundary layer and interacted with the freestream.

At St = 0.16, the reverse flow region appears to decrease as L increases from 2 to 5 and it then increases as L increases further to 6 as shown in figure 6.17. The velocity in the boundary layer increases slightly due to the presence of the vortical structures. For L = 3, an obvious control effect appears as the size of the separation region reduces greatly. The maximum velocity in the reverse flow drops to 0.026m/s and the start position of the reverse flow moves up to 10.6mm. Due to the high velocity ratio, the vortical structure penetrates outside the boundary layer to cause the drop of velocity in the region from 0mm to 15mm, seen in the velocity profile in figure 6.17. At L = 4, no visible difference is observed from the velocity contour comparing with the L = 3 case. However, it can be seen that the velocity in the region between 5mm and 20mm drops further due to the high velocity ratio. As L increases to L = 5, the flow becomes fully reattached as seen in figure 6.16d and no reverse flow appears in the separation region seen from the velocity profile in figure 6.17. Due to the further increase of velocity ratio, the velocity in the region between 0mm and 20mm is reduced further than the previous case. As the stroke length increases to L = 6, the velocity in the separation region decreases rather than increase. The reason is that the velocity ratio is so high that the trailing legs of the tilted vortex ring type of vortical structure have moved too far away from the near-wall region.

At St = 0.24, a good control effect appears at L = 2 and the separation region becomes fully reattached, as seen from figure 6.18a. From the velocity profile shown in figure 6.19, no positive velocity appears in the separation region and the overall velocity from 0mm to 12.5mm increases when compared with the baseline case. At L = 3, the flow in the separation region becomes separated again, although its size is smaller than that of the baseline case. This is because the vortical structures have moved outside the upstream boundary layer, which is indicated by a decrease of the velocity in the region between 0mm to 20mm. For the same reason, the control effect worsens as L increases to 4 and the vortical structures moves further away from the separation region. As L = 5, the control effect becomes a little better than that at L = 4, as the size of separation region is smaller and the magnitude of the reverse flow velocity becomes smaller. It is believed that at L > 4 the primary vortical structure becomes saturated causing the

excessive vorticity to be deposited into its trailing legs hence increases the strength of the trailing legs which are located nearer to the wall. Due to the higher velocity ratio, the primary vortical structure penetrates deeper into the free stream, indicated by a decrease of the velocity in the region of y = 15mm to 30mm, seen in figure 6.19. At L = 6, the flow is still separated although the control effect becomes better than that at L = 5.

At St = 0.32, little control effect is seen at L = 1.5 since the vortical structures are quite weak, shown in figure 6.20. As L increases, a good control effect is achieved at L = 2. It then worsens at L = 3.0 before it recovers at L = 6. This observation is similar to what has been discussed for the St = 0.24 cases. As the stroke length increases, the primary vortical structures moves away further from the separation region, which is indicated by the velocity decrease in the velocity profile in figure 6.21. The strength of the trailing legs of the tilted vortex ring type of structures becomes stronger with an increase of the stroke length, which brings the momentum to the boundary layer and produces a better control effect.

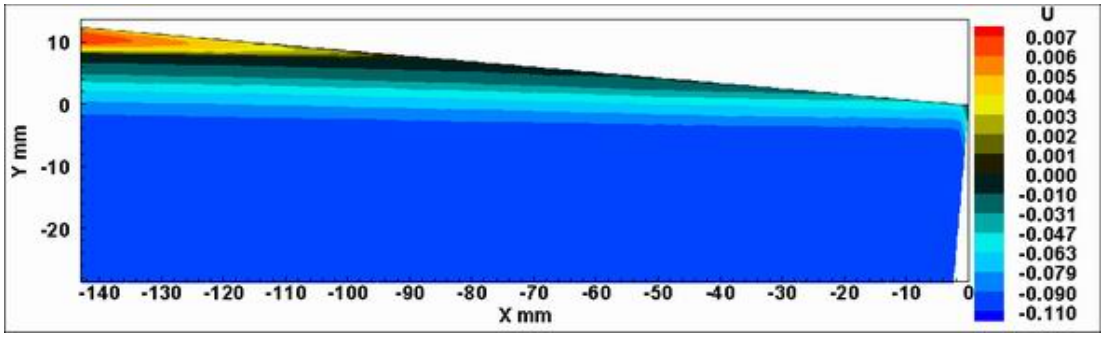

a)

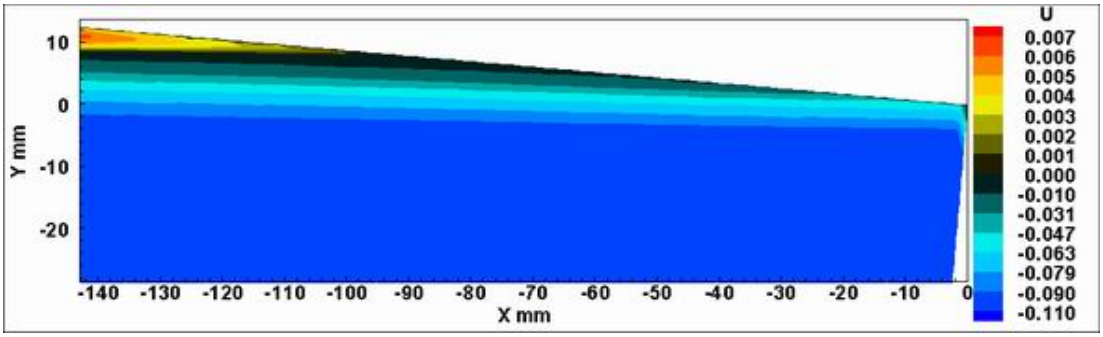

b)

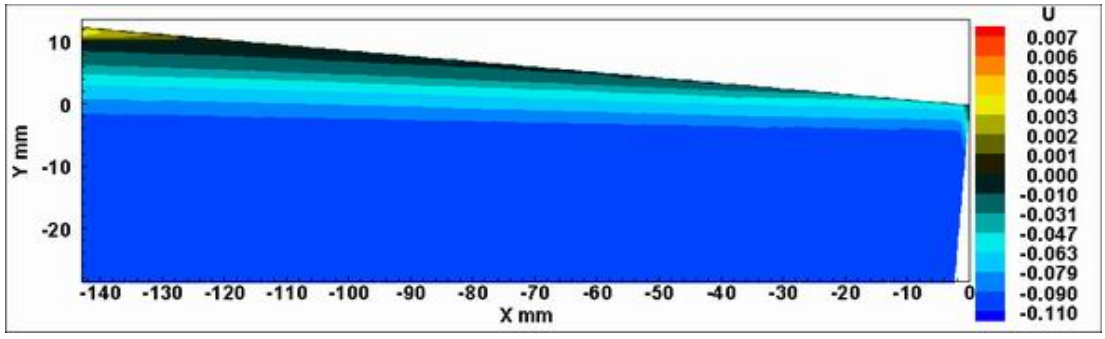

c)

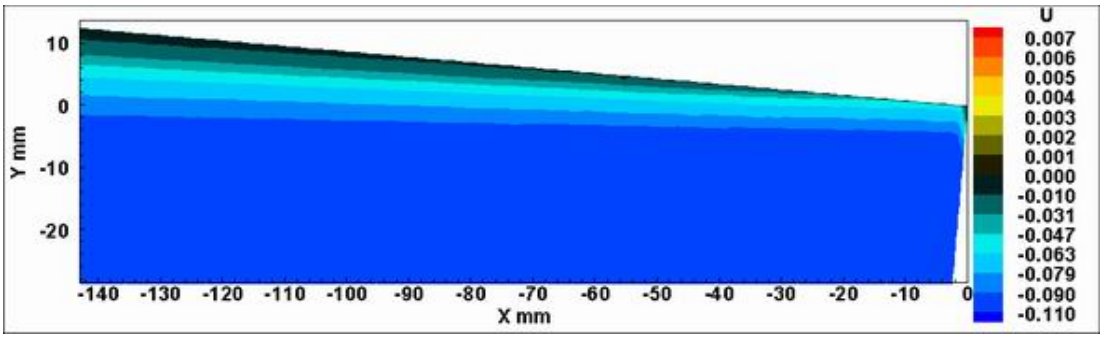

d)

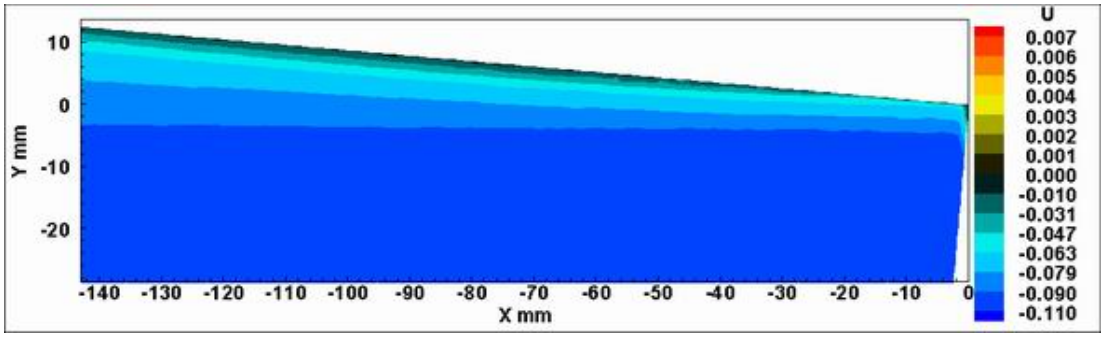

e)

Figure 6.12 Contours of velocity in streamwise direction at the separation region with synthetic jet actuators operated at St = 0.04 a) L = 2; b) L = 4; c) L = 5; d) L = 7 and e) L = 9 (U: m/s)

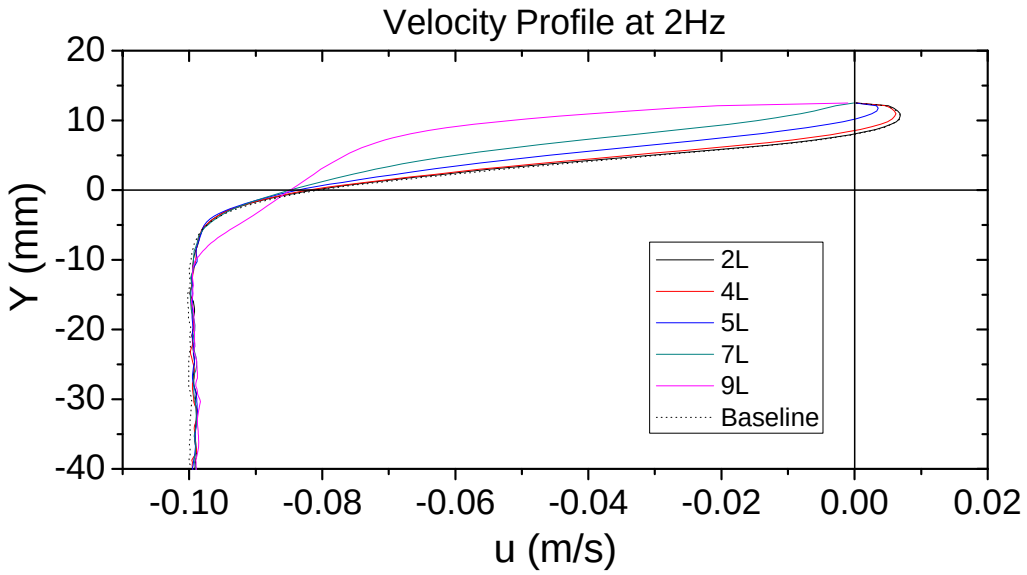

Figure 6.13 Velocity profile along the vertical direction at 143mm downstream of the start of the inclined plate at St = 0.04

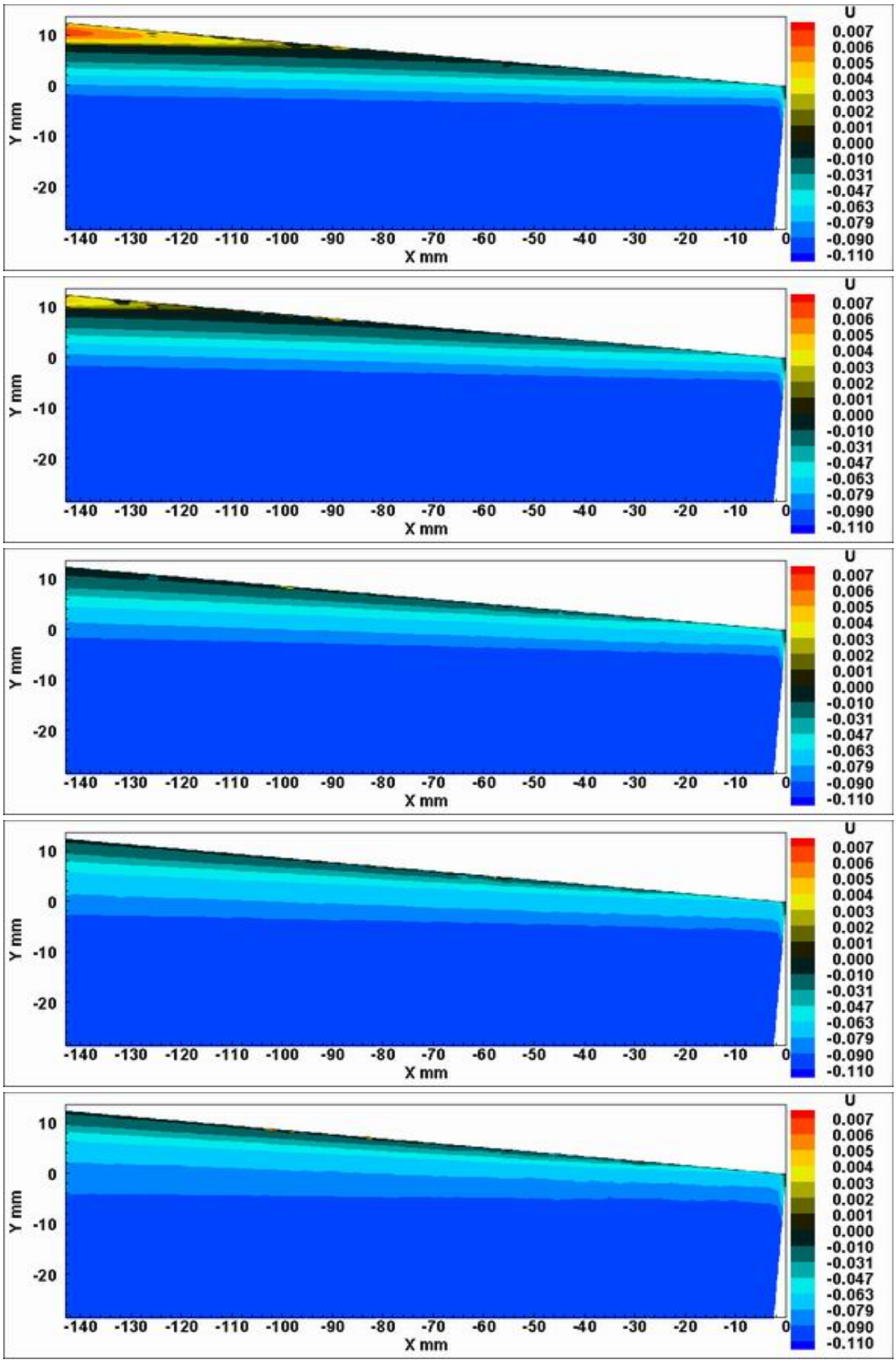

Figure 6.14 Contours of velocity in streamwise direction at the separation region with synthetic jet actuators operated at *St* = 0.08 a) *L* = 2; b) *L* = 3; c) *L* = 4; d) *L* = 5 and e) *L* = 6 (U: m/s)

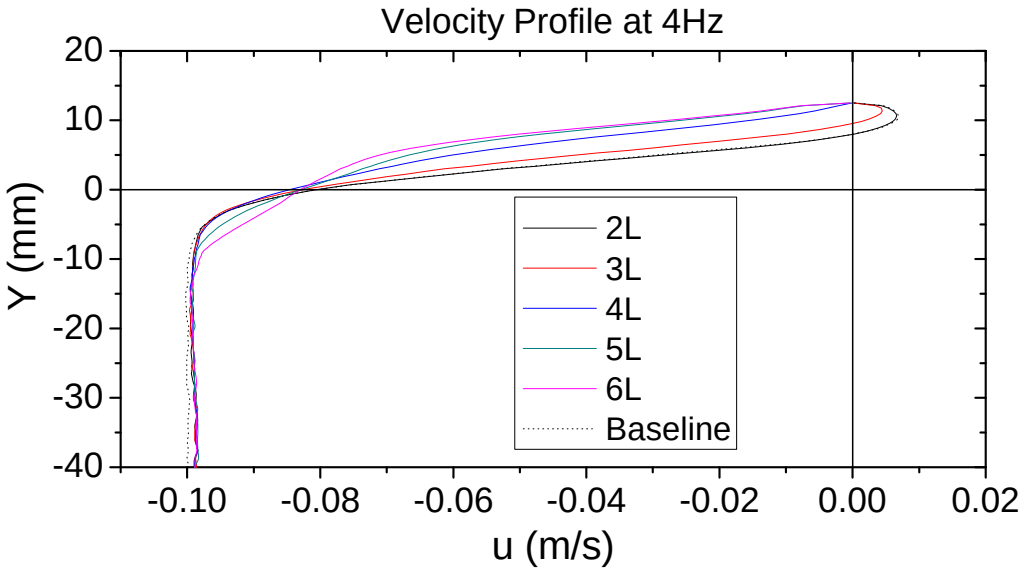

Figure 6.15 Velocity profile along the vertical direction at 143mm downstream of the start of the inclined plate at *St* = 0.08

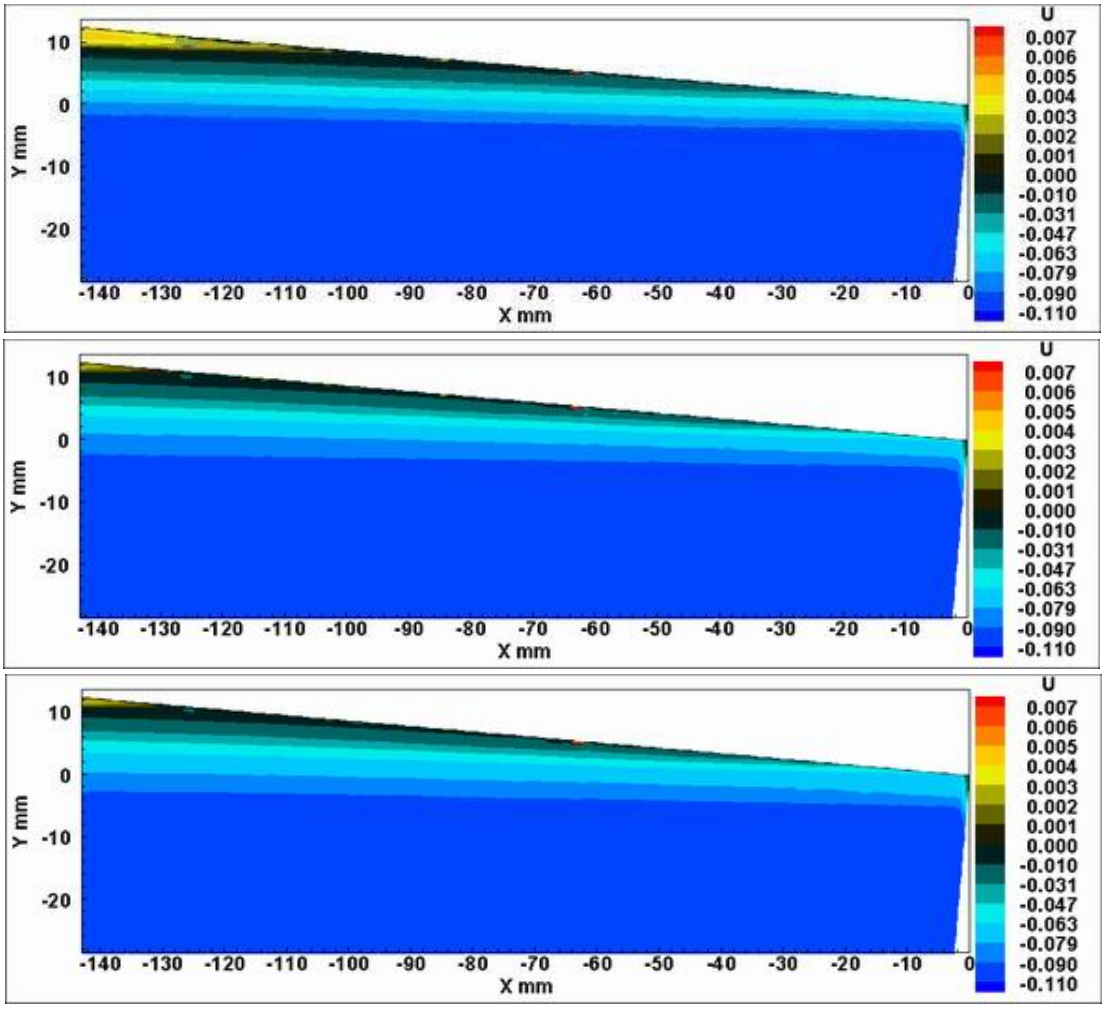

a)

b)

c)

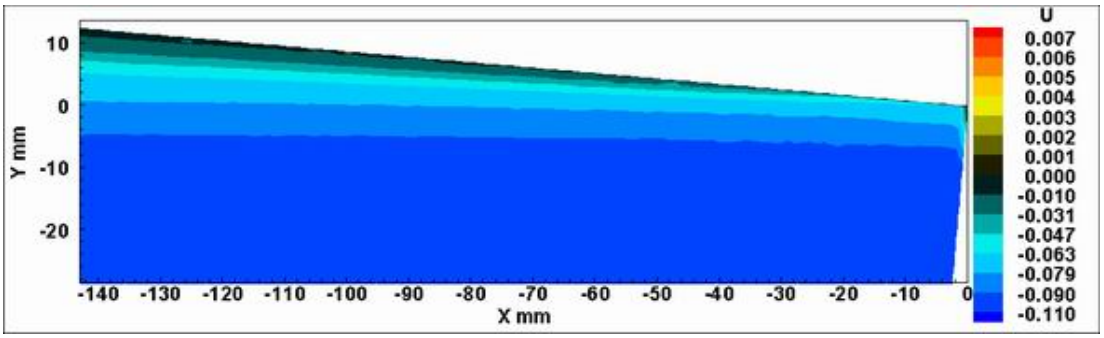

d)

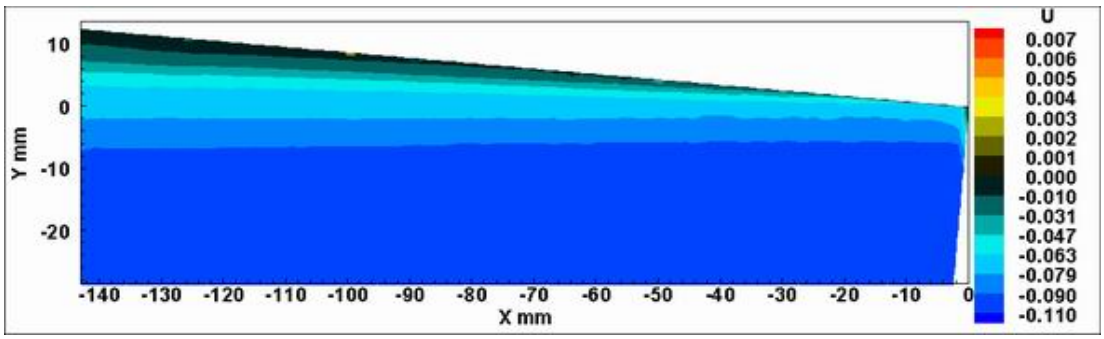

e)

Figure 6.16 Contours of velocity in streamwise direction at the separation region with synthetic jet actuators operated at *St* = 0.16 a) *L* = 2; b) *L* = 3; c) *L* = 4; d) *L* = 5 and e) *L* = 6 (U: m/s)

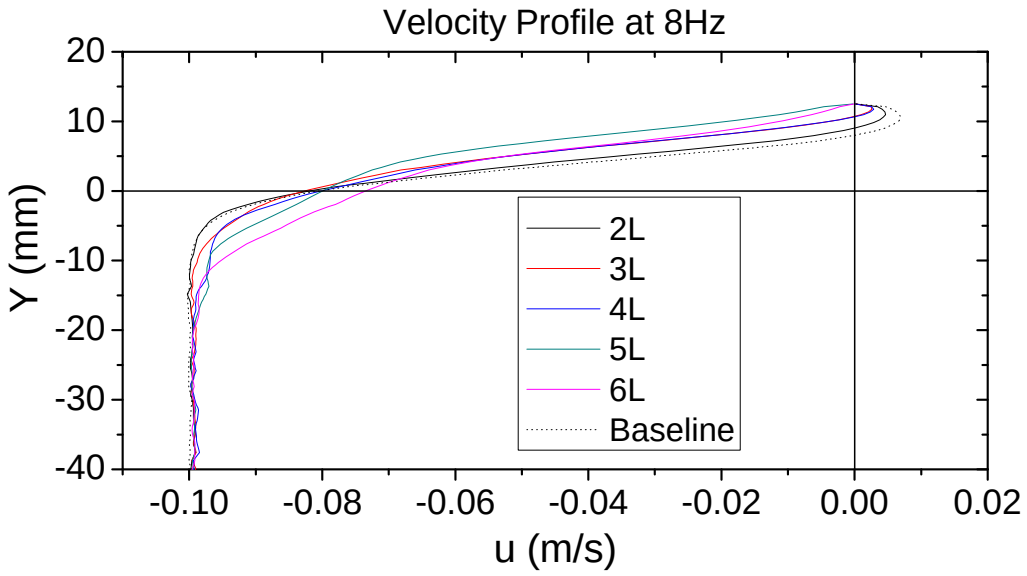

Figure 6.17 Velocity profile along the vertical direction at 143mm downstream of the start of the inclined plate at *St* = 0.16

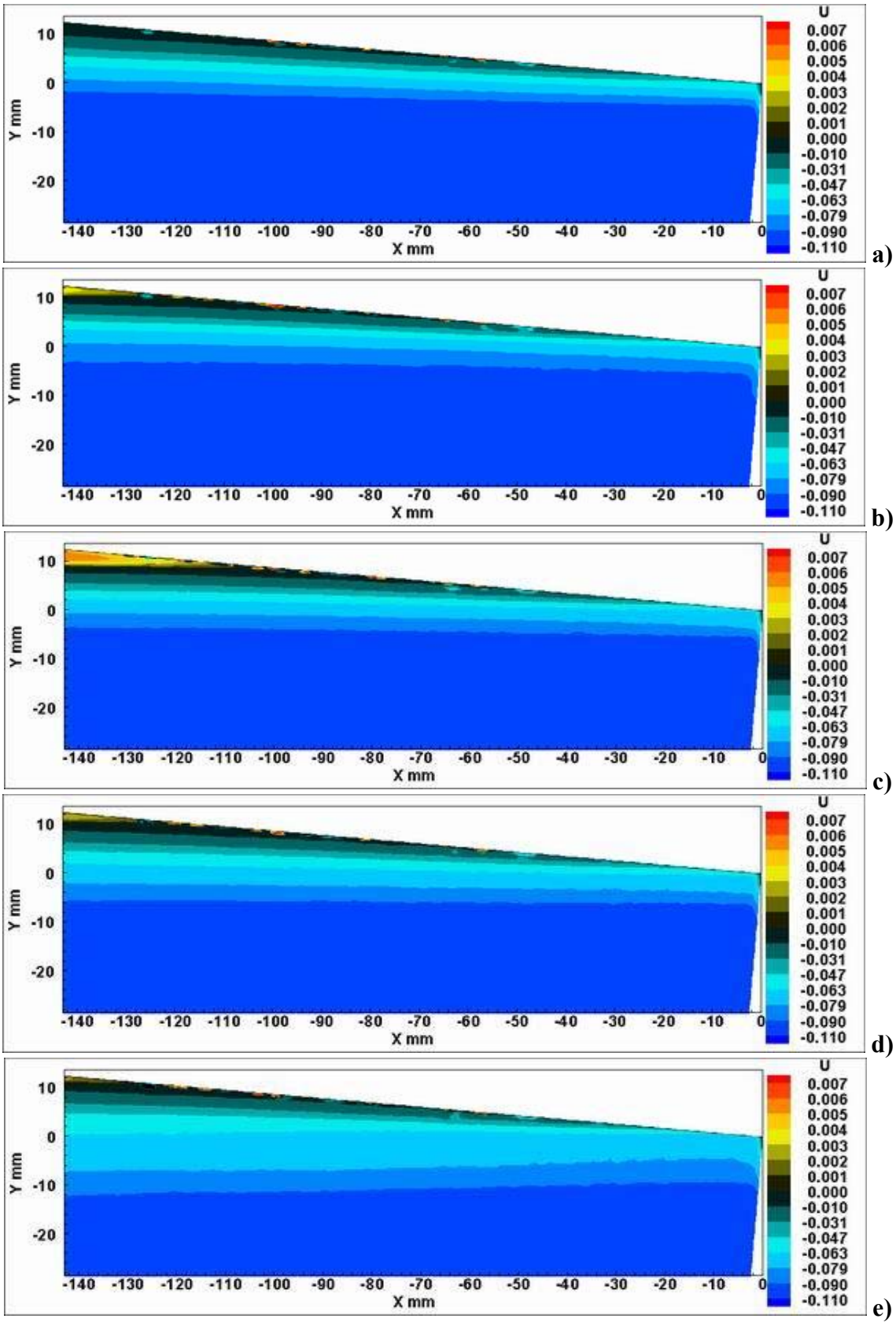

Figure 6.18 Contours of velocity in streamwise direction at the separation region with synthetic jet actuators operated at *St* = 0.24 a) *L* = 2; b) *L* = 3; c) *L* = 4; d) *L* = 5 and e) *L* = 6 (U: m/s)

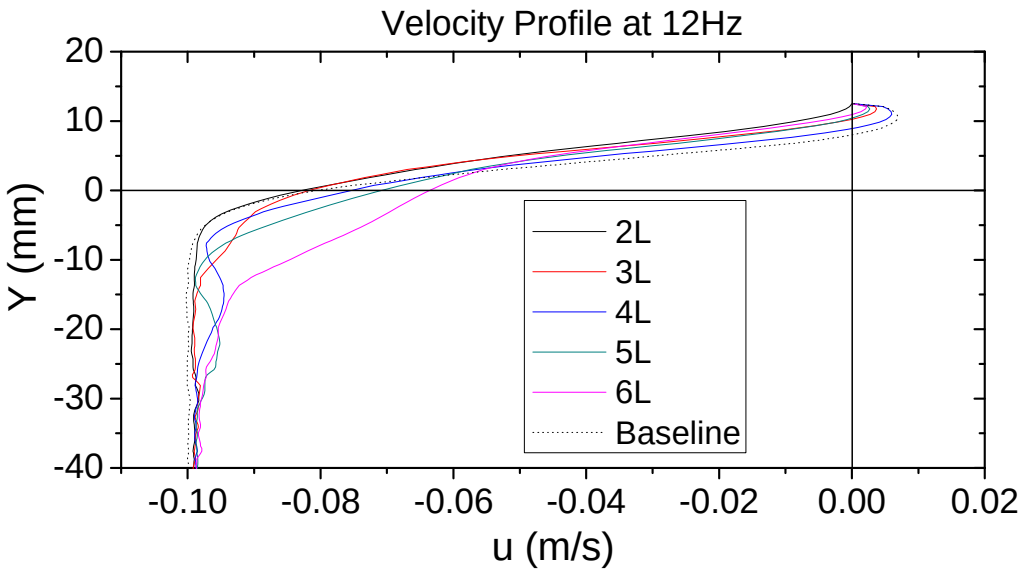

Figure 6.19 Velocity profile along the vertical direction at 143mm downstream of the start of the inclined plate at *St* = 0.24

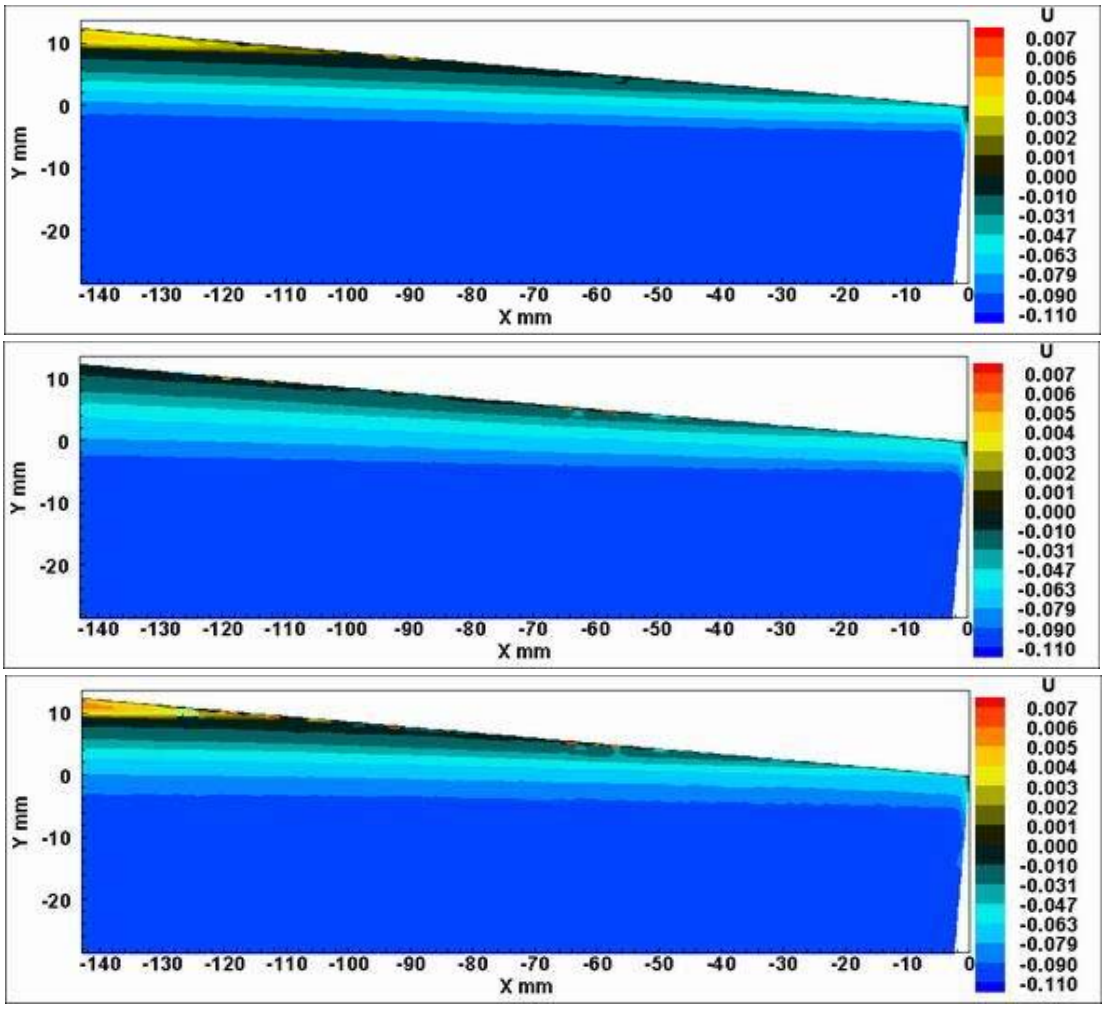

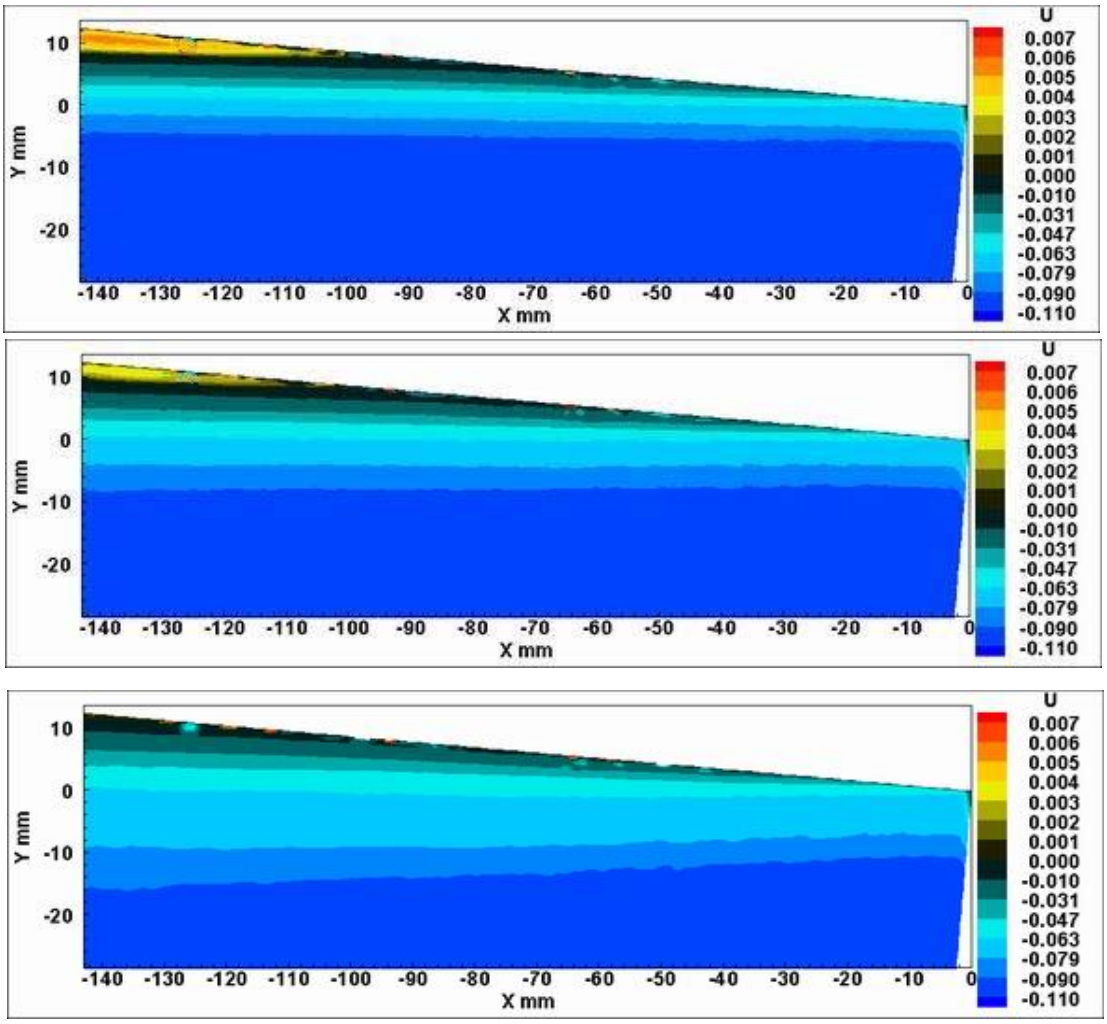

Figure 6.20 Contours of velocity in streamwise direction at the separation region with synthetic jet actuators operated at St = 0.32 a) L = 1.5; b) L =2; c) L = 3; d) L = 4; e) L = 5 and f) L = 6 (U: m/s)

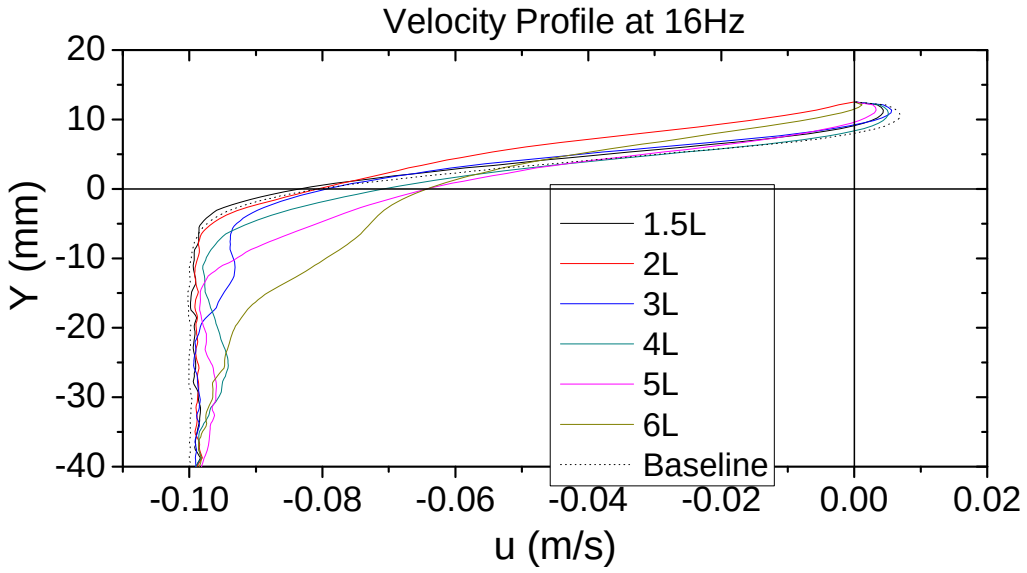

Figure 6.21 Velocity profile along the vertical direction at 143mm downstream of the start of the inclined plate at St = 0.32

6.4 PIV Measurements on the Spanwise Plane

Since the interaction between the synthetic jets and the separated flow is three-dimensional, PIV measurements on a plane parallel to the flap at a distance about 1.5mm from the flap surface were undertaken so as to obtain the information about the extent of flow separation delay by the synthetic jet array The distance of the measurement plane from the flap surface is the smallest that is possible so as to minimise the reflection of the finite laser sheet to an acceptable level.

Figure 6.22 shows the contour of time-averaged streamwise velocity together with the streamlines on the spanwise plane parallel to the inclined plate for the baseline case. The streamwise location where the streamlines from upstream begin to divert sideways is identified as the location of separation line. It can be seen from figure 6.22 that the separation line is located at about 27% of the chord length of the flap equivalent to 54mm downstream of the start of the inclined plate. This is in a good agreement with the location of separation (50mm) identified from the PIV measurements on the streamwise central plane discussed in the previous section.

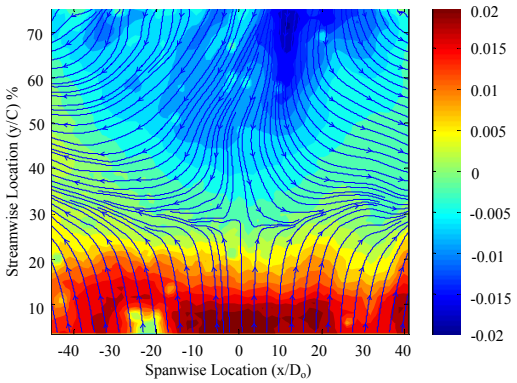

Figure 6.22 Time-averaged streamwise velocity contour and streamlines on a plane parallel to the inclined plate for the baseline case (contour units: m/s)

6.4.1 Comparison of Flow Control Effectiveness

In order to evaluate the flow control effectiveness of synthetic jets operating at different conditions, the contours of time-averaged streamwise velocity superimposed with the streamline on the spanwise plane parallel to the inclined plate are examined.

At St = 0.04, no visible separation delay is observed at L = 2 and VR = 0.08, as shown in figure 6.23a. As L increases to 4 and VR to 0.16, a separation delay near the central region can be observed. A further delay in separation is seen at L = 5 and VR = 0.2 where the region appears in the shape of two high-speed streaks. The region with

separation delay spans $6D_o$ on each side of the central plane which is in accordance to the width of the synthetic jet array. An even stronger separation delay is achieved at L = 6 with a visible two-streak pattern. As L increases to 7 and 8, the separation line appears to be pushed beyond the downstream edge of the PIV measurement area. A single high-speed streak is observed in these cases.

According to Jabbal and Zhong (2006), each hairpin type of vortical structures produced by synthetic jets will produce two high-speed streaks one each side of the stretched legs of the hairpin which trail along the wall. Due to the spanwise growth of the hairpin vortices as they propagate downstream and the small spacing between the adjacent jets in the synthetic jet array tested in the present experiment ($3D_o$), the impact of each individual hairpin vortex are expected to merge making the streak pattern produced by individual jets indistinguishable. It is noted that the merging of streak patterns for a synthetic jet array with a jet spacing of $6D_o$ which is located at the same distance upstream to the baseline separation line is already obvious (Zhang and Zhong, 2009). Compared to their experiment, the merging is expected to be more pronounced in the present experiment, which is responsible for the fewer individual streaks observed. On the other hand, the flow control is seen to be stronger as a result of merging.

At St = 0.08, no visible separation delay is seen at L = 2 and VR = 0.16 as shown in figure 6.24. The separation delay appears as L and VR increase to 3 and 0.24, along with the appearance of two high-speed streaks. The separation is delayed further as VR increases to 0.32 and 0.48 with the appearance of one high-speed streak. Interestingly, the level of separation delay reduces at L = 8 and VR = 0.64 in the central region. However, the synthetic jets are so strong that they begin to affect the entire separated flow by causing a significant separation delay in the flow further outboard. As L and VR increase further to L = 9 and VR = 0.72, the impact of the synthetic jet spreads outwards further.

At St = 0.16, no visible separation delay is again observed at L = 2, and VR = 0.32, as shown in figure 6.25. As the L and VR increase to L = 3 and VR = 0.48, a pronounced separation delay is observed along with the one-streak pattern. The level of separation delay drops at L = 4 and VR = 0.64 but it peaks again as L increases to L = 5 (VR = 0.8) and 6 (VR = 0.96). This is believed to be caused by the transformation of the types of the vortical structures from hairpin vortices to tilted vortex rings and subsequent strengthening of tilted vortex ring type of structures as L increases. Again at higher L, the synthetic jets appear to alter the separated flow globally.

At St = 0.32, a very good control effect is observed at L = 2 and VR = 0.64, as shown in figure 6.26. The level of separation delay drops as L increases to L = 3 and VR = 0.96, which caused the primary vortical structures moves away further from the separation region. Similarly at higher L = 4 and VR = 1.28, the synthetic jets appear to alter the separated flow globally.

In order to evaluate the flow control effect of the synthetic jets quantitatively, the distance from the space- and time-averaged separation line across a spanwise distance of $6D_o$ on each side of the central plane to the start of the inclined plate is calculated as a percentage of the length of the inclined plate. The results are presented as a contour in the space of dimensionless stroke length and diaphragm frequency, as shown in figure 6.27.

It appears from figure 6.27 that the distribution of control effect from the PIV measurement is similar to the results from the LIF visualisation shown in figure 6.8. Generally, a good control effect is achieved at between VR = 0.3 to 0.7 for $St < 0.12$ and $St > 0.28$. From the understanding of the vortical structures derived in chapter 5, the vortical structures responsible for the good control effect within this parameter range are classified as hairpin vortices which propagate within the undisturbed boundary layer.

It should be noted that due to the spanwise growth of the hairpin vortices as they propagate downstream and the small spacing between the adjacent jets in the synthetic jet array tested in the present experiment ($3D_o$), the impact of each individual hairpin vortex merges making the streak pattern produced by individual jets indistinguishable. Therefore in most cases, the footprints of the synthetic jets in the separated flow region appear as a single high-speed streak. The extent of flow separation delay is found to be higher than the cases when the jet spacing is twice as large which can be seen as an advantage.

Overall, the best flow separation effect is achieved at the highest Strouhal number (St = 0.32), which is able to push the separation line downstream significantly. At this condition, closely spaced stretched vortex ring type structures are observed. At this Strouhal number St = 0.32, the spacing between consecutive vortical structures produced by the synthetic jets is about 60% of the local boundary layer thickness, assuming they propagate within the boundary layer at the freestream velocity. For practical flow control applications, it is desirable to achieve the same level of separation delay using minimum energy expenditure which implies a minimum diaphragm displacement or L at least for shaker-driven synthetic jet actuator like that one used in

this project. Hence for the experimental conditions tested in this study, operating the synthetic jets at $L = 2$ with a VR of around 0.5, which generates vortical structures with a streamwise spacing not larger than the local boundary layer thickness before separation, seems to deliver the best flow control effect with the least energy consumption. In practice, the diaphragm frequency should be coupled with the diaphragm resonance and Helmholtz resonance in the cavity so as to achieve further energy saving.

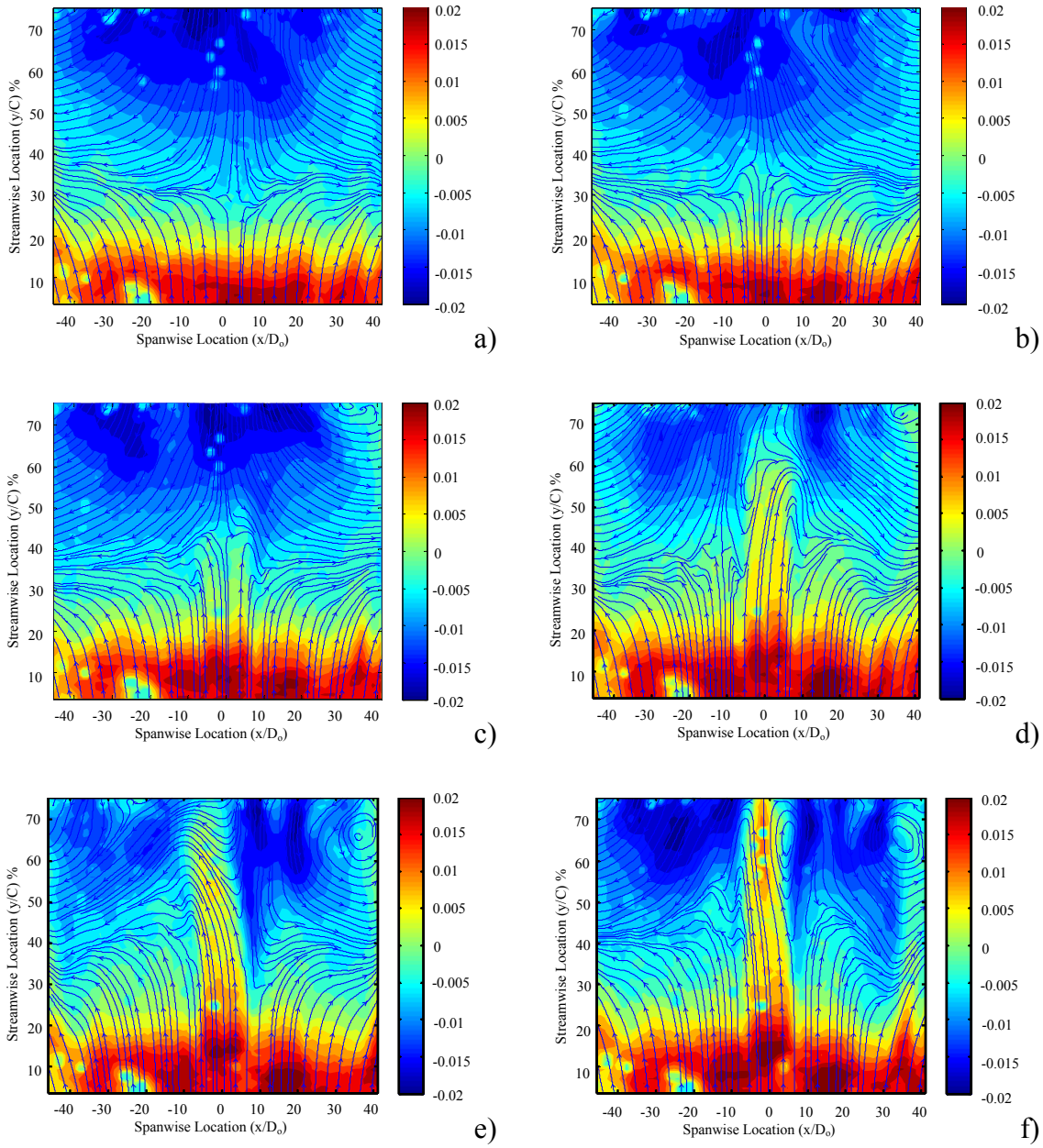

Figure 6.23 Contours and streamlines of averaged velocity on a plane parallel to the inclined plate showing the footprint induced by synthetic jet actuators operated at $St = 0.04$ a) $L = 2$, $VR = 0.08$; b) $L = 4$, $VR = 0.16$; c) $L = 5$, $VR = 0.2$; d) $L = 6$, $VR = 0.24$; e) $L = 7$, $VR = 0.28$ and f) $L = 8$, $VR = 0.32$ (contour units: m/s)

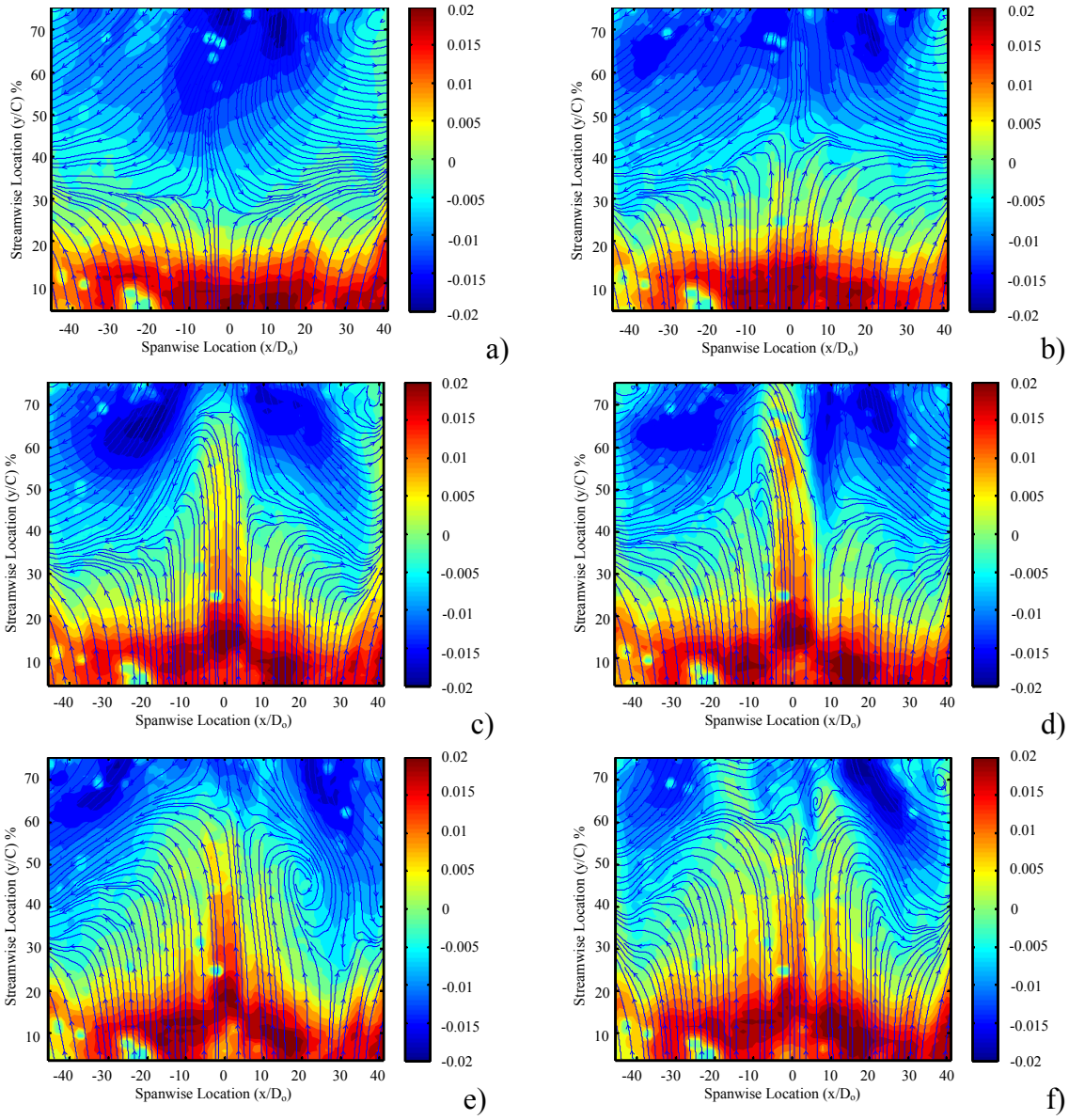

Figure 6.24 Contours and streamlines of averaged velocity on a plane parallel to the inclined plate showing the footprint induced by synthetic jet actuators operated at *St* = 0.08 a) *L* = 2, *VR* = 0.16; b) *L* = 3, *VR* = 0.24; c) *L* = 4, *VR* = 0.32; d) *L* = 6, VR = 0.48; e) *L* = 8, *VR* = 0.64 and f) *L* = 9, *VR* = 0.72 (contour units: m/s)

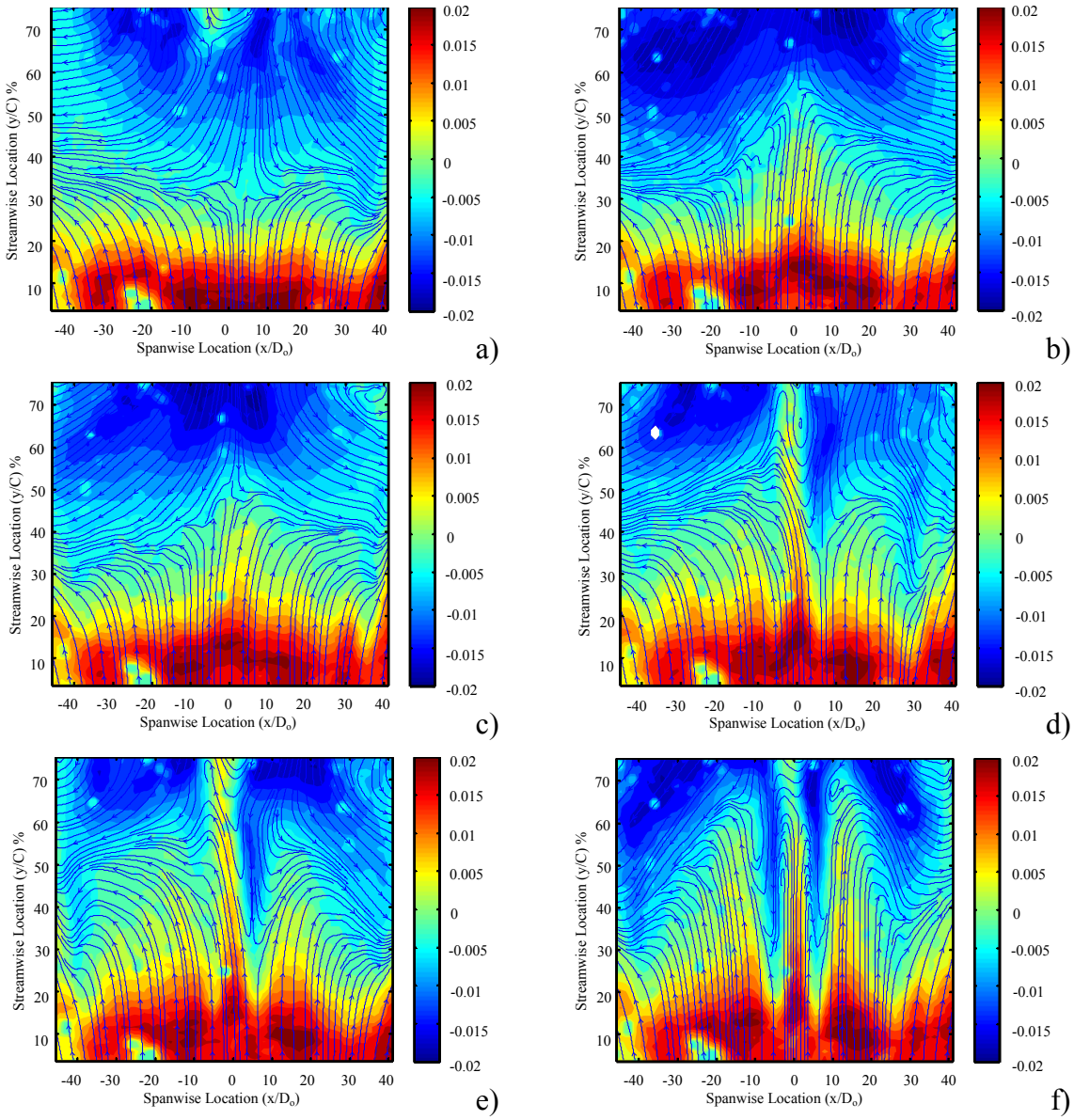

Figure 6.25 Contours and streamlines of averaged velocity on a plane parallel to the inclined plate showing the footprint induced by synthetic jet actuators operated at *St* = 0.16 a) *L* = 2, *VR* = 0.32; b) *L* = 3, *VR* = 0.48; c) *L* = 4, *VR* = 0.64; d) *L* = 5, *VR* = 0.80; e) *L* = 6, *VR* = 0.96 and f) *L* = 7, *VR* = 1.12 (contour units: m/s)

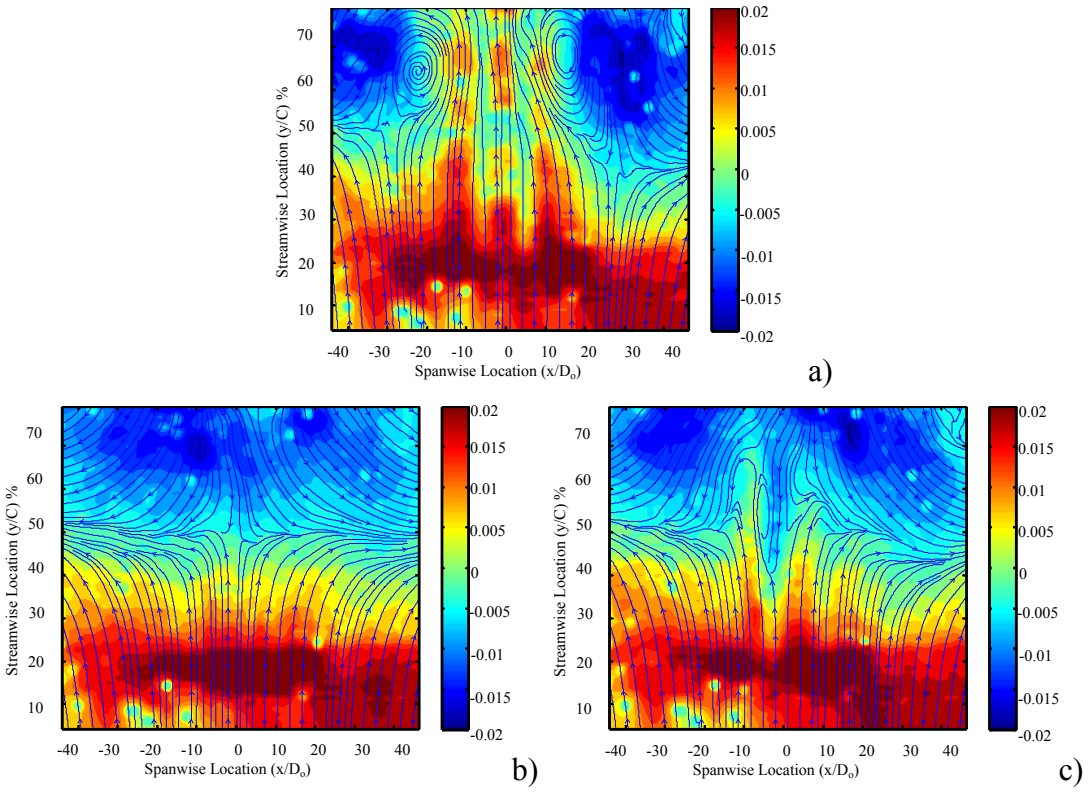

Figure 6.26 Contours and streamlines of averaged velocity on a plane parallel to the inclined plate showing the footprint induced by synthetic jet actuators operated at *St* = 0.32 a) *L* = 2, *VR* = 0.64; b) *L* = 3, *VR* = 0.96 and c) *L* = 4, *VR* = 1.28 (contour units: m/s)

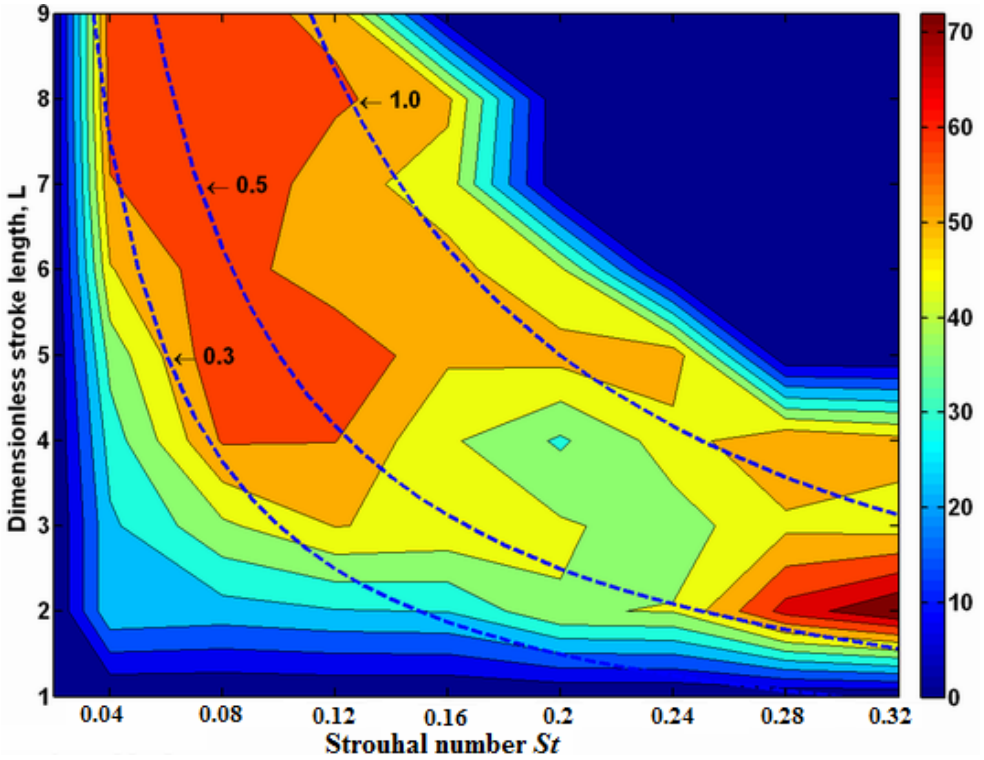

Figure 6.27 Contours of separation control effect under various Strouhal number and dimensionless stroke length (dashes lines are lines with constant *VR*)

6.5 Summary of Findings

In this Chapter, three experiments have been undertaken to study the flow control using a synthetic jet array in a separated laminar flow over a flap in water. Laser induced florescent flow visualisation technique was used to reveal the control effect of synthetic jet array. PIV was employed in both streamwise and spanwise direction to obtain the information about the extent of flow separation delay using synthetic jets operating at different actuation conditions. To summarise the findings from the investigation, it has been found that:

- Different extents of flow separation delay were achieved using synthetic jets operating at different conditions as confirmed by the three separate experiments.
- Based on the results, two contour maps showing the effectiveness of separation control at different actuator operating conditions are produced, one from the visualisation experiment and the other from PIV measurements on the spanwise plane. Both contour maps are in good agreement with each other, revealing similar regions with a good flow control effect.
- Overall, it is found that a good control effect is associated with the presence of hairpin type of structures and a VR in the range of 0.3 to 0.7 which ensures vortical the structures produced by the synthetic jets have a desirable strength and are close to the wall.
- Due to the spanwise growth of the hairpin vortices as they propagate downstream and the small spacing between the adjacent jets in the synthetic jet array tested in the present experiment ($3D_o$), the impact of each individual hairpin vortex merges making the streak pattern produced by individual jets indistinguishable. Therefore in most cases, the footprints of the synthetic jets in the separated flow region appear as a single high-speed streak. The extent of flow separation delay is found to be higher than the cases when the jet spacing is twice as large which can be seen as an advantage.
- For practical flow control application, it is also desirable to achieve the same level of separation control using minimum energy expenditure which implies a minimum diaphragm displacement. Hence for the experimental conditions tested in this thesis, operating the synthetic jets at L around 2 and a VR around 0.6, would deliver the best flow control effect with the least energy consumption.

7 Conclusions and Recommendations

In this final chapter, the main findings from the current research are summarised and some suggestions for future research are also given.

7.1 Conclusions

In this thesis, the behaviour of synthetic jet in quiescent condition, the interaction between synthetic jets and a boundary layer, and the flow separation control effectiveness using an array of synthetic jets have been investigated experimentally. Various experimental techniques including dye flow visualisation, smoke-wire visualisation, fluorescent dye visualisation and Particle Image Velocimetry have been used to qualitative and quantitative information of the flow field. Overall, this thesis has improved the understanding of the behaviour of synthetic jets in quiescent, the interaction of synthetic jets with a boundary layer, and the separation control effect of an array of synthetic jets. The aims and objectives set up in the first Chapter have been achieved.

The main findings from the research are listed as follows:

- It is found that the non-dimensional stroke length L determines the extent of the effect of the onset of suction cycle on the vortex ring and at a low L the vortex ring will be severely weaken by the suction cycle. As a result, if the vortex ring formed is issued into a boundary layer, the suction will have strong impact on the upstream branch of the ring, resulting in the formation of a highly asymmetric vortical structure.
- The Stokes number (S) plays an important role in determining the strength of vortex roll-up as it affects the thickness of the Stokes layer inside the orifice duct hence the shape of the exit velocity profile from the orifice. For the synthetic jet actuator used in the current thesis, a minimum Stokes number of about 9.4 is required to ensure the occurrence of an appreciable vortex roll-up for a dimensionless stroke length greater than 2. This finding implies that in order to ensure an appreciable vortex roll-up desirable for effective flow control, a micro-scale synthetic jet actuator has to be operated at a much higher frequency so as to exceed the threshold value of S.

- The characteristic of synthetic jets of different scales will be identical when the dimensionless stroke length (L), Stokes number (S) and Reynolds number (Re_L) are the same. On the basis of these scaling parameters, the finding acquired from the studies on macro-scale actuators can be applicable to micro-scale actuators, which are more difficult to be measured. Although the linear relationships between (L and Re_L) and actuator operating conditions observed for macro-scale synthetic jets are no longer valid for micro-scale synthetic jets, the linear relationships between the dimensionless jet performance parameters and (L and Re_L) still exist for micro-scale synthetic jets. This finding enables the performance modelling of micro-scale synthetic jet actuators to be simplified.
- It has been identified that three types of vortical structures are produced as a result of the interaction of a synthetic jet with a laminar boundary layer, which are hairpin vortices, stretched vortex rings and tilted vortex rings. Hairpin vortices and stretched vortex rings experience an asymmetric development, as the upstream branches of the vortices are weakened by the vorticity in the boundary layer. Conversely, tilted and distorted vortex rings experience a symmetrical development due to increased jet strength.
- Different extents of flow separation delay were achieved using synthetic jets operating at different conditions. Based on the results, two contour maps showing the effectiveness of separation control at different actuator operating conditions are produced, one from the visualisation experiment and the other from PIV measurements on the spanwise plane. Both contour maps are in good agreement with each other, revealing similar regions with a good flow control effect. Overall, it is found that a good control effect is associated with the presence of hairpin type of structures and a VR in the range of 0.3 to 0.7 which ensures vortical the structures produced by the synthetic jets have a desirable strength and are close to the wall.
- Due to the spanwise growth of the hairpin vortices as they propagate downstream and the small spacing between the adjacent jets in the synthetic jet array tested in the present experiment ($3D_o$), the impact of each individual hairpin vortex merges making the streak pattern produced by individual jets indistinguishable. Therefore in most cases, the footprints of the synthetic jets in the separated flow region appears as a single high-speed streak. The extent of

flow separation delay is found to be higher than the cases when the jet spacing is twice as large which can be seen as an advantage.

- For practical flow control application, it is also desirable to achieve the same level of separation control using minimum energy expenditure which implies a minimum diaphragm displacement. Hence for the experimental conditions tested in this thesis, operating the synthetic jets at L around 2 and a VR around 0.6, would deliver the best flow control effect with the least energy consumption.

7.2 Recommendations

In order to implement the synthetic jet actuators for flow separation control at full-scale flight conditions, there is a plenty of scopes for future development. Here three possible areas where further research can be undertaken are suggested.

This thesis has studied the types of vortical structures produced as a result of the interaction between synthetic jets and a zero-pressure gradient laminar boundary layer, and their flow separation control effectiveness over a flap. Therefore, the future research needs to extend to a turbulent boundary layer to verity if the types of vortical structures generated are similar to those in found a laminar flow and conditions at which they exist. In addition, the separation control effectiveness of the different vortical structures in an incipiently separated turbulent boundary layer, subjected to adverse pressure gradients should be studied.

In the flow control experiment conducted in this thesis, the jet spacing and the spacing between the jet array and the separation line are fixed so as to evaluate the effect of changing synthetic jet operating conditions. The jet spacing and the spacing between the jet array and the separation line are, in fact, two additional important parameters which can be varied in order to seek for a stronger flow control effect hence their effects are worth exploring in the future experiments.

In this project, synthetic jets issued through a normal circular orifices. More effective injection of momentum and vorticity could be obtained by using pitching or skewing orifices relative to the incoming flow. Hence some further studies of the behaviour of pitched and skewed synthetic jets could be carried out.

Reference

Acarlar, M.S and Smith, C.R.; A study of hairpin vortices in a laminar boundary layer, Part 2: Hairpin vortices generated by fluid injection; *Journal of Fluid Mechanics*, Vol. 175, pp. 43-83, 1987

Adrian, R.J.; Twenty years of particle image velocimetry; *Experiments in Fluids*, Vol. 39, pp. 159-169, 2005

Adrian, R.J.; Multi-point optical measurement of unsteady flow; *Int. J. Heat & Fluid Flow*, Vol. 7, pp. 127-145, 1986

Adrian, R.J.; Particle-imaging techniques for experimental fluid mechanics; *Annual Rev. Fluid. Mech.*, Vol. 22, pp. 261-304, 1991

Ahuja, K.K., Whipkey, R.R. and Jones, G.S.; Control of turbulent boundary layer flow by sound; AIAA Paper 83-0726, 1983

Amitay M., Kibens V., Parekh D. and Glezer A.; The dynamics of flow reattachment over a thick airfoil controlled by synthetic jet actuators; AIAA Paper 99-1001, 1999

Amitay M., Smith B.L. and Glezer A.; Aerodynamic flow control using synthetic jet technology; AIAA Paper 98-0208, 1998

Amitay, M., Smith, D.R., Kibens, V., Parekh, D. and Glezer A.; Aerodynamic flow control over an unconventional airfoil using synthetic jet actuators; *AIAA Journal*, Vol. 39, NO. 3, March 2001

Amitay, M. and Glezer, A.; Controlled transients of flow reattachment over stalled airfoils; *International Journal of Heat and Fluid flow*, Vol. 23, pp. 690-699, 2002

Attinello, J.S.; Flow control - the integration of power plant and airframe for future aircraft; Bureau of Aeronautics Research Division, Report No. DR-1745, 1952

Attinello, J.S.; Design and engineering features of flap blowing installations; In: Lachmann, G.V.; Boundary layer and flow control. Its principles and application; Vol. 1, New York, Pergamon Press, pp. 463-515, 1961

Auerbach, D.; Some open questions on the flow of circular vortex rings; Fluid Dynamics Research, Vol. 3, pp. 209-213, 1988

Benjamin, T.B.; The alliance of practical and analytical insights into the non-linear problems of fluid mechanics; In Germain, P. and Nayroles, B. editors, Applications of methods of Functional Analysis in Mechanics, Lecture Notes in Mathematics, Vol. 503, pp. 8-28. Springer-Verlag, 1976

Bernard, P.S. and Wallace, J.M.; Turbulent Flow; *Analysis Measurement and Prediction*, Whiley, 2002

Betz, A.; History of boundary layer control in Germany; In: Lachmann, G.V.; Boundary layer and flow control. Its principles and application; Vol. 1, New York, Pergamon Press, pp. 1-20, 1961

Bewley T.R.; Flow control: new challenges for a new Renaissance; *Progress in Aerospace Sciences*, Vol. 37, pp. 27-58, 2001

Bushnell, D. M.; Turbulence sensitivity and control in wall flows; *Theoretical Approaches to Turbulence, Applied Mathematical Sciences*, Vol. 58, pp. 1-19, 1985

Carriere, P. and Eichelbrenner E.A.; Theory of flow reattachment by a tangential jet discharging against a strong adverse pressure gradient; In: Lachmann, G.V.; Boundary layer and flow control. Its principles and application; Vol. 1, New York, Pergamon Press, pp. 209-231, 1961

Cary, A. W., Donovan, J. F., and Kral, L.D.; Flow Structure Development over an Electromagnetic Turbulence Control (EMTC) Actuator; ASME Paper No. FEDSM99-6932, Proceedings of the 3rd ASME/JSME Joint Fluids Engineering Conference,

Symposium on Control of Wall-Bounded and Free-Shear Flows, eds. Kral, L. D. and Shakouchi, T., San Francisco, CA, July, 1999

Cater, J.E and Soria, J.; The evolution of round zero-net-mass-flux jets; *Journal of Fluid Mechanics*, Vol. 472, pp. 167-200, 2002

Cattafesta, L. N. III, Garg, S. and Choudhari, M.; Active control of flow-induced cavity resonance; AIAA Paper 97-1804, 4th AIAA Shear Flow Control Conference, Snowmass, CO, June, 1997

Cattafesta, L. N. III, Shukla, D., Garg, S. and Ross, J. A.; Development of an adaptive weapons-bay suppression system; AIAA Paper No. 99-1901, 5th AIAA Aeroacoustics Conference, Seattle, WA, May, 1999

Chang, Y.K and Vakili, A.D.; Dynamics of vortex rings in crossflow; *Physics of Fluids*, Vol. 7, No. 7, pp. 1583-1597, 1995

Collins, F.G. and Zelenevitz, J.; Influence of sound upon separated flow over wings; *AIAA Journal*, Vol. 13, No. 3, pp.408-10, 1975

Collis, S.S., Joslin, R.D., Seifert, A. and Theofilis, V.; Issues in active flow control: theory, control, simulation and experiment; Progress in Aerospace Sciences, Vol. 40, No. 4-5, pp. 237-289, 2004

Crook, A.; The Control of Turbulent Flows using Synthetic jets Actuators; PhD Dissertation, School of Engineering, The University of Manchester, UK, 2002

Crook, A., Crowther, W.J. and Wood, N.J.; A parameter study of a synthetic jet in a cross flow; 22nd International Congress of Aeronautical Sciences, Harrogate, UK, 2000

Crook A., Sadri A.M., and Wood N.J.; The development and implementation of synthetic jets for the control of separated flow; AIAA Paper 99-3176, 1999

Crook, A. and Wood, N.J.; Measurements and visualisations of synthetic jets; In AIAA 39th Aerospace Science Meeting and Exhibit, Reno, Nevada, 2001

Crook, A. and Wood, N.J.; A parametric investigation of a synthetic jet in quiescent conditions; 9th International Symposium on Flow Visualisation, Edinburgh, UK, 2000

Crook, A. and Wood, N.J.; Measurements and visualization of synthetic jets; AIAA Paper 2001-0145, 39th Aerospace Meeting and Exhibit, Reno, Nevada, USA, 8-11 January 2001

Cui, J., Agarwal, R.K. and Cary, A.W.; Numerical simulation of the interaction of a synthetic jet with a turbulent boundary layer; AIAA 2003-3458, 33rd Fluid Dynamics Conference & Exhibit, Orlando, USA, 23-26 June, 2003

Didden, N.; Untersuchung laminarer, instabiler ringwerbel mittels laser Doppler anemometrie; Technical Report Technical Report 64, Max Planck Institut fÄur Stoemungsforschung und der Aerodyna, Versuchsanst, 1977

Didden, N.; On the formation of vortex rings: Rolling-up and production of circulation; *Journal of Applied Mechanics and Physics (ZAMP)*, Vol. 30, pp. 101-116, 1979

Donovan, J. F., Kral, L. D., and Cary, A. W.; Numerical Simulation of a Lorentz Force Actuator; AIAA Paper 97-1918, 4th AIAA Shear Flow Control Conference, Snowmass, CO, June, 1997

Donovan, J. F., Kral, L. D. and Cary, A. W.; Active Flow Control Applied to an Airfoil; AIAA Paper 98-0210, 36th AIAA Aerospace Sciences Meeting, Reno, NV, January, 1998

Dowling, A.P. and Ffowcs Williams, J.E.; Sound and Sources of Sound, Ellis Horwood, Chichester, England, UK, 1983

Fiedler, H.E. and Fernholz, H.H.; On management and control of turbulent shear flows; *Prog. Aerospace Sci*., Vol. 27, pp. 305-387, 1990

Flatt, J.; The history of boundary layer control research in the United States of America; In: Lachmann, G.V.; Boundary layer and flow control. Its principles and application; Vol. 1, New York, Pergamon Press, pp. 122-143, 1961

Fugal S.R., Smith B.L., and Spall R.E.; A numerical study of 2-D synthetic jet formation; ASME Heat Transfer/Fluids Engineering Summer Conference, HT-FED2004-56854, 2004

Fugal, S.R., Smith, B.L. and Spall, R.E.; Displacement amplitude scaling of a two dimensional synthetic jet; *Physics of Fluids*, Vol. 17, No. 4, 045103, 2005

Fujisawa, N.; Oguma, Y. and Nakano, T.; Measurements of wall-shear-stress distribution on an NACA0018 airfoil by liquid-crystal coating and near-wall particle image velocimetry (PIV); Measurement Science and Technology, Vol. 20, No. 6, 2009

Gad-el-Hak, M.; Introduction to Flow Control; In Flow Control: Fundamentals and Practices; Gad-el-Hak, M., Pollard, A. and Bonnet, J-P. (editors), Springer, pp. 1-107, 1998

Gallas, Q., Holman, R., Nishida, T,, Carroll, B., Sheplak, M. and Cattafesta, L.; Lumped element modeling of piezoelectric-driven synthetic jet actuators; *AIAA Journal*, Vol. 41, No. 2, pp. 240-247, 2003a

Gharib, M., Rambod, E. and Shariff, K.; A universal time scale for vortex ring formation; *Journal of Fluid Mechanics*, Vol. 360, pp. 121-140, 1998

Gilarranz, J. L. and Rediniotis, O. K.; Compact, high-power synthetic jet actuators for flow separation control; In Paper AIAA 2001-0737, Proc. 39th AIAA Aerospace Sciences Meeting and Exhibit, 2001

Glezer, A.; The formation of vortex rings; *Phys. Fluids*, Vol.31, No. 12, pp. 3532-3542, Dec., 1988

Glezer, A. and Amitay, M.; Synthetic jets; *Annual Review of Fluid Mechanics*, Vol. 34, pp. 503-529, 2002

Gomes, L.D., Crowther, W.J., and Wood, N.J.; Towards a practical piezoceramic diaphragm based synthetic jet actuator for high subsonic applications – effect of excitation and frequency on effectiveness and efficiency, Paper 122, IUTAM Symposium on Flow Control and MEMS, London, UK, Sep 2006b

Greenblatt, D and Wygnanski, I.J.; The control of flow separation by periodic excitation; *Progress in Aerospace Sciences*, Vol. 36, pp. 487-545, 2000

Harrison, T.J.; Separation control on high lift systems using vane vortex generators; PhD thesis, School of Mechanical, Aerospace and Civil Engineering, The University of Manchester, 2006

Haidari, A.H and Smith, C.R.; The generation and regeneration of single hairpin vortices; *Journal of Fluid Mechanics*, Vol. 277, pp. 135-162, 1994

Head, M.R.; History of research on boundary layer control for low drag in UK; In: Lachmann, G.V.; Boundary layer and flow control. Its principles and application; Vol. 1, New York, Pergamon Press, pp. 104-21, 1961

Head, M.R and Bandyopadyay, P.; New aspects of turbulent boundary-layer structure; *Journal of Fluid Mechanics*, Vol. 107, pp. 297-338, 1981

Ho, C.-M. and Tai, Y.-C.; Review: MEMS and its applications for flow control; *ASME Journal of Fluid Engineering*, Vol. 118, pp. 437-447, 1996

Ho, C.-M. and Tai, Y.-C.; Micro-Electro-Mechanical Systems (MEMS) and fluid flows; *Annual Review of Fluid Mechanics*, Vol. 310, pp. 579-612, 1998

Holman, R., Utturkar, Y., Mittal, R., Smith, B.L. and Cattafesta, L.; Formation criterion for synthetic jets; *AIAA Journal*, Vol. 43, No. 10, pp. 2110-2116, 2005

Houghton, E.L and Carpenter, P.W.; Aerodynamics for engineering students; Oxford Butterworth Heinemann, 2003

Jabbal, M., Wu, J. and Zhong, S.; The performance of round synthetic jet in quiescent flow; *The Aeronautical Journal of the Royal Aeronautical Society*, pp. 385-393, June 2006

Jabbal, M., Tang, H. and Zhong, S.; The effect of geometry on the performance of synthetic jet actuators; Paper 2.11, 25th International Congress of the Aeronautical Sciences (ICAS), Hamburg, Germany, 3-8 September 2006

Jabbal, M. and Zhong, S.; The near wall effect of synthetic jets in a laminar boundary layer; AIAA 2006-3180, 3rd Flow Control Conference, San Francisco, US, 5-8 June 2006.

Jabbal, M.; Understanding the behaviour of synthetic jets in a boundary layer for flow separation control; PhD thesis, School of Mechanical, Aerospace and Civil Engineering, The University of Manchester, 2008

Janhavi, S. A., Mark S., David, P. A. and Louis C.; MEMS-based electrodynamics synthetic jet actuators for flow control applications; IUTAM SYMPOSIUM ON FLOW CONTROL AND MEMS, IUTAM Bookseries, Vol. 7, Part 1, pp. 25-32, 2008

Katz, Y., Horev, E. and Wygnanski, I.; The forced turbulent wall jet; *Journal of Fluid Mechanics*; Vol. 242, pp. 577-610, 1992

Keane, R. D. and Adrian, R. J.; Theory of cross-correlation analysis of PIV images; Applied Scientific Research; Vol. 49, pp. 191-215, 1992

Kinsler, L.E., Frey, A.R., Coppens, A.B., and Sanders, J.V.; Fundamentals of Acoustics, 3rd Edition, John Wiley & Sons, New York, 1982

Kral, L.D.; Active flow control technology; ASME Fluids Engineering Division Technical Brief, 1998

Lamb, S.H.; Hydrodynamics; Cambridge University Press, Cambridge, England, 1997

Lee, C.Y and Goldstein, D.B.; Two-dimensional synthetic jet simulation; *AIAA Journal*, Vol. 40, No. 3, pp. 510-516, 2002

Li, M.; Flow and Heat Transfer Characteristics of Impinging Circular Synthetic Jets; PhD thesis, School of Mechanical, Aerospace and Civil Engineering, The University of Manchester, 2007

Liddle, S.C. and Crowther, W.J.; Systems and certification issues for active flow control systems for separation control on civil transport aircraft; AIAA 2008-0158, 46th Aerospace Sciences Meeting & Exhibit, Reno, USA, 7-10 January 2008

Lin, J.C.; Control of turbulent boundary-layer separation using micro-vortex generators; AIAA paper 99-3404, 1999

Lin J.C.; Robinson S.K., McGhee R.J. and Valarezo W.O.; Separation control on high-lift airfoils via micro-vortex generators; *Journal of Aircraft*, Vol. 31, No. 6, pp. 1317-1323, 1994

Lockerby, D.A. and Carpenter, P.W.; Modeling and design of microjet actuators, AIAA Journal, Vol. 42, No. 2, pp. 220-227, 2004

Lockerby, D.A., Carpenter, P.W. and Davies, C.; Is Helmholtz resonance a problem for micro-jet actuators?; Flow, Turbulence and Combustion, Vol. 78, Nos. 3-4, pp. 283-308, 2007

Lord Kelvin; Vortex statics; Philosophical Magazine, Vol. 10, pp. 97-109, 1880

Lumley, J. and Blossey, P.; Control of turbulence; *Annual Review of Fluid Mechanics*; Vol. 310, pp. 311-327, 1998

Magill J. and McManus K.; Exploring the feasibility of pulsed jet separation control for aircraft configurations; *Journal of Aircraft*, Vol. 38, No. 1, pp. 48-56, 2001

Mallinson, S.G., Reizes, J.A. and Hong, G.; An experimental and numerical study of synthetic jet flow; *The Aeronautical Journal*, Vol. 105, pp. 41-49, 2001

McCormick D.C.; Boundary layer separation control with directed synthetic jets; AIAA Paper 2000-0519, 2000

McManus K. and Magill J.; Separation control in incompressible and compressible flows using pulsed jets; AIAA Paper 96-1948, 1996

McMichael, J. M.; Progress and prospects for active flow control using Microfabricated Electro-Mechanical Systems (MEMS); AIAA Paper 96-0306, 34th AIAA Aerospace Sciences Meeting, Reno, NV, January, 1996

Melling, A.; Tracer particles and seeding for particle image velocimetry; *Measurement Science and Technology*, Vol. 8, pp. 1406-1416, 1997

Merzkirch, W.; Flow Visualisation; 2nd ed. Academic Press, Orlando, 1987

Milanovic, I.M. and Zaman, KBMQ.; Synthetic jet in crossflow; *AIAA Journal*, Vol. 43, No. 5, pp. 929-940, 2005

Mittal, R., Rampunggoon, P. and Udaykumar, H.S.; Interaction of a synthetic jet with a flat plate boundary layer; AIAA 2001-2773, 31st Fluid Dynamics Conference&Exhibit, Anaheim, USA, 11-14 June, 2001

Modi, V.J., Hill, S.S. and Yokomizo, T.; Drag reduction of trucks through boundary-layer control; *J. Wind Eng. Ind. Aerodyn.*, Vol. 54, pp. 583-94, 1995

Mohseni, K. and Gharib, M.; A model for the universal time scale of vortex ring formation; *Physics of Fluids*, Vol. 10, No.10, pp. 2436-2438, 1998

Moin, P. and Bewley, T.R.; Feedback control of turbulence, *Appl. Mech. Rev.*, Vol. 47, No. 6, part2, June 2004

Müller, M.O., Bernal, L.P., Miska, P.K., Washabaugh, P.D., Chou, T-K.A., Parviz, B.A., Zhang, C. and Najafi, K.; Flow structure and performance of axisymmetric synthetic jets; AIAA 2001-1008, 39th Aerospace Sciences Meeting & Exhibit, Reno, USA, 8-11 January, 2001

Narasimha, S. and Prasad, S.N.; Leading edge shape for flat plate boundary layer studies; *Experiments in Fluids*, Vol. 17, No. 5, pp. 358-360, 1994

Neuburger, D. and Wygnanski, I.; The use of a vibrating ribbon to delay separation on two dimensional airfoils; Proceedings of Air Force Academy Workshop on Unsteady Separated Flow (Colorado Springs, CO), edited by F. J. Seiler, Research Labs. Rept. TR-88-0004, U. S. Air Force Academy, 1987

Nishri, B and Wygnanski, I.; Effects of periodic excitation on turbulent flow separation from a flap; *AIAA Journal*, Vol. 36, No. 4, pp. 547-556, 1998

Nosenchuck, D. M., Brown, G. L., Culver, H. C., Eng, T. I., and Huang, I. S.; Spatial and temporal characteristics of boundary layers controlled with the Lorentz force; Extended Abstract; Twelfth Australasian Fluid Mechanics Conference, Sydney, Australia, 1995

Nosenchuck, D. M. and Brown, G. L.; The Direct Control of Wall Shear Stress in a Turbulent Boundary Layer; MAE Report T1954, Princeton University, Princeton, New Jersey, 1992

Nosenchuck, D. M.; Boundary layer control using the Lorentz force; Proceedings of the Forum on Control of Transitional and Turbulent Flows, ASME Fluids Engineering Conference, Vol.237, 1996

Onsrud, G., Person, L. N. and Saetran, L. R.; On the measurement of wall shear stress; Experiment in Fluids; Vol. 5, No. 1, pp. 11-16, 1987

Poisson-Quinton, Ph.; Recherches theoriques et experimentales sur la controle de couche limits; 7th Congress of Applied Mechanics, London, September 1948

Poisson-Quinton, Ph. and Lepage, L.; Survey of French research on the control of boundary layer and circulation In: Lachmann, G.V.; Boundary layer and flow control. Its principles and application; Vol. 1, New York, Pergamon Press, pp. 21-73, 1961

Prandtl, L.; Über Flüssigkeitsbewegung bei sehr kleiner Reibung (On the motion of fluid with very small viscosity); Proceedings of the 3rd International Mathematical Congress, Heidelberg, Germany, pp. 484-491, 1904

Raffel, M., Willert, C. and Kompenhan, J.; Particle Image Velocimetry: A Practical Guide; Springer-Verlag, Berlin, 1998

Rathnasingham, R. and Breuer, K. S.; Coupled fluid-structural characteristics of actuators for flow control; *AIAA Journal*, Vol. 35, No. 5, pp. 832-837, 1997

Rediniotis, O.K., Ko J., Yue X., and Kurdila A.J.; Synthetic jets: their reduced order modeling and applications to flow control; AIAA Paper 99-1000, 1999

Reneaux, J.; Overview on drag reducing technologies for civil transport aircraft; European Congress on Computational Methods in Applied Science and Engineering, Jyvaskyla, Finland, 24-28 July 2004

Rizzetta, D.P., Visbal, M.R. and Stanek, M.J.; Numerical investigation of synthetic jet flow fields; *AIAA Journal*, Vol. 37, No. 8, pp. 919-927, 1999

Rosenfield, M., Rambod, E. and Gharib, M.; Circulation and formation number of laminar vortex rings; *Journal of Fluid Mechanics*, Vol. 376, pp. 297-318, 1998

Ryan, H. and Yogen, U.; Formation criterion for the synthetic jets; *AIAA Journal*, Vol. 43, No. 10, October, 2005

Saffman, P.G.; Vortex Dynamics; Cambridge University Press, Cambridge, England, 1992

Schaeffler, N.W.; The interaction of a synthetic jet and a turbulent boundary layer; AIAA 2003-0643, 41st Aerospace Sciences Meeting & Exhibit, Reno, USA, 6-9 January, 2003

Schlichting, H. and Gersten, K.; Boundary layer theory; 8th Revised and Enlarged Edition; Springer; 2000

Sellars, N.; Flow control – innovative technologies to increase aircraft performance; University of Manchester lecture, BAE SYSTEMS 2003

Seifert A., Bachar T., Koss D., Shepshelovich M., and Wygnanski I.; Oscillatory blowing, a tool to delay boundary layer separation; *AIAA Journal*, Vol. 31, No. 11, pp. 2052-2060, 1993

Seifert, A. and Pack, L. G.; Oscillatory control of separation at high Reynolds Numbers; AIAA Paper 99-0214, 1999a

Seifert, A., Darabi, A., and Wygnanski, I.; Delay of airfoil stall by periodic excitation; *AIAA J Aircraft*, Vol. 33, No. 4, pp. 691-8, 1996

Shariff, K. and Lenoard, A.; Vortex rings; *Annual Review of Fluid Mechanics*, Vol. 24, pp. 235-279, 1992

Shepshelovich, M., Koss, D., Wygnanski, I. and Seifert, A.; Active flow control on low Re Airfoils; AIAA Paper 89-0538, January, 1989

Shusser, M. and Gharib, M.; Energy and velocity of a forming vortex ring; *Physics of Fluids*, Vol. 12, No. 3, pp. 618-621, 2000

Shusser, M., Gharib, M. and Mohseni, K.; A new model for inviscid vortex ring formation; AIAA Paper 99-3805, Proc. 30th AIAA Fluid Dynamics Conference, June 28-July 1, 1999

Shuster, J.M. and Smith, D.R.; A study of the formation and scaling of a synthetic jet; AIAA Paper 2004-0090; 42nd AIAA Aerospace Sciences Meeting and Exhibition, Reno, Nevada, USA ,5-8 January, 2004

Smith, B.L. and Glezer, A.; The formation and evolution of synthetic jets; *Physics of Fluids*, Vol. 10, No. 9, pp. 2281-2297, 1998

Smith, B.L. and Glezer, A.; Vectoring and small-scale motions effected in free shear flows using synthetic jet actuators; AIAA Paper 97-0213, 35th AIAA Aerospace Sciences Meeting, Reno, NV, January, 1997

Smith, B.L. and Swift, G.W.; Synthetic jets at large Reynolds number and comparison to continuous jets; AIAA Paper 2001-3030, 31st AIAA Fluid Dynamics conference and Exhibition, Anaheim, California, USA, 11-14 June 2001

Smith, B.L and Swift, G.W.; A comparison between synthetic jets and continuous jets; *Experiments in Fluids*, Vol. 34, pp. 467-472, 2003

Smith, B.L., Trautman, M.A. and Glezer, A.; Controlled interactions of adjacent synthetic jets; AIAA Paper 1999-0669, 37th Aerospace Sciences Meeting & Exhibit, Reno, USA, 11-14 January 1999

Smith D.R., Amitay M., Kibens K., Parekh D.E. and Glezer A.; Modification of lifting body aerodynamics using synthetic jet actuators; AIAA Paper 1998-0209, 1998

Sumer, B. M., Arnskov, M. M., Christiansen, N, and Jorgensen, F. E.; Two-component hot-film probe for measurements of wall shear stress; Experiments in Fluids; Vol. 15, No. 6, pp. 380-384, 1993

Tachie, M.F., Bergstrom, D.J., Balachandar, R. and Ramachandran, S.; Skin friction correlation in open channel boundary layers; *Journal of Fluids Engineering*; Vol. 123, pp. 953-956, 2001

Tang, H.; Performance modeling of synthetic jet actuators for flow separation control; PhD thesis, School of Mechanical, Aerospace and Civil Engineering, The University of Manchester, 2006

Tang, H. and Zhong, S.; The effect of actuator geometry on the performance of synthetic jets; CEAS/KATnet Conference on Key Aerodynamic Technologies, Bremen, Germany, 20-22 June 2005

Tang, H. and Zhong, S.; Incompressible flow model for synthetic jets actuators; *AIAA Journal*, Vol. 44, No. 4, pp. 908-912, 2006

Tang, H. and Zhong, S.; Modeling of the characteristics of synthetic jet actuators using the lumped element model; Third AIAA Flow Control Conference, AIAA Paper 2006-3696, San Francisco, USA, 2006

Thmoshenko, S. and Woinowsky-Krieger, S.; Theory of Plates and Shells; Second Edition, McGraw-Hill, London, 1959

Warsop, C.; MEMS and microsystems technologies – their potential and status for drag reduction and separation control; European Congress on Computational Methods in Applied Science and Engineering (ECCOMAS), Jyväskylä, Finland, 24-28 July 2004.

Warsop, C., Hucker, M., Press, A.J. and Dawson, P.; Pulsed air-jet actuators for flow separation control; Flow, Turbulence and Combustion, Vol. 78, Nos. 3-4, pp. 255-281, 2007.

Wood, N.J., Sadri, A.M. and Crook, A.; Control of turbulent flow separation by synthetic jets; AIAA Paper 2000-4331, 18th AIAA Applied Aerodynamics Conference, Denver, USA, 14-17 August, 2000

Wu, J.Z., Lu, X.Y., Denny, A. G., Fan, M. and Wu, J.M.; Post-Stall Flow Control on an Airfoil by Local Unsteady Forcing; *Journal of Fluid Mechanics*, Vol. 71, pp. 21-58, 1998

Yao, C., Chen, F.J., Neuhart, D. and Harris, J.; Synthetic jet flow field database for CFD validation; AIAA Paper 2004-2218, 2nd AIAA Flow Control Conference, Portland, USA, 28 June - 1 July, 2004

Zaman, K.B.M.Q., Bar-Sever, A. and Mangalam, SM.; Effect of acoustic excitation on the flow over a low-Re airfoil; *J. Fluid Mech.*, Vol. 182, pp. 127-48, 1987

Zaman, K.B.M.Q.; Effect of acoustic excitation on stalled flows over an airfoil; *AIAA Journal*, Vol. 30, No. 6, 1992

Zhang, S.Y. and Zhong, S.; An experimental investigation of flow separation control using an array of synthetic jets; 39th AIAA Fluid Dynamics Conference, San Antonio, Texas, 22-25 June 2009

Zhong, S., Mullef, F. and Wood, N.J.; Interaction of circular synthetic jets with a laminar boundary layer; *Aeronaut Journal*, Vol. 109, pp. 461-470, 2005

Zhou, J., Adrian, R.J., Balachandar, S. and Kendall, T.M.; Mechanisms for generating coherent packets of hairpin vortices in channel flow; *Journal of Fluid Mechanics*, Vol. 387, pp. 353-396, 1999

Zhou, J. and Zhong, S.; Numerical Simulation of the Interaction of a Circular Synthetic Jet with a Boundary Layer; Computers and Fluids; Vol. 38, No. 2, pp. 393-405, 2009